Technische Universität München
TUM School of Engineering and Design

Advanced Numerical Modelling of Particle-laden Turbulent Flow with Emphasis on Fine Sediment Infiltration into Static Gravel Bed

Atul Jaiswal

Vollständiger Abdruck der von der TUM School of Engineering and Design der Technischen Universität München zur Erlangung eines

Doktors der Ingenieurwissenschaften (Dr.-Ing.)

genehmigten Dissertation.

Vorsitz:		Prof. Dr.-Ing. Markus Disse
Prüfende der Dissertation:	1.	Priv.-Doz. Dr.-Ing. habil. Minh Duc Bui
	2.	Prof. Dr. phil. Nils Rüther
	3.	Prof. Dr. Stefan Haun

Die Dissertation wurde am 26.09.2024 bei der Technischen Universität München eingereicht und durch die TUM School of Engineering and Design am 04.02.2025 angenommen.

माँ और दादीमाँ को समर्पित

– अंकी

Abstract

Fluid-particle systems are omnipresent in nature and industrial applications. In hydraulic engineering, sediment transport exemplifies a fluid-particle system that can be mathematically described and analyzed in greater detail by a system of differential equations in the Eulerian-Eulerian, and Eulerian-Lagrangian frameworks. In this dissertation, the Eulerian-Lagranagian framework is applied, combining Computational Fluid Dynamics (CFD) with the Discrete Element Method (DEM), commonly referred as the CFD-DEM approach.

Sediment transport is a complex process governed by many inter-dependent variables such as flow, turbulence, particle size, and shape. I focus on a specific sub-process of sediment transport, "fine sediment infiltration into a static gravel bed", crucial for various fluvial and ecological dynamics. The process of fine sediment infiltration can be categorized as a dense fluid-particle system, where not only fluid-particle but also particle-particle interaction becomes significant. This dissertation investigates the influences of flowing water, turbulence modelling, particle size distribution (PSD), and particle shape on the simulation of fine sediment infiltration. Before applying the CFD-DEM approach to study fine sediment infiltration, the unresolved CFD-DEM method is critically evaluated regarding the coupling regime, turbulence modelling, particle characteristics, computational feasibility, and method limitations, referencing a dispersed fluid-particle system.

Unlike conventional sediment transport models that use empirical equations to estimate sediment transport parameters, the CFD-DEM approach provides detailed flow and particle-scale information. However, the CFD-DEM approach requires high-performance computing (HPC) due to heavy DEM computations and high-fidelity CFD, involving coupling between CFD and DEM to capture fluid-particle interactions. The method also has constraints concerning the number and size of particles, limiting its application only to detailed investigations with a limited number of particles and up to a certain extent of flow resolution. Flow field resolution depends on whether turbulence is modelled (e.g., Reynolds-Averaged Navier-Stokes; RANS) or resolved to a certain extent (e.g., Large Eddy Simulation; LES).

Numerical simulations are performed using OpenFOAM-based software packages. For evaluating the CFD-DEM approach, two similar yet different particle-tracking solvers in OpenFOAM are employed: "DPMFoam" and "pimpleLPTFoam". The solver "DPMFoam" is a standard solver in OpenFOAM, whereas "pimpleLPTFoam" is a self-compiled solver designed to investigate the effects of particle fraction in each CFD cell. Additionally, to accurately represent gravel and sand particles, OpenFOAM was coupled with a separate DEM software, called LIGGGHTS, using the CFDEM-Coupling code.

Evaluating the CFD-DEM method reveals that simple dispersion models, typically employed to recover the lost turbulence fluctuations due to RANS averaging, tend to underpredict particle dispersion. Hence, more sophisticated dispersion models should be implemented under the RANS-DEM framework to capture accurate particle behaviour in a turbulent flow. Turbulence-resolving approaches like LES-DEM can offer more realistic particle behaviour in turbulent flows. However, LES-DEM is rarely feasible due to constraints requiring particles to be smaller than CFD cell sizes in the unresolved CFD-DEM. In such cases, especially near walls where smaller cell sizes are needed to resolve the boundary layer, the dynamic LES turbulence models can mitigate the limitations of static LES turbulence models. For highly dispersed flows, having small particle concentrations, one-way coupling, and neglecting particle fractions in each CFD cell can still suffice to predict accurate particle behaviour in turbulent flow, saving considerable computational resources.

Applying the unresolved CFD-DEM approach to model the fine sediment infiltration reveals that (1) the occurrence of different infiltration behaviours (bridging or percolation) are independent of gravel bed thickness and only depend on relative fine sediment size, and (2) the definition of a sufficient thick gravel bed is necessary to distinguish between bridging and percolation behaviours. Investigating the effects of flowing water on the infiltration process supports Cui's hypothesis that fine sediment infiltration driven by intra-gravel flow behaves similarly to fine sediment infiltration driven by gravity. Essentially, the fine sediment infiltration process is mainly gravity-dominated as long as the gravel bed remains immobile.

Particle shape effects concerning non-sphericity and irregularities are implicitly included in the numerical model by restricting the rolling of spherical particles. It was shown that particle shape effects significantly impact the infiltration process, and considering particle shape effects by using rolling resistance models seems to be the most efficient way. Particle size distribution (PSD) investigation for the infiltration process suggests that reducing the grain-size classes in PSD of gravel and fine sediment is necessary to realize the CFD-DEM simulation within a reasonable timeframe and computational resources. However, the reduction in grain classes is only justified when the infiltrating characteristics of fine sediment and gravel are not significantly modified, and the size ratio remains within the thresholds of infiltration behaviors (bridging or percolation). Particle shape and PSD effects are linked to the size ratio thresholds, aiding researchers and hydraulic engineers in determining when to use rolling resistance models and deciding how many grain-size classes are needed to replicate the non-homogeneity and poly-dispersity found in natural fluvial systems. Finally, based on the research conducted within this doctoral project, some recommendations are made to manage the fine sediment to sustain a healthy river ecosystem.

Kurzzusammenfassung

Fluid-Partikel-Systeme sind in der Natur und in industriellen Anwendungen allgegenwärtig. Im Wasserbau ist der Sedimenttransport ein Beispiel für ein Fluid-Partikel-System, das mathematisch durch ein System von Differentialgleichungen im Eulerian-Eulerian und Eulerian-Lagrangian Rahmen beschrieben und detaillierter analysiert werden kann. In dieser Dissertation, der Eulerian-Lagranagian Rahmen angewandt, der die numerische Strömungsmechanik (CFD) mit der Diskrete-Elemente-Methode (DEM) kombiniert, was allgemein als CFD-DEM-Ansatz bezeichnet wird.

Der Sedimenttransport ist ein komplexer Prozess, der von vielen voneinander abhängigen Variablen wie Strömung, Turbulenz, Partikelgröße und Partikelform bestimmt wird. Ich konzentriere mich auf einen spezifischen Teilprozess des Sedimenttransports, die Feinsedimentinfiltration in statisches Kiesbett“, die für verschiedene fluviale und ökologische Dynamiken von Bedeutung ist. Dieser Prozess wird als dichtes Fluid-Partikel-System betrachtet, bei dem sowohl die Wechselwirkungen zwischen Fluid und Partikeln als auch zwischen den Partikeln untereinander von Bedeutung sind. In dieser Dissertation werden die Einflüsse von fließendem Wasser, Turbulenzmodellierung, Partikelgrößenverteilung (PSD) und Partikelform auf die numerische Simulation von Feinsedimentinfiltration untersucht. Vor der Anwendung der CFD-DEM-Ansatz zur Untersuchung der Feinsedimentinfiltration wird die unaufgelöste CFD-DEM-Ansatz kritisch hinsichtlich des Kopplungsregimes, der Turbulenzmodellierung, der Partikel-Eigenschaften, der rechnerischen Durchführbarkeit und der Methodenbeschränkungen unter Bezugnahme auf ein disperses Fluid-Partikel System bewertet.

Im Gegensatz zu konventionellen Sedimenttransportmodellen, die empirische Gleichungen zur Schätzung von Sedimenttransportparametern verwenden, liefert der CFD-DEM-Ansatz detaillierte Strömung und partikelaufgelöste Informationen. Der CFD-DEM-Ansatz erfordert jedoch aufgrund der umfangreichen DEM-Berechnungen und der High-Fidelity-CFD, die eine Kopplung zwischen CFD und DEM beinhaltet, um die Wechselwirkungen zwischen Flüssigkeit und Partikeln zu erfassen, Hochleistungscomputer (HPC). Die Methode hat auch Einschränkungen in Bezug auf die Anzahl und Größe der Partikel, so dass sie nur für detaillierte Untersuchungen mit einer begrenzten Anzahl von Partikeln und bis zu einem bestimmten Grad der Strömungsauflösung geeignet ist. Die Auflösung des Strömungsfeldes hängt davon ab, ob die Turbulenz modelliert (z. B. Reynolds-Averaged Navier-Stokes; RANS) oder bis zu einem bestimmten Grad aufgelöst (z. B. Large Eddy Simulation; LES) wird.

Numerische Simulationen werden mit OpenFOAM-basierten Softwarepaketen durchgeführt. Zur Bewertung der CFD-DEM-Ansatz werden zwei ähnliche, aber auch unterschiedliche Partikelverfolgungslöser in OpenFOAM verwendet: ”DPMFoam“ und ”pimpleLPTFoam‘. Der Solver ”DPMFoam“ ist ein Standard-Solver in OpenFOAM, während ”pimpleLPTFoam“ ein selbst kompilierter Solver ist, der entwickelt wurde, um die Auswirkungen des Partikelanteils in jeder Berechnungszelle

zu untersuchen. Um Kies- und Feinsedimentpartikel genau darzustellen, wurde OpenFOAM mit einem separaten DEM-Softwarepaket namens LIGGGHTS gekoppelt, das den CFDEM-Coupling-Code verwendet.

Die Bewertung der CFD-DEM-Ansatz zeigt, dass einfache Dispersionsmodelle, die in der Regel eingesetzt werden, um die durch die RANS-Mittelung verloren gegangenen Turbulenzschwankungen auszugleichen, die Partikeldispersion tendenziell unterbewerten. Daher sollten Anspruchsvollere Dispersionsmodelle im Rahmen der RANS-DEM implementiert werden, um das Partikelverhalten in einer turbulenten Strömung genau zu erfassen. Turbulenzauflösende Ansätze wie LES-DEM kann ein realistischeres Partikelverhalten in turbulenten Strömungen bieten. LES-DEM ist jedoch nur selten durchführbar, da die Partikel in der unaufgelösten CFD-DEM-Ansatz kleiner sein müssen als die CFD-Zellengröße. In solchen Fällen, insbesondere in der Nähe von Wänden, wo kleinere Zellgrößen zur Auflösung der Grenzschicht erforderlich sind, können die dynamischen LES-Turbulenzmodelle die Einschränkungen der statischen LES-Turbulenzmodelle abmildern. Bei stark dispergierten partikelbeladene Strömungen, einseitige Kopplung und die Vernachlässigung von Partikelanteilen in jeder Berechnungszelle ausreichen, um ein genaues Partikelverhalten in der turbulenten Strömung vorherzusagen, was erhebliche Rechenressourcen spart.

Die Anwendung des ungelösten CFD-DEM-Ansatzes zur Modellierung der Feinsedimentinfiltration zeigt, dass (1) das Auftreten verschiedener Infiltrationsverhalten (Überbrückung oder Versickerung) unabhängig von der Kiesbettdicke ist und nur von der relativen Feinsedimentgröße abhängt, und (2) die Definition eines ausreichend dicken Kiesbetts notwendig ist, um zwischen Überbrückungs- und Versickerungsverhalten zu unterscheiden. Die Untersuchung der Auswirkungen von fließendem Wasser auf den Infiltrationsprozess unterstützt die Hypothese von Cui, dass sich Feinsediment, das durch Fließen im Kiesbett infiltriert wird, ähnlich verhält wie Feinsediment, das durch die Schwerkraft infiltriert wird. Im Wesentlichen ist der Prozess der Feinsedimentinfiltration überwiegend schwerkraftgesteuert, solange das Kiesbett unbeweglich bleibt.

Partikelformeffekte in Bezug auf Nicht-Kugelförmigkeit und Unregelmäßigkeiten wurden in das numerische Modell implizit berücksichtigt, indem das Rollen von kugelförmigen Partikeln eingeschränkt wird. Es wurde gezeigt, dass Partikelformeffekte den Infiltrationsprozess erheblich beeinflussen, und die Berücksichtigung der Partikelformeffekten durch Rollwiderstandsmodelle scheint der effizienteste Weg zu sein. Die Untersuchung der Partikelgrößen-verteilung (PSD) für den Infiltrationsprozess legt nahe, dass eine Reduzierung der Korngrößenklassen in der PSD von Kies und Feinsediment notwendig ist, um die CFD-DEM Simulation innerhalb eines angemessenen Zeitrahmens und mit vertretbaren Rechenressourcen durchzuführen. Die Reduzierung der Korngrößenklassen ist jedoch nur dann gerechtfertigt, wenn die Infiltrationseigenschaften von Feinsediment und Kiesbett nicht wesentlich verändert werden und das Größenverhältnis innerhalb der Schwellenwerte des Infiltrationsverhaltens (Überbrückung oder Versickerung) bleibt. Die Partikelform und die PSD-Effekte sind mit den Schwellenwerten für das Größenverhältnis verknüpft, was Forschern und Wasserbauingenieuren dabei hilft, zu bestimmen, wann Rollwiderstandsmodelle verwendet werden sollten und wie viele Korngrößenklassen erforderlich sind, um die Inhomogenität und Poly-Dispersität, die in natürlichen Flusssystemen zu finden sind, nachzubilden. Abschließend werden auf der Grundlage der im Rahmen dieses Promotionsprojekts durchgeführten Forschung einige Empfehlungen für den Umgang mit Feinsedimenten zur Erhaltung eines gesunden Flussökosystems gegeben.

Preface

This dissertation is submitted to the TUM School of Engineering and Design, Technical University of Munich (TUM) in Munich, Germany, for partial fulfilment of the requirements for the degree of Doctorate (Dr.-Ing.). The requirements are also supplemented by the completion of academic training and subject-specific courses: River Engineering and Hydromorphology (3 credits), Environmental Hydrodynamic Modelling (6 credits), TUM kickoff Seminar, and a Faculty-wide Poster Session.

This is a cumulative dissertation based on the following 1 conference paper and 3 peer-reviewed journal papers:

1. Jaiswal, A.; Bui, M.D.; Rutschmann, P. Simulation of Particle-laden Turbulent Flow in OpenFOAM. *Proceedings of the 39th IAHR World Congress*, 19-24 June 2022. Pages 4328-4335. https://doi.org/10.3850/IAHR-39WC2521711920221242

2. Jaiswal, A.; Bui, M.D.; Rutschmann, P. Evaluation of RANS-DEM and LES-DEM Methods in OpenFOAM for Simulation of Particle-laden Turbulent Flows. *Fluids* 2022, 7, 337. https://doi.org/10.3390/fluids7100337

3. Jaiswal, A.; Bui, M. D.; Rutschmann, P. On the Process of Fine Sediment Infiltration into Static Gravel Bed: A CFD–DEM Modelling Perspective. *River Research and Applications* 2024, 40(1), 29–48. https://doi.org/10.1002/rra.4215

4. Jaiswal, A.; Bui, M.D.; Rüther, N.; Rutschmann, P. Influence of Rolling Resistance and Particle Size Distribution in the Simulation of Sand Infiltration into the Static Gravel Bed. *Water* 2024, 16, 1947. https://doi.org/10.3390/w16141947

In addition to the above-mentioned papers, the research conducted within the scope of the doctoral research was also presented at three reputed international conferences: (1) the 39th IAHR World Congress (2022), Granada, Spain, (2) the 40th IAHR World Congress (2023), Vienna, Austria, and (3) the 11th International Conference on Multiphase Flow (2023), Kobe, Japan.

In the introduction chapter, I defined the state-of-the-art and research gaps in terms of fine sediment infiltration and numerical simulation approaches. I provided the theoretical background, including the governing equations, together with the advanced numerical models used in this dissertation. In the end, I concluded the overall contribution of the study along with some recommendations and future research outlook. The introduction section also contains a summary of the above-mentioned publications, along with the author's contributions.

Acknowledgements

First and foremost, I would like to thank my supervisor, PD Dr.-Ing. Habil. Dipl.-Math. Minh Duc Bui for the offer and opportunity to do a dissertation at the Chair of Hydraulic Engineering. I would like to express my heartiest gratitude to my mentor, Prof. Nils Rüther; thank you for your trust, support, and encouragement. I would also like to acknowledge the support from Prof. Peter Rutschmann during the initial phase of my doctoral project. In the study, they also supported me with guidance, mentoring, and encouragement.

I am also grateful to my current and previous colleagues and staff members at the Chair of Engineering for their help in my research, fruitful discussions, and fun times besides work. Among many individuals at the Chair, special thanks to Dr. Subhojit Kadia for valuable discussions and support during the writing phase of this dissertation. I would also like to mention and thank Bertalan Alapfy's timely support, which helped me to secure some extra time and funding for my doctoral research.

This doctoral project is supported by a scholarship from Konrad-Adenauer-Stiftung (KAS). I would like to sincerely thank KAS for considering me for the prestigious scholarship program, which not only supports its scholarship holders in terms of monetary support but also educates them through seminars covering a wide range of national and international topics. I also acknowledge Deutscher Akademischer Austauschdienst (DAAD), which funded my exchange semester at TUM during my master's studies, exposing me to Germany, which eventually resulted in my decision to do a doctorate from TUM.

I am also grateful to my school teachers and undergraduate and postgraduate professors, who have helped me to grow, gather information and knowledge, and become a curious individual. I must acknowledge that it is their cumulative contributions that directly or indirectly helped me to achieve my goals successfully. Among the long list of those individuals, Prof. Subashisa Dutta from IIT Guwahati and Prof. Benu Gopal Mahapatra from KIIT Bhubaneswar must be specially acknowledged, who boosted my confidence and played very important roles in shaping my academic career.

I would like to thank my dearest and special friends, Dr. Michael David Bartoschek and Dr. Mahendra Singh Tomar, who continuously supported and encouraged me during the doctoral project.

My father's sacrifices for my achievements, love and support can't be described in words; without his sacrifices, nothing would have been possible for me. I consider myself lucky and fortunate to have a big supportive family and many friends.

Contents

List of Figures

List of Abbreviations

1D	: One-Dimensional;
2D	: Two-Dimensional;
3D	: Three-Dimensional;
AMG	: Algebraic Multi-Grid;
AMR	: Adaptive Mesh Refinement;
ANN	: Artificial Neural Network;
BFS	: Backward Facing Step;
CDT	: Constant Directional Torque;
CFD	: Computational Fluid Dynamics;
CPU	: Central Processing Unit;
CRW	: Continuous Random Walk;
DEM	: Discrete Element Method;
DNS	: Direct Numerical Simulation;
DRW	: Discrete Random Walk;
EIM	: Eddy Interaction Model;
EPSD	: Elastic-Plastic Spring-Dashpot;
FDM	: Fictitious Domain Method;
GPU	: Graphics Processing Unit;
HPC	: High Performance Computing;
IMB	: Immersed Boundary Method;
LBM	: Lattice-Boltzmann Method;
LES	: Large-Eddy Simulation;
LIGGGHTS	: LAMMPS Improved for General Granular and Granular Heat Transfer Simulations;
MAE	: Mean Average Error;
MFM	: Multi Fluid Model;
MSE	: Mean Square Error;
MultiPAC	: MultiParameter Approach to assess Colmation;
NS	: Navier-Stokes;
OpenFOAM	: Open Field Operation And Manipulation;
PINN	: Physics-Informed Neural Network;
PP	: Point-Particle;
R	: Correlation Coefficient;
RANS	: Reynolds-averaged Navier-Stokes;

RAS : Reynolds-Averaged Simulation;
rms : root mean square;
RMSE : Root Mean Square Error;
SGS : Sub-Grid Scale;
SST : Shear Stress Transport;
TFM : Two-Fluid Model;
TKE : Turbulent Kinetic Energy;
VANS : Volume-Averaged Navier-Stokes;

List of Symbols

β= momentum transfer coefficient (kg/m$^3 s$);
C_D= interfacial drag coefficient (unitless);
$c(k)$= total number of particles in contact with paticle k (unitless);
D= turbulent dispersion coefficient (m$^2/s$);
$\mathrm{D}_{15,\mathrm{Gravel}}$= gravel size at which 15 percent of the material is finer (m);
$\mathrm{D}_{85,\mathrm{Sand}}$= sand size at which 85 percent of the material is finer (m);
δ_{ij}= Kronecker delta (unitless);
δ_k= Kronecker delta (unitless);
d_p= particle diameter (m);
Δt= time step (s);
$\Delta t_{\mathrm{total}}$= simulation time (s);
ΔV= control volume or volume of each CFD cell i (m^3);
ε= turbulent dissipation rate (m$^2/s^3$);
ϵ_f= fluid volume fraction in each CFD cell (unitless);
ϵ_p= particle volume fraction in each CFD cell (unitless);
ϵ_s= solid (particle) volume fraction in each CFD cell (unitless);
F_B= Basset force (N);
$F_{c,kl}$= inter-particle contact force on particle between particle k and particle l (N);
F_D= drag force (N);
$F_{d,kl}$= inter-particle damping force between particle k and particle l (N);
$F_i^{(c(kl))}$= particle-particle interaction force between particle k and l in direction i (N);
$F_i^{(f(k))}$= surface forces acting on particle k in direction i (including drag, lift, added-mass, basset history forces, etc.: coupled forces) (N);
$F_i^{(g(k))}$= body forces acting on particle k in direction i (including gravity, buoyancy: uncoupled forces) (N);
F_L= lift force (N);
F_P= pressure force (N);
$F_{pf,k}$= fluid-particle interaction force on particle k (N);
$f_{VM,k}$= virtual mass force on particle k (N);
F_{VM}= virtual mass force (N);
F_τ= viscous shear force (N);
$f_{B,k}$= Basset force on particle k (N);
$f_{d,k}$= drag force on particle k (N);

f_i^p= volumetric fluid-particle interaction momentum source in direction i (N/m^3);
f_k''= other minor forces on particle k (N);
f_M= local mean value of the force on each particle by its surrounding fluid (N/m^3);
f_M'= local mean value of the minor forces on each particle by its surrounding fluid (N/m^3);
$f_{Mag,k}$= Magnus lift force on particle k (N);
$f_{\nabla p,k}$= pressure gradient force on particle k (N);
$f_{\nabla\cdot\tau,k}$= viscous force on particle k (N);
$f_{pf}^{\text{Set-I}}$= volumetric fluid-particle interaction momentum source in Set-I (N/m^3)
$f_{pf}^{\text{Set-II}}$= volumetric fluid-particle interaction momentum source in Set-II (N/m^3)
$f_{pf}^{\text{Set-III}}$= volumetric fluid-particle interaction momentum source in Set-III (N/m^3)
$f_{Saff,k}$= Saffman lift force on particle k (N);
f_{TD}= volumetric turbulent dispersion force (N/m^3);
g_i= gravitational acceleration in direction i (m/s^2);
I= unit matrix (unitless);
$I^{(k)}$= moment of inertia of particle k (kgm^2);
$\overline{k_R}$= resolved turbulent kinetic energy (m^2/s^2);
l= turbulence length scale (m);
λ= effective bulk viscosity (Ns/m^2);
λ_i= random factor with Gaussian distribution (unitless);
$m^{(k)}$= mass of particle k (kg);
$M_i^{(c(kl))}$= particle-particle interaction moment between particle k and l in direction i (Nm);
$M_{r,kl}$= torque generated due to non-sphericity (rolling friction torque) between particle k and l (Nm);
$M_{t,kl}$= torque generated by tangential force between particle k and l(Nm);
μ= dynamic viscosity or effective shear viscosity of fluid (Ns/m^2);
μ_f= dynamic viscosity for fluid phase (Ns/m^2);
μ_s= dynamic viscosity for solid phase (Ns/m^2);
n= number of particles per unit volume (1/m^3);
$n^{c(k)}$= number of particles colliding with particle k (unitless);
ν= kinematic viscosity of fluid (m^2/s);
ν_T= eddy viscosity or turbulent viscosity (m^2/s);
N_{uniform}= number of uniform cells (unitless);
Ω= whole computational domain (unitless);
Ω_F= fluid domain (unitless);
Ω_p= particle domain (unitless);
$\omega^{p(k)}$= rational velocity of particle k; (rad/s);
p= fluid pressure (N/m^2);
$\overline{p}(x,t)$= resolved (or filtered) component of fluid pressure (m/s);
φ= local mean value of particle-particle interaction force (N/m^3);
p_s= solid phase pressure (N/m^2);
r= unit random factor (unitless);
Re= Reynolds number (unitless);
ρ= density of fluid (kg/m^3);
ρ_f= fluid phase density (kg/m^3);
ρ_p= density of particle (kg/m^3);
ρ_s= solid phase density (kg/m^3);
$\overline{R_{ij}}$= resolved rate of strain tensor (1/s);
Re_p= particle Reynolds number (unitless);
Re_τ= turbulent Reynolds number (unitless);

S= tensor representing "Raynolds stresses" for the particle phase (N/m^2);
$\overline{S_{ij}}$= resolved rate of strain tensor in RANS (mean stress tensor) (1/s);
σ_T= turbulent Schmidt number (unitless);
St= Stokes number (unitless);
t= time (s);
τ= fluid shear stress tensor (N/m^2);
τ_e= Kolmogorov time scale (s);
τ_f= shear stress tensor for fluid phase (N/m^2);
τ_{ij}^R= residual stresses (N/m^2);
τ_k= turnover time of large eddies (s);
τ_p= particle response or reaction time (s);
τ_s= shear stress tensor for solid phase (N/m^2);
$\overline{u}(x,t)$= resolved (or filtered) component of fluid velocity (m/s);
$u'(x,t)$= residual (or sub-grid scale) component of fluid velocity in LES (m/s);
= fluctuating component of fluid velocity in RANS (m/s);
u', v', w'= root mean square value (rms) of solution of transport equations of
= turbulent kinetic energy (TKE; k) (m/s);
U_f= fluid phase velocity (m/s);
u_i= fluid velocity field in direction i (m/s);
$u_i^{\mathrm{DNS}}\left(x^{p(k)}(t),t\right)$= DNS solution for fluid velocity field in direction i at the location of particle k (m/s);
$\langle u_i(x,t)\rangle$= time-averaged component of fluid velocity (m/s);
u_i^{LES}= LES resolved fluid velocity (m/s);
$u_i^{(p(k))}$= velocity of particle k in direction i (m/s);
u_i^{RANS}= RANS resolved (time-averaged) fluid velocity (m/s);
$(u_i)^{(s(k))}$= fluid velocity at the location of particle or fluid velocity seen by particle (m/s);
$\overline{u_i u_j}$= filtered product of velocity components (m^2/s^2);
$u^{p(k)}$= translational velocity of particle k
U_s= solid phase velocity (m/s);
u_τ= friction velocity (m/s);
$u(x,t)$= instantaneous fluid velocity (m/s);
V= total volume of each CFD cell; total volume of fluid and particle in each CFD cell (m^3);
V_p= particle volume in each CFD cell (m^3);
$w_i^{(p(k))}$= angular velocity of particle k in direction i (1/s);
x= space (m);
$\boldsymbol{\xi}$= fluid phase stress tensor (N/m^2);
$\boldsymbol{\xi}_s$= solid stress tensor stress tensor (N/m^2);
y= distance of first cell centre from wall (m);
y^+= non-dimensional distance of first cell centre from wall (unitless) = $\rho u_\tau y/\mu$;

Chapter 1

Introduction

1.1 Background

Since the beginning of humankind, human-river interactions have shaped our present and future. Rivers are essential for development and in sustaining a livelihood. Our dependency on the river systems is undeniable. A few examples are drinking water, irrigation, hydro-power, aqua-culture, and inland navigation. Managing rivers for human benefit requires modifying the natural river systems by building hydraulic structures such as dams, weirs, river training works, and diversion structures. Rivers are not only primary resources for hydraulic and water infrastructures but also habitats for other living species, including fish, invertebrates, and many micro-organisms, comprising an ecosystem. These obstructions in the river systems, caused by human interventions, disrupt the natural continuity in terms of flow and sediment transport processes. As a result, river ecology and transport processes in river systems are negatively affected. In the context of climate change, these adverse effects of disrupting river systems can have catastrophic consequences. Therefore, a proper understanding of hydraulic, morphological and transport processes and the river's response to these obstructions is required to sustain healthy river systems.

Sediment transport is a complex, multi-variable and inter-dependent process involving many factors governing it, including flow, turbulence, particle size distribution (PSD), and particle shape, among many others. Sediment transport is a combined term used for suspended and bedload transport processes. Bedload transport is the mode of sediment transport where the sediment particles slide, roll, or travel in a succession of low jumps, termed saltation, but belong close to the bed, from where they may leave temporarily (Dey, 2014). Bed load transport further involves sub-processes of erosion, deposition and infiltration of fine sediment from/into gravel substrate (see Figure 1.1). Depending on flow, turbulence, particle sizes and shapes, the transport rate of coarser and finer fractions might differ, resulting in armouring (Dietrich et al., 1989; Wilcock and DeTemple, 2005) and clogging processes (Cui et al., 2008; Gibson et al., 2010; Schälchli, 1992; Wu and Huang, 2000) in the gravel bed.

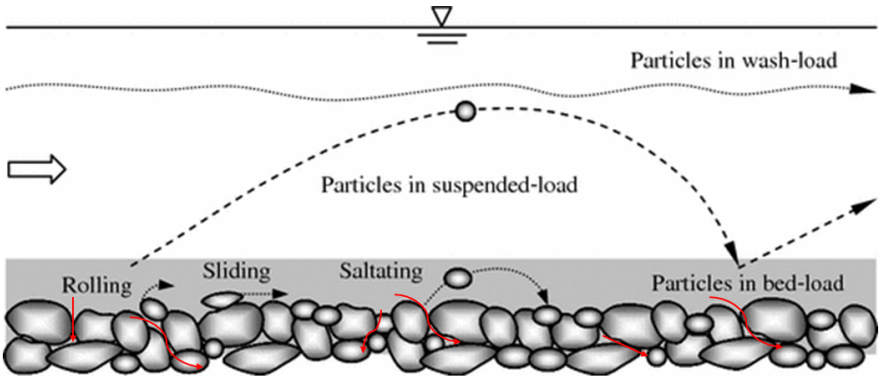

Figure 1.1: Schematic of different modes of sediment transport, including fine sediment infiltration shown in red (adapted from Dey (2014)).

The morphological evolution of gravel-bed rivers, involving simultaneous occurrences of several modes of sediment transport processes, is among the key processes in the fluvial systems affected by river disruption (Haun and Dietrich, 2021). There can be mainly two distinguishable fine sediment transport processes near the gravel bed (conceptually shown in Figure 1.2): the depositional phase during low flow seasons and the removal phase during high flow seasons (Bui, 2019; Grams and Wilcock, 2014).

During low flow conditions, the deposited fine sediment can further be infiltrated into the pores of the gravel bed. Fine sediment pulse joining the river system results in loss of interstitial pore space in the gravel bed, which could be arising from natural and anthropogenic activities such as dam removal (Bednarek, 2001; Born et al., 1998; Cui et al., 2006; Cui and Wilcox, 2005; Elmsahli and Sinka, 2021; Pollard and Reed, 2004; Stanley et al., 2002), dredge material disposal, forest fires (Minshall et al., 2001; Vieira et al., 2004), watershed land use changes (Lisle, 1989; Swanson and Dyrness, 1975) and mining activities (Parker et al., 1996). Fine sediment infiltration can be further categorized into two distinct behaviours: bridging and unimpeded static percolation (or percolation). In the bridging case, fine sediment gets clogged in the upper surface layer of the gravel bed, precluding subsequent infiltration. In the percolation case, the fine sediment can reach the bottom of the gravel bed and fill the gravel deposit from bottom to top onwards.

In high flow conditions, fine sediment can be remobilized to remove the infiltrated sediment from the gravel bed to rejuvenate the river ecology (Cui et al., 2008; Downs et al., 2009; Petticrew et al., 2007). The pore space can be again made available for reproduction and living purposes for fish and other micro-organisms. A flood event can be combined with a suitable flushing activity, artificially created by releasing clear water through gates/spillways of dams, to remove and remobilize the deposited fine sediment in the gravel bed downstream. The deposited and infiltrated fine sediment in the upper surface layer of the gravel bed (infiltrated through the bridging process) can be removed up to some extent with a high flood event. However, removing fine sediment from deeper layers (infiltrated through the percolation process) is extremely difficult, if not impossible.

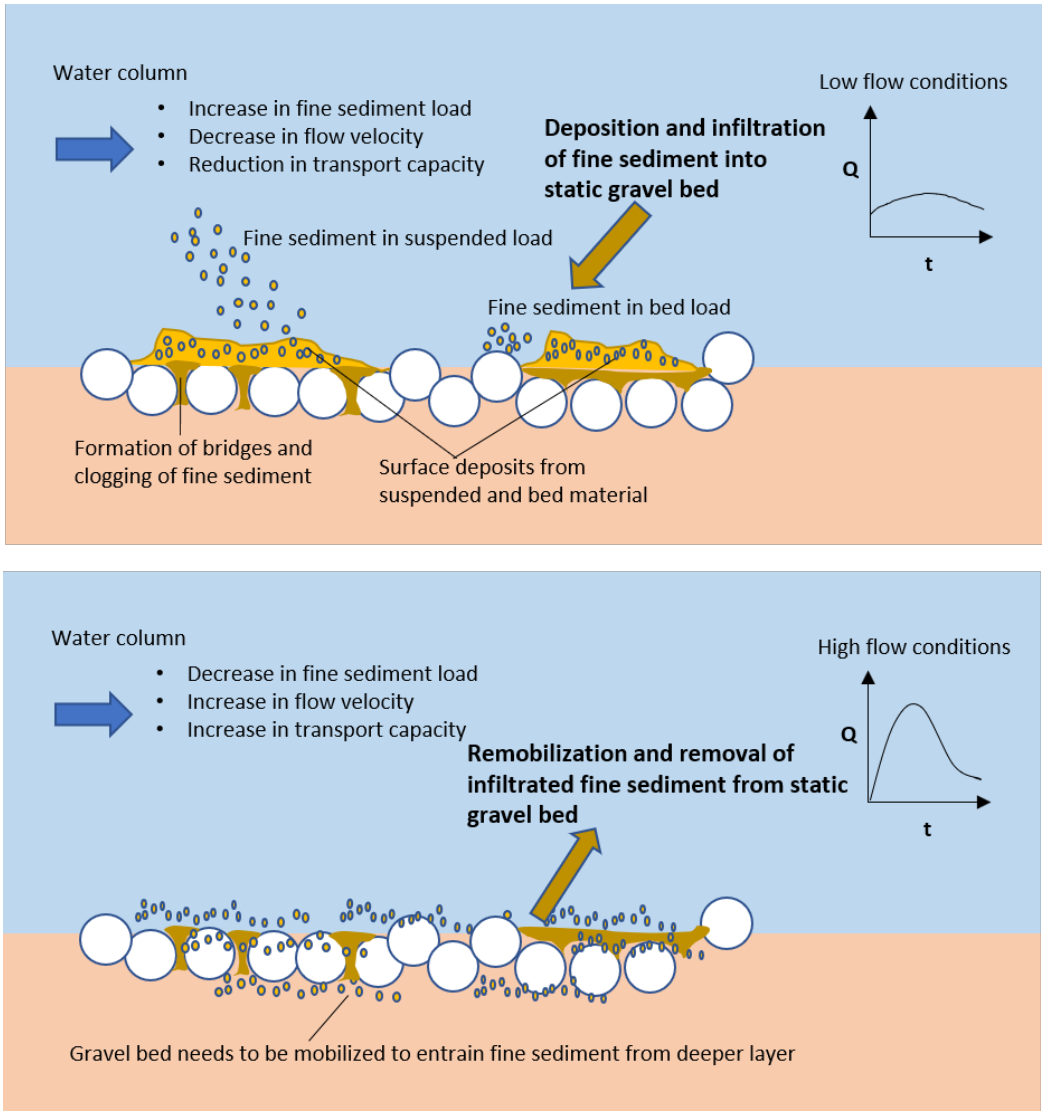

Figure 1.2: Conceptual diagram showing the mechanisms of (a) fine sediment deposition and infiltration into static gravel bed (b) remobilization and removal of fine sediment from static gravel bed (adapted from Wharton et al. (2017)).

The interstitial pore space in gravel bed is crucial for fluvial geomorphology, exchange processes between the river and groundwater, and river ecosystem (Cui et al., 2008; Gibson et al., 2009; Jaiswal et al., 2024; Mayar et al., 2022; Negreiros et al., 2023; Wooster et al., 2008). Therefore, predicting how the pore space varies in the gravel bed as a result of fine sediment infiltration could be of great importance in eco-hydraulic management and fine sediment budgeting. Advanced numerical simulations, focusing on the sub-process of fine sediment infiltration into gravel bed, complement the physical experiments and field investigations. Furthermore, the advanced numerical simulations can provide detailed insights into the complex physics involved in the multi-variable and inter-dependent process of fine sediment infiltration.

1.2 Computational Methods to Model Sediment Transport Processes

Sediment transport involves flowing and interacting water and sediments and can be categorized as a fluid-particle system and precisely described with a set of physics-based governing equations. Different approaches can be employed to simulate fluid-particle systems depending on the aim and scope of the study and the computational resources available. The computational approach involves the numerical solution of one or more governing differential equations of continuity, momentum, and energy for the fluid phase, along with the differential equation for the particle phase (Papanicolaou et al., 2008). Based on the formulations of equations in the spatial and temporal scales, the models can be classified into three different modelling approaches: one-dimensional (1D), two-dimensional (2D), and three-dimensional (3D) models. Furthermore, the model can be categorized as steady or unsteady approaches.

1D and 2D models are the simplest and preferred for engineering applications, where simplified Navier-Stokes' equations (depth-averaged/area-averaged) are numerically solved for the fluid phase, and the particle phase is routed using simple empirical transport equations. 1D and 2D models only provide the flow information as depth-averaged flow in 2D and area-averaged flow in 1D modelling approaches. This also means that the effects of turbulence do not directly appear in the empirical transport equations for the particle phase, because turbulence is neither resolved in 1D and 2D models, nor do the simple empirical models contain any parameter related to turbulence. Furthermore, these empirical equations are not universal, therefore, only valid for similar scenarios as that of original experiments. Particularly for sediment transport in rivers and fluvial systems, the empirical models, developed from flume experiments, are used to calculate the sediment transport rates. The most famous empirical sediment transport equations are DuBoy, Shield, Mayer-Peter-Mueller, Yang, Acker and White, Engelund and Hansen, Bargold, Einstein, Brook, Lane, and Kalinske equations, which were developed for bed load transport, suspended load transport, and combined load transport. These transport equations result in different transport rates for the same flow and sediment conditions (Tayfur, 2021). The inconsistencies among the empirical approaches stem from the fact that each empirical formulation is developed from a particular laboratory experimental condition. Nevertheless, the above-mentioned empirical formulations of sediment transport can also be coupled with 3D equations for the fluid phase (Navier-Stokes equations). However, the sediment transport is still routed with empirical transport equations instead of physics- and process-based equations.

More advanced approaches are based on the involved physics in transport processes for both fluid and particle phases. These physics- and process-based methods can also be applied to study sediment transport, a fluid-particle system, in greater detail. Compared to 1D and 2D modelling approaches, in the 3D hydrodynamic approach, also called computational fluid dynamics (CFD), partial differential equations (PDEs) are numerically solved, not only for the fluid phase but also for the particle phase. Depending upon how the particle phase is treated, the 3D approach can be further sub-categorized into Eulerian-Eulerian and Eulerian-Lagrangian methods, schematically demonstrated in Figure 1.3. The Eulerian-Eulerian method treats both fluid and particle phases as a continuum, where the fluid phase is treated as Newtonian fluid, and the particle phase is treated as non-Newtonian fluid. Therefore, the Eulerian-Eulerian method is called the Two-Fluid Model (TFM). The Eulerian-Eulerian method solves continuity and momentum equations (Navier-Stokes

equations), considering interphase momentum transfer between fluid and particle phases. Since the particles are discrete entities, representing them as continuum media results in the loss of particle-scale information but saves significant computational resources. The Eulerian-Lagnaranian method treats the fluid phase as a continuum media; Navier-Stokes equations (CFD) are numerically solved. The particles are treated as discrete entities and tracked using Newton's second law of motion, called the Discrete Element Method (DEM). Similar to the Eulerian-Eulerian method, fluid and particle phases are also coupled with the interphase momentum transfer mechanism in the Eulerian-Lagrangian method. Compared to the Eulerian-Eulerian method (TFM), a more detailed approach combining CFD and DEM for multiphase systems called the Eulerian-Lagrangian method (CFD-DEM modelling), proves to be advantageous over many other options in terms of computational efficiency and numerical convenience (Zhu et al., 2007).

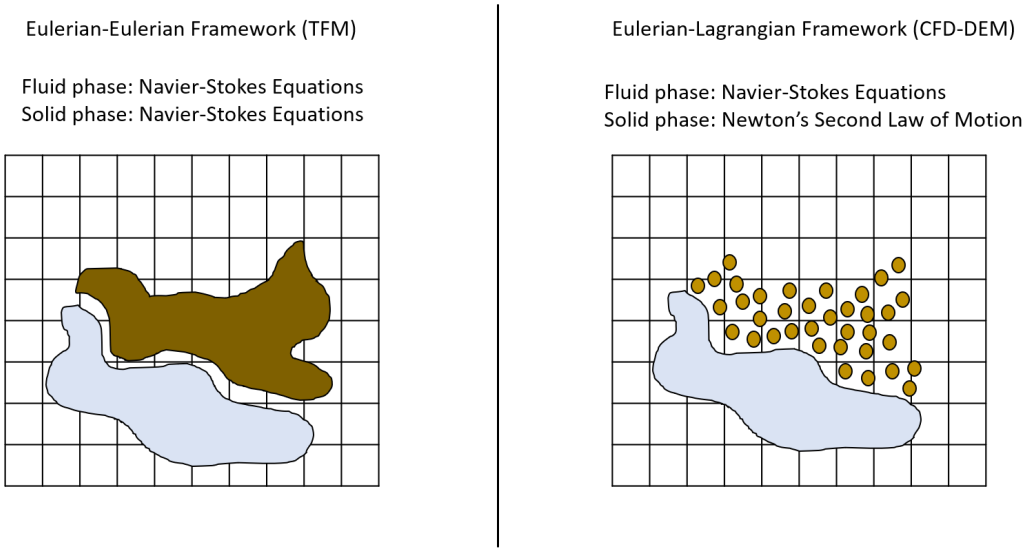

Figure 1.3: Schematic of treatment for fluid and particle (solid) phases in Eulerian-Eulerian and Eulerian-Lagrangian frameworks.

Depending on the resolutions of CFD mesh (cell size) and particle diameter, the Eulerian-Lagrangian (CFD-DEM) approach can be further categorized into the resolved CFD-DEM and unresolved CFD-DEM methods (Kloss et al., 2012). The resolved CFD-DEM resolves the fluid flow fields at smaller scales than the particle diameter, assuming the no-slip on the particle surface to couple the phases. The fluid flow solution scale is coarser than the particle diameter in the unresolved CFD-DEM, and fluid-particle interaction forces (e.g., virtual mass, drag, lift) couple the fluid and particle phases (Bérard et al., 2020). In other words, the resolved CFD-DEM allows particles to be larger than the CFD cell sizes, as forces acting on particles are calculated by integrating the stresses over the surface of particles. The resolved CFD-DEM is more accurate but is notoriously computationally intensive and limited to a maximum order of 10^3 number of particles. The unresolved CFD-DEM allows a greater number of particles (order of 10^7) than the resolved CFD-DEM. However, the unresolved CFD-DEM must have particles smaller than CFD cell sizes, otherwise the governing equations collapse. Similar to single-phase fluid flow, CFD equations can be solved at different levels of flow resolution, namely, Direct Numerical Simulations (DNS), Large Eddy Simula-

tions (LES), and Reynolds-Averaged-Navier-Stokes (RANS) equations. However, the achievability of a higher resolution for fluid flow is not only restricted due to extensive computational requirements to resolve different scales of turbulence but also due to the pre-requisite of the particle being smaller than CFD cell sizes in the unresolved CFD-DEM (Jaiswal et al., 2022). Due to complex physics in fluid-particle systems and high computational requirements, only limited studies on sediment transport processes have been available in the literature both in the Eulerian-Eulerian (Bakhtyar et al., 2009; Cheng et al., 2017) and the Eulerian-Lagrangian (Guo et al., 2018; Shi and Yu, 2015; Sun and Xiao, 2016a,b; Wildt et al., 2022) frameworks.

1.3 Research Objectives

The CFD-DEM method is yet to be exploited to its full capacity for understanding sediment transport processes, primarily due to computational limitations. In this dissertation, the unresolved CFD-DEM method is employed to study the fine sediment infiltration into static gravel bed in greater detail, focusing on the effects of flowing water, particle shape, and particle size distribution (PSD). The following five specific objectives are covered in this dissertation:

- A comprehensive study of the CFD-DEM approach, focusing on its origins and how it relates to other advanced methods for fluid-particle systems in terms of the underlying equations
- Evaluation of RANS-DEM and LES-DEM methods under unresolved CFD-DEM framework in their ability to predict accurate physics concerning fluid and particle phases
- Investigation of the process of fine sediment infiltration into static gravel bed with emphasis on bridging and percolation behaviours by employing unresolved CFD-DEM method
- Quantification of the effects of flowing water, particle shape (non-sphericity and irregularity) and particle size distribution (PSD) in modelling of fine sediment infiltration
- Recommendations for the modelling of sediment transport and fine sediment management strategies to sustain a healthy river ecosystem

1.4 Research Methodology

The unresolved CFD-DEM framework is employed to simulate near-bed sediment transport processes, focusing on the sub-process of fine sediment infiltration. Before the method is employed for the study's primary objective, which is studying fine sediment infiltration into static gravel bed, the unresolved CFD-DEM method is thoroughly evaluated in its ability to accurately predict particle-laden flow with RANS and LES flow resolutions. For this purpose, particle-laden backward-facing step (BFS) flow (Fessler and Eaton, 1999) is considered and simulated in OpenFOAM. Simulated fluid and particle phase results are compared and validated against the measurement data from the reference experiment in terms of mean flow, turbulent fluctuations, and particle dispersion. In addition to a pre-compiled particle tracking solver in OpenFOAM, called "DPMFoam," a self-compiled solver, "pimpleLPTFoam" is also used to assess the unresolved CFD-DEM method in modelling fluid-particle systems with an emphasis on effects of particle fraction in each CFD cell.

The unresolved CFD-DEM approach is further pursued to simulate fine sediment infiltration into static gravel bed. To achieve actual particle size in numerical simulations (instead of the simplified point particle (PP) approach), a coupled framework is employed by coupling OpenFOAM (CFD code) with LIGGGHTS (DEM code) using CFDEM-Coupling (a separate code for data transfer between OpenFOAM and LIGGGHTS). Here, we first emphasized our investigation to understand the effects of flowing water and turbulence modelling on fine sediment infiltration. In doing so, two different sets of simulations are performed for different geometrical size ratios (sand-gravel size) of a binary mixture, considering flowing water (CFD-DEM) and neglecting flowing water (pure DEM) effects on the infiltration process. Later, special attention is given to particle shape and particle size distributions (PSDs) effects on infiltrating characteristics of fine sediment in gravel bed. An efficient approach is used to include particle shape effects implicitly without resolving their actual shape in numerical simulations of fine sediment infiltration into static gravel bed. Effects of non-sphericity and irregularity in particle shape are included by rolling resistance models.

All the simulations are performed with open-source codes, namely, OpenFOAM, LIGGGHTS, and CFDEM-Coupling. Standalone OpenFOAM software is employed to assess the unresolved CFD-DEM method's ability to predict fluid-particle physics. Later on, a coupled approach of OpenFOAM and LIGGGHTS with CFDEM-Coupling is utilized for the simulation of fine sediment transport processes near gravel bed. Paraview and MATLAB are used for postprocessing.

1.5 Structure of Dissertation

This dissertation aims to apply an advanced numerical method, the unresolved CFD-DEM, to simulate and investigate the fine sediment transport processes near the vicinity of the gravel bed, focusing on sub-processes of fine sediment deposition and infiltration. We aim to shed more light on the complex processes occurring near and within gravel bed. Flow, turbulence, particle shape, and particle size distributions (PSDs) are given special attention. This dissertation is organized such that each chapter can be read independently without going back and forth. The dissertation is based on peer-reviewed and open-source published articles in international journals and conferences, conducted at the Chair of Hydraulic Engineering, Technical University of Munich (TUM), Germany.

Chapter 2: The comprehensive theory of the Eulerian-Lagrangian method is presented. We start with the Eulerian-Eulerian method (Two-Fluid Model; TFM), which is the origin of equations developed for the Eulerian-Lagrangian method (CFD-DEM). The Eulerian-Lagrangian method is described in greater detail by differentiating resolved and unresolved CFD-DEM. Direct numerical simulations (DNS), Large Eddy simulations (LES), and Reynolds-averaged Navier-Stokes (RANS) methods are discussed in the context of multiphase flow.

Chapter 3: Two different particle tracking solvers, "DPMFoam" (pre-compiled, standard OpenFOAM solver) and "pimpleLPTFoam" (self-compiled solver), are employed to evaluate the effects of particle fraction in each computational cell for particle-laden turbulent flows. The chapter is published in the proceedings of *39th IAHR World Congress* in 2022.

Chapter 4: RANS-DEM and LES-DEM methods in the framework of the unresolved CFD-DEM are employed to evaluate the method's efficiency to accurately predict fluid and particle phase results in terms of mean flow, turbulent fluctuations, and particle dispersion. Several aspects of fluid-particle systems concerning the coupling level, particle boundary conditions, and dispersion

modelling in RANS and LES approaches, are discussed in detail. The chapter is published as an article in the international journal *Fluids* from MDPI in 2022.

Chapter 5: The unresolved CFD-DEM method is employed to simulate and investigate the fine sediment infiltration into the static gravel bed. The sand infiltration process is distinguished between two distinct behaviours: bridging and unimpeded static percolation (or percolation). Different size ratios corresponding to various geometrical configurations of gravel-sand mixtures are considered, and simulations are performed with flowing water (coupled CFD-DEM simulation) and without flowing water (pure DEM simulation) effects. The simulations aim to validate Cui's hypothesis: fine sediment infiltration through intra-gravel flow is similar to fine sediment infiltration driven by gravity. The chapter is published as an article in the international journal *River Research and Applications* from WILEY in 2024.

Chapter 6: Numerical simulations are performed to investigate the effect of particle shape and particle size distributions (PSDs) on the infiltrating characteristics of fine sediment in the gravel bed. Particle shape is implicitly incorporated by restricting the particle rotation by artificially adding the rolling resistance. The effects of rolling resistance models are evaluated in terms of their ability to predict the anticipated infiltration process (bridging or percolation). The effects of PSDs on the infiltration process are tested by reducing the number of grain-size classes in the PSDs of gravel and fine sediment. Both particle shape and PSDs are related to the size ratio $D_{15,Gravel}/D_{85,Sand}$, assuring physical and realistic replication of fine sediment infiltration. The chapter is published as an article in the international journal *Water* from MDPI in 2024.

Chapter 7: A summary and future outlook of the research conducted are given in this chapter.

1.6 Research Outcomes

The main research outcomes of the Ph.D. project are compiled in the form of three published articles in international peer-reviewed journals. The findings were also presented at international peer-reviewed conferences, and one chapter in this dissertation is taken from the conference proceedings. A brief summary of each publication, along with the author's contributions, is given below.

1.6.1 Simulation of Particle-laden Turbulent Flow in OpenFOAM

Main results: A new solver (pimpleLPTFoam) is compiled and compared with the standard OpenFOAM solver (DPMFoam) in its ability to model particle-laden turbulent flow. The particle-laden BFS, also considered in section 1.6.2, was taken as a reference case. The RANS-DEM approach is adapted to predict particle dispersion behaviour across the step. Some of the results overlap with section 1.6.2. However, major scientific outcomes from this article should be pointed out separately, which are:

- The solver "pimpleLPTFoam" can be used instead of "DPMFoam" to simulate the dispersed fluid-particle systems when the particle concentration is small ($O{\sim}10^{-5}$), which can predict the same accurate results as that of DPMFoam but can save significant computational resources.

- The solver "pimpleLPTFoam" neglects the particle concentration in each computational cell by assuming the fluid fraction in each computational cell is 1. The accurate performance of pimpleLPTFoam for dispersed particle-laden systems is simply due to the fact that the number

of particles in each cell is not enough to modify fluid flow fields.

Authors' contribution: Atul Jaiswal and Minh Duc Bui designed the methodology for the study. Peter Rutschmann guided the work. The extended abstract was written by Atul Jaiswal and reviewed by Minh Duc Bui and Peter Rutschmann. Atul Jaiswal prepared and delivered the oral presentation at the conference.

1.6.2 Evaluation of RANS-DEM and LES-DEM Methods in OpenFOAM for simulation of particle-laden turbulent flows

Main results: The unresolved CFD-DEM method is evaluated in its ability to predict the physics of fluid and particle phases in open-source code OpenFOAM. Both RANS-DEM and LES-DEM approaches are employed to model particle-laden turbulent flow across a backward step (BFS) flow, which is a dispersed fluid-particle system. Special attention is given to particle boundary conditions, turbulence models, turbulence dispersion models, and coupling between fluid and particle phases.

- One-way coupling regime between fluid and particle phases should be sufficient when the particle concentration is small (O$\sim 10^{-5}$). In other words, one can neglect the momentum transfer term in the fluid flow equations (effects of particles on the fluid phase), saving significant computational resources, provided particle concentration is small.

- In the RANS-DEM framework, simple turbulence dispersion models based on the Discrete Random Walk (DRW) are highly inefficient in recovering the lost turbulence fluctuations arising from RANS averaging. This is due to the fact that DRW type of dispersion models utilize only the modelled turbulent kinetic energy, under the assumption of turbulence isotropy, to calculate turbulent fluctuating velocity and its effect on overall particle trajectory.

- In the LES-DEM framework, one often has to compromise with coarser mesh resolution ($y^+ > 1$) due to the limitation of the unresolved CFD-DEM, which imposes that particle size must be smaller than CFD cell size in all regions of the domain. In this scenario, dynamic LES turbulence models overcome the poor performance of static turbulence models. It is recommended to use dynamic LES turbulence models for fluid-particle systems, where the particle size often restricts refinement on the CFD side, limiting the flow resolution.

- For the cases, where particle velocity data at the domain boundaries are not available, and extension inlet channel length is not possible due to computational limitations, the best numerical approach for estimating particle boundary condition might be to inject particles with (0 0 0) m/s of injection velocity.

- Both RANS-DEM and LES-DEM are restricted in recovering the turbulence fluctuation and their effects on particle trajectory, which are lost (due to RANS averaging) and/or not resolved (due to coarser CFD cell sizes in LES). RANS-DEM, LES-DEM, point-particle DNS-DEM, and particle-resolved DNS-DEM (resolved CFD-DEM) are still limited to simple cases with few particles. More efficient algorithms, advanced computational architecture, and high-performance computing (HPC) facilities are required to utilize the CFD-DEM approach for fluid-particle systems in greater detail.

Authors' contribution: The adapted case, considered and presented in the paper, was selected by Atul Jaiswal and Minh Duc Bui. Atul Jaiswal and Minh Duc Bui designed the methodology for the study. Atul Jaiswal performed the numerical simulations, including pre-and postprocessing. Atul Jaiswal interpreted the results with the support of Minh Duc Bui and Peter Rutschmann. The original draft of the manuscript was prepared by Atul Jaiswal and reviewed by Minh Duc Bui and Peter Rutschmann.

1.6.3 On the process of fine sediment infiltration into static gravel bed: A CFD-DEM modelling perspective

Main results: The unresolved CFD-DEM method is employed to investigate the fine sediment infiltration process into the static gravel bed. The particle tracking solvers in standalone OpenFOAM software treat particles as point particles (PP) with a certain mass. This means actual particle size, shape, and their interactions cannot be accurately modelled with standalone OpenFOAM, especially for dense particle systems such as fine sediment infiltration. To overcome this limitation, OpenFOAM coupled with a separate particle simulator, called LIGGGHTS, is employed using CFDEM-Coupling code. The theoretical size ratios, corresponding to different geometrical configurations for a binary mixture of mono-disperse spherical particles representing bridging and percolation processes, are considered and simulated with flowing water (coupled CFD-DEM) and without flowing water (pure DEM) effects. The effects of several RANS turbulence models on the infiltration process are also studied.

- The fine sediment infiltration into the static gravel process seems to be predominantly gravity-dominated, supporting Cui's hypothesis (Cui et al., 2008) that fine sediment infiltration through intra-gravel flow is similar to fine sediment infiltration driven by gravity. This suggests that the infiltration process can be modelled as a pure granular system as long as the gravel bed remains immobile. This observation enables researchers and engineers to predict the infiltration scenarios relatively quickly without worrying much about the effects of flowing water.
- The fine sediment process is distinguished between bridging and percolation processes. The occurrences of different infiltration processes are independent of gravel bed thickness; rather, they only depend on the relative grain size distribution of fine sediment and gravel (i.e., size ratio).
- To clearly distinguish between bridging and percolation processes, a definition of a sufficiently thick enough gravel bed is necessary. We hypothesized that a gravel bed deeper than five times the coarsest gravel diameter can be considered as a thick enough gravel bed.
- As long as the mean flow fields are correctly captured with the considered turbulence model and the gravel bed remains immobile, the turbulence models seem not to affect the final state of infiltration. This also indicates that the process of fine sediment infiltration into the static gravel bed is predominantly gravity-driven.

Authors' contribution: Minh Duc Bui proposed the idea of numerically investigating fine sediment infiltration. Atul Jaiswal performed the simulations, data curation, and interpreted the results. Minh Duc Bui supported all stages, from idea implementation to result interpretation. Atul Jaiswal wrote

the original draft of the manuscript, which was reviewed and rewritten by Minh Duc Bui. Peter Rutschmann supervised the study.

1.6.4 Influence of rolling resistance and particle size distribution in the simulation of sand infiltration into static gravel bed

Main Results: Several flume experiments, originally conducted by Gibson et al. (2009), are considered and numerically simulated. The experiment covers a range of sand-gravel combinations, which results in different infiltration behaviours (i.e., bridging and percolation). Section 1.6.3 focuses on the effects of flowing water on the fine sediment infiltration into a static gravel bed, assuming the particles are spherical and simplifying the sand-gravel systems to be represented by a binary mixture. With the simplification of the system, it is successfully demonstrated that the fine sediment infiltration is predominantly a gravity-dominated process. Considering this fact, the process is modelled as pure granular media under the pure DEM framework. Special attention is given to particle shape and particle size distributions (PSDs), which have either been simplified or not considered in previous studies. Particle shape effects on the sand infiltration process are implicitly incorporated by rolling resistance models, which seem to be the most efficient way of dealing with particle shapes in fluvial systems, where each sediment could have a different shape. To test the PSD effects on the infiltration process, the exact/full PSDs and the simplified versions (simplified and oversimplified PSD) for gravel and sand from the original flume experiment are considered, and their effect on the anticipated infiltration process (bridging or percolation) is discussed.

- Rolling resistance models efficiently incorporate particle shape effects when modelling quasi-static systems such as sand infiltration into a static gravel bed.

- Comparing different rolling resistance models shows that all the considered models (CDT, EPSD, and EPSD2) can capture particle shape effects, wherever the shape effects seem to be vital. The EPSD model performs marginally better than the other two models. These models implicitly consider particle shape, which adds artificial resistance to particle rotation. These models help in getting correct infiltration behaviour for bridging cases ($D_{15,Gravel}/D_{85,Sand} < 10.6$). However, the additional rolling resistance can also lead to non-physical and undesirable results for percolation cases ($D_{15,Gravel}/D_{85,Sand} > 15.4$). Therefore, it should be used carefully depending on the relative sand-gravel size.

- The simplification in PSDs is necessary to realize advanced methods (Lagrangian particle tracking) for fluvial systems. However, oversimplification could entirely modify the characteristics of gravel bed and infiltrating fine sediment, resulting in entirely different infiltration behaviours than anticipated. Therefore, a decent number of gravel and sand classes (we recommend 4-5 grain-size classes) is required to mimic the non-homogeneity and poly-dispersity found in natural fluvial sediments. It could be a good compromise between the accuracy and realizability of numerical simulations with a decent domain size, which can capture the correct bulk behaviour of fine sediment in gravel bed.

- We also showed that the infiltrating characteristics concerning particle shape and PSD are linked to size ratio $D_{15,Gravel}/D_{85,Sand}$. The size ratio can be used to decide if the rolling resistance is required for numerical simulations or not. Furthermore, the size ratio is the main

factor that should not be significantly modified when simplifying the PSDs for gravel and sand. As long as $D_{15,Gravel}$ and $D_{85,Sand}$ remain in the same range of values as full/exact PSDs, simplification is justified and should not result in unphysical results concerning the anticipated infiltration process.

Authors' contribution: Atul Jaiswal proposed the idea of implicit treatment for non-sphericity and irregularity and their effects on the fine sediment infiltration process. Atul Jaiswal and Minh Duc Bui designed the study. Nils Rüther provided the resources regarding monetary and computational facilities and guided the study. Peter Rutschmann supervised the study. Atul Jaiswal conducted the numerical simulations. The results were interpreted together. The manuscript was prepared by Atul Jaiswal. Minh Duc Bui, Nils Rüther, and Peter Rutschmann reviewed the manuscript and helped rewrite it.

Chapter 2

Overview of Numerical Frameworks to Simulate Fluid-Particle Systems – Theoretical Background and Governing Equations

Fluid-particle systems, characterized by particle-laden and droplet-laden turbulent flows, are omnipresent in nature and in industrial applications. Well-known examples are clouds, which consist of a large number of small water droplets, separation of small particles from an air flow in industrial cyclones, evaporating milk droplets in spray dryers, and sediment transport in rivers and seas. According to Crowe (2012), five key factors contribute to the turbulence modulation induced by particles: (1) surface effects: particle size normalized by a length scale d_p/l; (2) inertial effects: flow Reynolds number Re and particle Reynolds number Re_p; (3) response effects: particle response time τ_p or Stokes number St ; (4) loading effects: particle volume fraction ϵ_p; and (5) interaction effects: particle-particle as well as particle-wall. Due to various factors involved, the physics of the fluid-particle system is notoriously difficult to replicate in numerical simulations and often requires many simplifications due to computational limitations. Different numerical approaches exist to model a fluid-particle system within the aim and scope of research and application, which can be applied to numerically simulate the fluid-particle system under consideration.

The advanced methods to model fluid-particle systems can be mainly classified into two categories: Eulerian-Eulerian (e.g. Two-Fluid Model; TFM) and Eulerian-Lagrangian (e.g. Computational Fluid Dynamics-Discrete Element method; CFD-DEM) frameworks. Among these approaches, the particle phase is described either in the continuum description at a macroscopic level (Eulerian-Eulerian framework) or in the discrete description at the microscopic level (Eulerian-Lagrangian framework).

2.1 Eulerian-Eulerian Framework

In the Eulerian-Eulerian approach, each phase is treated as a continuous medium interpenetrating the other phase, and is represented by the macroscopic conservation equations, which are valid throughout the entire flow domain. This method is commonly known as the Two-Fluid Model (TFM), or when more than two phases are considered, it is called the Multi Fluid Model (MFM) (Ishii and Hibiki, 2010). Two-Fluid Model (TFM) can be used to study systems involving fluid-solid phases. This approach requires less computational effort than the Eulerian-Lagrangian approach. However, the discrete character of the dispersed phase is lost due to the averaging procedure. The kinetic theory of granular flow is usually employed to describe the solid properties (Gidaspow 1994). Some studies, mainly limited to the chemical engineering domain, used the kinetic theory of granular flow to simulate fluid-solid systems (Asegehegn et al., 2011; Cloete et al., 2012; Shuai et al., 2012; Yusuf et al., 2011). Recently, the TFM is getting more attention and is applied to model sediment transport in open channel flows as well (Ahadi et al., 2019; Chauchat et al., 2017; Chiodi et al., 2014; Zhong et al., 2011).

The Two-Fluid Model (TFM) considers the flow field that is subdivided into two single-phase regions with moving and interpenetrating interfaces between the phases. The standard single-phase conservation equations are valid for each sub-region. In theory, a two-phase flow model can be formulated in terms of the local instantaneous variable. However, the mathematical difficulties in using the local instantaneous formulations may be insurmountable in many practical cases. Hence, the macroscopic two-fluid model is derived based on the local instantaneous equations using proper averaging methods (Liu, 2014).

The continuity (Equations 2.1 and 2.2) and momentum (Equations 2.3 and 2.4) equations for fluid and solid phases for each CFD cell, following condition $\epsilon_f + \epsilon_s = 1$, are written as:

$$\frac{\partial \epsilon_f}{\partial t} + \nabla \cdot (\epsilon_f \rho_f \mathbf{U}_f) = 0 \tag{2.1}$$

$$\frac{\partial \epsilon_s}{\partial t} + \nabla \cdot (\epsilon_s \rho_s \mathbf{U}_s) = 0 \tag{2.2}$$

$$\frac{\partial (\epsilon_f \rho_f \mathbf{U}_f)}{\partial t} + \nabla \cdot (\epsilon_f \rho_f \mathbf{U}_f \mathbf{U}_f) = -\epsilon_f \nabla p + \nabla \cdot (\epsilon_f \tau_f) + \beta(\mathbf{U}_s - \mathbf{U}_f) + \epsilon_f \rho_f \mathbf{g} \tag{2.3}$$

$$\frac{\partial (\epsilon_s \rho_s \mathbf{U}_s)}{\partial t} + \nabla \cdot (\epsilon_s \rho_s \mathbf{U}_s \mathbf{U}_s) = -\epsilon_s \nabla p - \nabla p_s + \nabla \cdot (\epsilon_s \tau_s) + \beta(\mathbf{U}_f - \mathbf{U}_s) + \epsilon_s \rho_s \mathbf{g} \tag{2.4}$$

The fluid phase is assumed as a Newtonian fluid, and its stress tensor is defined using the Newtonian-stress-strain relation. Similarly, the shear stress tensor of the solid phase is assumed to be a non-Newtonian fluid. following Equations 2.5 and 2.6.

$$\tau_f = \mu_f \left[\nabla \mathbf{U}_f + (\nabla \mathbf{U}_f)^T\right] - \frac{2}{3}\mu_f (\nabla \cdot \mathbf{U}_f)\, \mathbf{I} \tag{2.5}$$

$$\tau_s = \mu_s \left[\nabla \mathbf{U}_s + (\nabla \mathbf{U}_s)^T\right] + \left(\lambda_s - \frac{2}{3}\mu_s\right)(\nabla \cdot \mathbf{U}_s)\,\mathbf{I} \tag{2.6}$$

Depending upon the resolution of the CFD for fluid and solid (particle) phases, additional terms to the fluid-particle interaction term might be required to be included. In RANS simulations in the Eulerian-Eulerian description (Two-Fluid Model; TFM), where only mean flow statistics for both fluid and solid (particle) phases are resolved, and turbulent fluctuations are lost, additional turbulent dispersion force (f_{TD}) might be included. This is achieved by adding turbulence dispersion force (f_{TD}) directly to the NS equations. Turbulence dispersion force mainly results in the dispersion of particles (or bubbles) from high to low volume fraction regions due to fluid turbulent fluctuations (Laviéville et al., 2017). Burns et al. (2004) derived an expression averaging the drag force contribution, considering the dominant combined action of turbulent eddies and drag: dispersed particles get caught up in continuous-phase turbulent eddies, and are transported by the effect of interphase drag. Following the authors, Equation 2.7 with Schmidt number equal to 0.9, covers a large range of flows without needing an adjustable constant. The model writes:

$$f_{TD} = -\epsilon_s C_D \frac{\nu_T}{\sigma_T}\left(\frac{\nabla \epsilon_s}{\epsilon_s} - \frac{\nabla \epsilon_f}{\epsilon_f}\right) \tag{2.7}$$

2.2 Eulerian-Lagrangian Framework

In the Eulerian-Lagrangian method, the continuous fluid phase is described in the Eulerian framework (called CFD), and the discrete particle phase is solved in the Lagrangian framework (called DEM). For the fluid phase, Navier-Stokes equations, modified for multiphase systems, are numerically solved (Computational Fluid Dynamics; CFD), and the motion of each particle is tracked using Newton's second law of motion (Discrete Element Method; DEM). The Eulerian-Lagrangian method is also termed the CFD-DEM approach. Coupling between the fluid (CFD) and particle (DEM) phases is achieved through mass, momentum, and energy transfers (Wen et al., 2022). The level of coupling between the fluid and particle phase mainly depends on the volumetric fraction of particles (solid material) $\epsilon_p = V_p/V$ in the system, where V_p is particle volume, and V is the total volume of particles and fluid (Elghobashi, 1994).

Considering the continuum fluid phase as an unsteady incompressible flow, the standard NS equations are modified to incorporate the particle-fluid interactions and the particle fraction in each computational cell (shown in Model A formulation of the unresolved CFD-DEM, discussed later in detail), resulting in volume-averaged NS (VANS) Equations 2.8 and 2.9. Newton's second law of motion describes the discrete particle phase (Equations 2.10, 2.11, and 2.12). In relation to notations used in TFM, the fluid velocity $\mathbf{U}_f = u_i$.

$$\frac{\partial \epsilon_f}{\partial t} + \frac{\partial (\epsilon_f u_i)}{\partial x_i} = 0 \tag{2.8}$$

$$\frac{\partial (\epsilon_f u_i)}{\partial t} + u_j \frac{\partial (\epsilon_f u_i)}{\partial x_j} = -\frac{1}{\rho}\frac{\partial (\epsilon_f p)}{\partial x_i} + \nu \frac{\partial^2 (\epsilon_f u_i)}{\partial x_j \partial x_j} + \epsilon_f g_i - \frac{f_i^p}{\rho} \tag{2.9}$$

$$m^{(k)} \frac{\partial u_i^{(p(k))}}{\partial t} = \sum_{l=1}^{n^{(c(k))}} F_i^{(c(kl))} + F_i^{(f(k))} + F_i^{(g(k))} \tag{2.10}$$

$$I^{(k)} \frac{\partial \omega_i^{(p(k))}}{\partial t} = \sum_{l=1}^{n^{(c(k))}} M_i^{(c(kl))} \tag{2.11}$$

$$\frac{dx_i^{(p(k))}}{dt} = u_i^{(p(k))} \tag{2.12}$$

The continuum (fluid) and discrete (particle) phases interact with each other; therefore, governing equations for fluid and particle phases must be coupled. The coupling regime mainly depends on the volumetric particle concentration ($\epsilon_p = 1 - \epsilon_f$). Several studies have emphasised on one-way and two-way coupling (Benra et al., 2011; Chen et al., 2019; Kitagawa et al., 2001; Ruetsch and Meiburg, 1994) for dilute particle-laden flows and fluid-structure interaction. Depending on the coupling regime, specific terms vanish in the respective governing equations. A classification map is depicted in Figure 2.1, which can be used to incorporate the level of coupling in numerical simulations (Elghobashi, 1994).

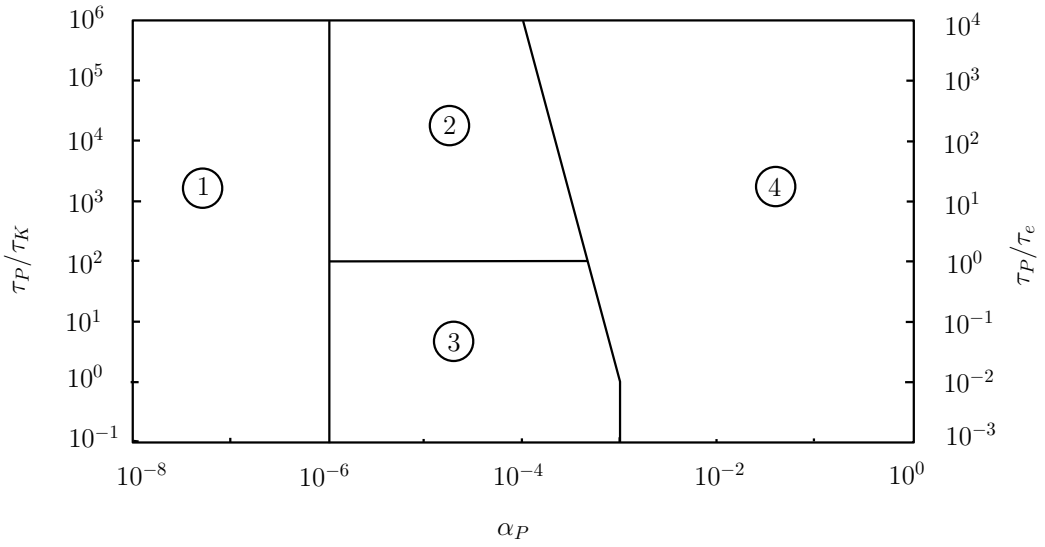

Figure 2.1: Classification map (adapted from (Elghobashi, 1994)), showing the level of coupling required for numerical simulations and interaction between particles and turbulence for (1) one-way coupling, (2) two-way coupling where particles enhance turbulent production, (3) two-way coupling where particles enhance turbulence dissipation, (4) four-way coupling.

The coupling is achieved by the momentum transfer mechanism. Depending on the fluid-particle system under consideration, the contribution of each hydrodynamic force can vary. In general, main hydrodynamic forces are: drag force (F_D), lift force (F_L), virtual mass force (F_{VM}), Basset force (F_B), pressure force (F_P), viscous shear (F_τ), as shown in Equation 2.13.

$$F_i^{(f(k))} = F_D + F_L + F_{VM} + F_B + F_P + F_\tau \tag{2.13}$$

Each hydrodynamic force is caused by different factors, and some of them are only present in an unsteady state system (Bérard et al., 2020). The contribution and significance of each hydrodynamic force in the total fluid-particle interaction term also depends on the fluid-particle system under consideration (Armenio and Fiorotto, 2001; M Kuerten, 2016). The treatment for the pressure and viscous forces and their inclusion/exclusion in total fluid-particle interaction term depends on the CFD-DEM formulation to describe the fluid-particle system (Model A, B or Bfull; discussed later in detail). Different models can be employed for other coupled forces, such as drag, lift, basset history, and virtual mass forces. In small, dense, and heavy particles, the drag force is a major contributor to fluid-particle interaction terms (Jaiswal et al., 2022). The most famous drag models are Stokes drag (Stokes, 1880), Gidaspaw (Gidaspow, 1994), Syamlal-O'Brien (Syamlal et al., 1989), Di-Felice (Di Felice, 1994), Ergun-Wen-Yu (Wen and Yu, 1966), Hill-Koch-Ladd (Koch et al., 2001) and Schiller-Naumann (Schiller, 1933). Irrespective of which hydrodynamic forces are considered in the fluid-particle interaction term, the classification map, shown in Figure. 2.3, can be used to decide the level of coupling between the fluid and particle phases. The coupling regime can be categorized into three regimes: one-way, two-way, and four-way coupling.

- One-way coupling (fluid $\rightarrow$ particle): when the volumetric concentration of particles is small ($\epsilon_p < 10^{-6}$), the fluid flow fields affect the particle motion, but particles have a negligible effect on the fluid flow fields. This results in only specific terms being considered in the governing CFD-DEM equations as follows:

$$F_i^{(f(k))} \neq 0, \quad f_i^p = 0, \quad F_i^{(c(kl))} = 0 \tag{2.14}$$

- Two-way coupling (fluid $\longleftrightarrow$ particle): when the volumetric concentration of particles increases ($10^{-3} < \epsilon_p < 10^{-6}$), both fluid and particles affect each other's motion. Two-way coupling can be further categorized into two categories, a first where particles enhance the turbulence dissipation and a second where particles enhance turbulence production, which depends on the ratio of particle reaction time ($\tau_p = \frac{\rho_p d_p^2}{18\rho\nu}$) to the Kolmogorov time scale ($\tau_e = \frac{l}{u}$) and to the turnover time of large eddies ($\tau_k = \left(\frac{\nu}{\varepsilon}\right)^{1/2}$) respectively. Two-way coupling results in the following in the CFD-DEM equations:

$$F_i^{(f(k))} \neq 0, \quad f_i^p \neq 0, \quad F_i^{(c(kl))} = 0 \tag{2.15}$$

- Four-way coupling (fluid $\longleftrightarrow$ particle, particle $\longleftrightarrow$ particle): When the volumetric concentration of particles further increases ($\epsilon_p > 10^{-3}$), the interaction among particles becomes significant. In this regime, fluid and particle affect each other's motion; additionally, the particle collision term needs to be included in the governing equations:

$$F_i^{(f(k))} \neq 0, \quad f_i^p \neq 0, \quad F_i^{(c(kl))} \neq 0 \tag{2.16}$$

Since the CFD-DEM governing equations can be only solved numerically, this approach can be further divided into two groups: the resolved and unresolved CFD-DEM approaches (Bérard et al., 2020; Kloss et al., 2012; Vega et al., 2021). The resolved and unresolved CFD-DEM approaches differ in their treatment of how the fluid-particle interaction term is calculated and the prerequisites for such treatments. The resolved CFD-DEM allows to have particles larger than CFD cell size, but the unresolved CFD-DEM method is only valid when particles are smaller than CFD cell size (see Figure 2.2).

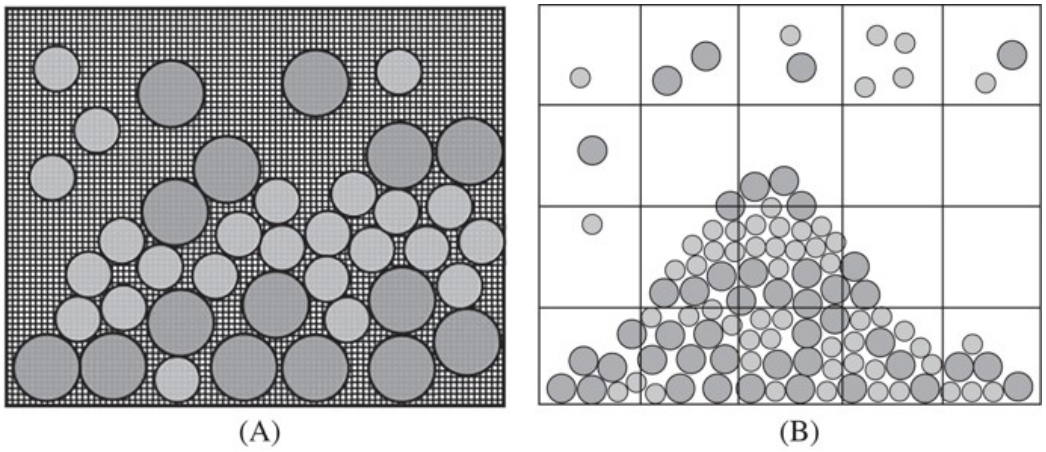

Figure 2.2: (A) Resolved CFD-DEM, the CFD cells are smaller than the particles; and (B) unresolved CFD-DEM, the CFD cells are coarser than the particles (adapted from Bérard et al. (2020)).

2.2.1 Resolved CFD-DEM (Particle-resolved DNS)

In the most detailed method, called the particle-resolved CFD-DEM or particle-resolved DNS, the flow around each particle (or droplet) is resolved, and the motion of a particle (or droplet) follows from the external and hydrodynamic forces exerted by the surrounding fluid. Since the flow around a particle (or droplet) needs to be resolved, this simulation method is only possible if the spacing of the computational grid is small compared to the size of a particle. This restricts the application of this method to the fluid-particle system, where particles are large compared to the smallest scales of the turbulent flow and/or relatively small numbers of particles. Various numerical methods have been developed for particle-resolved direct numerical simulation (DNS). One of them is a body-fitted spherical grid around the particles, sometimes embedded in a cartesian grid for the whole computational domain (Bagchi and Balachandar, 2003; Burton and Eaton, 2005; Vreman, 2016). Extension of this method to moving particles is not straightforward due to particle collisions that occur and lead to the overlap of the spherical grid of one particle with another particle. For bubbles moving in a turbulent flow, the front-tracking method has been developed, which allows the simulation of hundreds of bubbles (Kuerten and Vreman, 2005; Tryggvason et al., 2013). Larger numbers of particles in a turbulent flow have been reached using the Immersed Boundary Method (IBM) (Picano et al., 2015; Uhlmann, 2008), where a cartesian grid is used throughout the computational domain. The Immersed Boundary Method (IBM) and Adaptive Mesh Refinement (AMR) have opened the doors for moving particles, allowing particle interaction with each other and with fluid flow, but still limited to a minimal number of particles (Salih et al., 2019). Also, the Lattice-Boltzmann Method

(LBM), which is entirely different from the traditional CFD-DEM method, as both fluid and particle phases are described in the Lagrangian framework, has also been applied for the simulation of particle-laden turbulent flow (Ten Cate et al., 2004). All of the methods mentioned above, resolving turbulent flow in greater detail, are restricted to relatively small numbers of particles, which are larger than the Kolmogorov length scale (M Kuerten, 2016).

In the most famous resolved CFD-DEM approach, called the Fictitious Domain Method (FDM) (Patankar et al., 2000), only one velocity and pressure field exists for both fluid and particle phases. Those regions covered by particles have the same velocity as the particle itself. The governing equations in FDM for fluid and particle phases, along with boundary and initial conditions, can be found elsewhere (Shirgaonkar et al., 2009; Kloss et al., 2012), where these equations hold on the whole domain $\Omega = \Omega_F + \Omega_P$.

2.2.2 Unresolved CFD-DEM

The unresolved CFD-DEM solves the flow at larger scales using filtering (LES)/averaging (RANS) methods, which thus, in return, can only be applied to particles smaller than the CFD cell size. To ensure model accuracy and stability, the fluid mesh is required to be at least 3 times the size of the largest particle diameter (He et al., 2024; Wang et al., 2019; Zhou et al., 2019). Alternatively, the particles can be assumed as point particles (PP), representing point objects with a certain mass, and whereupon direct numerical simulations (DNS) can be performed, called PP DNS-DEM. The application of PP DNS-DEM to particles larger than the Kolmogorov length scale is questionable and highly discouraged (Jaiswal et al., 2022). DNS, LES and RANS approaches, which solve the NS equations, resolve the turbulence flow to a certain extent, and have their own limitations in terms of accuracy and computational cost. The different sub-approaches of solving fluid phase (CFD) and treatment of particle phase (DEM) can be combined under the unresolved CFD-DEM approach and sub-grouped into PP DNS-DEM, LES-DEM and RANS-DEM approaches. Unlike resolved CFD-DEM, where fluid-particle forces are calculated by integrating the fluid stress over the particle's surface, some empirical equations are used to calculate the fluid-particle interaction forces in the unresolved CFD-DEM. Irrespective of the turbulence treatment (DNS, LES and RANS equations used to solve the fluid phase), one condition must be satisfied: the particles must be smaller than the CFD cell sizes. In other words, particles cannot be larger than the CFD cell size, thus restricting the resolution on the CFD side and making the CFD resolution dependent on the particle size. Under such scenarios, where particle size approaches cell size or becomes larger than cell size, momentum smoothing and cell clustering could be applied. Using source smoothing, fluid cells are clustered together, forming a coarser fluid mesh when resolving the fluid-particle interaction (Song and Park, 2020; Zhang et al., 2023; Zhou et al., 2024). The unresolved CFD-DEM can be applied based on the required CFD resolution, the number and size of particles, and the computational resources available to accommodate the level of complexity.

A schematic diagram, showing the iteration mechanism in the unresolved CFD-DEM, is shown in Figure 2.3. Particles are initialized and projected onto CFD mesh, where the volume fraction of fluid and fluid-particle interaction forces in each cell is calculated. The fluid-particle interaction term is added as a source term in NS equations, which is solved iteratively. The newly calculated flow fields (flow velocity and pressure) are transferred to the DEM side, where in addition to particle-particle and body forces (e.g. gravity, buoyancy), the fluid-particle forces determine the new position of

particles and are tracked with Newton's second law of motion. The DEM time steps need to be smaller than the CFD time steps; therefore, only after some DEM iterations, the data is transferred to the CFD side. This process is repeated till the desired time steps. In calculating fluid-particle interaction forces, one needs information regarding fluid velocity at the location of each particle $(u_i)^{(s(k))}$; based on its calculation, the unresolved CFD-DEM can be categorised into PP DNS-DEM, LES-DEM and RANS-DEM.

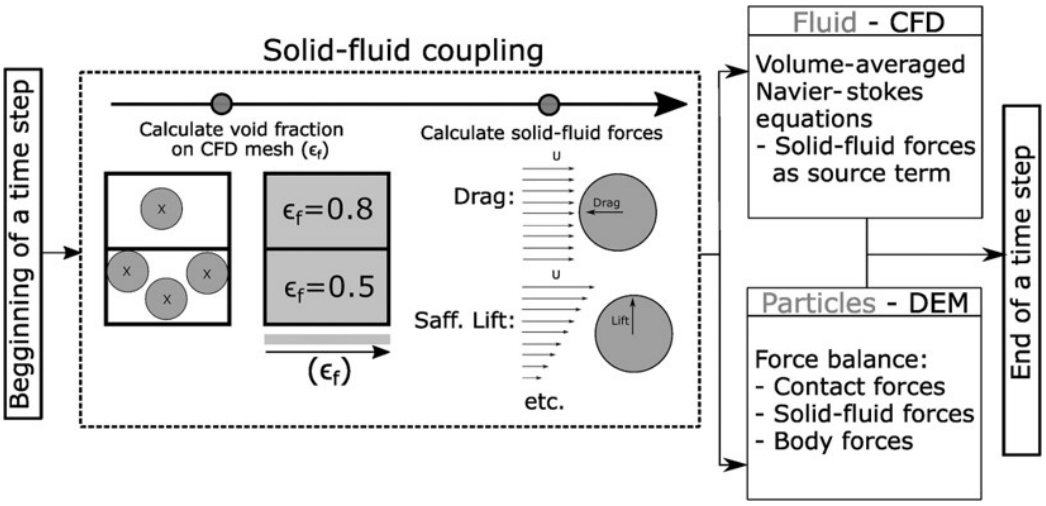

Figure 2.3: Schematic of the unresolved CFD-DEM, showing the calculations involved in CFD (fluid phase) and DEM (particle phase) sides, coupled to transfer data from one phase to another (adapted from Bérard et al. (2020)).

2.2.2.1 PP DNS-DEM

DNS solves the full NS equations numerically (Equations 2.8 and 2.9), thus resolving everything from the largest scale to the smallest dissipative eddies present in the system. In DNS under consideration of the point-particles (PP) approach, the velocity of the fluid at the particle location can be obtained directly from the DNS solution, such that

$$u_i^{(s(k))} = u_i^{\mathrm{DNS}}\left(x^{p(k)}(t), t\right) = u_i\left(x^{p(k)}(t), t\right) \tag{2.17}$$

Since turbulent flows possess a varying range of time and length scales, the exact solution (DNS), even for the simplest turbulent flows, requires enormous computational resources and extreme fine meshing. Initial estimation of computational resources required for DNS can be made based on Kolmogorov scales (smallest time, length and velocity scales) in the system. The total number of grid points and time steps requirements for single-phase DNS for uniform spacing can be estimated as:

$$N_{\mathrm{uniform}} = (100\,\mathrm{Re}_\tau)^{\frac{9}{4}} \tag{2.18}$$

$$N_{\text{time}} = \frac{\Delta t_{\text{total}}}{\Delta t} \tag{2.19}$$

$$\Delta t = \frac{0.003l}{\sqrt{\text{Re}_\tau \, u_\tau}} \tag{2.20}$$

$$\text{Re}_\tau = \frac{u_\tau l}{\nu} \tag{2.21}$$

2.2.2.2 LES-DEM

Compared to DNS, where nearly all the computational effort is used to resolve the smallest dissipative eddies, LES resolves the flow only up to the inertial subrange, not all the way to the dissipative scales. The basic idea of LES is to resolve only large-scale turbulence, while small-scale turbulence is modelled. The LES-DEM could be a good balance between accuracy and computational feasibility, saving huge computational effort yet resulting in high-resolution flow information. LES converges to DNS when finer meshing and smaller time steps are used.

In LES, the instantaneous flow field $u(x,t)$ is decomposed into resolved (or filtered) component $\overline{u}(x,t)$ and residual (or sub-grid scale; SGS) component $u'(x,t)$ by a filtering operation as follows:

$$u_i(x,t) = \overline{u}_i(x,t) + u_i'(x,t) \tag{2.22}$$

$$\overline{u}_i(x,t) = \int u_i(x',t) G(x,x';\Delta)\, dx' \tag{2.23}$$

Using LES for decomposition, the exact NS equations are reduced to filtered NS equations as follows:

$$\frac{\partial \epsilon_f}{\partial t} + \frac{\partial (\epsilon_f \overline{u}_i)}{\partial x_i} = 0 \tag{2.24}$$

$$\frac{\partial \epsilon_f \overline{u}_i}{\partial t} + \overline{u}_j \frac{\partial \epsilon_f \overline{u}_i}{\partial x_j} = -\frac{1}{\rho}\frac{\partial \epsilon_f \overline{p}}{\partial x_i} + \nu \frac{\partial^2 \epsilon_f \overline{u}_i}{\partial x_j \partial x_j} + \epsilon_f g_i - \frac{f_i^p}{\rho} + \frac{\partial \tau_{ij}^R}{\partial x_j} \tag{2.25}$$

The filtering operation results in extra terms, called residual stresses (τ_{ij}^R) in the original NS equations. One can see that the resulting equations are very similar to the original equations except for additional terms called residual stress tensor (τ_{ij}^R), which are defined as:

$$\tau_{ij}^R = \overline{u}_i \overline{u}_j - \overline{u_i u_j} = 2\rho \nu_T \overline{R_{ij}} - \frac{1}{3}\rho k_R \delta_{ij} \tag{2.26}$$

$$\overline{R_{ij}} = \frac{1}{2}\left[\frac{\partial \overline{u}_i}{\partial x_j} + \frac{\partial \overline{u}_j}{\partial x_i}\right] \tag{2.27}$$

Calculation of residual stress tensor (τ_{ij}^R) is based on the Boussinesq hypothesis of eddy viscosity (turbulence viscosity ν_T). Various models are available for this purpose, such as Smagorinsky, one-equation model (kEqn), dynamic Smagorinsky, dynamicKEqn, Spallart-Allmaras and many others.

When particle response time (Stokes number) is large compared to the smallest time scale resolved in LES, the sub-grid scales fluid velocity do not significantly influence the particle's motion (M Kuerten, 2016; Uijttewaal and Oliemans, 1996; Yeh and Lei, 1991). Under such scenarios, the LES solution can be equated to the fluid velocity at the location of the particle.

$$u_i^{(s(k))} = u_i^{\mathrm{LES}}\left(x^{p(k)}(t), t\right) = \overline{u}_i\left(x^{p(k)}(t), t\right) \tag{2.28}$$

2.2.2.3 RANS-DEM

Unlike PP DNS-DEM and LES-DEM, the resolved fluid velocity with RANS-DEM at the location of the particle is only the mean flow value and turbulence fluctuating velocity is completely lost. In RANS, the instantaneous flow field u(x,t) decomposes into a time average component $\langle u_i(x,t)\rangle$ and a fluctuating component $u_i'(x,t)$:

$$u_i(x,t) = \langle u_i(x,t)\rangle + u_i'(x,t) \tag{2.29}$$

$$\langle u_i(x,t)\rangle = \lim_{T\to\infty}\frac{1}{T}\int_0^T u_i(x,t)\,dt \tag{2.30}$$

The resulting averaged NS equations have the form:

$$\frac{\partial \epsilon_f}{\partial t} + \frac{\partial(\epsilon_f\langle u_i\rangle)}{\partial x_i} = 0 \tag{2.31}$$

$$\frac{\partial \epsilon_f\langle u_i\rangle}{\partial t} + \langle u_j\rangle\frac{\partial(\epsilon_f\langle u_i\rangle)}{\partial x_j} = -\frac{1}{\rho}\frac{\partial \epsilon_f\langle p\rangle}{\partial x_i} + \nu\frac{\partial^2 \epsilon_f\langle u_i\rangle}{\partial x_j\partial x_j} + \epsilon_f g_i - \frac{f_i^p}{\rho} - \frac{\partial\langle u_i'u_j'\rangle}{\partial x_j} \tag{2.32}$$

In the above equations, some new terms appear $\langle u_i'u_j'\rangle$ called Reynolds stresses, which are also modelled based on eddy viscosity.

$$\rho\langle u_i'u_j'\rangle = 2\rho\nu_T\overline{S_{ij}} - \frac{2}{3}\rho k\delta_{ij} \tag{2.33}$$

$$\overline{S_{ij}} = \frac{1}{2}\left[\frac{\partial\langle u_i\rangle}{\partial x_j} + \frac{\partial\langle u_j\rangle}{\partial x_i}\right] \tag{2.34}$$

The terms $\langle u_i'u_j'\rangle$, although named as Reynolds stresses, have a unit of stress only when multiplied by the fluid density ρ. Like LES, eddy viscosity ν_T can be calculated based on several models such as k-ε, k-ω, k-ω SST and many others.

The resulting fluid velocity at the location of a particle $u_i^{(s(k))}$ can be equated to the sum of the RANS (mean) velocity field and the modelled turbulent fluctuations.

$$u_i^{(s(k))} = u_i^{\mathrm{RANS}}\left(x^{p(k)}(t), t\right) + u_i' = \langle u_i\left(x^{p(k)}(t), t\right)\rangle + u_i' \tag{2.35}$$

The lost turbulent fluctuation u_i' should be recovered to predict correct particle behaviour in turbulent flows (Minier et al., 2014). It must be mentioned that the inclusion of turbulent fluctuation depends on the fluid-particle system under consideration and might not be necessary within the aim and scope of studying the considered fluid-particle system.

There are mainly two types of modelling approaches to account for missing turbulent fluctuations: either by adding stochastic noise forcing to the NS equations (Kuczaj and Geurts, 2006) or by adding an additional velocity to the particle equation of motion (Simonin et al., 1993). To recover the lost turbulent fluctuations in the RANS approach and add this recovered velocity to the particle's location (fluid velocity seen by particle), some stochastic models are available. The stochastic models are also called as dispersion models, which can be categorized into Discrete Random Walk (DRW) and Continuous Random Walk (CRW) type of dispersion models, depending upon which equations are used to recover the lost turbulence fluctuations (Dehbi, 2008). The CRW offers a more physically sound way of recovering lost turbulent fluctuation u_i', where non-dimensional Langevin equations are considered to mimic turbulence. The DRW model, also known as the Eddy Interaction Model (EIM), is simplest and based on the assumption that the fluctuating components are randomly distributed Gaussian variables whose root mean square (rms) value are equal and reduced from the turbulent kinetic energy (TKE; k), such as:

$$u_i' = \lambda_i \sqrt{\overline{u'^2}} \tag{2.36}$$

$$\sqrt{\overline{u'^2}} = \sqrt{\overline{v'^2}} = \sqrt{\overline{w'^2}} = \sqrt{\frac{2k}{3}} \tag{2.37}$$

There is another approach to recover the lost turbulent fluctuations at the particle's position u_i', which arises from RANS averaging. It applies the concept of turbulent dispersion coefficient (D), which is calculated based on the turbulent viscosity ν_T and turbulent Schmidt number σ_T, following the relation $D = \frac{\nu_T}{\sigma_T}$ to estimate turbulent fluctuating velocity. The newly calculated turbulent fluctuating velocity u_i' is added to the mean flow velocity (RANS solution). The following implantation is done in the CFDEM-Coupling:

$$u_i' = r\sqrt{\frac{6D}{\Delta t}} \tag{2.38}$$

2.3 Origin of Different Formulations in CFD-DEM Framework

The implementation of the CFD-DEM model in the Eulerian-Lagrangian framework, as pointed out by Feng and Yu (2004), lies in three aspects: the formulation of governing equations, the coupling scheme for numerical computation and the calculation of particle–fluid interaction forces.

The derivation of CFD-DEM equations is closely related to the continuum approach due to the

fact that fluid flow is still modelled at the macroscopic local average level (Zhou et al., 2010). In the Two-Fluid Model (TFM), there are three different sets of formulations, namely Set-I, Set-II, and Set-III. These formulations are more general but less detailed than hydrodynamic models (Model BFull, Model A and Model B). Due to this reason, concepts of model A and model B are more popular in TFM modelling.

Set-I: Anderson and Jackson (1967) derived the first set of governing equations for fluid and solid phases, considering them as continuum media. The motion of fluid and solid phases are described by Equations 2.39 and 2.40, respectively. The Set-I equations cannot be used unless the undetermined terms or dependency of ξ, φ, $\mathbf{S}$ and f_M on the voidage, the local mean velocities and pressure are known (Zhou et al., 2010).

$$\rho_f \epsilon_f \left[\frac{\partial \mathbf{U}_f}{\partial t} + \nabla \cdot (\mathbf{U}_f \mathbf{U}_f)\right] = \nabla \cdot \boldsymbol{\xi} - n f_M + \rho_f \epsilon_f \mathbf{g} \tag{2.39}$$

$$\rho_s \epsilon_s \left[\frac{\partial \mathbf{U}_s}{\partial t} + \nabla \cdot (\mathbf{U}_s \mathbf{U}_s)\right] = n\varphi - \nabla \cdot \mathbf{S} + n f_M + \rho_s \epsilon_s \mathbf{g} \tag{2.40}$$

Set-II: Set-II equations exploit the possibility of finding the most appropriate form for the undetermined terms in Set-I. Anderson and Jackson (1967) derived some constitutive equations: (i) $n\varphi - \nabla \cdot \mathbf{S} = \nabla \cdot \boldsymbol{\xi}_s$, which represents solid stress tensor, (ii) $\boldsymbol{\xi}$ and $\boldsymbol{\xi}_s$ are analogous to that for stress tensor in a Newtonian fluid and written to $\boldsymbol{\xi} = -p\delta_k + f(\lambda, \mu, \mathbf{u})$, (iii) decomposition of $n f_M$ into two components macroscopic and detailed variations in fluid stress tensor and written to $n f_M = n\left(\frac{V_p \nabla \cdot \boldsymbol{\xi}}{\Delta V}\right) + n f'_M = \epsilon_s \nabla \cdot \boldsymbol{\xi} + n f'_M$. Using these constitutive relations results in Set-II equations, where equations 2.41 and 2.42 describe the motion of fluid and particle phases, respectively.

$$\rho_f \epsilon_f \left[\frac{\partial \mathbf{U}_f}{\partial t} + \nabla \cdot (\mathbf{U}_f \mathbf{U}_f)\right] = \epsilon_f \nabla \cdot \boldsymbol{\xi} - n f'_M + \rho_f \epsilon_f \mathbf{g} \tag{2.41}$$

$$\rho_s \epsilon_s \left[\frac{\partial \mathbf{U}_s}{\partial t} + \nabla \cdot (\mathbf{U}_s \mathbf{U}_s)\right] = \epsilon_s \nabla \cdot \boldsymbol{\xi} + n f'_M + \rho_s \epsilon_s \mathbf{g} + \nabla \cdot \boldsymbol{\xi}_s \tag{2.42}$$

Set-III: Jackson (1963), and Anderson and Jackson (1967) indicated that the particle-fluid interaction term can be written in another form. This could eliminate the fluid stress tensor from solid phase equations. In particular, to eliminate the fluid stress tensor $\boldsymbol{\xi}$, an equation is obtained by multiplying equation 2.41 with $(1 - \epsilon_f)/\epsilon_f$ and subtracting it from Equation 2.42, giving Equation 2.43.

$$\rho_s \epsilon_s \left[\frac{\partial \mathbf{U}_s}{\partial t} + \nabla \cdot (\mathbf{U}_s \mathbf{U}_s)\right] = \frac{n f'_M}{\epsilon_f} - \rho_f \epsilon_s \mathbf{g} + \rho_f \epsilon_s \left[\frac{\partial \mathbf{U}_f}{\partial t} + \nabla \cdot (\mathbf{U}_f \mathbf{U}_f)\right] + \rho_s \epsilon_s \mathbf{g} + \nabla \cdot \boldsymbol{\xi}_s \tag{2.43}$$

It can be seen that elimination of fluid stress tensor $\boldsymbol{\xi}$ has introduced a buoyancy term $(-\rho_f \epsilon_s \mathbf{g})$ and a fluid acceleration term $\rho_f \epsilon_s \left[\frac{\partial \mathbf{U}_f}{\partial t} + \nabla \cdot (\mathbf{U}_f \mathbf{U}_f)\right]$ into the particle phase equation. If the fluid

acceleration term approaches zero or is much smaller than $\frac{nf'_M}{\epsilon_f} - \rho_f \epsilon_s \mathbf{g}$, then the total fluid-particle interaction term can be written in the form of the Equation 2.44.

$$nf_M = \frac{nf'_M}{\epsilon_f} - \rho_f \epsilon_s \mathbf{g} \tag{2.44}$$

Incorporating Equation 2.44 in Equation 2.39 and Equation 2.40 and considering $n\varphi - \nabla \cdot \mathbf{S} = \nabla \cdot \boldsymbol{\xi}_s$, gives the third set of equations (Set-III), where Equations 2.45 and 2.46 describe the motion of fluid and particle phases, respectively.

$$\rho_f \epsilon_f \left[\frac{\partial \mathbf{U}_f}{\partial t} + \nabla \cdot (\mathbf{U}_f \mathbf{U}_f) \right] = \nabla \cdot \boldsymbol{\xi} - [nf'_M - \rho_f \epsilon_s \mathbf{g}] + \rho_f \epsilon_f \mathbf{g} \tag{2.45}$$

$$\rho_s \epsilon_s \left[\frac{\partial \mathbf{U}_s}{\partial t} + \nabla \cdot (\mathbf{U}_s \mathbf{U}_s) \right] = \nabla \cdot \boldsymbol{\xi}_s + [nf'_M - \rho_f \epsilon_s \mathbf{g}] + \rho_s \epsilon_s \mathbf{g} \tag{2.46}$$

From the derivation of Set-III equations, it is clear that they are conditional and only valid if the flow is steady and uniform. This means that the following condition must be satisfied (Equation 2.47).

$$\rho_f \epsilon_s \left[\frac{\partial \mathbf{U}_f}{\partial t} + \nabla \cdot (\mathbf{U}_f \mathbf{U}_f) \right] = 0 \tag{2.47}$$

The above-mentioned formulations (Set-I, Set-II and Set-III) exist in another form, called hydrodynamic models, which is more intuitive and easier to interpret in terms of hydrodynamic forces. The hydrodynamic models, namely Model A, Model B and Model Bfull, have been used to solve fluid phase in both TFM and CFD-DEM approaches. The difference in Models A and B (or Bfull) depends on the treatment of the pressure source term in the governing equations. Generally speaking, if the pressure is attributed to the fluid phase alone, it is referred to as Model B or Bfull. If the pressure is shared by both the fluid and solid phases, it is referred to as Model A. On comparing the three formulations of (Set-I, Set-II and Set-III) with those hydrodynamics models. It can be seen that, in principle, Model A is consistent with Set-II and Model B with Set-III. Set-III (or Model B) is derived from Set-I equations with the assumption of steady and uniform flow (Equation 2.47). Set-I can be termed as original Model B or Model Bfull. Most researchers prefer model A as reflected in software packages FLUENT, CFX and OpenFOAM use Model A based equations.

Model Bfull (Set-I):

$$\begin{cases} \rho_f \epsilon_f \left[\dfrac{\partial \mathbf{U}_f}{\partial t} + \nabla \cdot (\mathbf{U}_f \mathbf{U}_f) \right] = -\nabla p - f_{pf}^{\text{Set-I}} + \nabla \cdot \tau + \rho_f \epsilon_f \mathbf{g} \\ f_{pf}^{\text{Set-I}} = \dfrac{1}{\Delta V} \displaystyle\sum_{k=1}^{n} (f_{d,k} + f_{\nabla p,k} + f_{\nabla \cdot \tau,k} + f''_k) \end{cases} \tag{2.48}$$

Model A (Set-II):

$$\begin{cases} \rho_f \epsilon_f \left[\dfrac{\partial \mathbf{U}_f}{\partial t} + \nabla \cdot (\mathbf{U}_f \mathbf{U}_f) \right] = -\epsilon_f \nabla p - f_{pf}^{\text{Set-II}} + \epsilon_f \nabla \cdot \tau + \rho_f \epsilon_f \mathbf{g} \\ f_{pf}^{\text{Set-II}} = \dfrac{1}{\Delta V} \sum_{k=1}^{n} (f_{d,k} + f_k'') \end{cases} \tag{2.49}$$

Model B (Set-III):

$$\begin{cases} \rho_f \epsilon_f \left[\dfrac{\partial \mathbf{U}_f}{\partial t} + \nabla \cdot (\mathbf{U}_f \mathbf{U}_f) \right] = -\nabla p - f_{pf}^{\text{Set-III}} + \nabla \cdot \tau + \rho_f \epsilon_f \mathbf{g} \\ f_{pf}^{\text{Set-III}} = \dfrac{1}{\epsilon_f \Delta V} \sum_{k=1}^{n} (f_{d,k} + f_k'') - \dfrac{1}{\Delta V} \sum_{k=1}^{n} (\rho_f V_{p,k} \mathbf{g}) \end{cases} \tag{2.50}$$

The fluid-particle interaction forces on particle k is categorized into dominant forces such as drag ($f_{d,k}$), pressure gradient ($f_{\nabla p,k}$), viscous forces ($f_{\nabla \cdot \tau,k}$) and other minor forces (f_k''). The other minor forces include virtual mass ($f_{VM,k}$), Basset ($f_{B,k}$), Saffman ($f_{Saff,k}$) and Magnus lift ($f_{Mag,k}$) forces. Therefore, the relation for the fluid-particle interaction term, referring to original formulations (Set-I, Set-II, Set-III) can be written as shown in Equations 2.51, 2.52, 2.53 and 2.54.

$$f_k'' = f_{\text{VM},k} + f_{\text{B},k} + f_{\text{Saff},k} + f_{\text{Mag},k} \tag{2.51}$$

$$f_{pf}^{\text{Set-I}} = n f_M = -\epsilon_s \nabla p + \epsilon_s \nabla \cdot \tau + n f_M' = \frac{1}{\Delta V} \sum_{k=1}^{n} (f_{d,k} + f_{\nabla p,k} + f_{\nabla \cdot \tau,k} + f_k'') \tag{2.52}$$

$$f_{pf}^{\text{Set-II}} = n f_M' = n f_M - (-\epsilon_s \nabla p + \epsilon_s \nabla \cdot \tau) = \frac{1}{\Delta V} \sum_{k=1}^{n} (f_{d,k} + f_k'') \tag{2.53}$$

$$f_{pf}^{\text{Set-III}} = n f_M' - \rho_f \epsilon_s g = \frac{1}{\epsilon_f \Delta V} \sum_{k=1}^{n} (f_{d,k} + f_k'') - \frac{1}{\Delta V} \sum_{k=1}^{n} (\rho_f V_{p,k} g) \tag{2.54}$$

The treatment of solid phase in DEM under CFD-DEM equations is quite different from traditional TFM. In the CFD-DEM method, one has to consider the coupling between DEM at the particle scale and CFD at the continuum scale. Using the soft-sphere approach originally proposed by Cundall and Strack (1979), the translational and rotational motion of particle k with mass m^k and moment of inertia I^k can be written as:

$$m^k \frac{du^{p(k)}}{dt} = F_{pf,k} + \sum_{l=1}^{n^{c(k)}} (F_{c,kl} + F_{d,kl}) + m^k g \tag{2.55}$$

$$I^i \frac{d\omega^{p(k)}}{dt} = \sum_{l=1}^{n^{c(k)}} (M_{t,kl} + M_{r,kl}) \tag{2.56}$$

The fluid-particle interaction force $F_{pf,k}$, which is the fluid-particle interaction term in the particle phase. f_{pf} and F_{pf} are the sum of all fluid-particle interaction forces at the CFD cell level for the fluid phase and at the individual particle level for the solid phase, respectively, and similar to f_M in the TFM. The fluid-particle interaction term includes the so-called drag force $f_{d,k}$, pressure gradient force $f_{\nabla p,k}$, viscous force $f_{\nabla\cdot\tau,k}$ due to fluid shear stress or deviatoric stress, and other usually not so relevant forces $f_k^{''}$ such as virtual mass force $f_{VM,k}$, Basset force $f_{B,k}, k$, lift forces such as the Saffman force $f_{Saff,k}$, and Magnus force $f_{Mag,k}$. Usually buoyancy force is included in the pressure gradient force. Therefore, the total particle-fluid interaction force on particle k can be written as:

$$F_{pf,k} = f_{d,k} + f_{\nabla p,k} + f_{\nabla\cdot\tau,k} + f_k'' \tag{2.57}$$

Similar to the fluid phase, the interaction force has different forms corresponding to Set-I (Model Bfull), Set-II (Model A) and Set-III (Model B) in the solid phase (particle phase).

Model Bfull (Set-I):

$$F_{pf,k} = f_{d,k} + f_{\nabla p,k} + f_{\nabla\cdot\tau,k} + f_k'' \tag{2.58}$$

Model A (Set-II):

$$F_{pf,k} = f_{d,k} + f_{\nabla p,k} + f_{\nabla\cdot\tau,k} + f_k'' \tag{2.59}$$

Model B (Set-III):

$$F_{pf,k} = \frac{f_{d,k} + f_k''}{\epsilon_f} - \rho_f V_{p,k} g \tag{2.60}$$

Model BFull (Set-I) and Model A (Set-II) are, in principle, the same and interchangeable forms. Let's take Model Bfull form as shown in Equation 2.61. The derivation below closely follows the paper of (Zhou et al., 2010) and can be referred for more information.

$$\rho_f \epsilon_f \left[\frac{\partial \mathbf{U}_f}{\partial t} + \nabla \cdot (\mathbf{U}_f \mathbf{U}_f) \right] = -\nabla p - f_{pf}^{\text{Set-I}} + \nabla \cdot \tau + \rho_f \epsilon_f \mathbf{g} \tag{2.61}$$

Here $f_{pf}^{\text{Set-I}}$ is the sum of all the fluid forces action on the particle (drag + viscous + pressure gradient + other minor forces), such that

$$f_{pf}^{\text{Set-I}} = n f_M = -\epsilon_s \nabla p + \epsilon_s \nabla \cdot \tau + n f_M' = \frac{1}{\Delta V} \sum_{k=1}^{n} (f_{d,k} + f_{\nabla p,k} + f_{\nabla\cdot\tau,k} + f_k'') \tag{2.62}$$

Putting equation 2.62 in Equation 2.61,

$$\rho_f \epsilon_f \left[\frac{\partial \mathbf{U}_f}{\partial t} + \nabla \cdot (\mathbf{U}_f \mathbf{U}_f)\right] = -\nabla p - (-\epsilon_s \nabla p + \epsilon_s \nabla \cdot \tau + n f'_M) + \nabla \cdot \tau + \rho_f \epsilon_f \mathbf{g}$$

$$\rho_f \epsilon_f \left[\frac{\partial \mathbf{U}_f}{\partial t} + \nabla \cdot (\mathbf{U}_f \mathbf{U}_f)\right] = -\nabla p + \epsilon_s \nabla p - \epsilon_s \nabla \cdot \tau - n f'_M + \nabla \cdot \tau + \rho_f \epsilon_f \mathbf{g}$$

$$\rho_f \epsilon_f \left[\frac{\partial \mathbf{U}_f}{\partial t} + \nabla \cdot (\mathbf{U}_f \mathbf{U}_f)\right] = \nabla p(-1 + \epsilon_s) + \nabla \cdot \tau(1 - \epsilon_s) - n f'_M + \rho_f \epsilon_f \mathbf{g}$$

$$\rho_f \epsilon_f \left[\frac{\partial \mathbf{U}_f}{\partial t} + \nabla \cdot (\mathbf{U}_f \mathbf{U}_f)\right] = -\nabla p(1 - \epsilon_s) + \nabla \cdot \tau(1 - \epsilon_s) - n f'_M + \rho_f \epsilon_f \mathbf{g}$$

Using $\epsilon_s + \epsilon_f = 1$

$$\rho_f \epsilon_f \left[\frac{\partial \mathbf{U}_f}{\partial t} + \nabla \cdot (\mathbf{U}_f \mathbf{U}_f)\right] = -\nabla p\, \epsilon_f + \nabla \cdot \tau\, \epsilon_f - n f'_M + \rho_f \epsilon_f \mathbf{g}$$

$$\rho_f \epsilon_f \left[\frac{\partial \mathbf{U}_f}{\partial t} + \nabla \cdot (\mathbf{U}_f \mathbf{U}_f)\right] = -\epsilon_f \nabla p + \epsilon_f \nabla \cdot \tau - n f'_M + \rho_f \epsilon_f \mathbf{g}$$

As $n f'_M = f_{pf}^{\text{Set-II}} = n f_M - (-\epsilon_s \nabla p + \epsilon_s \nabla \cdot \tau) = \frac{1}{\Delta V} \sum_{k=1}^{n} (f_{d,k} + f''_k)$ is the sum of interaction forces including drag and other minor forces only,

$$\rho_f \epsilon_f \left[\frac{\partial \mathbf{U}_f}{\partial t} + \nabla \cdot (\mathbf{U}_f \mathbf{U}_f)\right] = -\epsilon_f \nabla p + \epsilon_f \nabla \cdot \tau - f_{pf}^{\text{Set-II}} + \rho_f \epsilon_f \mathbf{g} \tag{2.63}$$

As one can see, we started from Model BFull (Set-I) in Equation 2.61 and landed up with Model A (Set-II) in Equation 2.63 just by mathematical manipulation. The sets of equations in Model BFull (Set-I) and Model A (Set-II) in the CFD-DEM are generic and mathematically equivalent. On the other hand, Model B (Set III) is only valid for conditionally valid for steady and uniform flow. In the dissertation, Model A (Set-II) equations are employed for evaluation of the unresolved CFD-DEM and later on also for application to study fine sediment infiltration.

Chapter 3

Simulation of Particle-laden Turbulent Flow in OpenFOAM

This chapter is published as:
Jaiswal, A.; Bui, M.D.; Rutschmann, P. Simulation of Particle-laden Turbulent Flow in OpenFOAM. *Proceedings of the 39th IAHR World Congress*, 19-24 June 2022. Pages 4328-4335.
https://doi.org/10.3850/IAHR-39WC2521711920221242

Note: In the governing equations, the symbols for fluid (α) and particle fractions (α_p), used in this chapter, differ from the usual symbols used throughout the Dissertation for fluid (ϵ_f) and particle fractions (ϵ_p).

Proceedings of the 39th IAHR World Congress
19–24 June 2022, Granada, Spain
doi://10.3850/IAHR-39WC2521716X20221242

Simulation of Particle-laden Turbulent Flow in OpenFOAM

Atul Jaiswal[1], Minh Duc Bui[2] and Peter Rutschmann[3]

[1,2,3] Technical University of Munich (TUM), Munich, Germany
jaiswal.atul2018@gmail.com

Abstract

Our work attempts to provide a comprehensive analysis of modelling two-phase flows (fluid-particle) with regard to computational requirements, available models, challenges and limitations. The adopted case (particle-laden backward facing step (BFS) flow) is numerically simulated in the framework of Eulerian-Lanrangian method (RANS-DEM) using OpenFOAM. Firstly, the case was simulated as single-phase (fluid without particles) using solver pimpleFOAM in order to define the simulation parameters and the meshing requirement, giving good agreement with the measured fluid velocity profiles in the experiment. Later on, the case was modified as a two-phase system by including the particles and simulated using two similar yet different solvers namely DPMFoam (standard OpenFOAM solver) and pimpleLPTFoam (self-compiled solver). The simulation results obtained from these two solvers demonstrate almost no difference due to small concentration of particles, indicating that one can save significant computational resources by not considering void fraction in the governing fluid flow equations. Investigation on the coupling regime demonstrates almost no difference in predicted fluid and particle velocity profiles corresponding 1-way and 2-way coupling, as the small number of particles in each CFD cell are unable to modify flow fields significantly. Analysis on different initial velocities of particles shows that by proving zero initial velocity to the particles, they get the opportunity to attain the real velocity depending upon the flow around them and the particle response time (Stokes number). Our study shows that RANS-DEM with simple dispersion models is unable to predict the particle dispersion correctly, thus more sophisticated dispersion models are required.

Keywords: Particle-laden Turbulent Flows; RANS-DEM; Dispersion Model; OpenFOAM

1. INTRODUCTION

Particle-laden flows can be observed almost everywhere from nature to industrial and biological processes and have been interesting to the scientific community for decades. Physical experiments and numerical simulations help us to understand these processes in detail but have their own limitations in terms of infrastructure required for specific tasks and fields of study. Additionally, being a two-phase system (fluid being continuum phase and particle being discrete phase) involves complex physics including fluid-particle and particle-particle interaction, turbulence modification etc., thus difficult to model.

According to Crowe et al. (2011), five key factors that appear to contribute to the turbulence modulation induced by particles are: (1) Surface effects: particle size normalized by a length scale d_p/l; (2) Inertial effects: flow Reynolds number Re and particle Reynolds number Re_p; (3) Response effects: particle response time τ_p or Stokes number St; (4) Loading effects: particle volume fraction α_p; (5) Interaction effects: particle-particle, particle-wall. Due to the complex physics involved, physical experiments considering all the factors are usually not possible. On the other hand, numerical simulations of these multi-variable systems would help us to understand such systems in greater detail but currently available models and computational capacity restrict its application and are generally limited to simple cases and small number of particles.

Two phase systems (fluid-particles) can be modelled in two different frameworks namely Eulerian-Eulerian and Eulerian-Lagrangian (also called CFD-DEM method) method. Eulerian-Eulerian method is computationally less expensive but on the cost of losing the discrete nature of particles, whereas Eulerian-Lagrangian method treats particles as discrete entities, thus requires enormous computational resources. More specifically, in CFD-DEM approach, fluid phase is resolved using the Navier Stokes equation (applying DNS/LES/RANS methods) and each particle present in the system is tracked using Newton's second law of motion. One of the biggest challenges for numerical simulations of particle-laden flows is resolving fluid flow fields as precisely as possible with limited computational resources, as for the cases with complex geometry and higher Reynolds number, computational requirement increases potentially. Some averaging (RANS) and filtering (LES) approaches can be used to get the required information with comparative lesser computational cost and usually used for engineering applications. The Discrete Element Method (DEM) can be used to

Proceedings of the 39th IAHR World Congress
19–24 June 2022, Granada, Spain

model the mechanical behavior of granular flows and to simulate the forces acting on each particle and its motion. Additionally, particles being tracked in DEM framework, demands additional computational resources even when fluid phase is resolved using RANS/LES methods. Furthermore, modelling of particle's motion in turbulent flow is difficult because it involves both the modelling of the surrounding flow field, resulting pressure gradients and modelling of the particle-flow interaction, which involves the local flow around the particle and the forces resulting from stress applied on the particle by the flow (Brennen, 2005). With the currently available computational resources, it is still quite difficult to find the trade off and compromise between the level of flow resolution obtained (DNS/LES/RANS) and the required computational efforts in order to predict the correct particle dispersion and trajectories. Some recent studies focusing on RANS-DEM approach and dispersion modelling in fluid-particle systems can be found in the literature (Greifzu et al., 2016; Kasper et al., 2019; Mofakham and Ahmadi, 2020; Xiang, 2019).

Commercial software such as Fluent EDEM, STAR-CCM+ and AVL-fire (Mohammadreza, 2014; Jajcevic et al., 2013; Eppinger et al., 2011; Fries et al., 2011; Spogis,2008), in-house CFD programs like LESOCC (Breuer and Alletto, 2012) and research codes (Wu et al., 2014; Capecelatro and Desjardins, 2013; Deb and Tafti, 2013; Drake and Calantoni, 2001) can be applied to CFD-DEM simulations but the accessibility of these solvers is limited. On the other hand, some open source CFD code such as OpenFOAM (OpenCFD Limited, n.d.) has accelerated the research in the field. We have used OpenFoam-v1912 to simulate particle-laden BFS flow (Fessler and Eaton, 1999) under the framework of RANS-DEM method. Effects of 1-way and 2-way coupling on fluid and particle velocity profiles are studied. Different options to approximate the particle initial velocity are discussed and a suitable approach (when exact initial velocity of particles is not available) is suggested. Furthermore, two different particle-tracking solvers (DPMFoam and pimpleLPTFoam) are used to simulate the case in order to investigate the effect on void fraction in governing equations and corresponding fluid and particle phase results. The comparative analysis between different particle tracking solvers hints that it might be appropriate not to consider void fraction in fluid flow equations when particle concentration is small, which could save significant computational cost.

2. GOVERNING EQUATIONS

Adopted Eulerian-Lagrangian method uses Reynolds averaged Navier Stokes equation to resolve the fluid flow fields and particles are tracked by solving Newton's second law of motion.

Reynolds-averaged Navier Stokes equations (RANS) for Newtonian, incompressible fluid flow considering the solid fraction ($\alpha_p = 1 - \alpha$) in each computational cell are described as:

$$\frac{\partial \alpha}{\partial t} + \frac{\partial \alpha u_i}{\partial x_i} = 0 \quad [1]$$

$$\frac{\partial \alpha u_i}{\partial t} + u_j \frac{\partial \alpha u_i}{\partial x_j} = -\frac{1}{\rho}\frac{\partial \alpha p}{\partial x_i} + \upsilon \frac{\partial^2 \alpha u_i}{\partial x_j \partial x_j} + \alpha g_i - \frac{f_i^p}{\rho} + \frac{\partial \tau_{ij}^R}{\partial x_j} \quad [2]$$

Where, $u_i$and p are the Reynolds-averaged flow velocity and pressure fields, ρ is fluid density, υ is the kinematic viscosity, g_i is the gravitational acceleration, f_i^p is the momentum transfer term from particle phase, τ_{ij}^R are the Reynold's stresses (based on eddy-viscosity), x_i and t represents space and time respectively.

Newton's second law of motion describing trajectories of point particles (PP) as per the equations below:

$$m_i \frac{\partial u_i^p}{\partial t} = \sum_{j=1}^{n_i^c} F_{ij}^c + F_i^f + F_i^g \quad [3]$$

$$\frac{dx_i^p}{dt} = u_i^p \quad [4]$$

Where, m_i is the particle mass, u_i^p and x_i^p are the velocity and location of particle, F_{ij}^c is the contact forces between particles, F_i^f is the surface forces acting on particle (drag and pressure gradient forces are considered for the simulations), F_i^g is the body force (consists of gravity and buoyant forces). Contact forces

between the particles (F_{ij}^{c}) is not considered in the numerical simulations due to that fact that particles concentration is small (dilute flow) and probability of particles being in contact is almost zero. OpenFOAM considers particles to be point-particle (PP), therefore torque acting on particles doesn't contribute in their trajectory. The considered point-particle (PP) approach also serves the purpose of keeping the particle size smaller than CFD cell size, which is main assumption of unresolved CFD-DEM.

3. COUPLING BETWEEN FLUID AND PARTICLE PHASES

The fluid and particle phases are coupled using momentum transfer mechanisms affecting the motion of each other. The coupling regime can be categorized into three types namely 1-way, 2-way and 4-way coupling. According to Elghobashi (1994), this depends on the volumetric fraction of solid materials (α_p=V_p/V) in the system, where V_p and V are particle volume and total volume respectively. When α_p < 10^{-6}, 1-way coupling is considered, where fluid flow affects the motion of particles but the particles have negligible effect on the fluid flow fields. 2-way coupling occurs when $10^{-6} < \alpha_p < 10^{-3}$ i.e. fluid and particles, both affect the motion of each other. 2-way coupling can be further categorized into two categories, a first where particles increase the turbulence dissipation and a second where particles increase turbulence production, that depends on the ratio of particle reaction time ($\tau_p = \rho_p d_p^2/18\rho\upsilon$) to the Kolmogorov time scale ($\tau_k = (\upsilon/\epsilon)^{1/2}$) and to the turnover time of large eddies ($\tau_e = l/u$) respectively, where ρ_p is the density of particle, d_p is the diameter of particle, ρ is the density of fluid, υ is the kinematic viscosity of fluid, ϵ is turbulence dissipation rate, l is turbulence length scale and u is the fluid velocity. When the particle volume fraction further increases $\alpha_p > 10^{-3}$, 4-way coupling should be applied, where particle-particle interaction is considered in addition to fluid-particle interaction. We have investigated the effect of 1-way and 2-way coupling regime in simulated fluid and particle phase results

4. DISPERSION MODEL

RANS provides only the mean flow field statistics and information of the fluctuating component of flow fields is lost due to averaging. In order to recover that information and include the effect of those fluctuations (turbulence) on the trajectory of particles, simple stochastic models are used, which are based on Discrete Random Walk (DRW) type dispersion modelling. In the DRW type dispersion models, the fluctuating component is calculated from the turbulent kinetic energy (k), which is provided by the turbulence models (we considered, k-ω SST model in our simulations) applied to close the RANS equations.

The following equation describes the dispersion model used to calculate fluctuating component:

$$u_i' = \sqrt{\frac{2}{3}k}\, x_{rnd}\, e_i \qquad [5]$$

Where, x_{rnd} is a random factor reproduces a probability density function with Gaussian distribution with an expected value μ = 0 and standard deviation σ = $\sqrt{\frac{2}{3}k}$. e_i is a unit vector, that point either in a random direction (in StochasticDispersionRAS) or in -∇k (in GradientDispersionRAS). Our initial investigation reveals that there are very minor differences in predicted particle dispersion with these dispersion models and StochasticDispersionRAS performs slightly better than GradientDispersionRAS. Therefore, we have used StochasticDispersionRAS model for our RANS-DEM simulations.

5. SOLVERS DESCRIPTION

Solver pimpleFoam is used for single-phase simulations, which uses PIMPLE algorithm to couple pressure and velocity fields, thus providing the flexibility of using Courant number higher than 1. For two-phase simulations, we use two similar yet different particle-tracking solvers (DPMFoam and pimpleLPTFoam) in OpenFOAM to simulate our RANS-DEM simulations. Solver DPMFoam is a standard particle-tracking solver which is provided with standard OpenFOAM installation. Additionally, a self-compiled particle tracking solver pimpleLPTFoam (Kasper, 2018) is used, which is very similar to solver DPMFoam except it does not consider solid fraction in each computational cell resulting α = 1 in the corresponding governing equations. Both the solvers solve the exact same sets of equations by coupling fluid and particle phase and also use the PIMPLE algorithm for pressure-velocity coupling.

Proceedings of the 39th IAHR World Congress
19–24 June 2022, Granada, Spain

The RANS-DEM simulation of the case (particle-laden BFS flow) subjected same initial and boundary conditions using the solvers DPMFoam and pimpleLPTFoam provides comparative performance evaluation of those solvers concerning fluid and particle phase results and computational cost. The advantage of using pimpleLPTFoam is that it can significantly reduce computational cost, especially in terms of processing power, when the particle concentration is small.

6. CASE DESCRIPTION AND NUMERICAL SETUP

Benchmark experiment of particle-laden BFS flow by Fessler and Eaton (1999) is numerically simulated in 3-D using the C++ CFD toolbox (OpenFOAM-v1912). Test section from the original experiment is considered for numerical simulations and has dimensions as specified in the figure 1.

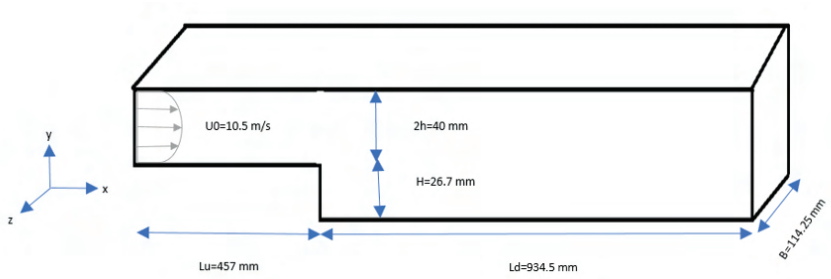

Figure 1. Geometry of test section (Backward-facing step).

The experimental facility provides a fully developed turbulent air flow with center-line velocity of 10.5 m/s, along with the particles injected at a certain mass flow rate. The Reynolds number based on centerline velocity is 13800 and 18400 at the channel section (based on channel half height ***h***) and at the step (based on step height ***H***) respectively. In order to achieve the fully developed flow at the inlet, mapped boundary condition is applied, where flow fields are mapped from 400 mm downstream of the inlet resulting a fully developed turbulent flow with centerline velocity (U0) of 10.5 m/s and average velocity (Uavg) of 9.39 m/s. Copper particles having diameter ~70 μm are injected from inlet at 10% mass loading. In the numerical model particle injection and its initial velocity are tested in different scenarios, as the exact particle velocity profile at the inlet (boundary) was not measured in the original experiment. Assuming all the particles have attained a constant velocity (injection velocity) as they reach the inlet of the BFS, two extreme bounds of particle injection velocity are tested, where particles are injected with (10.5, 0, 0) m/s (upper bound) and (0, 0, 0) m/s (lower bound) of injection velocity. Additionally, assuming particles have attained the velocity that follows the mean fluid velocity profile at the inlet (i.e. particles injected at the center will have an injection velocity similar to the centerline velocity of the fluid, particle injected near to the walls will have almost zero injection velocity due to no-slip boundary condition applied for the fluid phase) is also tested. This approach provides the idea to approximate the real particle velocities for the cases where exact information about particle initial velocity is not available.

In our single and two-phase simulations, we used the RANS approach to resolve the fluid flow fields. For that, we used the standard k-ω SST (kOmegaSST) turbulence model. We have made it sure that the single-phase results match with the experimental data before particles are included in it. The fluid, particle and geometry characteristics considered for numerical simulations can be found in table 1.

Table 1. fluid and particle-phase characteristics and geometry considered for numerical setup.

Fluid (air): Density (ρ) = 1.225 kg/m^3 Kinematic viscosity (ν) = 1.5e^{-5} m^2/s Centerline velocity (U0) at inlet= (10.5 0 0) m/s Average velocity (Uavg) at inlet = (9.39 0 0) m/s
Particles (copper): Particle size distribution (PSD): Normal distribution with expected value of 68.2 μm and standard deviation of 10.9 μm Density, ρ_p = 8800 kg/m^3 Mass flow rate of particle (mass loading), $\dot{m}_p/\dot{m}_f$ = 10%
Geometry: Channel half-height, h =20 mm

Channel span, Lu = 457 mm Expansion channel length, Ld = 935 mm Step height, H = 26.7 mm Width (B) = 114.25 mm

7. RESULTS AND DISCUSSION

Form figure 2, one can see that the simulated streamwise fluid mean velocity profiles match quite well with the experimental data at all measurement locations. The simulated flow re-attachment point (x/H~7) is also very close to the experimentally observed flow re-attachment point (x/H~7.4). We see almost no difference in simulated fluid velocity profiles for 1- and 2-way coupling, as the lower particle concentrations are unable to modify the fluid phase results. The results verify that it is sufficient to consider 1-way coupling when particle concentration is below threshold suggested by Elghobashi (1994). Here, we have only shown the fluid phase results for the case corresponding to particle injection velocity (10.5 0 0) m/s. The fluid phase results for the cases corresponding to other two particle injection velocities are very similar.

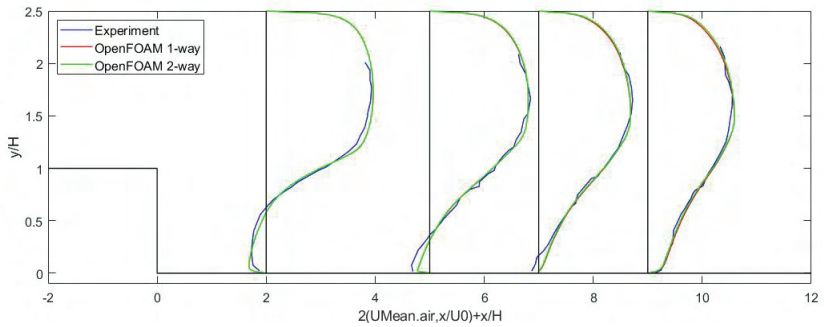

Figure 2. Comparisons of experimental and OpenFOAM simulated (with DPMFoam) streamwise fluid mean velocity profiles at the measurement locations for 1-way and 2-way coupling for the case corresponding to particle injection velocity 10.5 m/s.

On comparing discrete phase (particle) results with the experimental data (see Figure 3), simulated particle velocity profiles are in good accordance with the experiment, wherever the particles are found in the domain but their dispersion is considerably underpredicted. One can clearly see that a very small number of particles are found below the step. Hardalupas et al. (1992) demonstrated that particles will be dispersed into the recirculation region only when their large eddy Stokes number is less than one. According to the considered case (70 μm copper particles in presence of air), the large eddy Stokes number was found to be 6.9, which is significantly greater than one. Following this, it can be justified that very a smaller number of particles being found below the step (y/H<1) before the flow re-attachment point (x/H~7) but even after the flow re-attachment, the number of particles below the step (y/H<1) remains quite low indicating inability of the dispersion models (Discrete Random Walk; DRW) to model turbulence effects on particles. Observing the effect of coupling regime on particle phase results demonstrates that predicted particle velocity profiles are also very similar for 1-way and 2-way coupling like fluid phase results. As the exact particle velocity profile at the inlet of BFS was not measured in the experiment but needed for numerical simulations, we have also investigated the effect of different particle injection velocity on predicted fluid and particle velocity profiles. When particles are injected with (10.5, 0, 0) m/s of injection velocity from the inlet of BFS (figure 3(a)), the particle velocities at all measurement locations are over-predicted. Predicted particle velocity profiles remain over-predicted even when particles are injected with the velocity that follows the mean fluid velocity profile at the inlet (figure 3(b)). Interestingly, when particles are injected with (0, 0, 0) m/s of injection velocity (figure 3(c)), the particle velocity profiles give a much better match with the experimental data. This analysis suggests that it might be best approach (for the cases where particle injection velocity is not measured in the experiment) to provide zero initial velocity to the particles and let them attain the real physical velocity according to the flow around them and their ability to response (particle Stokes number) to it. Nevertheless, this approach of estimating initial particle velocity is case-dependent and may be software-specific. The results might look different when upstream channel length increases. In all the case, we found that particles

Proceedings of the 39th IAHR World Congress
19–24 June 2022, Granada, Spain

move more or less like a patch and a very small number of particles are dispersed below the step (y/H<1) even after re-attachment point (x/H~7) for all RANS-DEM cases, indicating inability of simple dispersion models to include turbulence effect on particle's trajectory.

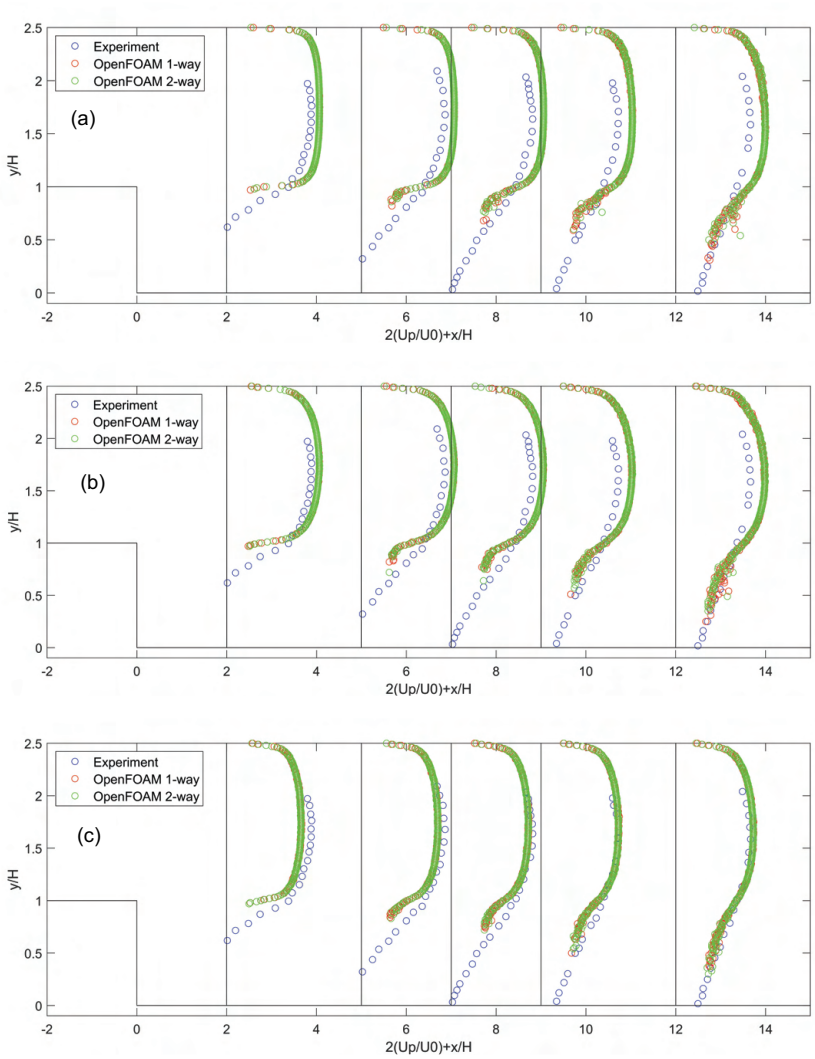

Figure 3. Comparison of experimental and OpenFOAM simulated (with DPMFoam) average streamwise particle velocity profiles at the measurement locations for 1-way and 2-way coupling. (a) particle injection velocity as (10.5, 0, 0) m/s, (b) particle injection velocity same as that of fluid velocity profile at inlet, (c) particle injection velocity as (0, 0, 0) m/s.

Figure 4 shows the mean particle velocity plots corresponding to two different particle tracking solvers namely DPMFoam (standard OpenFOAM solver) and pimpleLPTFoam (self-compiled). We found almost no difference in predicted fluid and particle velocity profiles and their dispersion as well. This can be explained, as small concentration of particles (10% mass flow rate) results very small number of particles in each computational cell and particle fraction (1-α) remains almost near to zero. Under this circumstance, it seems reasonable to use pimpleLPTFoam instead of DPMFoam. This can save significant computational resources

as one doesn't need to correct the calculated fluid fields for the solid fraction. However, it is not recommended to use pimpleLPTFoam for higher particle concentration/mass flow rate, where particle fraction (1-ϵ) in each computational cell will no longer be near to zero.

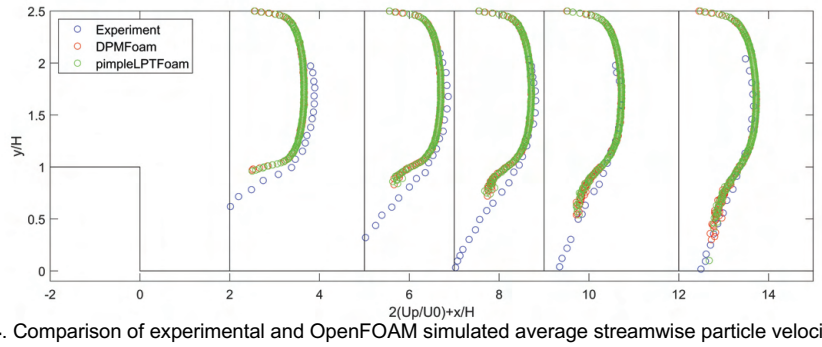

Figure 4. Comparison of experimental and OpenFOAM simulated average streamwise particle velocity profiles at the measurement locations 2-way coupling corresponding to particle injection velocity as (0, 0, 0) m/s with DPMFoam and pimpleLPTFoam.

8. SUMMERY AND CONCLUSIONS

Eulerian-Lagrangian (more specifically RANS-DEM) approach is used to simulate the particle-laden flow in OpenFOAM. Different aspects of numerical simulations in such a detailed method regarding accuracy, computational cost and limitations are investigated and discussed. Analysis on coupling regime indicates almost no difference in simulated fluid and particle velocity profiles for 1- and 2-way coupling due to small concentration of particles. Investigation on different particle injection velocities suggests that it might be the best approach to provide zero initial velocity to the particle and let them attain the real physical velocity according to the flow around them when exact data is not measured or available in the literature. Comparing different particle-tracking solvers suggests that particle fraction in each computational cell might be neglected when particles are small in numbers, this can save significant computational resources. We also found that in the framework of RANS-DEM, the simple dispersion model (DRW) implemented in OpenFOAM is not able to incorporate the turbulence effect on particles accurately as it assumes the turbulence to be isotropic which doesn't hold true for complex geometries and wall bounded flows. A more sophisticated dispersion model such as continuous random walk (CRW) might improve the particle dispersion but its implementation in OpenFOAM is out of the scope of this study. On the other hand, more detained methods such as large eddy simulation (LES) or direct numerical simulation (DNS) to resolve the fluid flow statistics might improve particle dispersion considerably. LES/DNS does not require an extra dispersion model but at the cost of huge computational requirements.

9. ACKNOWLEDGEMENTS

We would like to thank the Leibniz Supercomputing Centre (LRZ) for providing the computational resources required for our study. We also would like to acknowledge the CFD-online community (https://www.cfd-online.com/) for giving the platform to discuss the CFD related problems with the experts. The study was conducted during the PhD research at TUM with KAS scholarship, we are greatly thankful to Konrad-Adenauer-Stiftung (KAS) for making this possible.

10. REFERENCES

Brennen, C.E. (2005). *Fundamentals of Multiphase Flows*. Cambridge University Press.

Breuer, M. and Alletto, M. (2012). Efficient simulation of particle-laden turbulent flows with high mass loadings using LES. *International Journal of Heat and Fluid Flow*, *35*, 2–12. https://doi.org/10.1016/j.ijheatfluidflow.2012.01.001

Capecelatro, J. and Desjardins, O. (2013). An Euler–Lagrange strategy for simulating particle-laden flows. *Journal of Computational Physics*, *238*, 1–31. https://doi.org/10.1016/j.jcp.2012.12.015

Proceedings of the 39th IAHR World Congress
19–24 June 2022, Granada, Spain

Crowe, C.T., Schwarzkopf, J.D., Sommerfeld, M. and Tsuji, Y. (2011). *Multiphase Flows with Droplets and Particles* (Second edition). CRC Press. https://www.taylorfrancis.com/books/9780429106392 https://doi.org/10.1201/b11103

Deb, S. and Tafti, D.K. (2013). A novel two-grid formulation for fluid–particle systems using the discrete element method. *Powder Technology*, *246*, 601–616. https://doi.org/10.1016/j.powtec.2013.06.014

Drake, T.G. and Calantoni, J. (2001). Discrete particle model for sheet flow sediment transport in the nearshore. *Journal of Geophysical Research: Oceans*, *106*(C9), 19859–19868. https://doi.org/10.1029/2000JC000611

Elghobashi, S. (1994). On predicting particle-laden turbulent flows, *52(4)*, 309–329.

Eppinger, T., Seidler, K. and Kraume, M. (2011). DEM-CFD simulations of fixed bed reactors with small tube to particle diameter ratios. *Chemical Engineering Journal*, *166*(1), 324–331. https://doi.org/10.1016/j.cej.2010.10.053

Fessler, J.R. and Eaton, J.K. (1999). Turbulence modification by particles in a backward-facing step flow. *Journal of Fluid Mechanics*, *394*, 97–117. https://doi.org/10.1017/S0022112099005741

Fries, L., Antonyuk, S., Heinrich, S. and Palzer, S. (2011). DEM–CFD modeling of a fluidized bed spray granulator. *Chemical Engineering Science*, *66*(11), 2340–2355. https://doi.org/10.1016/j.ces.2011.02.038

Greifzu, F., Kratzsch, C., Forgber, T., Lindner, F. and Schwarze, R. (2016). Assessment of particle-tracking models for dispersed particle-laden flows implemented in OpenFOAM and ANSYS FLUENT. *Engineering Applications of Computational Fluid Mechanics*, *10*(1), 30–43. https://doi.org/10.1080/19942060.2015.1104266

Hardalupas, Y., A.M.K.P. Taylor and Whitelaw, J.H. (1992). Particle Dispersion in a Vertical round Sudden-Expansion Flow. *Philosophical Transactions: Physical Sciences and Engineering*, *341*(1662), 411–442. http://www.jstor.org/stable/54153

Jajcevic, D., Siegmann, E., Radeke, C. and Khinast, J.G. (2013). Large-scale CFD–DEM simulations of fluidized granular systems. *Chemical Engineering Science*, *98*, 298–310. https://doi.org/10.1016/j.ces.2013.05.014

Kasper, R. (2018, March 22). *Particle Simulation with OpenFOAM® Introduction, Fundamentals and Application.* University of Rostock. German OpenFOAM User meeting 2018 (GOFUN 2018).

Kasper, R., Turnow, J. and Kornev, N. (2019). Multiphase Eulerian–Lagrangian LES of particulate fouling on structured heat transfer surfaces. *International Journal of Heat and Fluid Flow*, *79*, 108462. https://doi.org/10.1016/j.ijheatfluidflow.2019.108462

Mofakham, A. A. and Ahmadi, G. (2020). On random walk models for simulation of particle-laden turbulent flows. *International Journal of Multiphase Flow*, *122*, 103157. https://doi.org/10.1016/j.ijmultiphaseflow.2019.103157

Mohammadreza E. (2014). *experimental and numerical investigations of horizontal pneumatic conveying* [Dissertation].

OpenCFD Limited. (n.d.). *OpenFOAM-v1912* [Computer software]. https://www.openfoam.com

Spogis N. (2008). *Multiphase Modeling Using EDEM-CFD Coupling for FLUENT*. 3rd latin Americal CFD Workshop Applied to the Oil Industry, Brazil.

Wu C.L., Ayeni O., Berrouk A.S. and Nandakumar K. (2014). Parallel algorithms for CFD-DEM modeling of dense particulate flows. *Chemical Engineering Science*, *118*, 221–244. https://doi.org/10.1016/j.ces.2014.07.043

Xiang, L. (2019). *RANS simulations and dispersion models for particles in turbulent flows.* KTH, School of Engineering Sciences (SCI), Mechanics, Sweden.

Chapter 4

Evaluation of RANS-DEM and LES-DEM Methods in OpenFOAM for Simulation of Particle-laden Turbulent Flows

This chapter is published as:
Jaiswal, A.; Bui, M.D.; Rutschmann, P. Evaluation of RANS-DEM and LES-DEM Methods in OpenFOAM for Simulation of Particle-laden Turbulent Flows. *Fluids* 2022, 7, 337.
https://doi.org/10.3390/fluids7100337

Note: In the governing equations, the symbols for fluid (α) and particle fractions (α_p), used in this chapter, differ from the usual symbols used throughout the Dissertation for fluid (ϵ_f) and particle fractions (ϵ_p).

fluids

MDPI

Article

Evaluation of RANS-DEM and LES-DEM Methods in OpenFOAM for Simulation of Particle-Laden Turbulent Flows

Atul Jaiswal *, Minh Duc Bui and Peter Rutschmann

Chair of Hydraulic and Water Resources Engineering, Technical University of Munich (TUM), Arcisstr. 21, 80333 Munich, Germany
* Correspondence: atul.jaiswal@tum.de; Tel.: +49-(89)-289-23161

Abstract: CFD-DEM modelling of particle-laden turbulent flow is challenging in terms of the required and obtained CFD resolution, heavy DEM computations, and the limitations of the method. Here, we assess the efficiency of a particle-tracking solver in OpenFOAM with RANS-DEM and LES-DEM approaches under the unresolved CFD-DEM framework. Furthermore, we investigate aspects of the unresolved CFD-DEM method with regard to the coupling regime, particle boundary condition and turbulence modelling. Applying one-way and two-way coupling to our RANS-DEM simulations demonstrates that it is sufficient to include one-way coupling when the particle concentration is small ($O \sim 10^{-5}$). Moreover, our study suggests an approach to estimate the particle boundary condition for cases when data is unavailable. In contrast to what has been previously reported for the adopted case, our RANS-DEM results demonstrate that simple dispersion models considerably underpredict particle dispersion and previously observed reasonable particle dispersion were due to an error in the numerical setup rather than the used dispersion model claiming to include turbulence effects on particle trajectories. LES-DEM may restrict extreme mesh refinement, and, under such scenarios, dynamic LES turbulence models seem to overcome the poor performance of static LES turbulence models. Sub-grade scale effects cannot be neglected when using coarse mesh resolution in LES-DEM and must be recovered with efficient modelling approaches to predict accurate particle dispersion.

Keywords: particle-laden BFS; turbulent flows; dispersion model; unresolved CFD-DEM; RANS-DEM; LES-DEM; OpenFOAM

Citation: Jaiswal, A.; Bui, M.D.; Rutschmann, P. Evaluation of RANS-DEM and LES-DEM Methods in OpenFOAM for Simulation of Particle-Laden Turbulent Flows. *Fluids* **2022**, *7*, 0. https://doi.org/

Academic Editors: Mehrdad Massoudi and Sourabh V. Apte

Received: 5 September 2022
Accepted: 12 October 2022
Published: 21 October 2022

1. Introduction

Two-phase systems consisting of a continuum phase (fluid) and a discrete phase (particles) are prevalent in industrial processes, biological phenomena, and nature. The behavior of solid particles in continuous fluid flow is determined by complex physics and depends on the particle and fluid characteristics and flow regime. According to Crowe et al. [1], five key factors contribute to the turbulence modulation induced by particles: (1) Surface effects: particle size normalized by a length scale d_p/l; (2) inertial effects: flow Reynolds number Re and particle Reynolds number Re_p; (3) response effects: particle response time or Stokes number St; (4) loading effects: particle volume fraction α_p; and (5) interaction effects: particle-particle as well as particle-wall. Numerical simulations of such systems can be helpful in providing a detailed insight into the complex physics involved in particle motion. However, modelling of particle motions in turbulent flow is difficult because it involves the modelling of the surrounding flow field and resulting pressure gradients as well as the particle-flow interaction, which involves the local flow around the particle and the forces resulting from the stress applied on the particle by the flow [2].

In computational fluid dynamics (CFD), both phases can be treated as continuum medium, also called the Eulerian–Eulerian method, in which Navier–Stokes (NS) equations are solved for each phase, including the momentum exchange between the phases. The Eulerian–Eulerian method is computationally less expensive but at the cost of losing the

discrete nature of particles. On the other hand, a Lagrangian method is adopted for granular systems, also called the Discrete Element Method (DEM), where each particle is tracked using Newton's second law of motion. With an increase in computational power, advancements in CFD and DEM, and improved solution algorithms over the last decade, the new and more detailed approach combining CFD and DEM for multiphase systems, called the Eulerian–Lagrangian method (CFD-DEM), has become a popular tool to investigate particle-laden flows. In particular, numerical approaches combining the CFD and DEM have proven to be advantageous over many other options in terms of computational efficiency and numerical convenience [3]. In CFD-DEM, the continuum phase (fluid) is resolved using the NS equations, whereas the discrete phase (particles) is tracked by solving Newton's second law of motion for each particle in the fluid system. The continuum and discrete phase are also coupled with each other using momentum transfer mechanisms. This coupling level depends on the volumetric fraction of solid material $\alpha_p = V_p/V$ in the system, where V_p is particle volume, and V is total volume of particles and fluid. A classification map is depicted in Figure 1, which can be used to incorporate the level of coupling in numerical simulations [4]. Furthermore, the approximated CFD solution can be obtained using Reynolds-averaged Navier–Stokes equations (RANS) or Large-Eddy simulation (LES), instead of solving the flow using Direct Numerical Simulation (DNS), which could save significant computational efforts, especially when tracking particles using DEM.

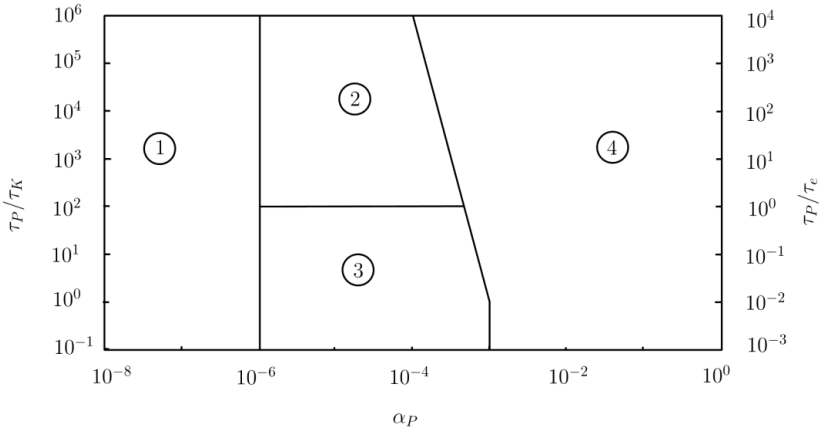

Figure 1. Classification map [4] showing the level of coupling required for numerical simulations and interaction between particles and turbulence for ① one-way coupling, ② two-way coupling where particles enhance the turbulent production, ③ two-way coupling where particles enhance the turbulence dissipation, ④ four-way coupling.

The CFD-DEM method can be categorized into two approaches: unresolved and resolved CFD-DEM. Unresolved CFD-DEM solves the flow at larger scales using filtering (LES)/averaging (RANS) methods and can only be applied to particles smaller than the CFD cell size. In unresolved CFD-DEM, some empirical equations are used to calculate the fluid forces acting on the particles and the calculated fluid forces are included as additional terms in governing DEM equations. In contrast, resolved CFD-DEM (particle resolved DNS) can be applied to larger particles than the CFD cell size, where extreme fine meshing is used to obtain detailed information on turbulence flow and forces acting on particles are directly obtained by integrating fluid stress over the particle surface. In resolved CFD-DEM, various techniques such as Adaptive mesh refinement (AMR) and Immersed boundary method (IBM) are becoming popular, but are limited to a minimal number of particles [5]. Additionally, the particles can be assumed as point-particles (PP), representing point objects

with a certain mass and whereupon DNS can be performed. Unlike resolved CFD-DEM, here the forces acting on the particles are calculated using empirical equations, but the application of PP DNS-DEM to particles larger than Kolmogorov scale is questionable and highly discouraged.

DNS-DEM studies [6,7] are limited to simple flows, a small number of particles, and mainly to the PP approach due to heavy computational requirements. DNS performed on PP in rough-wall pipe with a small Reynold's number indicates that particle volume fraction (α_p) and Stokes number (St) play an important role in turbulent modification [8]. Recently, a two-way coupled DNS study on particle-laden flow highlighted the effects of the particle Stokes number (St) on near-wall turbulence [9]. Resolved CFD-DEM (particle resolved DNS) is only possible if the spacing of the computational grid is small compared to the size of a particle, therefore restricting its application to large particles compared to the smallest scales of the turbulent flows and/or relatively small number of particles [10]. Even for single-phase fluid systems, DNS is not possible for the cases with high Reynolds numbers and complex geometries due to computational limitations.

RANS-DEM is another economical approach where the mean flow fields are obtained, and additional dispersion models incorporate the turbulence effect on the particle's trajectories. An accurate evaluation of instantaneous velocity fluctuations is required for the realistic evaluation of turbulent diffusion effects for accurate predictions of particle dispersion and deposition on surfaces [11,12]. A number of RANS-DEM studies on simple cases [13,14] indicate that these simple dispersion models cannot accurately obtain the lost fluctuating component due to averaging of NS equations. In contrast, Greifzu et al. [15] showed that the simple dispersion models are indeed able to predict correct particle dispersion even for more complex flow (particle-laden BFS flow). However, we found out that their conclusion was due to an error in the numerical setup (refer to the results and discussion section for details). Therefore, further investigation is necessary to reach a unanimous conclusion about the ability of the simple dispersion models in incorporating the effect of turbulent fluctuations on particle motion.

A sensible and efficient approach would be LES-DEM, which might be a good compromise between accuracy and computational feasibility. However, one also has to be cautious about the sub-grid scales (SGS) fluid fluctuating motion seen by the particles, because in several investigations, the effects of SGS on particle motion were shown to be significant and hence should not be neglected [16–19], especially when the particle response time is the same order of magnitude as that of the smallest time scale resolved in LES. To recover the dynamic consequences of the SGS in the LES-DEM framework, stochastic models such as an explicit stochastic forcing in the equations of particle motion were suggested [20,21]. Furthermore, the size of LES meshes in unresolved CFD-DEM is restricted by the requirement of particles being significantly smaller than the CFD cell size, unless particles are considered as PP. This restriction prevents finer meshes near the boundaries (y^+~1) and can lead to poor performance of the static LES turbulence model, which require very fine boundary meshes. Dynamic LES turbulence models could be adopted to avoid the poor performance of static LES models in cases of low mesh resolutions.

On one hand, commercial software such as Fluent EDEM, STAR-CCM+ and AVL-fire [22–26], in-house CFD programs such as LESOCC [27], and research codes [28–31] can be applied to CFD-DEM simulations, but the accessibility of these solvers is limited. On the other hand, some open-source CFD codes, such as OpenFOAM [32] have accelerated research in the field. Some coupled CFD-DEM codes [33,34] are also available, which couple OpenFOAM and DEM software such as LAMPS/LIGGGHTS and are not limited to PP.

Particle-laden backward facing step (BFS) flow is popular among researchers in the field due to its simple geometry and ability to produce interesting turbulent features concerning flow separation and re-attachment. A few LES-DEM simulations on particle-laden BFS have been performed [35–40], and some have attained a reasonable agreement with the experiment. These LES-DEM studies used extreme fine meshing (y^+~1) and were

mainly based on the PP approach. The particle-laden BFS flow adopted in our study had previously been numerically simulated by Greifzu et al. [15] in the context of RANS-DEM. The authors concluded that RANS-DEM (and the simple dispersion model therein) predicts the correct fluid and particle velocity profiles, as well as the particle dispersion. Interestingly, we found that their OpenFOAM numerical setup was erroneous as a fluid density of 1000 kg/m^3 (water) instead of 1 kg/m^3 (air) was used, although in the original experiment the fluid was air, not water. Despite using an incorrect fluid density value, the authors obtained an excellent agreement with the experimental data. However, these results are questionable, as the density of the fluid should have been 1 kg/m^3 as in the original experiment—therefore requiring a reinvestigation.

Despite several experimental and numerical studies, fluid-particle systems remain poorly understood due to the complex physics involved, such as turbulent modulation and complex fluid-particle and particle-particle interaction. The CFD-DEM method could provide detailed insights into these multivariable and interdependent phenomena and can be employed for large scale engineering applications. However, due to the huge computational requirements and associated limitations of the CFD-DEM method, finding the trade-off and compromise between the levels of flow resolution obtained (DNS/LES/RANS) and the required computational efforts to predict the correct particle dispersion and trajectories is difficult.

Here, we focus on different aspects of modelling such flows in terms of the computational requirements, the available models, as well as the challenges and limitations. In particular, we perform RANS-DEM and LES-DEM simulations in 3D for particle-laden BFS flow. Special attention is given to the ability of the respective approaches to predict particle dispersion, coupling regime, particle boundary conditions, and turbulence modelling. First, we discuss the theoretical background of the Eulerian–Lagrangian method (CFD-DEM) in detail, focusing on the RANS and LES methods for resolving the fluid flow fields. The following method and numerical setup section highlights the fundamental structural differences in the numerical setup for different approaches adopted in our study. Furthermore, the RANS-DEM and LES-DEM simulation results for the fluid and particle phases are compared, especially in relation to particle dispersion. Additionally, different aspects of the CFD-DEM method with regard to the coupling regime and particle boundary conditions were investigated and their effects on fluid and particle phase results are discussed. Before including particles into the system, single-phase RANS and LES simulations are also performed and its accuracy in predicting mean and turbulent flow statistics with different turbulence models are assessed. Taken together, RANS-DEM requires more sophisticated dispersion models to predict correct particle dispersion, and LES-DEM has limitations in terms of the flow resolution obtained, the computational resources required, and the prerequisites of unresolved CFD-DEM, preventing extreme fine meshing unless the particles are considered as PP.

2. CFD-DEM Approach and the Governing Equations

The unresolved CFD-DEM approach was adopted to investigate the two-phase system containing fluid as a continuum and the particles as discrete mediums. The full NS equations describe the continuum fluid phase for unsteady incompressible flow, which is a slightly modified version of the standard NS equations to incorporate the particle fraction in each computational cell. Newton's second law of motion describes the discrete particle phase.

$$\frac{\partial \alpha}{\partial t} + \frac{\partial \alpha u_i}{\partial x_i} = 0, \tag{1}$$

$$\frac{\partial \alpha u_i}{\partial t} + u_j \frac{\partial \alpha u_i}{\partial x_j} = -\frac{1}{\rho}\frac{\partial \alpha p}{\partial x_i} + \upsilon \frac{\partial^2 \alpha u_i}{\partial x_j \partial x_j} + \alpha g_i - \frac{f_i^p}{\rho}, \tag{2}$$

$$m^{(k)} \frac{\partial u_i^{p(k)}}{\partial t} = \sum_{l=1}^{n^{c(k)}} F_i^{c(kl)} + F_i^{f(k)} + F_i^{g(k)}, \tag{3}$$

$$I^{(k)}\frac{\partial \mathrm{w}_i^{p(k)}}{\partial t} = \sum_{l=1}^{n^{c(k)}} M_i^{c(kl)}, \tag{4}$$

$$\frac{dx_i^{p(k)}}{dt} = u_i^{p(k)}. \tag{5}$$

where:

α = volume fraction of fluid in each cell; unitless
u_i = fluid velocity field in direction i; m/s
p = fluid pressure; N/m^2
v = kinematic viscosity of fluid; m^2/s
g_i = gravitational acceleration in direction i; m/s^2
ρ = density of fluid; kg/m^3
$m^{(k)}$ = mass of particle k; kg
$n^{c(k)}$ = number of particles colliding with particle k; unitless
$I^{(k)}$ = moment of inertia of particle k; kgm^2
$u_i^{p(k)}$ = velocity of particle k in direction i; m/s
$\mathrm{w}_i^{p(k)}$ = angular velocity of particle k in direction i; 1/s
$F_i^{f(k)}$ = surface forces acting on particle k (including drag, lift, added-mass, basset history forces etc.: coupled forces); N
f_i^p = volumetric fluid-particle interaction momentum source in direction i; N/m^3
$F_i^{g(k)}$ = body forces acting on particle k; (gravity + buoyancy: uncoupled forces)
$= m^{(k)} g_i \left(1 - \frac{\rho}{\rho^p}\right)$; N
ρ^p = density of particle; kg/m^3
$F_i^{c(kl)}$ = particle-particle interaction/contact force between particle k and l; N
$M_i^{c(kl)}$ = particle-particle interaction moment between particle k and l; Nm
x and t are space and time with units m and s, respectively.
$M_i^{c(kl)}$ = particle-particle interaction moment between particle k and l; Nm
x and t are space and time with units m and s, respectively.

OpenFOAM considers the particles as point-particles (PP), meaning that they are represented as point objects having a certain mass. This assumption automatically neglects the torque acting on the particles, meaning that OpenFOAM does not consider Equation (4) in calculating the trajectories of the particles.

In the above equations, the momentum transfer term consists of several forces coupled between the continuum phase and discrete phase, such as drag force, lift force, pressure gradient force, basset history force, added-mass force, etc. In the references, it has been established that the major contribution in the momentum transfer term originates from the drag force [41], and lift force is more relevant for light particles than heavy particles [10]. The particles considered in the present study are dense copper particles. Therefore, the lift force seems to be insignificant for our case. However, we have also included the pressure gradient force in addition to the drag force in our numerical setup. Ultimately, the coupled forces term reduces to:

$$F_i^{f(k)} = F_i^{D(k)} + F_i^{PG(k)}, \tag{6}$$

$$F_i^{D(k)} = \frac{3}{4}\frac{\rho}{\rho^p}\frac{m^{(k)}}{d^{(k)}} C_D \left(u_i^{s(k)} - u_i^{p(k)}\right)\left|u_i^{s(k)} - u_i^{p(k)}\right|, \tag{7}$$

$$C_D = \begin{cases} \frac{24}{Re^{p(k)}}\left(1 + \frac{1}{6}\left(Re^{p(k)}\right)^{\frac{2}{3}}\right) & when \quad Re^{p(k)} \le 1000 \\ 0.424 & when \quad Re^{p(k)} \ge 1000 \end{cases}, \tag{8}$$

$$Re^{p(k)} = \frac{d^{(k)}\left|u_i^{s(k)} - u_i^{p(k)}\right|}{v}, \tag{9}$$

$$F_i^{PG(k)} = \frac{\pi}{6}(d^{(k)})^3 \rho \frac{Du_i^{s(k)}}{Dt}. \tag{10}$$

From the equations above, one can see that to calculate forces acting on particles (thus to calculate their trajectories), information is needed on the fluid velocity at the location of particle (${u_i}^{s(k)}$). We obtain this information from the fluid phase solution (CFD). The solution of fluid phase can be categorized into three types, namely Direct Numerical Simulation (DNS), Large-Eddy Simulation (LES), and Reynolds-averaged Navier–Stokes equations (RANS), depending on the level of flow resolution needed and the computational resources available.

2.1. Direct Numerical Simulation (DNS)

DNS solves the full NS equations numerically, thus resolving everything from the largest scale to the smallest dissipative eddies present in the system. In DNS under consideration of the point-particles (PP) approach, the velocity of the fluid at the particle location can be obtained directly from the DNS solution.

$${u_i}^{s(k)} = {u_i}^{DNS}(x^{p(k)}(\mathrm{t}), \mathrm{t}) = u_i\,(x^{p(k)}(\mathrm{t}), \mathrm{t}). \tag{11}$$

Since turbulent flows possess a varying range of time and length scales, the exact solution (DNS), even for the simplest turbulent flows, requires enormous computational resources and extreme fine meshing. Initial estimation of the computational resources required for DNS can be made based on Kolmogorov scales (smallest time, length and velocity scales) in the system. In our case, the Kolmogorov length scale is about 170 µm, meaning the mesh resolution should be smaller than 170 µm for DNS. It has been demonstrated that the restrictions that DNS needs for simple channel flow in terms of grid point and time steps [42], thus require huge computational resources even for simple channel flow. Computational resources requirement by DNS in the sense of both processor speed and memory size for storing intermediate results is vast and increases exponentially with the Reynolds number of the flow. In order to obtain the maximum possible information about the flow fields with an affordable computational cost, the full NS equations are approximated with some averaging/filtering approaches. The resulting averaged/filtered NS equations have almost the same form as the original NS equations with additional terms, which can be calculated based on eddy viscosity.

2.2. Large-Eddy Simulation (LES)

LES aims to resolve large-scale turbulence while small-scale turbulence is modelled using the filtering operation. Compared to DNS, where nearly all the computational effort is used to resolve the smallest dissipative eddies, LES resolves only up to the inertial subrange, not all the way to the dissipative scales. This can save significant computational effort, yet preserves enough information of the fluid flow. LES converges to DNS when finer meshing and smaller time steps are used.

The common idea behind LES is to decompose the instantaneous flow field $u(x,t)$ into resolved (or filtered) component $\overline{u}(x,t)$ and residual (or sub-grid scale; SGS) component $u'(x,t)$ by a filtering operation, as follows:

$$u_i(x,t) = \overline{u_i}(x,t) + {u_i}'(x,t), \tag{12}$$

$$\overline{u_i}(x,t) = \int u_i(x',t)\,G(x,x';\Delta)\,dx', \tag{13}$$

where, $G(x,x';\Delta)$ is the filter function that depends on mesh discretization. The filtering operation results in extra terms, called residual stresses (τ_{ij}^R) in the original NS equations. Calculation of residual stresses is based on the Boussinesq hypothesis of eddy viscosity (turbulence viscosity v_T), which is being modelled. Various models are available for this purpose, such as Smagorinsky, one-equation model (kEqn), dynamic Smagorinsky,

dynamicKEqn, Spallart–Allmaras, and many others. We found that the dynamicKEqn turbulence model was able to predict correct flow fields in terms of mean and fluctuating components with reasonable accuracy, whereas static turbulence models were performing poorly with provided mesh resolution.

In cases where the particle response time (Stokes number) is large compared to the smallest time scale resolved in LES, the fluid velocity of the sub-grid scales does not significantly influence the particle's motion [10,43,44]. Considering this, one does not need an extra dispersion model to incorporate the effect of turbulence in the particle's motion; thus, the LES solution can be directly equated to the fluid velocity at the location of the particle.

$$u_i{}^{s(k)} = u_i{}^{LES}(x^{p(k)}(t), t) = \overline{u_i}(x^{p(k)}(t), t). \tag{14}$$

2.3. Reynolds-Averaged Navier–Stokes Equations (RANS)

RANS resolve only the mean flow statistics; thus, RANS solution for fluid flow fields cannot be directly equated with the fluid velocity at the location of the particle. In RANS, the instantaneous flow field $u(x,t)$ decomposes into a time average component $\langle u(x,t) \rangle$ and a fluctuating component $u'(x,t)$:

$$u_i(x,t) = < u_i(x,t) > + u_i{}'(x,t), \tag{15}$$

$$< u_i(x,t) > = \lim_{T \to \infty} \frac{1}{T} \int_0^T u_i(x,t)\, dt. \tag{16}$$

The averaging operation results in some new terms, $< u_i' u_j' >$, called Reynolds stresses, to appear in the original NS equations, which are also modelled based on eddy viscosity. The terms $< u_i' u_j' >$, although named as Reynolds stresses, have a unit of stress only when multiplied by the fluid density ρ. Similar to LES, eddy viscosity v_T can be calculated based on several models such as k-ε, k-ω, k-ω SST and many others. We used the k-ω SST model to close the Reynolds-averaged NS equations of our RANS and RANS-DEM simulations, as it was the best performing.

In RANS, the effect of fluctuating components (turbulence) on particles is incorporated using some dispersion models [45]. The resulting fluid velocity at the location of a particle ($u_i{}^{s(k)}$) can be equated to the sum of the RANS (mean) velocity field and the modelled fluctuations.

$$u_i{}^{s(k)} = u_i{}^{RANS}(x^{p(k)}(t), t) + u_i{}' = < u_i(x^{p(k)}(t), t) > + u_i{}'. \tag{17}$$

All three approaches (DNS, LES, and RANS) for calculating the fluid velocity at the location of particles have their limitations in terms of accuracy and computational cost and can be adopted as per the details required and computational resources available. Figure 2 shows the extent of modelling certain types of turbulent models [46], where DNS resolves everything from the largest to the smallest dissipative eddies present in the system. LES resolves up to energy-containing eddies while dissipative eddies are modelled. RANS resolves only the mean flow statistics, and the fluctuating components are modelled. More information on the implementation of the turbulence models used in our RANS-DEM and LES-DEM and the dispersion models can be found on the OpenFOAM webpage [32]. We have used RANS-DEM and LES-DEM approaches to solve particle-laden BFS flow and investigated the case by comparing the fluid and particle-phase results with the experimental data and literature.

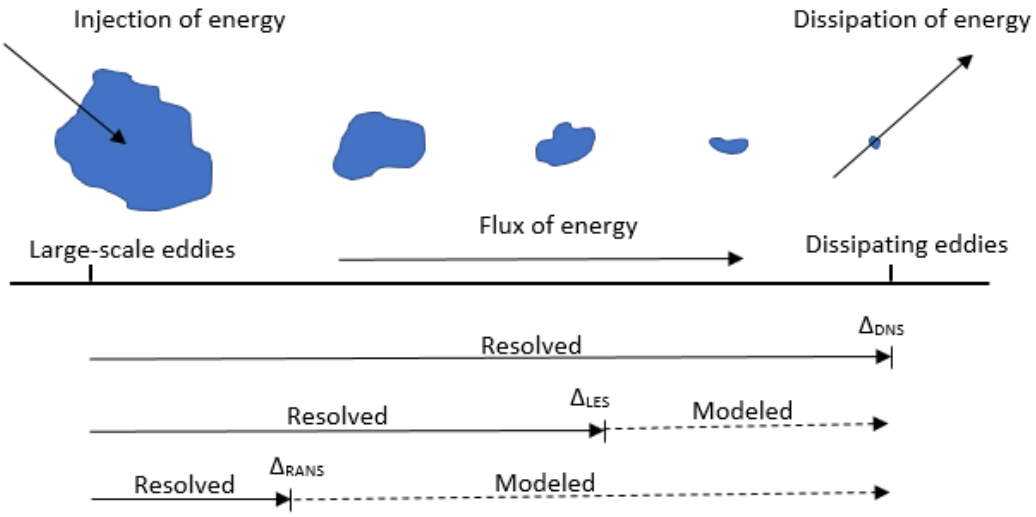

Figure 2. Extent of modelling for certain types of turbulent flows [46].

2.4. Particle Dispersion Modelling

The approximated NS equations provide mean (RANS)/filtered (LES) flow statistics and information about turbulent fluctuations are lost due to simplifications of original NS equations. The fluid-particle interaction forces ($F_i^{f(k)}$) such as pressure gradient force, added mass force, drag force and history force, contain unfiltered components and are required to be estimated to close certain terms in particle equations of motion. In LES-DEM, the sub-grid scales only have a small effect on the particle's trajectories, especially when the particle response time is large compared to the typical time scales of the turbulent flow and the smallest time scale resolved in LES. However, the sub-grid scales can be significant in many physical processes such as in turbophoresis [17]. On the other hand, the effect of turbulent fluctuations must be included in RANS-DEM to predict realistic particle trajectory. There are mainly two types of modelling approaches to account for missing turbulent fluctuations: either by adding stochastic noise forcing to the NS equations [47] or by adding an additional velocity to the particle equation of motion [48]. The stochastic models, which aim to recover the lost turbulence effects on a particle's trajectories, can be formulated based on (a) transport equations of the turbulent kinetic energy (Discrete Random Walk; DRW, or Eddy Interaction Model; EIM) or (b) generalized Langevin equation (Continuous Random Walk; CRW). We have considered the DRW/EIM stochastic model in our numerical simulation. Here, particles are assumed to be trapped by an eddy during its lifetime, resulting in the mean flow fields seen by the particles being those of the fluid and the fluctuating components, which are randomly distributed following Gaussian distribution, whose root mean square values are equal and deduced from the turbulent kinetic energy.

In OpenFOAM, two dispersion models are available to model the turbulent fluctuations u_i', namely *StochasticDispersionRAS* and *GradientDispersionRAS* models, which are basically DRW/EIM type of stochastic dispersion models. These dispersion models use the turbulent kinetic energy (TKE; k) provided by the RANS solution to model the turbulence fluctuations such that,

$$u_i' = \sqrt{\frac{2}{3}k}\, x_{rnd}\, e_i \tag{18}$$

where x_{rnd} is a random factor that reproduces a probability density function with Gaussian distribution with an expected value $\mu = 0$ and standard deviation $\sigma = \sqrt{\frac{2}{3}k}$. e_i is a unit

vector that points either in a random direction (in *StochasticDispersionRAS*) or in $-\nabla k$ (in *GradientDispersionRAS*).

2.5. Coupling between Continuum and Discrete Phases

As shown in Figure 1, the continuum and discrete phases interact with each other and are required to be coupled. Several studies have emphasized on one-way and two-way coupling [49–52] for dilute particle-laden flows and fluid-structure interaction. Depending on the coupling regime, specific terms vanish in the respective governing equations. The coupling regime required for numerical simulations can be made using the volumetric particle concentration (α_p).

- One-way coupling (fluid $\rightarrow$ particle): when the volumetric concentration of particles is small ($\alpha_p < 0.0001\%$), the fluid flow fields affect the particle motion, but particles have a negligible effect on fluid flow fields. This results in only specific terms being considered in the governing CFD-DEM equations as follows:

$$F_i^{f(k)} \neq 0;\ f_i^p = 0;\ F_i^{c(kl)} = 0. \tag{19}$$

- Two-way coupling (fluid $\leftarrow\rightarrow$ particle): when the volumetric concentration of particles increases ($0.1\% < \alpha_p < 0.0001\%$), both fluid and particles affect each other's motion. Two-way coupling can be further categorized into two categories, one in which particles enhance the turbulence dissipation and a second in which particles enhance turbulence production, which depends on the ratio of particle reaction time ($\tau_p = \rho_p d_p^2/18\rho\upsilon$) to the Kolmogorov time scale ($\tau_k = (\frac{\upsilon}{\varepsilon})^{1/2}$) and to the turnover time of large eddies ($\tau_e = l/u$), respectively, where ρ_p is the density of particle, d_p is the diameter of particle, ρ is the density of fluid, υ is the kinematic viscosity of fluid, ε is turbulence dissipation rate, l is turbulence length scale, and u is the fluid velocity. Two-way coupling results in the following CFD-DEM equations:

$$F_i^{f(k)} \neq 0;\ f_i^p \neq 0;\ F_i^{c(kl)} = 0. \tag{20}$$

- Four-way coupling (fluid $\leftarrow\rightarrow$ particle, particle $\leftarrow\rightarrow$ particle): When the volumetric concentration of the particles further increases ($\alpha_p > 0.1\%$), the interaction among particles becomes significant. In this regime, fluid and particle affect each other's motion; additionally, the particle collision term needs to be included in the governing equations:

$$F_i^{f(k)} \neq 0;\ f_i^p \neq 0;\ F_i^{c(kl)} \neq 0. \tag{21}$$

3. Method and Numerical Setup

The original experiment [53] includes a blower and particle feeders, where the blower injects fluid (air), and the particle feeders feed the particles into the system at a specific mass flow rate. This arrangement provides uniform fluid velocity and particle loading at the inlet of the development section, which has a length of 5.2 m, ensuring that the turbulent flow is fully developed at the inlet of the test section (backward facing step; BFS) and gives the particles enough time/length to become uniformly mixed with the fluid flow and attain equilibrium with the fluid phase before it reaches the inlet of BFS. The fully developed turbulent flow has a centerline velocity of 10.5 m/s, and the Reynolds numbers based on it are 13,800 and 18,400 at the channel section (based on channel half-height h) and at the step (based on step height H), respectively. The geometry of the test section, fluid (air) and particle-phase description in the experiment and their corresponding adoption for numerical simulations are shown in Table 1.

Table 1. Geometry, fluid, and particle phase characteristics in the original experiment [53] and their corresponding setting for the numerical setup.

	Experimental Setup	**Our Numerical Setup**
Geometry	Channel half-height, h = 20 mm Channel span, Lu = 457 mm Step height, H = 26.7 mm Expansion ratio (H + 2h/2h) = 5:3 Aspect ratio (B/H) = 17:1	Channel half-height, h = 20 mm Channel span, Lu = 457 mm Expansion channel length, Ld = 935 mm Step height, H = 26.7 mm Width (B) = 114.25 mm
Continuum phase (air)	Centerline velocity, U0 = 10.5 m/s Friction velocity, u_τ = 0.5 m/s Viscous length scale = 31 μm Dissipation, ϵ (centerline estimated) = 4.3 m^2/s^3 Kolmogorov length scale, η (Centerline estimated) = 170 μm Large eddy time scale, τ_f = 5H/U0 = 12.7 ms	Density (ρ) = 1.225 kg/m^3 Kinematic viscosity (υ) = 1.5×10^{-5} m^2/s Centerline velocity (U0) at Inlet = (10.5 0 0) m/s Average velocity (Uavg) at inlet = (9.39 0 0) m/s
Discrete phase (copper particle)	Nominal diameter, d_p= 70 μm Material = copper Number mean diameter = 68.2 μm Standard deviation of diameter = 10.9 μm Density, ρ_p= 8800 kg/m^3 Mass flow rate of particle (Mass loading), $\dot{m}_p/\dot{m}_f$= 10% Stokes mean particle time constant, $\tau_{p,\,stokes} = (2\rho_p + \rho)d_p^2/36\mu$= 130 ms Modified mean particle time constant, $\tau_p = \tau_{p,\,stokes}/\left(1 + 0.15Re_p^{0.687}\right)$= 88 ms Particle Reynolds number, $Re_p = \frac{d_p U_{rel}}{\upsilon}$= 5.5	Particle size distribution (PSD): Normal distribution with expected value of 68.2 μm and standard deviation of 10.9 μm Density, ρ_p= 8800 kg/m^3 Mass flow rate of particle (mass loading), $\dot{m}_p/\dot{m}_f$= 10%

The geometry considered (test section; BFS) for numerical simulation can be seen in Figure 3. Due to computational limitations, the development channel before the inlet of BFS is not considered in the geometry. To achieve a fully developed turbulent flow at the inlet of BFS without providing a development channel, mapped boundary conditions are applied, in which flow fields are mapped from 400 mm downstream of the inlet of BFS, resulting in a fully developed fluid velocity profile at the inlet of BFS with a centerline velocity (U0) of 10.5 m/s and average velocity (Uavg) of 9.39 m/s. Regarding the particle boundary condition in OpenFOAM, in addition to the mass flow rate (mass flux) of particles, one also needs to provide a particle injection velocity. In the original experiment, particle velocity was not measured at the inlet of the BFS; thus, no data is available for specifying boundary conditions at the model inlet concerning particle injection velocity. We have tested several boundary conditions for the particle injection velocity. Assuming that all the particles have attained a constant velocity (injection velocity) as they reach the inlet of the BFS, two extreme bounds of particle injection velocity are tested, where the particles are injected with (10.5, 0, 0) m/s (upper bound) and (0, 0, 0) m/s (lower bound) of injection velocity. Furthermore, we assume that the particles have attained a velocity that follows the mean fluid velocity profile at the inlet, which is also tested (i.e., particles injected at the center will have an injection velocity similar to the centerline velocity of the fluid, whereas particles injected near to the walls will have almost zero injection velocity due to the no-slip boundary condition for the fluid phase). The options mentioned above for obtaining the best approximation of particle boundary conditions are tested against both the approaches adopted in our study to simulate particle-laden BFS flow.

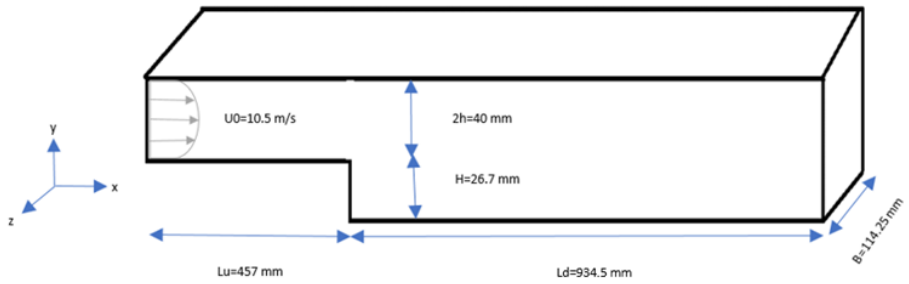

Figure 3. The geometry considered for numerical simulation.

RANS-DEM and LES-DEM simulations are performed in 3D. In the first step, RANS-DEM simulations were performed for a 10% mass loading of ~70 μm copper particles for one-way and two-way coupling. Although the volumetric particle fraction (O ~ 10^{-5}) lies in the range of two-way coupling, we have also considered one-way coupling in addition to two-way coupling under RANS-DEM to facilitate the comparison between them. Interestingly, our RANS-DEM results almost overlap for one-way coupling and two-way coupling, indicating that it should be enough to include one-way coupling, even when the particle concentration is slightly greater than the threshold suggested by Elghobashi [4]. However, we decided to only use two-way coupling for our LES-DEM simulations for 10% mass loading of ~70 μm copper particles due to the fact that the particle volume fraction lies in range of two-way coupling and the CPU time for the case was roughly the same for one-way and two-way coupled RANS-DEM simulations (~10 min more). RANS-DEM and LES-DEM have basic structural differences in their numerical setup as they both require different input parameters, depending on the models used to close the averaged/filtered NS equations. We have used the k-ω SST (kOmegaSST) and dynamicKEqn turbulence models in the case of RANS-DEM and LES-DEM, respectively. We have ensured that the single-phase results match the experimental data before the particles are included in it. In our single-phase LES simulations, we have tested the predictive capability of static turbulence model (kEqn) as well. Once the correctness of the single-phase results has been verified, the cases were modified to incorporate particles and solved using the DPMFoam solver. Although DPMFoam is based on the discrete parcel method (DPM), we have considered only one particle in each parcel, therefore it is equivalent to the discrete element method (DEM). More details about the RANS-DEM and LES-DEM case setup can be found in Table 2.

As mentioned in the introduction, unresolved CFD-DEM requires the CFD mesh to be much larger than the particle size. This is assured as the smallest CFD mesh cell size is 0.2 mm and 0.15 mm in our RANS and LES setup, respectively, which is much greater than the particle size (~70 μm), thus considering them as point-particles (PP) is justified. To resolve the interesting flow features developing near walls, mesh grading is performed, providing us with the flexibility to provide larger cells away from the wall, which saves some additional computational efforts. Mesh is also refined in streamwise direction near the step, whereas uniform mesh is used in spanwise direction. Before we finalize our final mesh, the mesh is refined in a stepwise manner until we obtain almost the same results for fluid and particle velocity profiles between consecutive refinements (grid independence). The selection y^+ as 3 instead of 1 in our LES-DEM simulations allowed us to keep the particle size significantly smaller than the CFD cell (PP approach), and extreme fine meshing is avoided due to computational limitations and the resources available. In the review published on LES simulations [54], it has been reported that dynamic LES models are expected to perform better than static models. Our investigation on LES turbulence models also showed that static LES turbulence models such as Smagorinsky or kEqn models cannot predict correct fluid velocity flow fields with the provided mesh resolution (y^+~3). Therefore, we used the dynamicKEqn model in our LES-DEM simulations, which

seems to overcome the poor performance of static turbulence models when using relatively coarse mesh resolution. However, standard DPMFoam solver does not come with dynamic turbulence models in OpenFOAM-v1912 (the solver used in our RANS-DEM and LES-DEM study), and we needed to compile the dynamicKEqn model as a separate library for two-phase systems and included it in our LES-DEM simulations.

Table 2. RANS-DEM and LES-DEM settings.

Description	RANS-DEM	LES-DEM
Solution domain	3-Dimension	3-Dimension
Turbulence model	kOmegaSST	dynamicKEqn with cubeRootVolume delta function
Dispersion model	StochasticDispersionRAS	-
Mesh resolution	1,105,280 hexahedra cells	3,533,376 hexahedra cells
y^+	-	~3
Resolved TKE	-	80–90%
boundary condition at inlet (air)	mappedPatch (Mapped from 400 mm downstream of inlet)	mappedPatch (Mapped from 400 mm downstream of inlet)
Front and back boundary treatment	Cyclic	Cyclic
Wall treatment	Wallfunctions	Resolved
Particle injection velocity at inlet (particle boundary condition)	(10.5, 0, 0) m/s (0, 0, 0) m/s Varying as per fluid velocity distribution	(10.5, 0, 0) m/s (0, 0, 0) m/s Varying as per fluid velocity distribution
Mass loading of particles	10%	10%
Coupling regime	One-way and two-way	Two-way
Simulation duration	1 s	3 s

OpenFOAM solvers, namely pimpleFoam and DPMFoam, are used for single and two-phase simulations, respectively, in OpenFOAM-v1912. Both pimpleFoam and DPMFoam use the pimple algorithm to couple velocity and pressure fields. Backward and least Squares schemes are used for time and gradient discretization, respectively. All the divergence terms are discretized using Gauss linear method. The resulting discretized equations were solved using algebraic multigrid (AMG) and algorithms based on a point-implicit linear equation solver (Gauss–Seidel). DEM data (particle position, velocity, etc.) are mapped onto CFD mesh, and particle volume fraction in each computational cell is calculated. The interaction forces are locally averaged in each cell and incorporated in NS equations and the calculated flow data are communicated back to the DEM side. All the simulations were performed in parallel on 56 processors in the Linux cluster of Leibniz Supercomputing Centre (LRZ). The total CPU computational time corresponding to different simulations can be found in Table 3.

Table 3. Total CPU computational time.

Simulation	Total CPU Computational Time (in Seconds)	
	RANS-DEM (Run Time = 1 s)	LES-DEM (Run Time = 3 s)
Single-phase	3925	29,682
Two-phase (one-way coupled)	12,693	-
Two-phase (two-way coupled)	13,385	109,921

Fluid and particle velocity profiles at the measurement locations are compared with the experimental data. Fluid flow fields can be directly extracted and plotted at the measurement locations from the OpenFOAM results. Time averaging on particles cannot be performed as done for the continuum phase (air) due to the discrete nature of the particles. The particles are evaluated in a slice around the measurement locations with a thickness of 0.15H and the center lies precisely at the measurement locations for every 0.1 s interval from the start to the end of the simulation. The slice thickness of 0.15H is adopted as the same slice thickness was considered for sampling the particles in the previous study [15]. The particle data collected for all the selected time intervals are combined, and averaging is performed in each slice on the particles with the same location (only the y-component). The resulting average particle velocity profiles are then compared with the experimental data.

4. Results and Discussion

The results shown below are arranged in such a way that they indicate the workflow adopted to investigate and solve the particle-laden BFS flow in OpenFOAM. The normalized mean and fluctuating fluid velocity profiles are compared with the experimental data at their respective measurement locations (x/H = 2, 5, 7, 9, 14). Normalized average particle velocity profiles are compared with observed data in the experiment at their respective measurement locations (x/H = 2, 5, 7, 9, 12) to assess the particle-phase results. We have somewhat amplified the normalized velocity fields in order to highlight the deviations.

4.1. Single-Phase RANS and LES

To obtain correct results for discrete phase (particles), one must have acceptable results for the continuum phase (air) with reasonable accuracy. Therefore, we first performed the single-phase RANS and LES simulations using the pimpleFoam solver, which is able to predict fluid velocity profiles with acceptable precision. For RANS and LES results, the methods and formulae used to calculate the fluctuating components (*Urms*) are different. Regarding the RANS models, for everything above mean flow fields, the fluctuating component is calculated (with the assumption of isotropic turbulence holds true) directly from the modelled turbulent kinetic energy (TKE; k) using Equation (22), which is the modelled part of the fluctuating component.

$$Urms = \sqrt{\frac{2}{3}k} \tag{22}$$

In LES simulations, we aim to resolve 80–90% TKE, and the calculated *Urms* represents the resolved fluctuating component. *Urms* is calculated by subtracting the mean flow field from the instantaneous flow fields, as shown below:

$$Urms = \sqrt{\frac{1}{N}\sum_{i=0}^{N}(U_i - UMean)^2} \tag{23}$$

$$UMean = \frac{1}{N}\sum_{i=0}^{N}U_i \tag{24}$$

where, U_i is the instantaneous velocity, *UMean* is the time-averaged velocity, and N is the total number of time steps.

Figure 4 compares simulated streamwise air mean and fluctuating velocity profiles under RANS (with kOmegaSST turbulence model) and LES (with kEqn and dynamicKEqn turbulence models) frameworks with the experiment data. It is evident from the streamwise air mean velocity profile plots (Figure 4a) that both RANS and LES (with dynamicKEqn turbulence model) predict the correct mean flow and are able to predict the re-attachment point (x/H ~ 7) quite accurately as observed in the original experiment (x/H ~ 7.4). On the

other hand, Figure 4b shows that the streamwise air fluctuating components (*Urms*) from RANS are somewhat underpredicted, which is not surprising as they represent only the modelled part of the turbulent fluctuations. LES (with dynamicKEqn turbulence model) is able to resolve the turbulent fluctuations more accurately and realistically than RANS. LES simulation with static turbulence model (kEqn) performs very poorly with provided LES mesh resolution ($y^+ \sim 3$). The static LES turbulence model is not only unable to predict flow separation but also overpredicts the mean flow and turbulent fluctuating velocities by a huge margin. In LES, the calculated mean and fluctuating velocities represent the statistical fields, which is a function of time over which the averaging is performed (in our case: 3 s). A more accurate and realistic approximation of flow statistics would be obtained if performed over a longer duration. In Figure 5, the simulated velocity fields are shown under (a) RANS and (b) LES (using dynamicKEqn turbulence model) frameworks, representing the level of resolution obtained under these approaches. RANS flow fields are very smooth as they represent mean values, while eddy generation and decay can be seen in LES flow fields. It must be emphasized that with the mesh resolution used in our LES simulations ($y^+ \sim 3$), static LES turbulence models were unable to predict correct fluid velocity profiles, whereas the dynamic LES turbulence model resulted in a relatively real estimation of mean and fluctuating fluid velocity with the used relatively coarser mesh, as shown in our fluid velocity plots.

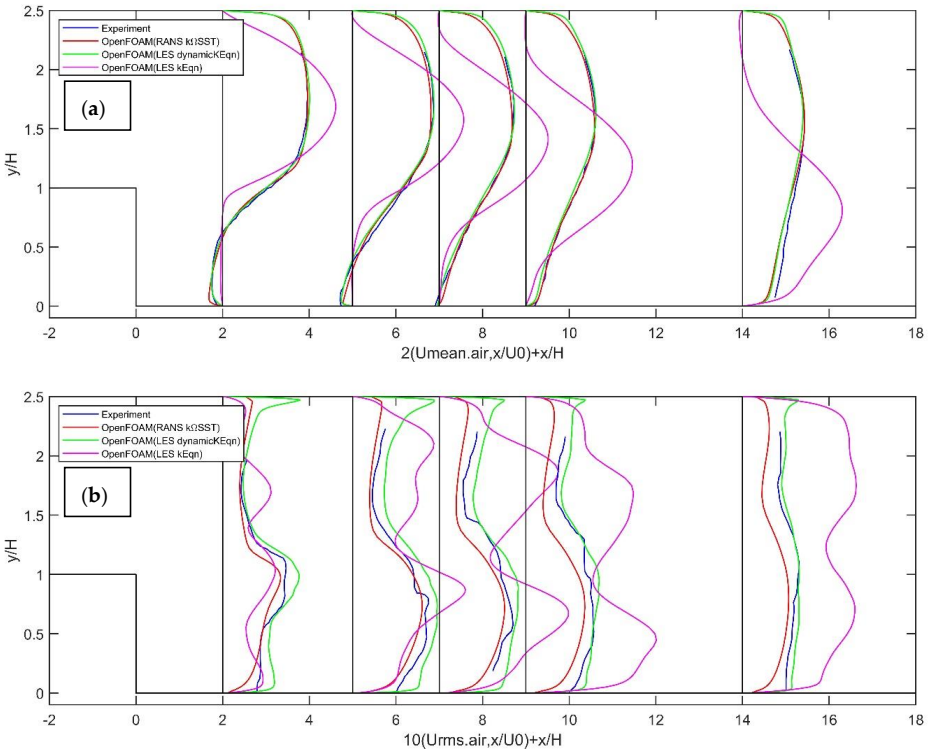

Figure 4. Comparisons of experimental and OpenFOAM simulated streamwise air (**a**) mean and (**b**) fluctuating velocity profiles at the measurement locations under RANS and LES frameworks.

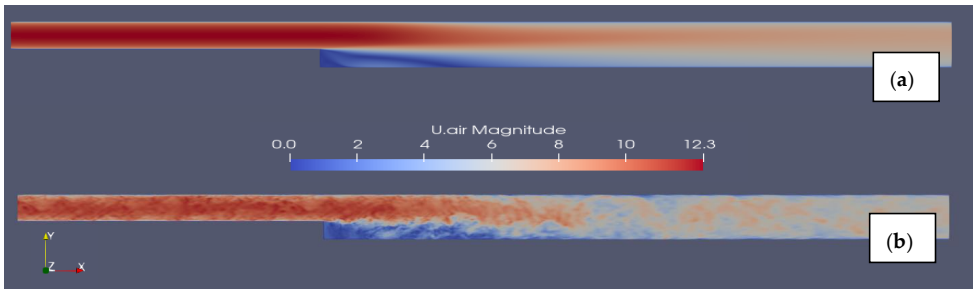

Figure 5. OpenFOAM simulated velocity fields (magnitude) under (**a**) RANS (kOmegaSST) and (**b**) LES (dynamicKEqn) frameworks.

In our next RANS-DEM and LES-DEM sections, we mainly focused on the simulation's accuracy in predicting particle dispersion on the influence of the carrier fluid (air) flow turbulence. However, even the presence of the particles can modify the turbulence, as discussed in the introduction. The potential modification in air turbulence due to the presence of particles is not explicitly discussed in this study. Additionally, the turbulence models employed do not consider the presence of particles as they are developed for single-phase fluid flow and some works have noticed the potential failure of employed turbulence models in specific flow scenarios [55]. However, new mathematical turbulence models considering the particle's presence are yet to be developed and do not come under the scope of this study.

4.2. RANS-DEM

We have investigated the effect of one-way and two-way coupling on the continuum and discrete phase results and found almost no difference between the results of either coupling regime. The mass flow rate of 10% and the corresponding volumetric fraction of particles is in order of ~10^{-5}, which is indeed in the range of the two-way coupling threshold suggested by Elghobashi [4]. Interestingly our one-way and two-way coupling results for fluid phase (Figure 6) and particle phase (Figures 7 and 8; red circles) almost overlap each other, suggesting that one-way coupling might also be adopted when particle volumetric fraction is slightly greater (O ~ 10^{-5}) than the threshold for one-way coupling. As demonstrated by our fluid and particle phase results, one-way coupling seems to be sufficient even for particle concentration in O ~ 10^{-5}, which is slightly greater than the standard threshold for one-way coupling.

Figure 9 also shows that when using RANS-DEM, the fluid mean velocity profiles agree very well with the experimental data, as in the single-phase results. For brevity, we show here streamwise air mean velocity profiles (Figure 9) only for two-way coupling corresponding to different particle boundary conditions (injection velocity), as they are very similar to RANS-DEM results for one-way coupling and single-phase RANS results. Figure 9 shows that the air-phase results are independent of particle injection velocities due to small particle concentration. Under the RANS-DEM framework, turbulent fluctuations are significantly underpredicted, which can be seen in single-phase plots, and this underprediction of turbulent fluctuation also reflects in particle velocity plots (Figures 7 and 8; red circles), where particles move roughly like a patch and do not disperse below the step ($y/H < 1$) even after flow re-attachment ($x/H \sim 7$). This underprediction of particle dispersion behind the step can also be seen in Figure 10a, which shows the particle spread behind the step at t = 1 s.

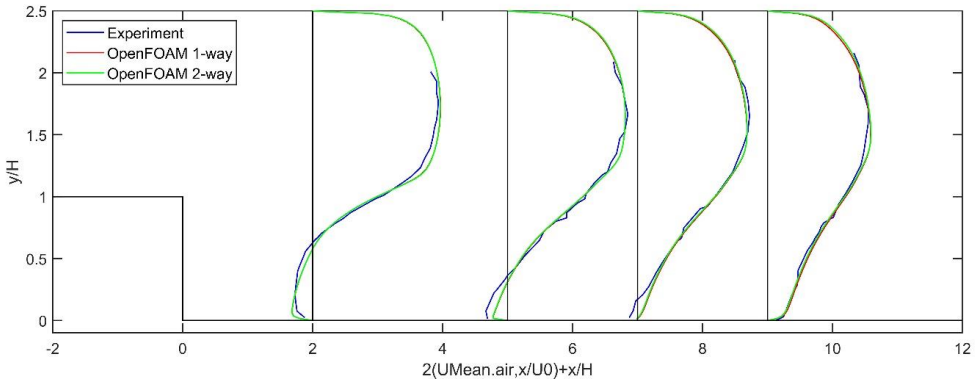

Figure 6. Comparisons of experimental and OpenFOAM simulated (RANS-DEM) streamwise air mean velocity profiles at the measurement locations for one-way and two-way coupling for the case corresponding to a particle injection velocity of 10.5 m/s.

One-way coupling

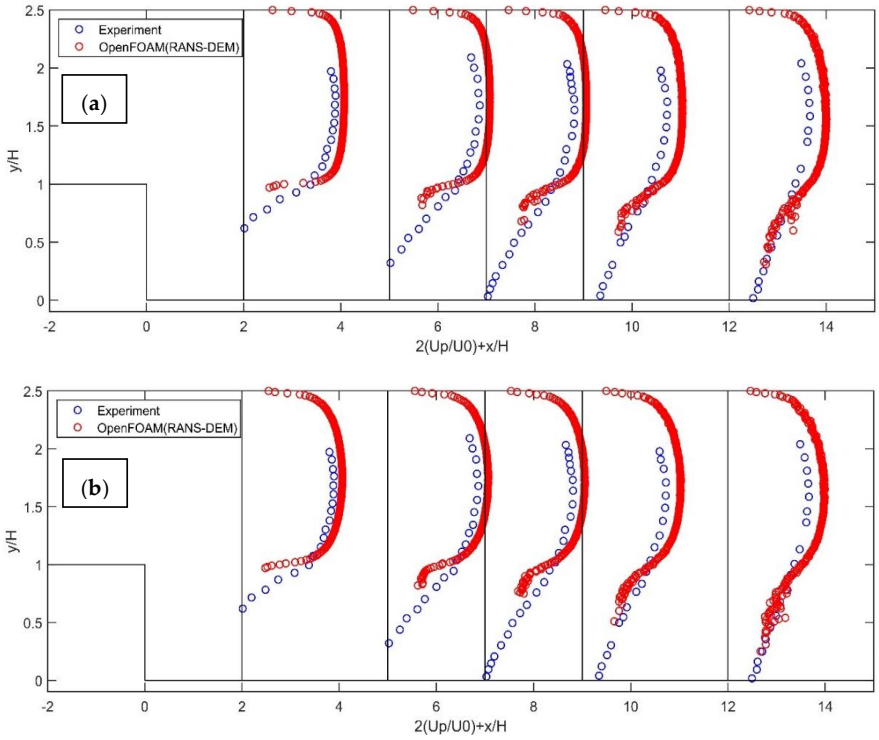

Figure 7. *Cont.*

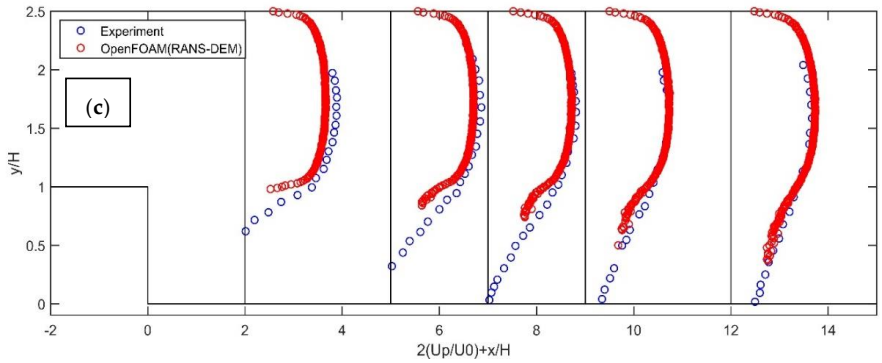

Figure 7. Comparisons of experimental and OpenFOAM simulated average streamwise particle velocity profiles at the measurement locations for one-way coupling and 10% mass loading of copper particles under RANS-DEM framework. (**a**) Particle injection velocity as (10.5, 0, 0) m/s, (**b**) particle injection velocity same as that of the fluid velocity profile at inlet, (**c**) particle injection velocity as (0, 0, 0) m/s.

Two-way coupling

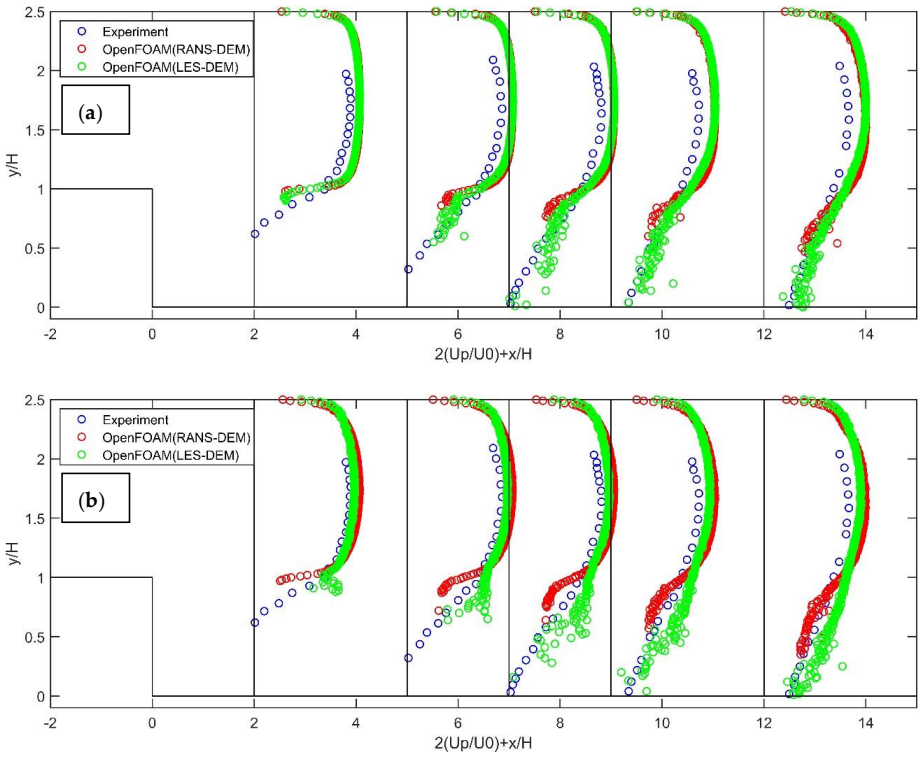

Figure 8. *Cont.*

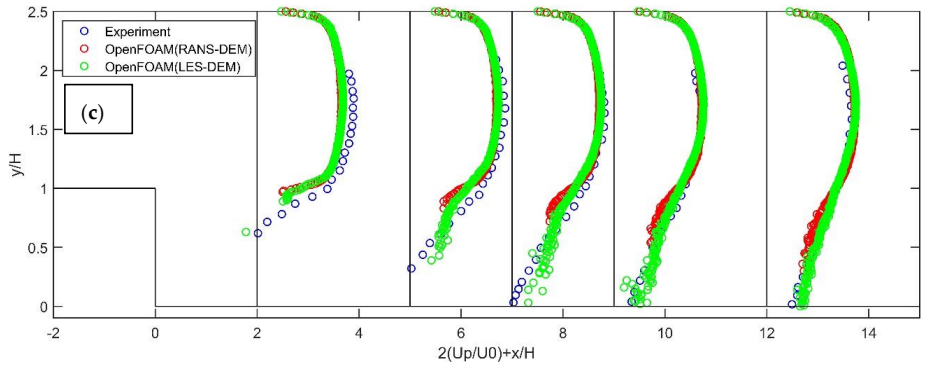

Figure 8. Comparisons of experimental and OpenFOAM simulated average streamwise particle velocity profiles at the measurement locations for two-way coupling and 10% mass loading of copper particles under RANS-DEM and LES-DEM frameworks. (**a**) Particle injection velocity as (10.5, 0, 0) m/s, (**b**) a particle injection velocity same as that of the fluid velocity profile at the inlet, (**c**) particle injection velocity as (0, 0, 0) m/s.

Two-way coupling

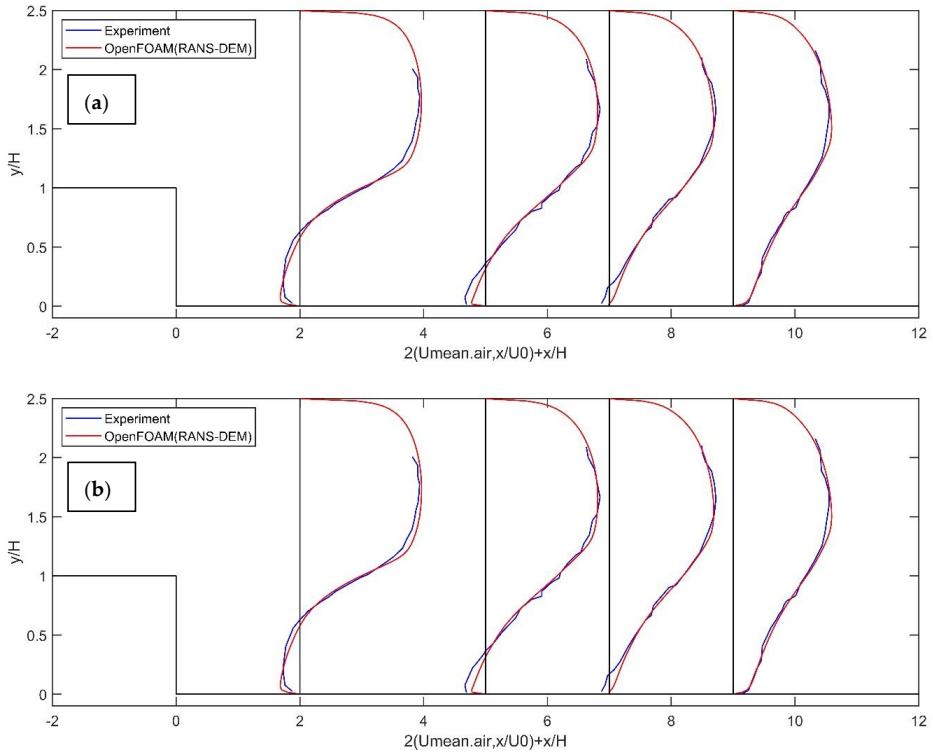

Figure 9. *Cont.*

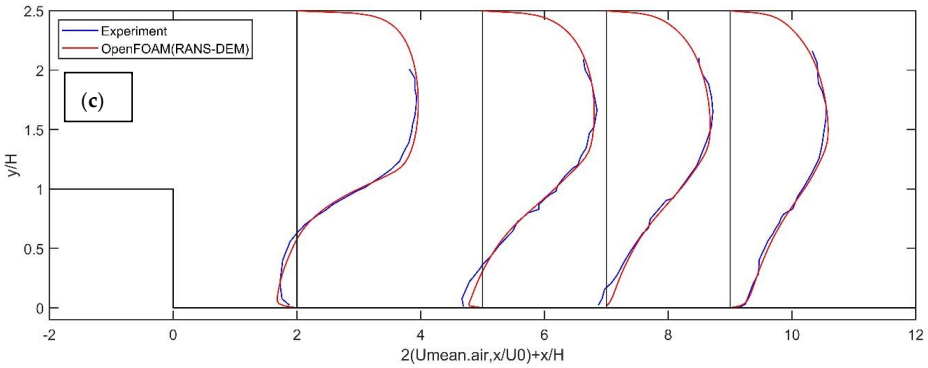

Figure 9. Comparisons of experimental and OpenFOAM simulated streamwise air mean velocity profiles at the measurement locations for two-way coupling and 10% mass loading of copper particles under RANS-DEM framework. (**a**) Particle injection velocity as (10.5, 0, 0) m/s, (**b**) particle injection velocity same as that of the fluid velocity profile at the inlet, (**c**) particle injection velocity as (0, 0, 0) m/s.

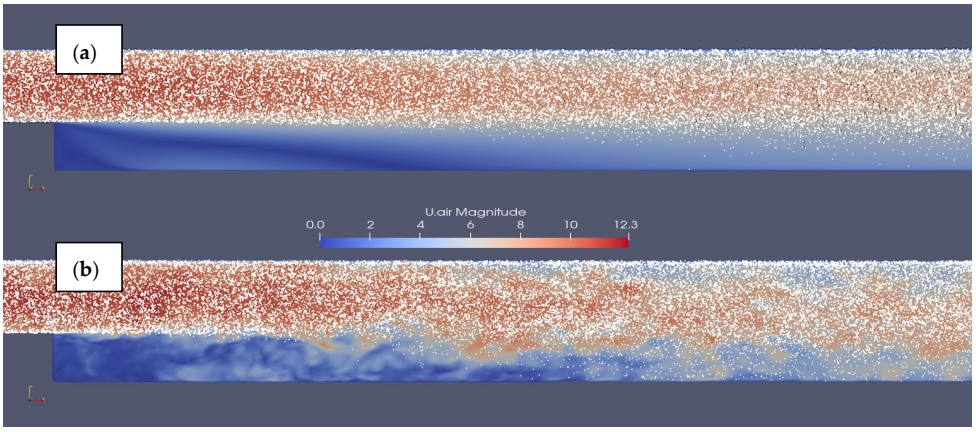

Figure 10. Screenshot showing particle dispersion behind the step at 1 s under (**a**) RANS-DEM and (**b**) LES-DEM frameworks.

One of the main questions that we tried to answer is: how effectively can RANS-DEM, with simple dispersion models, predict particle dispersion in turbulent flows? In other words, its effectiveness in obtaining instantaneous flow fields so that the turbulence effect on the particle's motion can be modelled accurately. For this purpose, two simple dispersion models are available in OpenFOAM, namely, *GradientDispersionRAS* and *StochasticDispersionRAS*, based on Equation (18). An initial investigation reveals that the *StochasticDispersionRAS* dispersion model gives slightly better results in relation to particle dispersion and was also adopted by Greifzu et al. [15] in their RANS-DEM numerical simulations. Therefore, we decided to use the *StochasticDispersionRAS* model in our RANS-DEM simulations. Figure 7 shows the normalized streamwise average particle velocity profiles corresponding to one-way coupling for different particle boundary conditions (injection velocity). The results demonstrate that particle-phase results are also very similar for one-way (Figure 7) and two-way coupling (Figure 8), but different particle injection velocities have a notable effect on particle-phase results, unlike air-phase results. When particles are injected with (10.5, 0, 0) m/s of injection velocity from the inlet of BFS (Figure 7a), the particle

velocities at all the measurement locations are overpredicted, and their dispersion (spread in the y-direction) is underpredicted. When particles are injected with the velocity that follows the fluid velocity profile at the inlet (Figure 7b), the results improved slightly but were still far from the experimental data, in which the particles moved roughly like a patch, and a minimal number of particles were dispersed below the step ($y/H < 1$). When particles are injected with (0, 0, 0) m/s of injection velocity (Figure 7c), the particle velocity profiles provide a better match with the experimental data, but the dispersion of the particles is still considerably underpredicted, similar to other RANS-DEM cases. It can also be seen from Figure 8 that a very similar particle dispersion behavior is observed, even for two-way coupling under the RANS-DEM framework. In the RANS-DEM framework, all the cases with different boundary conditions for the particle-phase and under the considered coupling regime underpredict the particle dispersion by a considerable margin and a minimal number of particles are found below the step ($y/H < 1$) even after the flow re-attachment point ($x/H \sim 7$). On the other hand, experimental data shows that particles disperse across the extended channel section until they reach the re-attachment point ($x/H \sim 7$), and, after this, the particle concentration below and above the step becomes almost uniform. Our analysis shows that the simple dispersion models (DRW) are ineffective in incorporating turbulence effects on the trajectory of particles.

In comparison to the RANS-DEM results of Greifzu et al. [15], our fluid flow results are in good agreement with them and with the experimental data as well, but the particle-phase results are entirely different. Their results showed that the RANS-DEM (and simple dispersion model therein) can predict the correct particle dispersion and their velocity profiles. Interestingly, we found that they were using a fluid density of 1000 kg/m^3 (water) instead of 1 kg/m^3 (air) in their OpenFOAM numerical setup, even though the fluid used in the experiment was air, not water. Using a density of 1000 kg/m^3 results in a higher body (buoyant force) and coupled forces (drag and pressure gradient force) acting on the particles, which would disperse the particles in the domain even before the re-attachment point, as observed in the particle velocity plots of Greifzu et al. [15]. It is demonstrated that particles will be dispersed into the recirculation region only when their large-eddy Stokes numbers are less than one [56]. The large-eddy Stokes numbers for fluid as air (density = 1 kg/m^3) and as water (density = 1000 kg/m^3) are found to be 6.9 and 0.053, respectively. Obviously, when the fluid density is that of water, the Stokes number is significantly smaller than one, so the particles will also be dispersed into the recirculation region (as they behave similar to tracers). Fluid flow results remain almost the same even if the density of water is used instead of air because the momentum transferred from the particle phase to the fluid phase remains of the same order of magnitude. This can be explained as small particle concentrations result only in a few numbers of particles in each computational cell and are simply not numerous enough to modify the fluid flow fields. So, even by considering two-way coupling and a density of fluid as that of water does not modify the fluid flow fields. This explanation also indicates that the previous observation regarding the ability of the simple dispersion model (DRW) in accurately incorporating turbulence effects on particle's trajectory is not true and supports our observation about simple dispersion models.

The dispersion models available in OpenFOAM are essentially discrete random walk (DRW) type models and are calculated using the modelled turbulent kinetic energy (TKE). These models are simple models based on rough assumptions, e.g., that the turbulence is isotropic in the whole domain, which leads to the inappropriate modelling of turbulence seen by particles. However, the turbulence is very anisotropic in the boundary layers, and this anisotropic behavior is even more significant for wall-bounded flows with complex geometries such as BFS flow. The shortcomings of the discrete random walk (DRW) type of dispersion models can be avoided by better treatment of boundary layer effects. For this purpose, an option could be the Continuous Random Walk (CRW) method to be included in OpenFOAM, which offers a more physically sound way of modelling particle dispersion [57]. The anisotropic behavior of turbulent flow is better modelled using the

CRW method, recently presented by Mofakham [13]. An alternative stochastic approach to describe the particle dispersion due to turbulence could be a straightforward generalization of the stochastic approach introduced by Pope [58], which was originally developed to describe single-phase flow. This approach is extended to describe the two-phase system by Peirano et al. [59]. Xiang [14] used this stochastic model in their numerical simulation in OpenFOAM and reported that it performs better than the already implemented dispersion models (DRW models) in OpenFOAM. Although even with their implemented stochastic model, the simulated particle dispersion was far from the reference data. There are also the Reynolds stress transport models (RSTM) that directly evaluate the components of Reynolds stresses and account for the anisotropy of turbulent fluctuations [60–62]. However, knowledge of instantaneous fluctuations is required for specific problems, such as the one involving particle dispersion and deposition. It was recently shown that a RANS approach in conjunction with RSTM and DRW does not improve the results in terms of particle dispersion, and that more sophisticated dispersion models such as CRW must be used [13].

In the original experiment, the particles traversed a sufficient distance (a development channel length of 5.2 m) before they reached the inlet of BFS. This assured that the particles had attained equilibrium with the fluid phase before the inlet of BFS, as they had enough time (at least three particle response time, in the worst case) to come to equilibrium with the fluid phase [53]. As at the inlet of BFS, the particle velocity profile was not measured and/or available in the literature, and we do not know the exact particle velocity when they reach the inlet of BFS. It is quite difficult to approximate the real particle velocities at the inlet of BFS without this development channel. Our results demonstrate that the straightforward assumption that all the particles have attained mean flow velocity seems unreasonable. The best approximation of particle injection velocity was found to correspond to an injection velocity of (0, 0, 0) m/s. This might be due to the fact that the particles may obtain real physical velocity depending upon the particle reaction time and fluid flow around it. The additional injection velocity, which one needs to provide along with the mass flux of the particles, does not seem to be necessary as we specify mass flux of particles (e.g., kg/s) that is injected from the inlet of the BFS. Once the particles are in the domain, they attain velocities depending upon the flow around them and the particle response time (Stokes number). However, this approach may vary in individual cases, and the results might look different when the inlet channel (before BFS) length is increased. It also depends on the different algorithms that different software use for particle generation and insertion. The best practice guidelines for CFD should still be the extension of the inlet channel length and allowing particles to develop real physical velocity, but this might be extra computational overhead for CFD-DEM simulations.

4.3. LES-DEM

We decided to perform LES-DEM simulations to investigate the case in more detail; fluid flow fields are calculated using the LES approach, then particle trajectories are calculated based on resolved LES fluid flow fields without considering additional models to include the effects of SGS on the motion of the particle. LES-DEM simulated fluid-flow fields agree well with the experimental data, such as single-phase LES simulations. LES-DEM simulated fluid velocity profiles are not shown here for the sake of brevity. The LES-predicted turbulent fluctuation was a significant improvement over the RANS approach (see Figure 4b), and this is also reflected in particle dispersion, as seen in Figure 8 (green circles) and Figure 10b.

Figure 8 shows normalized streamwise average particle velocity profiles for 10% mass loading of ~70 μm copper particles for two-way coupling corresponding to the different options concerning the particle injection velocities under RANS-DEM (red circles) and LES-DEM (green circles) frameworks. Compared to the RANS-DEM results, particle dispersion and velocity profiles have been improved considerably due to the ability of LES to resolve flow fields in greater detail and improved predictions in view of the improved representation of the flow field seen by the particles. Moreover, when the particles are

injected with an injection velocity of (10.5, 0, 0) m/s from the inlet (Figure 8a), the particle velocities at all measurement locations are slightly overpredicted. When particles are injected with an injection velocity that follows the fluid velocity profile at the inlet (Figure 8b), the particle velocity profiles seem to be slightly overpredicted compared to those observed in the experiment. When particles are injected with an injection velocity of (0, 0, 0) m/s from the inlet of BFS (Figure 8c), the particle velocity profiles give a reasonably good match with the experimental data at all the measurement locations. In all the three LES-DEM cases, a very small number of particles is found in the recirculation region, but after the re-attachment point (x/H ~ 7), enough particle dispersion is predicted as observed in the original experiment. Compared to the original experiment, our LES-DEM still underpredicts the particles' dispersion, especially in the recirculation region. Taking both the correctness of predicting particle velocity and their dispersion into account, we found that the best results were obtained when particles are injected with (0, 0, 0) m/s of injection velocity, and the probable reason of it being the best option to approximate the particle boundary condition without extending the inlet channel is already explained in our RANS-DEM section.

It can be clearly seen that the overall particle-phase results have improved considerably with the LES-DEM approach. The particle-phase results, especially its dispersion, under the LES-DEM framework can be further improved with increased mesh resolution (y^+~1) and/or with the inclusion of missing SGS in the equation of particle motion. However, one must always bear in mind that extreme fine meshing can cause stability problems, as CFD cells cannot be smaller than particle diameter under the unresolved CFD-DEM framework, and can thus only be applied under consideration of point-particles (PP). Additionally, further mesh refinement would require much more computational resources. A recent study indicates that the use of stochastic dispersion models is necessary even in the LES-DEM framework, especially for the fine particles, where the corresponding particle relaxation time is of the same order as the smallest fluid flow time scale [63]. Our LES-DEM results also indicate that the effect of SGS cannot be neglected and has a significant effect on particle trajectories, especially for the particles with a small Stokes number, which was also suggested by Ref. [10]. The effect of SGS on particle's trajectory seems to play an even more important role in LES-DEM simulations, where very fine meshes might not be possible due to the prerequisite of unresolved CFD-DEM, where a particle must be significantly smaller than the CFD cell size and must be recovered with efficient modelling approaches, as shown in our results.

5. Summary and Conclusions

In this work, we have assessed the capability of OpenFOAM to solve the particle-laden BFS flow in the different frameworks of RANS-DEM and LES-DEM. The RANS method only provides the mean flow fields. Therefore, an additional dispersion model is used to include the effect of turbulent fluctuation on the trajectory of particles. In contrast, LES can resolve up to energy-containing eddies, but several constraints such as particles being smaller than the CFD mesh in the unresolved CFD-DEM and computational limitations restrict the extreme refinement of CFD mesh. Thus, it is necessary to make a compromise between the accuracy obtained and the computational resources required, which is quite challenging. Collectively, the following conclusions can be drawn from our study:

- We found that the threshold of coupling regime suggested by Elghobashi [4] is rigidly formulated and it might be sufficient to include one-way coupling even when the particle concentration is in O ~ 10^{-5}, since we found almost no difference between the fluid and particle phase results for one-way and two-way coupling;
- Under the RANS-DEM framework, simple dispersion models based on DRW significantly underpredicted the particle dispersion. Consequently, more sophisticated dispersion models such as CRW must be used in conjunction with RANS-DEM. Previously claimed results about the ability of the simple dispersion models in accurately incorporating turbulence effects on particles were due to error in the numerical setup;

- When using relatively coarse mesh resolution ($y^+ > 1$), Dynamic LES turbulence models seem to overcome the poor performance of static LES turbulence models in predicting the mean and fluctuating components of turbulent flow. We recommend using dynamic LES models when extreme mesh refinement is not possible due to the limitation of particles being smaller than CFD cell size in unresolved CFD-DEM;
- Resolved CFD-DEM (particle resolved DNS) requires huge computational resources and is restricted to a small number of particles. Point particle DNS-DEM is also computationally expensive and should not be applied for larger particles than Kolmogorov length scale. The LES-DEM seems to be a good compromise between accuracy and computational feasibility. However, its application is mostly restricted to simple cases (point-particles or small particles) due to the constraint of the particles being smaller than the CFD cells in unresolved CFD-DEM. In addition, the unresolved component of the turbulent velocity (SGS) seems to have a significant effect on particle dispersion and cannot be neglected, especially when using larger y^+ in LES-DEM;
- Our analysis of different options for approximating the initial particle velocity (particle injection velocity) indicates that a suitable numerical approach might be to inject particles with (0, 0, 0) m/s of particle injection velocity. The difference between the results is small, but still might be appropriate so as to let the particles attain the real physical velocity according to physics, for the cases where the initial particle velocity is unavailable. However, this approach is case-dependent and software-specific. The best practice guidelines for CFD should still be the extension of the inlet channel length and allowing particles to develop real physical velocity, but this might be an extra computational overhead for CFD-DEM simulations.

From our point of view, one of the best options for gaining success in predicting dilute particle dispersion in turbulence flow can be an accurate calculation of the mean flow statistics and a good stochastic model, although here, further benchmarking is still necessary. More fundamental research and validations are required in both RANS-DEM and LES-DEM before the complex physics related to fluid-particle systems can be studied in detail, considering all factors such as surface, inertial, response, loading, and interaction effects into account. Application of RANS-DEM and LES-DEM for real problems would require larger CFD meshes, resulting in loss of information about turbulent fluctuations. If we could recover this lost information with simple yet efficient methods, then it would be of great engineering application. With the currently available computational resources, both resolved CFD-DEM (particle-resolved DNS-DEM) and point-particle DNS-DEM are still limited to simple cases with a small number of particles. More efficient algorithms and computer architecture are required to achieve this, and more research should be encouraged in this field.

Author Contributions: A.J. (conceptualization, investigation, data curation, writing—original draft), M.D.B. (supervision, writing—review and editing), P.R. (supervision). All authors have read and agreed to the published version of the manuscript.

Funding: This research received no external funding.

Institutional Review Board Statement: Not applicable.

Informed Consent Statement: Not applicable.

Data Availability Statement: The data presented in this study are available on request from the corresponding author.

Acknowledgments: We would like to acknowledge the CFD-online community (https://www.cfd-online.com/ (accessed on 4 September 2022)), which provided us with a platform to discuss the problem and solutions with experts from all over the world. We would like to thank Rüdiger Schwarze and his team (TU Freiberg) for confirming the error in their numerical setup, when reported. We would also like to thank Silvio Schmalfuß (Leibniz Institute for Tropospheric Research, Leipzig) and Robert Kasper (University of Rostock) for their valuable suggestions. We would like to thank the Leibniz Supercomputing Centre (LRZ) for providing computational resources. We appreciate the

help and continuous encouragement from Nils Rüther (TU Munich). A.J. gratefully acknowledges the Konrad-Adenauer-Stiftung (KAS) for a PhD scholarship. We thank the editor and anonymous reviewers for their constructive comments, which helped us to improve the manuscript.

Conflicts of Interest: On behalf of all authors, the corresponding author states that there is no conflict of interest.

References

1. Crowe, C.T.; Schwarzkopf, J.D.; Sommerfeld, M.; Tsuji, Y. *Multiphase Flows with Droplets and Particles*, 2nd ed.; CRC Press: Boca Raton, FL, USA; London, UK; New York, NY, USA, 2011.
2. Brennen, C.E. *Fundamentals of Multiphase Flows*; Cambridge University Press: Pasadena, CA, USA, 2005.
3. Zhu, H.P.; Zhou, Z.Y.; Yang, R.Y.; Yu, A.B. Discrete Particle Simulation of Particulate Systems: Theoretical Developments. *Chem. Eng. Sci.* **2007**, *62*, 3378–3396. [CrossRef]
4. Elghobashi, S. On predicting particle-laden turbulent flows. *Appl. Sci. Res.* **1994**, *52*, 309–329. [CrossRef]
5. Salih, S.Q.; Aldlemy, M.S.; Rasani, M.R.; Ariffin, A.K.; Ya, T.M.Y.S.T.; Al-Ansari, N.; Yaseen, Z.M.; Chau, K.W. Thin and sharp edges bodies-fluid interaction simulation using cut-cell immersed boundary method. *Eng. Appl. Comput. Fluid Mech.* **2019**, *13*, 860–877. [CrossRef]
6. Squires, K.D.; Eaton, J.K. Particle response and turbulence modification in isotropic turbulence. *Phys. Fluids A Fluid Dyn.* **1990**, *2*, 1191–1203. [CrossRef]
7. Elghobashi, S.; Truesdell, G.C. On the two-way interaction between homogeneous turbulence and dispersed solid particles. I: Turbulence modification. *Phys. Fluids A Fluid Dyn.* **1993**, *5*, 1790–1801. [CrossRef]
8. Chan, L.; Zahtila, T.; Ooi, A.; Philip, J. Turbulence Modification Due to Inertial Particles in a Rough-Wall Pipe. In Proceedings of the 22nd Australasian Fluid Mechanics Conference AFMC2020, Brisbane, Australia, 7–10 December 2020; The University of Queensland: Brisbane, Australia, 2020.
9. Lee, J.; Lee, C. The Effect of Wall-Normal Gravity on Particle-Laden Near-Wall Turbulence. *J. Fluid Mech.* **2019**, *873*, 475–507. [CrossRef]
10. Kuerten, J.G.M. Point-Particle DNS and LES of Particle-Laden Turbulent flow—A state-of-the-art review. *Flow Turbul. Combust.* **2016**, *97*, 689–713. [CrossRef]
11. Bocksell, T.L.; Loth, E. Stochastic modeling of particle diffusion in a turbulent boundary layer. *Int. J. Multiph. Flow* **2006**, *32*, 1234–1253. [CrossRef]
12. Loth, E. Numerical approaches for motion of dispersed particles, droplets and bubbles. *Prog. Energy Combust. Sci.* **2000**, *26*, 161–223. [CrossRef]
13. Mofakham, A.A.; Ahmadi, G. On random walk models for simulation of particle-laden turbulent flows. *Int. J. Multiph. Flow* **2020**, *122*, 103157. [CrossRef]
14. Xiang, L. RANS Simulations and Dispersion Models for Particles in Turbulent Flows. Master's Thesis, KTH, School of Engineering Sciences (SCI), Mechanics, Stockholm, Sweden, 2019.
15. Greifzu, F.; Kratzsch, C.; Forgber, T.; Lindner, F.; Schwarze, R. Assessment of particle-tracking models for dispersed particle-laden flows implemented in OpenFOAM and ANSYS FLUENT. *Eng. Appl. Comput. Fluid Mech.* **2016**, *10*, 30–43. [CrossRef]
16. Innocenti, A.; Marchioli, C.; Chibbaro, S. Lagrangian filtered density function for LES-based stochastic modelling of turbulent particle-laden flows. *Phys. Fluids* **2016**, *28*, 115106. [CrossRef]
17. Kuerten, J.G.M.; Vreman, A.W. Can turbophoresis be predicted by large-eddy simulation? *Phys. Fluids* **2005**, *17*, 011701. [CrossRef]
18. Marchioli, C.; Salvetti, M.V.; Soldati, A. Some issues concerning large-eddy simulation of inertial particle dispersion in turbulent bounded flows. *Phys. Fluids* **2008**, *20*, 40603. [CrossRef]
19. Salmanzadeh, M.; Rahnama, M.; Ahmadi, G. Effect of Sub-Grid Scales on Large Eddy Simulation of Particle Deposition in a Turbulent Channel Flow. *Aerosol Sci. Technol.* **2010**, *44*, 796–806. [CrossRef]
20. Bianco, F.; Chibbaro, S.; Marchioli, C.; Salvetti, M.V.; Soldati, A. Intrinsic filtering errors of Lagrangian particle tracking in LES flow fields. *Phys. Fluids* **2012**, *24*, 45103. [CrossRef]
21. Geurts, B.J.; Kuerten, J.G.M. Ideal stochastic forcing for the motion of particles in large-eddy simulation extracted from direct numerical simulation of turbulent channel flow. *Phys. Fluids* **2012**, *24*, 81702. [CrossRef]
22. Eppinger, T.; Seidler, K.; Kraume, M. DEM-CFD Simulations of Fixed Bed Reactors with Small Tube to Particle Diameter Ratios. *Chem. Eng. J.* **2011**, *166*, 324–331. [CrossRef]
23. Fries, L.; Antonyuk, S.; Heinrich, S.; Palzer, S. DEM–CFD modeling of a fluidized bed spray granulator. *Chem. Eng. Sci.* **2011**, *66*, 2340–2355. [CrossRef]
24. Jajcevic, D.; Siegmann, E.; Radeke, C.; Khinast, J.G. Large-Scale CFD–DEM Simulations of Fluidized Granular Systems. *Chem. Eng. Sci.* **2013**, *98*, 298–310. [CrossRef]
25. Mohammadreza, E. Experimental and Numerical Investigations of Horizontal Pneumatic Conveying. Ph.D. Thesis, The University of Edinburgh, Edinburgh, UK, 2014.
26. Spogis, N. Multiphase Modeling Using EDEM-CFD Coupling for FLUENT. In Proceedings of the 3rd Latin Americal CFD Workshop Applied to the Oil Industry, Rio de Janeiro, Brazil, 18–19 August 2008.

27. Breuer, M.; Alletto, M. Efficient simulation of particle-laden turbulent flows with high mass loadings using LES. *Int. J. Heat Fluid Flow* **2012**, *35*, 2–12. [CrossRef]
28. Capecelatro, J.; Desjardins, O. An Euler–Lagrange strategy for simulating particle-laden flows. *J. Comput. Phys.* **2013**, *238*, 1–31. [CrossRef]
29. Deb, S.; Tafti, D.K. A Novel Two-Grid Formulation for Fluid–Particle Systems Using the Discrete Element Method. *Powder Technol.* **2013**, *246*, 601–616. [CrossRef]
30. Drake, T.G.; Calantoni, J. Discrete particle model for sheet flow sediment transport in the nearshore. *J. Geophys. Res.* **2001**, *106*, 19859–19868. [CrossRef]
31. Wu, C.L.; Ayeni, O.; Berrouk, A.S.; Nandakumar, K. Parallel Algorithms for CFD-DEM Modeling of Dense Particulate Flows. *Chem. Eng. Sci.* **2014**, *118*, 221–244. [CrossRef]
32. OpenCFD Limited. *OpenFOAM, v1912*; OpenCFD Limited: Bracknell, UK, 2019; Available online: https://www.openfoam.com/news/main-news/openfoam-v1906 (accessed on 4 September 2022).
33. Kloss, C.; Goniva, C.; Hager, A.; Amberger, S.; Pirker, S. Models, algorithms and validation for opensource DEM and CFD-DEM. *Prog. Comput. Fluid Dyn.* **2012**, *12*, 140. [CrossRef]
34. Sun, R.; Xiao, H. SediFoam: A General-Purpose, Open-Source CFD-DEM Solver for Particle-Laden Flow with Emphasis on Sediment Transport. *Comput. Geosci.* **2016**, *89*, 207–219. [CrossRef]
35. Bing, W.; Hui Qiang, Z.; Xi Lin, W. Large-Eddy Simulation of Particle-Laden Turbulent Flows over a Backward-Facing Step Considering Two-Phase Two-Way Coupling. *Adv. Mech. Eng.* **2013**, *5*, 325101. [CrossRef]
36. Kasper, R.; Turnow, J.; Kornev, N. Numerical modeling and simulation of particulate fouling of structured heat transfer surfaces using a multiphase Euler-Lagrange approach. *Int. J. Heat Mass Transf.* **2017**, *115*, 932–945. [CrossRef]
37. Wang, B.; Wei, W.E.; Zhang, H. A study on correlation moments of two-phase fluctuating velocity using direct numerical simulation. *Int. J. Mod. Phys. C* **2013**, *24*, 1350068. [CrossRef]
38. Yu, K.F.; Lau, K.S.; Chan, C.K. Large eddy simulation of particle-laden turbulent flow over a backward-facing step. *Commun. Nonlinear Sci. Numer. Simul.* **2004**, *9*, 251–262. [CrossRef]
39. Yu, K.F.; Lau, K.S.; Chan, C.K. Numerical simulation of gas-particle flow in a single-side backward-facing step flow. *J. Comput. Appl. Math.* **2004**, *163*, 319–331. [CrossRef]
40. Yu, K.F.; Lee, E.W. Evaluation and modification of gas-particle covariance models by Large Eddy Simulation of a particle-laden turbulent flows over a backward-facing step. *Int. J. Heat Mass Transf.* **2009**, *52*, 5652–5656. [CrossRef]
41. Armenio, V.; Fiorotto, V. The importance of the forces acting on particles in turbulent flows. *Phys. Fluids* **2001**, *13*, 2437–2440. [CrossRef]
42. Wilcox, D.C. *Turbulence Modeling for CFD*, 2nd ed.; Printing (with Corrections); DCW Industries: La Cãnada, CA, USA, 1998.
43. Uijttewaal, W.S.J.; Oliemans, R.V.A. Particle dispersion and deposition in direct numerical and large eddy simulations of vertical pipe flows. *Phys. Fluids* **1996**, *8*, 2590–2604. [CrossRef]
44. Yeh, F.; Lei, U. On the motion of small particles in a homogeneous isotropic turbulent flow. *Phys. Fluids A Fluid Dyn.* **1991**, *3*, 2571–2586. [CrossRef]
45. Minier, J.P.; Chibbaro, S.; Pope, S.B. Guidelines for the Formulation of Lagrangian Stochastic Models for Particle Simulations of Single-Phase and Dispersed Two-Phase Turbulent Flows. *Phys. Fluids* **2014**, *26*, 113303. [CrossRef]
46. Sodja, J. Turbulence models in CFD. Master's Thesis, University of Ljubljana, Ljubljana, Slovenia, 2007.
47. Kuczaj, A.K.; Geurts, B.J. Mixing in manipulated turbulence. *J. Turbul.* **2006**, *7*, N67. [CrossRef]
48. Simonin, O.; Deutsch, E.; Minier, J.P. Eulerian prediction of the fluid/particle correlated motion in turbulent two-phase flows. *Appl. Sci. Res.* **1993**, *51*, 275–283. [CrossRef]
49. Benra, F.K.; Dohmen, H.J.; Pei, J.; Schuster, S.; Wan, B. A Comparison of One-Way and Two-Way Coupling Methods for Numerical Analysis of Fluid-Structure Interactions. *J. Appl. Math.* **2011**, *2011*, 853560. [CrossRef]
50. Chen, S.F.; Lei, H.; Wang, M.; Yang, B.; Dai, L.J.; Zhao, Y. Two-way coupling calculation for multiphase flow and decarburization during RH refining. *Vacuum* **2019**, *167*, 255–262. [CrossRef]
51. Kitagawa, A.; Murai, Y.; Yamamoto, F. Two-way coupling of Eulerian–Lagrangian model for dispersed multiphase flows using filtering functions. *Int. J. Multiph. Flow* **2001**, *27*, 2129–2153. [CrossRef]
52. Ruetsch, G.R.; Meiburg, E. Two-way coupling in shear layers with dilute bubble concentrations. *Phys. Fluids* **1994**, *6*, 2656–2670. [CrossRef]
53. Fessler, J.R.; Eaton, J.K. Turbulence modification by particles in a backward-facing step flow. *J. Fluid Mech.* **1999**, *394*, 97–117. [CrossRef]
54. Pope, S.B. Ten questions concerning the large-eddy simulation of turbulent flows. *New J. Phys.* **2004**, *6*, 35. [CrossRef]
55. Gimenez, J.M.; Idelsohn, S.R.; Oñate, E.; Löhner, R. A Multiscale Approach for the Numerical Simulation of Turbulent Flows with Droplets. *Arch. Comput. Methods Eng. State Art Rev.* **2021**, *28*, 4185–4204. [CrossRef]
56. Hardalupas, Y.; Taylor, A.M.K.P.; Whitelaw, J.H. Particle Dispersion in a Vertical Round Sudden-Expansion Flow. *Philos. Trans. Phys. Sci. Eng.* **1992**, *341*, 411–442.
57. Dehbi, A. *Stochastic Models for Turbulent Particle Dispersion in General Inhomogeneous Flows*; Paul Scherrer Institut: Villigen PSI, Switzerland, 2008.
58. Pope, S.B. Turbulent Flows. *Meas. Sci. Technol.* **2001**, *12*, 2020–2021. [CrossRef]

59. Peirano, E.; Chibbaro, S.; Pozorski, J.; Minier, J.P. Mean-field/PDF numerical approach for polydispersed turbulent two-phase flows. *Prog. Energy Combust. Sci.* **2006**, *32*, 315–371. [CrossRef]
60. Durbin, P.A. A Reynolds stress model for near-wall turbulence. *J. Fluid Mech.* **1993**, *249*, 465. [CrossRef]
61. Hanjalić, K.; Launder, B.E. A Reynolds stress model of turbulence and its application to thin shear flows. *J. Fluid Mech.* **1972**, *52*, 609–638. [CrossRef]
62. Pope, S.B. *Turbulent Flows*; Cambridge University Press: Cambridge, MA, USA, 2015.
63. Kasper, R.; Turnow, J.; Kornev, N. Multiphase Eulerian–Lagrangian LES of particulate fouling on structured heat transfer surfaces. *Int. J. Heat Fluid Flow* **2019**, *79*, 108462. [CrossRef]

Chapter 5

On the Process of Fine Sediment Infiltration into Static Gravel Bed: A CFD–DEM Modelling Perspective

This chapter is published as:
Jaiswal, A.; Bui, M. D.; Rutschmann, P. On the Process of Fine Sediment Infiltration into Static Gravel Bed: A CFD–DEM Modelling Perspective. *River Research and Applications* 2024, 40(1), 29–48.
https://doi.org/10.1002/rra.4215

Received: 22 May 2023 | Revised: 29 August 2023 | Accepted: 18 September 2023

DOI: 10.1002/rra.4215

RESEARCH ARTICLE

WILEY

On the process of fine sediment infiltration into static gravel bed: A CFD–DEM modelling perspective

Atul Jaiswal | **Minh Duc Bui** | **Peter Rutschmann**

Department of Hydraulic and Water Resources Engineering, Technical University of Munich (TUM), Munich, Germany

Correspondence
Atul Jaiswal, Department of Hydraulic and Water Resources Engineering, Technical University of Munich (TUM), Arcisstr. 21, 80333, Munich, Germany.
Email: atul.jaiswal@tum.de

Abstract

The gravel bed clogging, caused by infiltration and accumulation of fine sediment, degrades the river ecology. A proper understanding of the infiltration process, and underlying mechanism and causes, are necessary to take preventive measures. The process of fine sediment infiltration into static gravel bed is studied by distinguishing between bridging and percolation behaviours, as they affect the river ecology and physical processes occurring in the river system differently. However, several contradicting observations, concerning their occurrences, are reported. We employed the unresolved CFD–DEM method to simulate and investigate the infiltration process. The theoretical size ratios, corresponding to different geometrical configurations for a binary mixture of mono-disperse spherical particles, representing bridging and percolation processes, are considered and simulated with and without flowing water effects. The effects of several turbulence models on the infiltration process are also studied. We found that fine sediment infiltration in fluvial deposits is mainly gravity-dominated, supporting Cui's hypothesis that fine sediment infiltration through intra-gravel flow is similar to fine sediment infiltration driven by gravity. In contrast to consensus in the field, our results demonstrate that the occurrences of different infiltration processes (bridging and percolation) seem to be independent of gravel bed thickness, rather depend only on the relative grain size distribution of fine sediment and gravel. However, a precise definition of a 'thick enough' gravel bed is necessary to distinguish between bridging and percolation behaviours. Here, we hypothesize a suitable gravel bed thickness, which might be regarded as a 'thick enough' gravel bed.

KEYWORDS
bridging, fine sediment infiltration, static gravel bed, unimpeded static percolation, unresolved CFD–DEM

1 | INTRODUCTION

The interstitial pore space of the gravel substrate is crucial for fluvial geomorphology, the exchange processes between river and groundwater, and river ecosystems. Sediment transport studies have increasingly emphasized channel restoration and the quantification of environmental indices in response to natural or anthropogenic fine sediment pulses such as dam removal (Bednarek, 2001; Born et al., 1998; Cui et al., 2006; Cui & Wilcox, 2005; Doyle et al., 2003; Pollard & Reed, 2004; Stanley et al., 2002), dredge material disposal,

forest fires (Minshall et al., 2001; Vieira et al., 2004), watershed land use changes (Lisle, 1989; Swanson & Dyrness, 1975), and mining activities (Parker et al., 1996). Often, a large amount of fine sediment is flushed during dam removal operation, which is a standard practice to recover the reservoir capacity. Irrespective of the factors causing the fine sediment pulse, the infiltrated fine sediment results in the loss of the interstitial pore space in the gravel bed downstream. Therefore, predicting how the pore space varies in the gravel bed as a result of fine sediment infiltration could be of great importance in eco-hydraulic management and fine sediment budgeting.

While fine sediment might get infiltrated into the gravel bed through concurrent deposition of both fine sediment and coarse gravel. More often, fine sediment gets infiltrated into the static (immobile) gravel bed, especially in relatively low-flow conditions. The process of fine sediment infiltration into static gravel bed should be studied by distinguishing between two distinct infiltration processes, namely bridging and unimpeded static percolation, which result in loosely and densely packed gravel bed configurations, respectively. The distinction between bridging and unimpeded static percolation would be helpful to assess these processes, quantify their ecological impacts and accordingly take measures to prevent them. In bridging (or clogging) case, where fine sediment infiltrates only up to a limited depth, the majority of infiltrated fine sediment can be flushed by high flood events; thus, the gravel bed can be freed up from the infiltrated fine sediment. On the other hand, unimpeded static percolation results in deep entrainment of fine sediment. Hence, removing it from deeper layers of the gravel bed is difficult if not impossible. The schematic and experimentally observed unimpeded static percolation and bridging infiltration processes are shown in Figure 1 (Gibson et al., 2009). The process of fine sediment infiltration into static gravel bed has been intensively studied using physical experiments, theoretical and analytical models, and numerical simulations. However, the understanding of the process is still limited. Additionally, many contradicting observations were reported, as discussed in the following paragraphs.

One of the first studies on fine sediment infiltration into a static gravel bed, having a relatively shallow bed of thickness 1–2.7 times the coarsest gravel diameter, was conducted by Einstein (1968). Einstein observed the so-called unimpeded static percolation behaviour, where fine sediment first settles at the bottom of the gravel bed and gradually fills the interstices upwards. This behaviour was supported by other studies (Herrero et al., 2015; NCASI, 1981) and has also been documented in streams (Diplas & Parker, 1992; Evans & Wilcox, 2014; Lunt & Bridge, 2007). In contrast, the bridging (or clogging) type of infiltration process was observed (Beschta & Jackson, 1979; Carling, 1984; Frostick et al., 1984; Lisle, 1989; Schälchli, 1992), provided the gravel bed is thick enough. The bridging depth (or clogging depth) is approximately 2–5 times $d_{90,Gravel}$ (Beschta & Jackson, 1979; Diplas & Parker, 1992; Iseya & Ikeda, 1987). A stochastic model by Lauck (1991) reproduced both types of infiltration processes. His stochastic model is independent of how the fine sediment particles move downward within the gravel deposit framework (e.g., by gravity or intra-gravel flow), because lodging of the sediment particles is assumed solely a function of pore space geometry. With his model, he demonstrated that fine sediment fills the coarse sediment deposit from the bottom up when the size ratio of the bed material is large and the bed material is shallow. This was in support of observations that filling would occur from bottom to top onwards (unimpeded static percolation) if the gravel bed is shallow and fine sediment infiltrates only up to a finite depth (bridging or clogging) if the gravel bed is sufficiently thick. There is no clear specification in the literature regarding the gravel bed thickness, that is considered to be 'thick enough'. Here, we hypothesize (based on our results and previous research; discussed later on) that a gravel bed deeper than five times the coarsest gravel diameter can be considered as a thick bed.

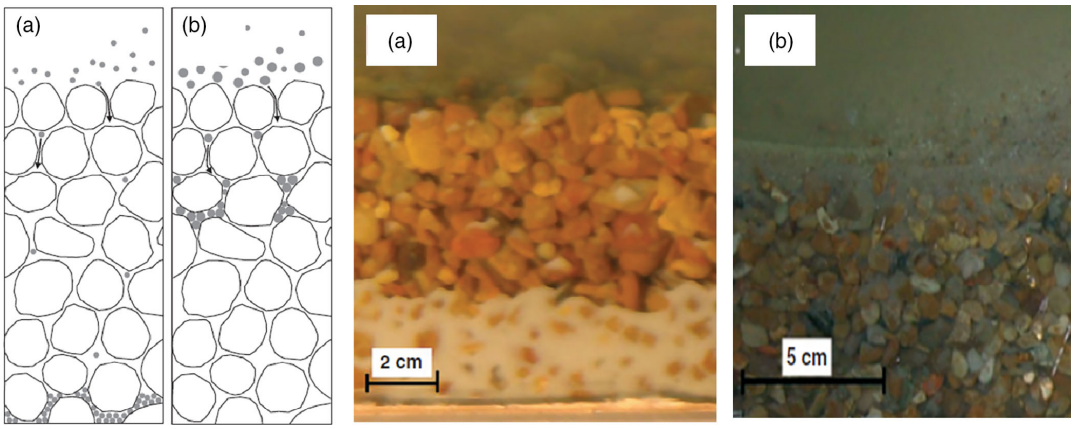

FIGURE 1 Schematic and experimentally observed (a) unimpeded static percolation and (b) bridging infiltration processes (Gibson et al., 2009). [Color figure can be viewed at wileyonlinelibrary.com]

Recently, Wooster et al. (2008) performed a set of flume experiments, where they observed only the bridging (or clogging) infiltration process into a static gravel bed, which was 8 times the coarsest gravel diameter deep (thick enough as per our hypothesis). They used different combinations of gravel and sand, whereby gravel ranged from 2 to 32 mm and sand had a geometric mean diameter of 0.35 mm and a standard deviation of 1.24. Cui et al. (2008) developed an analytical theory for the fine sediment infiltration into a static gravel bed and verified their theoretical model against experimental data from Wooster et al. (2008). They advocated that significant fine sediment infiltration occurs only up to a shallow depth (bridging or clogging behaviour), therefore fine sediment fraction follows an exponential decay function with the gravel bed depth. Interestingly, Gibson et al. (2009) observed both bridging and unimpeded static percolation behaviours within the same gravel bed, which was 10 times the coarsest gravel diameter deep (thick enough; thicker than the gravel bed considered in Wooster et al., 2008). This contradicts many previous observations, which claim that there will only be a bridging type of infiltration process, provided the gravel bed is thick enough. Gibson et al. (2009) related these two distinct infiltration processes to geotechnical filter theory. To quantify the gradation thresholds between these two processes, $d_{15,\text{Gravel}}$ is compared with $d_{85,\text{Fine Sediment}}$. For $d_{15,\text{Gravel}}/d_{85,\text{Fine Sediment}}$ ratios larger than 15.4, unimpeded static percolation, and for $d_{15,\text{Gravel}}/d_{85,\text{Fine Sediment}}$ ratios smaller than 10.6, bridging (or clogging) type of infiltration was observed. The size ratio for bridging (or clogging), observed in their experiment, is significantly higher than the theoretical and experimental geotechnical clogging criteria, which is normally 4–5. The standard filtering criteria used for filters in geotechnical engineering is thought by some to be a conservative design tool with inherent, undocumented safety factors (Kenney et al., 1985; Lone et al., 2005; Schuler & Brauns, 1993) and imprecise 'failure' criteria rather than theoretical process delineations. Sherard and Dunnigan (1989) put the process boundary at $d_{15,\text{Gravel}}/d_{85,\text{Fine Sediment}} = 9$, much closer to the boundary observed by Gibson et al. (2009). Due to the different particle size distributions (PSDs) of fine sediment and gravel used, different experimental setups and varying flow conditions in flume experiments, a straight-forward comparison is difficult. Claims have been made that only bridging type of infiltration occurs in nature (Beschta & Jackson, 1979; Carling, 1984; Cui et al., 2008; Frostick et al., 1984; Lisle, 1989; Schälchli, 1992; Wooster et al., 2008) and percolation is simply an artifact of shallow gravel bed (insufficiently thick gravel bed). Gibson et al. (2009) claim otherwise and advocate that bridging and unimpeded static percolation could occur within the same gravel deposit. Here, further studies should be done to solidify their observations and reach a unanimous conclusion concerning the occurrences of bridging and unimpeded static percolation.

More recently, a study by Huston (2014) used the litera ture-derived database to estimate the thresholds for bridging and unimpeded static percolation boundaries, combining 10 previously published studies, which included 146 data sets. They used median size ($d_{50,\text{Gravel}}$) and standard deviation (σ_{Gravel}) of gravel and median size ($d_{50,\text{Fine Sediment}}$) of fine sediment to represent bed-to-grain ratio. For $\frac{d_{50,\text{Gravel}}}{d_{50,\text{Fine Sediment}}\sigma_{\text{Gravel}}} > 27$ unimpeded static percolation and for $\frac{d_{50,\text{Gravel}}}{d_{50,\text{Fine Sediment}}\sigma_{\text{Gravel}}} < 27$ bridging behaviours were reported. The threshold suggested by Huston (2014) put the higher process boundaries than that of Gibson et al. (2009). Nevertheless, it is well-established and widely accepted that the size ratio of $d_{15,\text{Gravel}}/d_{85,\text{Fine Sediment}}$ remains the most reliable parameter to determine the process boundary (Honjo & Veneziano, 1989; Indraratna & Vafai, 1997; Sherard & Dunnigan, 1986), as the coarser portion of fine sediment and the finer portion of gravel are the important factors describing infiltration process (Indraratna & Locke, 1999). Huston (2014), based on regression analysis, suggested the bridging depth (or clogging depth) is positively correlated with gravel bed porosity and roughness Reynolds number, reflecting processes of gravity settling and turbulence-induced fluid pumping between gravel bed particles, respectively. On the other hand, Cui et al. (2008) suggested that the infiltration process is mainly gravity-dominated. Therefore, further investigation is necessary to conclude if gravity remains the most dominant factor governing the infiltration process.

Various theoretical and analytical packing models have also been developed and could be employed to understand the infiltration process. In this direction, theoretical models, originally developed to model interaction between base and filter materials in geotechnical engineering, introduced a term called 'controlling constriction size'. The controlling constriction size is defined as the largest base particle (fine sediment), which can pass through the filter (gravel bed). Considering the system of a binary mixture of spherical particles and the concept of controlling constriction size, the critical ratio of the entrance ($d_{\text{Fine Sediment}}/d_{\text{Gravel}}$) can be calculated based on idealized geometrical configurations. The theoretical critical ratio of entrance for dense (tetrahedra) and loose (cubic) packed beds are 0.154 and 0.414, respectively (Indraratna & Locke, 1999; Kenney et al., 1985). Some analytical packing models, mainly limited to binary and ternary mixtures of spherical particles, have also been developed (Yu et al., 1996). These models consider the geometrical packing limits to determine, how packing is formulated. The most popular packing models are linear and linear mixing packing models (Yu & Standish, 1991, 1993), where the critical ratio of the entrance is assumed to be 0.154, which corresponds to tetrahedral packing configuration. These analytical models are built upon the principle that for a given mono-sized particle assembly of spherical shape, there is an initial porosity ε_0 or initial specific volume $v_0 = 1/(1 - \varepsilon_0)$, which will decrease when particles of different sizes are added. With the addition of much smaller spheres, there is a regime of linear unmixing because the initial mono-sized particles retain their skeleton and simply have their gaps filled until the volume fraction of the added particles is sufficient to influence the skeleton. Alternatively, with the addition of marginally smaller particles, non-linear mixing occurs because the initial skeleton is disrupted to accommodate the additions. Modelling infiltration phenomena using these theoretical models, based on geometrical and analytical consideration, are indeed far from reality, but still could provide a fundamental basis for understanding infiltration mechanism. However, the infiltration process simulated with these models would still be lacking the effects of flowing water and turbulence, as these

models treat the system as a pure particle system. Here again, the question arises, to what extent these models can be applied to predict the infiltration process in fluvial deposits if it is hypothesized that fine sediment infiltration through intra-gravel flow is similar to fine sediment infiltration driven by gravity?

This hypothesis was first proposed by Cui et al. (2008). They developed an analytical theory to describe fine sediment infiltration into immobile gravel bed. The governing equations were derived from mass conservation with the assumption that fine sediment deposition per unit vertical distance into the deposit (trapping coefficient) is either constant or increases with fine sediment infiltration. The equations derived are similar to equations presented by Sakthivadivel and Einstein (1970), except for the equation for the trapping coefficient. Other than their claim that only bridging type of infiltration occurs in nature, they also hypothesized that fine sediment infiltration as a result of intra-gravel flow is similar to fine sediment infiltration driven by gravity. Similar assumptions were also made in Lauke's Stochastic model (Lauck, 1991), where the process is considered to be solely a function of pore space geometry, irrespective of how the fine sediment gets infiltrated into the gravel bed. Recently, a simple mathematical model (Herrero & Berni, 2016), based on Lauck's idea, could produce both bridging and unimpeded static percolation behaviours and verify Gibson et al.'s thresholds for their occurrences. However, this simple model also assumes the system to be a pure granular system and neglects the flowing water effects on the infiltration process. Further examination and validation are necessary to test the flowing water effects and Cui's hypothesis.

Modelling the mechanical behaviour of pure granular material using the discrete element method (DEM), first proposed by Cundall and Strack (1979), could also be adapted to simulate the infiltration processes. The DEM models can capture the realistic physical behaviour of particles, but consider the system to be pure granular media, that is, pure gravity-driven configuration. In this direction, Bui et al. (2019a, 2019b) have performed pure DEM simulations of the infiltration process, taking reference from the flume experiment conducted by Gibson et al. (2009). They were able to obtain quite good agreement with the experimental data, despite neglecting the effects of flowing water in their simulations. Although, it was not specifically mentioned in their papers, their observation has its roots in Cui's hypothesis. Nevertheless, the effects of flowing water on the infiltration process must be investigated to check the validity of the hypothesis. One can use computational fluid dynamics (CFD) to resolve the flow fields in greater detail and couple it with the DEM model to include the effect of flowing water. In this direction, we investigate the infiltration process by performing pure DEM and coupled CFD–DEM simulations. The coupled CFD–DEM method has various limitations concerning the number and the size of particles and is mainly categorized into two approaches, namely resolved and unresolved CFD–DEM. In the resolved approach, the fluid force acting on a particle can be calculated by integrating the fluid stress over the particle surface. For that purpose, a dense grid mesh is needed to obtain accurate fluid flow in CFD. Its applicability to particle-laden flow with a higher number of particles is limited due to the enormous computational cost. The unresolved method uses empirical models, based on the relative velocity and porosity, to calculate fluid–particle interaction forces. Therefore, a dense grid is not necessary to obtain the fluid-particle interaction forces. The unresolved method allows relatively high computational efficiency for bulk particle-laden flows. More information on the CFD–DEM methods can be found in papers (Bérard et al., 2020; Kloss et al., 2012; Zhou et al., 2010).

It is evident that many contradicting observations concerning the infiltration process were reported and the process is still not entirely understood. The different behaviours (e.g., bridging and percolation) in the infiltration process seem to be independent of gravel bed thickness, rather their occurrences only depend on the relative size of fine sediment and gravel; thus, eventually on the formed pore space geometry and its connectivity. Physical experiments of these complex systems generally lack detailed information and are often very expensive and time-consuming. Therefore, numerical simulations, based on the physics involved, could be of great importance in understanding the infiltration process and assessing its ecological impacts. One can use the median gravel size ($d_{50,Gravel}$) to simplify the system (Indraratna & Locke, 1999). These simplifications might be necessary to apply statistical, theoretical, analytical, and numerical models to study the infiltration process. We model the infiltration process using the CFD–DEM approach, considering theoretical packing thresholds of the binary mixture, representing bridging and unimpeded static percolation. With the help of numerical simulations, we mainly aim to answer following two questions: (1) Can bridging and unimpeded static percolation occur within the same gravel bed, and if their occurrences are independent of gravel bed thickness? (2) Comparing the coupled CFD–DEM simulations with pure DEM simulations for several size ratios, we aim to validate Cui's hypothesis (Cui et al., 2008), which suggests that fine sediment infiltration through intra-gravel flow is similar to fine sediment infiltration driven by gravity.

2 | METHODOLOGY

We investigated the infiltration process with the help of numerical modelling. Here, the mechanical behaviours of particles is incorporated by employing DEM and fluid flow is resolved using CFD approach. More specifically, we use the unresolved CFD–DEM approach to model the infiltration process, where flow fields are obtained by solving Reynolds Averaged Navier–Stokes (RANS) equations, and particles are treated as discrete entities and tracked using Newton's second law of motion. Compared to single-phase (fluid) systems, the presence of particles modifies the fluid flow field in the two-phase (fluid–particle) systems. The RANS equations are accordingly modified to include the effects of particle fraction on fluid flow fields by including porosity and fluid–particle interaction term in governing equations. The CFD–DEM method is computationally demanding and has several limitations in terms of the number and size of particles (Bérard et al., 2020; Kloss et al., 2012). With currently available computational resources and infrastructure, the maximum number of particles, which can be simulated with the applied unresolved

CFD–DEM method, even in large clusters, is in the order of 10^7. Furthermore, the unresolved CFD–DEM method cannot be applied for cases, where particle size is greater than the CFD cell size, thus hindering mesh refinement, especially near walls that might be necessary for certain turbulence-resolving techniques. This restricts us to resolve flow fields at a relatively coarser scale.

2.1 | Fluid phase

Fluid flow is resolved by solving modified Navier Stokes (NS) equations numerically, which include the effect of particle's presence on the flow fields by including porosity, and fluid–particle momentum exchange forces as an additional source term in governing equations (CFD equations). There are mainly two different formulations, describing the fluid flow in the presence of particles, namely model A and model B (or BFull), which are originally derived from a continuum description of the two-phase system (Bérard et al., 2020; Zhou et al., 2010). The main difference between these different formulations is related to their treatment of the fluid–particle interaction forces in continuum and discrete descriptions. We used model A, which is more popular and also implemented in commercial software such as FLUENT and CFX (Zhou et al., 2010). The modified NS equations for fluid flow, considering 'model A' formulation, are:

$$\rho_f\left[\frac{\partial \varepsilon_f}{\partial t}+\nabla.(\varepsilon_f \boldsymbol{u})\right]=0, \tag{1}$$

$$\rho_f \varepsilon_f\left[\frac{\partial \boldsymbol{u}}{\partial t}+\nabla.(\boldsymbol{u}\boldsymbol{u})\right]=-\varepsilon_f \nabla p-F^A_{pf}+\varepsilon_f \nabla.\tau+\rho_f \varepsilon_f \boldsymbol{g}, \tag{2}$$

where, ρ_f is fluid density, $\varepsilon_f=(1-\varepsilon_s)$ is porosity or volume fraction of fluid, ε_s is volume fraction of solid, u is the fluid flow velocity, p is fluid pressure, τ is fluid shear stress or deviatoric stress tensor, for Newtonian fluids $\tau=\mu\left[\nabla u+(\nabla u)^{-1}\right]-\frac{2}{3}\mu(\nabla.u)\delta_k$, g is acceleration due to gravity, F^A_{pf} is the fluid–particle interaction momentum exchange term, that includes drag force $f_{d,i}$ and other minor forces f_i'', if relevant in the system, such as virtual mass force f_{vm}, Basset force f_B, lift forces such as the Saffman force f_{saff}, and Magnus force f_{Mag}. One can see that pressure gradient and shear stress forces are not explicitly included in fluid–particle interaction term F^A_{pf}. Rather they are implicitly shared with the particle phase (solid phase), as seen in momentum equation where ∇p and $\nabla.\tau$ are multiplied by porosity. Therefore, the fluid–particle momentum exchange term can be written as:

$$F^A_{pf}=\frac{1}{\Delta V}\sum_{i=1}^{n}\left(f_{d,i}+f_i''\right). \tag{3}$$

2.2 | Particle phase

Particles are described as discrete entities and tracked using Newton's second law of motion (DEM equations). The CFD–DEM approach is quite different than traditional two-fluid method (TFM), especially concerning the treatment of fluid–particle interaction terms in the particle phase. In the CFD–DEM approach, one has to consider the coupling between DEM at the particle scale and CFD at the computational cell scale. Using the soft-sphere approach, originally proposed by Cundall and Strack (1979), the translational and rotational motion of particle i with mass m_i, and moment of Inertia I_i, can be written as:

$$m_i\frac{dv_i}{dt}=f^A_{pf,i}+\sum_{j=1}^{k_c}\left(f_{n,ij}+f_{t,ij}\right)+m_i g, \tag{4}$$

$$I_i\frac{d\omega_i}{dt}=\sum_{j=1}^{k_c}\left(M_{t,ij}+M_{r,ij}\right), \tag{5}$$

where v_i and ω_i are translational and angular velocities of the particle i, k_c is the number of particles in interaction with the particle i. The forces involved are: the particle–fluid interaction force $f^A_{pf,i}$, the gravitational force $m_i g$ and inter-particle forces, which include the normal particle–particle contact force $f_{n,ij}$ and tangential particle–particle contact force $f_{t,ij}$. The torque acting on particle i by particle j includes two components: $M_{t,ij}$, generated by tangential force and $M_{r,ij}$, commonly known as the rolling friction torque and caused by non-sphericity of particle (not included, as we consider spherical particles). The fluid–particle interaction term f^A_{pf}, similar to F^A_{pf} in the continuum description (fluid phase), is the sum of all fluid–particle interaction forces acting on individual particles by fluid flow, including drag force f_d, pressure gradient force $f_{\nabla p}$, viscous force $f_{\nabla.\tau}$ due to fluid shear stress or deviatoric stress, and other usually not so relevant forces f'', such as virtual mass force f_{vm}, Basset force f_B, lift forces such as the Saffman force f_{saff}, and Magnus force f_{Mag}. Usually buoyancy force is included in the pressure gradient force. Therefore, the total particle–fluid interaction force acting on particle i can be written as:

$$f^A_{pf,i}=f_{d,i}+f_{\nabla p,i}+f_{\nabla.\tau,i}+f_i''. \tag{6}$$

Compared to the fluid phase description in the model A formulation, where the interaction term only includes $f_{d,i}$ and f_i''. In the solid phase description, the fluid–particle interaction term includes all the forces that can possibly act on particles by moving fluid. The additional forces (pressure gradient and viscous forces) contributing to the interaction term for the solid phase is due to an additional term, namely solid stress tensor, other than the fluid–stress tensor shared between fluid and solid phase, that appears while deriving the continuum description for the solid phase.

2.3 | Fluid–particle interaction forces

The momentum exchange term in the CFD and DEM sides have different forces in contribution as per model formulation considered (model A or model B), briefly touched upon in Sections 2.1 and 2.2. Both formulations are theoretically equivalent and describe the same physics (Bérard et al., 2020). In the fluid–particle interaction term, the relative importance of different forces mainly depends on the density ratio (specific gravity) and fluid–particle system under consideration.

For dense and heavy particles, drag force (f_d) contributes at the most (Armenio & Fiorotto, 2001) and in some scenarios pressure gradient ($f_{\nabla p}$) and viscous forces ($f_{\nabla.\tau}$) become also important. Other minor forces f'' come into picture, only when considering light particles (Kuerten, 2016) and unsteady flow (Bérard et al., 2020). For the considered system involving sand and gravel in flowing water, other minor forces f''can be neglected. Therefore, drag, pressure gradient, and viscous forces are only considered in the fluid–particle interaction term. The general formulation of drag force on a single spherical particle is given by:

$$f_d = \frac{1}{2}\rho_f C_D A|u-v|(u-v), \tag{7}$$

where C_D is drag coefficient, A is area of sphere, and u and v are fluid and particle velocities, respectively. To characterize the drag force for multi-particle system, several models have been developed and nicely summarized in paper (Bérard et al., 2020). Initially, we tested several drag formulations for the considered case but they produced very similar results. Additionally, drag formulation of Koch and Hill (2001) seems to perform better for polydisperse particles and cover a broader range of Reynolds number. Considering this, we used the drag model developed by Koch and Hill (2001), which was implemented in following form:

$$f_d = f_0 + 0.5 f_1 \mathrm{Re}_p, \tag{8}$$

$$f_0 = \begin{cases} \dfrac{1+3\sqrt{\frac{\varepsilon_s}{2}}+\frac{135}{64}\varepsilon_s \ln\varepsilon_s + 16.14\varepsilon_s}{1+0.681\varepsilon_s - 8.48\varepsilon_s^2 + 8.16\varepsilon_s^3} & \text{for } \varepsilon_s < 0.4 \\ 10\dfrac{\varepsilon_s}{(1-\varepsilon_s)^3} & \text{for } \varepsilon_s > 0.4 \end{cases}, \tag{9}$$

$$f_1 = 0.0673 + 0.212\varepsilon_s + 0.0232/(1-\varepsilon_s)^5, \tag{10}$$

$$Re_p = \frac{\varepsilon_f d_p |u-v|}{\vartheta}, \tag{11}$$

where ε_s is the solid fraction, ε_f is the void fraction or porosity, u is the fluid velocity at the location of particle, v is the particle velocity, d_p is the particle diameter, and ϑ is the kinematic viscosity.

The forces due to pressure gradient and shear stresses are calculated using the following equations:

$$f_{\nabla p} = -V_p\left(\frac{\partial p}{\partial x}\right) = -\frac{1}{6}\pi d_p^3 \nabla P, \tag{12}$$

$$f_{\nabla.\tau} = V_p\left(\frac{\partial \tau_k}{\partial x_k}\right) = -\frac{1}{6}\pi d_p^3 \nabla.\tau. \tag{13}$$

2.4 | Particle–particle and particle–wall interaction forces

As shown in DEM equations, the particle's motion is due to the combined effects of gravity, fluid–particle interaction forces, and particle–particle contact forces. Particles' interaction with other particles (also with walls) is calculated based on the principle of the linear spring-dashpot model, usually known as the Hertz–Mindlin model (Johnson, 1987) shown in Figure 2. The total contact forces are calculated as the sum of the normal and tangential contact forces. The normal and tangential components of contact force are calculated based on the following equations:

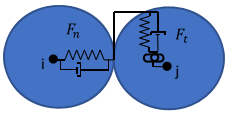

FIGURE 2 Simple spring-dashpot model. [Color figure can be viewed at wileyonlinelibrary.com]

$$f_n = -k_n\delta_n + c_n\Delta u_n, \tag{14}$$

$$f_t = \min\left\{\left|k_t\int_{tc,0}^{t}\Delta u_t dt + c_t\Delta u_t\right|, \mu f_n\right\}, \tag{15}$$

where Δu_n and Δu_t are the normal and tangential relative velocities of the particles in contact, respectively. k_n, k_t, c_n, and c_t are the normal and tangential spring and damping coefficients, which are functions of the overlap and depend on contact law implemented, either by linear or non-linear contact models, and δ_n is the normal overlap. The above formula also holds true for particle–wall contact. The integral term represents an incremental spring that stores energy from relative tangential motion, representing elastic tangential deformation of the particle surfaces that happened since the time when particle touched $t = t_{c,0}$. The second part, the dashpot, accounts for the energy dissipation of the tangential contact. The magnitude of the tangential force is truncated to fulfil the Coulomb friction limit with μ being the coefficient of friction, where the particles begin to slide over each other.

2.5 | Turbulence modelling

The CFD equations are presented in the form of full NS equations (Equations 1 and 2) modified for the two-phase systems. We used RANS equations to resolve the fluid flow fields. Due to Reynolds averaging, additional terms appear in momentum equations, called Reynolds stresses. The Reynolds stresses need to be calculated/modelled to close the RANS equations. One common approach is to calculate Reynolds stresses based on Boussinesq's hypotheses of eddy viscosity, which needs to be modelled. There are several models available to calculate the eddy viscosity, thus Reynolds stresses, such as kEpsilon, kOmega, kOmegaSST, and RNGkEpsilon, among many others. We have evaluated these turbulence models for our coupled CFD–DEM simulations in their ability to predict the flow and infiltration process.

It must be emphasized that the mathematical formulations of these turbulence models are developed based on studies on single

phase fluid flow and some works have noticed the potential failure of these turbulence models in specific flow scenarios (Gimenez et al., 2021). A straight-forward application of turbulence models, developed for single phase flow, to model two phase flow (fluid–particle) is probably not appropriate. However, new mathematical formulations for turbulence models considering the presence of particles are yet to be developed and do not come under the scope of this study.

2.6 | Numerical setup for pure DEM and coupled CFD–DEM simulations

All the simulations are performed with open-source CFD and DEM C ++ toolkits, namely OpenFOAM and LIGGGHTS, respectively. A separate CFDEM-Coupling code (Kloss et al., 2012) is deployed to couple the OpenFOAM and LIGGGHTS modules for coupled CFD–DEM simulations. The schematic of the applied unresolved CFD–DEM method is shown in Figure 3. The CFD (OpenFOAM) and DEM (LIGGGHTS) modules run sequentially and exchange data at a defined coupling interval. The DEM module initializes/updates the particle position, and the particle-related data such as diameter, position, and velocity are mapped onto CFD meshes. On the CFD side, fluid–particle interaction forces and porosity are calculated and averaged (volumetric) over each cell. Including the effects of fluid–particle interaction forces and porosity, NS equations are solved numerically. Newly obtained CFD flow fields such as velocity and pressure are transferred to the DEM side, where the new position and velocity of particles are calculated. This procedure is repeated till the specified run time.

Reference flume experiment (Gibson et al., 2009) was numerically simulated with the assumption that fine sediment and coarse gravel can be represented by spherical mono-size particles, representing a system of a binary mixture. Although due to this assumption, our simulations would not represent the exact gravel bed, void connectivity, and fine sediment infiltration as that of the original experiment. Yet, it should be able to provide enough information concerning the infiltration process and research questions, we aim to answer, as the assumptions made would not change involved physics. The geometry, particle and flow characteristics for pure DEM and coupled CFD–DEM simulations are summarized in Table 1. Flow conditions correspond to turbulent and subcritical flow, as Reynolds number and Froude number are (based on free surface velocity and water depth) 94,500 and 0.6, respectively. Three different size ratios of 0.154, 0.231, and 0.414 are chosen for both pure DEM and coupled CFD–DEM simulations. While size ratios of 0.154 and 0.414 correspond to tetrahedral (dense packing) and cubical (loose packing) geometrical packing configurations, respectively. The size ratio of 0.231 would represent a combination of both types of geometrical packing configurations. Median gravel size ($d_{50,\text{Gravel}} = 8$ mm) is chosen to represent the coarse gravel bed, and corresponding fine sediment size is calculated as 1.232, 1.848, and 3.312 mm for the size ratios of 0.154, 0.231, and 0.414, respectively. For our coupled CFD–DEM simulations, within the limitations of the unresolved CFD–DEM method, we obtain the open channel velocity profile (OCF) without resolving the interphase between air and water. The OCF is approximated using the symmetry boundary condition applied at the top boundary. This is a common CFD approach to model open channel flow without considering the air phase into the system.

The two main limitations of the unresolved CFD–DEM method, mentioned before, namely the number and size of particles, restricted us to resolve flow fields at relatively coarse scales (coarser than particle size) and also to reduce the domain size, which is significantly

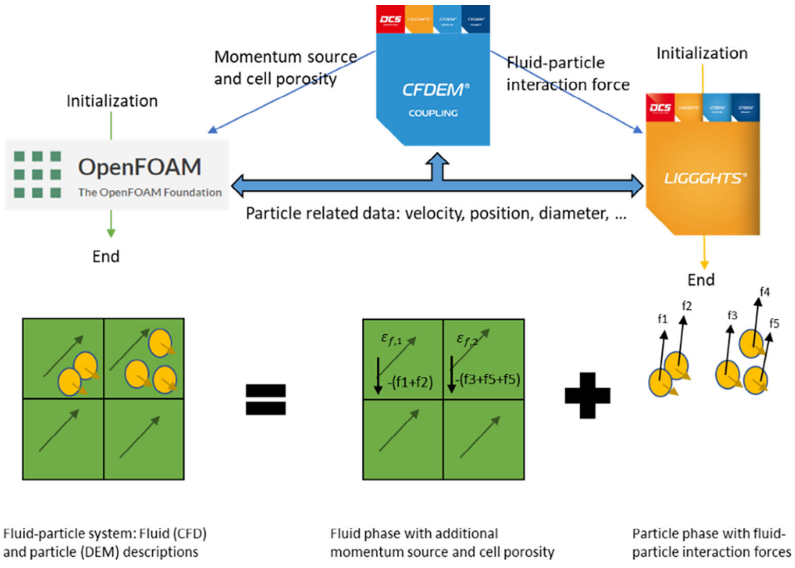

FIGURE 3 Schematic of unresolved CFD–DEM method implemented using OpenFOAM, LIGGGHTS and CFDEM-coupling modules. CFD, computational fluid dynamics; DEM, discrete element method. [Color figure can be viewed at wileyonlinelibrary.com]

TABLE 1 Geometry, particle and fluid flow characteristics for pure DEM and coupled CFD–DEM simulations.

	Coupled CFD–DEM simulations	Pure DEM simulations
Geometry	Gravel bed length = 0.15 m	Gravel bed length = 0.15 m
	Gravel bed width = 0.075 m	Gravel bed width = 0.075 m
	Gravel bed height = 0.1 m	Gravel bed height = 0.1 m
	Inlet channel length = 0.2 m	Simulation box = 0.15 × 0.2 × 0.075 m
	Channel width = 0.075 m	
	Outlet channel length = 0.05 m	
	Channel height (top boundary) = 0.14 m	
	Simulation box = 0.4 × 0.26 × 0.075 m	
Particle (gravel and sand)	Young's modulus = 5×10^6 N/m^2	Young's modulus = 5×10^6 N/m^2
	Density = 2,700 kg/m^3	Density = 2,700 kg/m^3
	Poisson's ratio = 0.45	Poisson's ratio = 0.45
	Coefficient of restitution = 0.4	Coefficient of restitution = 0.4
	Coefficient of friction = 0.5	Coefficient of friction = 0.5
	Gravel diameter = 8 mm	Gravel diameter = 8 mm
	Sand diameter = 1.232, 1.848 and 3.312 mm	Sand diameter = 1.232, 1.848 and 3.312 mm
Fluid (water)	Mean flow velocity = 0.675 m/s	-
	Density = 1,000 kg/m^3	
	Kinematic viscosity = 1×10^{-6} m^2/s	
	Reynolds number = 94,500	
	Froude number = 0.6	

smaller than the actual flume experiment. The original flume experiment, adopted for our numerical simulations, was conducted in a 26 m long and 0.9 m wide flume, which would contain a much greater number of particles than the method's limitation concerning the maximum number of particles ($O \sim 10^7$). To overcome these limitations, we consider a reduced domain, which is 0.4 m long and 0.075 m wide for coupled CFD–DEM simulations, and 0.15 m long and 0.075 m wide for pure DEM simulations. In addition to the gravel bed region of the domain, extended inlet and outlet channels are provided in coupled CFD–DEM simulations to ensure that the flow is fully developed, before it reaches the gravel bed region. The extended inlet channel also serves the purpose of providing extra space required behind the insertion plane to generate and inject fine sediment. Although, reduced domain (length- and width-wise) is considered for numerical simulations, we keep the same gravel bed height (0.1 m) and water depth (0.14 m) as that of the original experiment. Different CFD mesh resolutions in the gravel bed and channel regions of the domain are used, ensuring that the particles are smaller than the CFD cell size in each part of the domain. In the channel section, much finer CFD mesh resolutions could be provided, as only fine sediment gets transported in this region of the domain, allowing us to resolve flow in much greater detail in the channel section. It must be noted that both pure DEM and coupled CFD–DEM simulations have the same size of the gravel bed region of a length of 0.15 m, a width of 0.075 m, and a height of 0.1 m. To inject fine sediment, an insertion plane is used, which injects fine sediment at a specified mass flow rate for a specified duration. The insertion plane is located at 0.15 m downstream of the inlet because the desired insertion rate required some volume behind the insertion plane to generate and inject fine sediment. Due to the recirculation of flow and sediment from the outlet back to the inlet, and symmetry boundary conditions provided at the front and back planes, the effect of reduced domain size should vanish, and realistic flow and sediment transport in numerical simulations are expected, even with the reduced domain size. It must be emphasized that for pure DEM simulations, we have only considered the gravel bed region, and the fine sediment insertion plane is located above the gravel bed. Whereas, for coupled CFD–DEM simulations, the water flow enters through the inlet and fine sediment with desired mass flux is injected with an insertion plane located 0.15 m downstream of the inlet. Flow and fine sediment mass flux are linearly reduced for considered width of 0.075 m, which ensures that fine sediment and water flow are introduced at the same rate as that of the original experiment. The schematic diagram of the considered domain, with dimensions and boundary conditions, is shown in Figure 4.

Firstly, pure DEM simulations are performed for the size ratios of 0.154, 0.231, and 0.414. Pure DEM simulations would represent the infiltration process neglecting the flowing water effects. Keeping the same particle phase (DEM settings), the cases for each size ratio are modified to include the water flow and simulated with coupled CFD–DEM approach. All the simulations are performed with

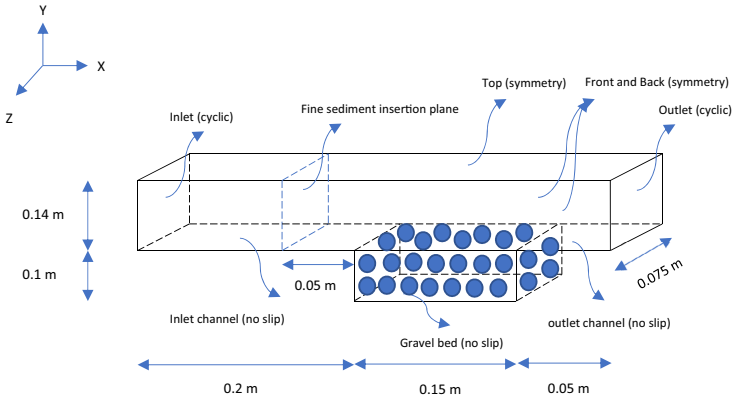

FIGURE 4 Domain considered with provided boundary conditions. [Color figure can be viewed at wileyonlinelibrary.com]

224 processors (28-way Intel Haswell-based nodes and FDR14 Infiniband interconnect, 64 GB RAM per node) in a Linux cluster. For both pure DEM and coupled CFD–DEM simulations, the initial gravel bed is created with an initial bulk porosity of 0.454 by pouring gravel particles in the gravel bed region and then fine sediment is inserted at a specified mass flow rate with water flow (for coupled CFD–DEM simulations) or without the water (for pure DEM simulations). The selection of the initial porosity of the created mono-sized gravel bed is in accordance with previous pure DEM simulations (Bui et al., 2019a) and recommendations provided in the review paper (Latham et al., 2002). The mean water flow velocity of 0.675 m/s, the same as that of the original flume experiment, is provided and recirculated (cyclic boundary condition at the inlet and outlet). In the coupled CFD–DEM simulations, the extended inlet and outlet channels ensure fully developed turbulent flow at the inlet, and recirculation of flow and sediment as well. This also allowed us to dampen off the effects of reducing the domain size, as a reduced domain with recirculation would be equivalent to a sufficiently long flume (ideally infinite length).

Usually, DEM time steps are much smaller than CFD time steps to ensure stable solutions and realistic particle behaviour. Whereas, the stability on the CFD side is ensured by the Courant number criteria. On the DEM side, it rather depends on Rayleigh and Hertz time criteria. The DEM time step needs to be chosen sufficiently small to capture the phenomenon of energy transmission through wave propagation. Generally, it is sufficient to assume that all the energy is transmitted through Rayleigh waves. Hertz time step ensures that particles remain in contact sufficiently long enough to detect proper interaction among them. The Rayleigh and Hertz times depend on particle characteristics and materialistic properties. The DEM timestep is usually within 10%–20% of these times. The DEM and CFD time steps are selected following these criteria. The coupling interval is then calculated as the ratio of the CFD time step to the DEM time step. The CFD and DEM modules run sequentially and transfer data at defined coupling intervals. The simulation run times are 100 s for pure DEM simulations and the coupled CFD–DEM simulations are run till, either

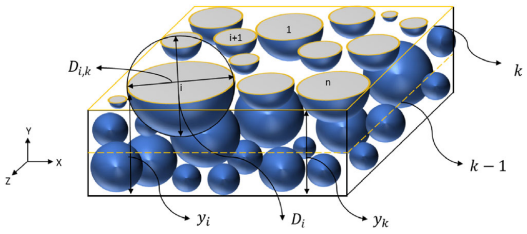

FIGURE 5 3D packing and circles generated cutting the packing by plane located at $y_{k.}$ [Color figure can be viewed at wileyonlinelibrary.com]

the gravel bed is completely filled or fine sediment got trapped in the bed, obstructing further infiltration. Fine sediment is inserted at the mass flow rate of 0.01 kg/s for 80 s in pure DEM simulations and for 100 s in coupled CFD–DEM simulations, in total injecting 0.8 and 1 kg of fine sediment for pure DEM and coupled CFD–DEM simulations, respectively.

3 | RESULTS

To evaluate porosity and fine sediment fraction profiles along the depth of the gravel bed, a Matlab code has been written (Equations 16–19). The simulation results contain the 3-D packing information (demonstrated in Figure 5), such as the position and diameter of infiltrated fine sediment and gravel particles. The 3-D packing is cut at several planes across the depth (100 such planes have been generated for the results presented here), generating circles of different diameters at each cutting plane. With 100 planes cutting over 10 cm gravel bed depth, data are obtained for every 1 mm (smaller than the smallest particle in the system) from top to bottom of the bed. The area of generated circles is summed up at each cutting plane, representing the area of the solid fraction at the cutting plane.

Porosity (n) at the cut plane is calculated as the area of void divided by the total area (solid and void areas). The fine sediment fraction (f_s) at the cut plane is calculated as the area of fine sediment particles divided by the area of fine sediment and gravel particles. Although, our calculation of porosity and fine sediment fraction is based on the area instead of volume ratios, it represents the porosity and fine sediment fraction at each cut plane and would be required to evaluate, how the porosity and fine sediment fraction varies along the depth of the gravel bed.

$$D_{i,k} = \sqrt{D_i^2 - 4(y_k - y_i)^2} \; if \; y_i - \frac{D_i}{2} \le y_k < y_i + \frac{D_i}{2}, \tag{16}$$

$$A_{i,k} = \frac{\pi D_{i,k}^2}{4}, \tag{17}$$

$$n = \frac{A_k - \left\{(\sum A_{i,k})_{\text{small}} + (\sum A_{i,k})_{\text{large}}\right\}}{A_k}, \tag{18}$$

$$f_s = \frac{(\sum A_{i,k})_{\text{small}}}{(\sum A_{i,k})_{\text{small}} + (\sum A_{i,k})_{\text{large}}}. \tag{19}$$

3.1 | Pure DEM simulations

By assuming that the process of fine sediment infiltration into static gravel bed can be described by a binary system of mono-sized spherical particles, theoretical packing limits based on different geometrical packing configurations are considered. The initial gravel bed and final infiltration state for the different size ratios after 100 s of simulation run time are shown in Figure 6. The size ratio of 0.154, which ideally represents the tetrahedral packing configuration, results in a densely filled gravel bed. As expected for the size ratio of 0.154, fine sediment first settles at the bottom of the bed, and then filling occurs from bottom to top onwards, a so-called unimpeded static percolation is observed. For the size ratio of 0.414, which ideally represents cubical packing configuration, a so-called bridging behaviour is found, where fine sediment particles get clogged just below the gravel bed surface, precluding subsequent infiltration. A mixed behaviour is observed for the size ratio of 0.231, where some fine sediment particles are clogged in the gravel bed and some could reach the bottom of the gravel bed, representing simultaneous occurrence of both bridging and percolation infiltration processes. Fine sediment could also infiltrate to the bottom of the gravel bed for the size ratio of 0.231, but it generates a relatively less densely packed gravel bed, as compared to the size ratio of 0.154. The bulk porosity of the initially created gravel bed is 0.454 and it is reduced to 0.2166, 0.2879, and 0.4158 for size ratios 0.154, 0.231, and 0.414 after the infiltration process, respectively.

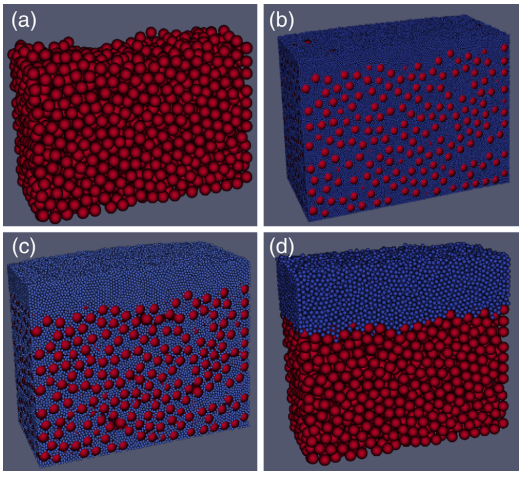

FIGURE 6 Initial gravel bed (a) and pure DEM simulated infiltration state at the end of simulation for size ratios of (b) 0.154, (c) 0.231 and (d) 0.414. DEM, discrete element method. [Color figure can be viewed at wileyonlinelibrary.com]

Figure 7 shows the detailed porosity (Figure 7a) and fine sediment fraction (Figure 7b) profiles along the gravel bed depth. One can see that a significant reduction in porosity is predicted for size ratios of 0.154 and 0.231. This reduction in porosity is almost uniform from the bottom to the top of the gravel bed, as fine sediment could infiltrate till the bottom of the gravel bed and filling could occur from bottom to top onwards. In contrast to this, the reduction in porosity is limited to the first 2 cm of the gravel bed for the size ratio of 0.414. After this depth, which is equivalent to 2.5 times the gravel diameter, no change in porosity is found. Fine sediment fraction profiles also support these behaviours for different size ratios. It can be seen that fine sediment first settles at the bottom and fills the voids upwards, for a size ratio of 0.154 and more or less for a size ratio of 0.231 as well. For a size ratio of 0.414, a bridging behaviour is observed and no fine sediment particle is found below 2 cm of the gravel bed surface. For the bridging case (size ratio 0.414), the maximum depth to which fine sediment could infiltrate is found to be ~2.5 times the gravel diameter, which aligns with the previously observed bridging depth (Beschta & Jackson, 1979; Diplas & Parker, 1992; Iseya & Ikeda, 1987). Small fluctuations in fine sediment fraction and porosity profile plots, along the gravel bed, might be due to our approach of considering porosity and fine sediment fraction as area average values, although porosity and fine sediment fraction are volume-based quantities. These fluctuations are more predominant at the bottom of the gravel bed, which might be due to wall effects and wall–particle interactions.

From Figures 6 and 7, it is also evident that different infiltration processes such as bridging, unimpeded static percolation, or a combination of both processes, could occur with the same gravel bed. In contrast to the consensus in the field, this observation suggests that the occurrences of bridging and percolation behaviours are independent of gravel bed thickness. We emphasize again that the gravel bed should be sufficiently thick enough to distinguish between these two different infiltration processes. It is still an open question: what depth of gravel bed is considered to be thick enough? Our hypothesized definition of a 'thick enough' gravel bed (thickness >5 times the coarsest gravel diameter) is reasonable and sufficient to distinguish between

these infiltration processes. The bridging depth is 2–5 times the $d_{90,Gravel}$, therefore the gravel bed needs to be thicker than this to make a distinction between different infiltration processes. Closely observing the porosity and fine sediment fraction profiles, one can see that if the depth of the gravel bed was less than the bridging depth (in our case, 2 cm or 2.5 times gravel diameter), one would have misinterpreted the bridging as a percolation process. Fine sediment could easily infiltrate till the bridging depth and one needs a thicker gravel bed to clearly see if further fine sediment infiltration beyond the bridging depth occurs or not. Although, our hypothesis seems reasonable, it is based on previously observed bridging depth (Beschta & Jackson, 1979; Diplas & Parker, 1992; Iseya & Ikeda, 1987) and our simulations on the simple case of constant bed thickness and mono-size spherical particles for gravel and fine sediment. A more thorough investigation might be necessary, where the bed size, a wide range of gravel and fine sediment, and non-sphericity should be considered, before our hypothesized definition of a 'thick enough' gravel bed is standardized.

3.2 | CFD–DEM simulations

To model the infiltration process with the coupled CFD–DEM approach, numerical simulations are performed in two stages. In the first stage, pure DEM simulations are performed to create the gravel bed with pre-defined porosity. In the second stage, CFD–DEM coupling is activated, where fine sediment particles are injected from the insertion plane at a desired mass flow rate and recirculated from the outlet to the inlet along with water flow. The simulation run times and required CPU times are summarized in Table 2, comparing them with their pure DEM counterparts. For smaller size ratios, it takes longer CPU time to reach the equilibrium infiltration state or steady-state condition (fine sediment is either clogged or has completely filled the gravel bed). The simulations for smaller size ratios are slower due to the increase in complexity and the number of calculations required, as a greater number of particles are required to represent the same mass for smaller size ratios. The CPU time increases several folds (at least ~6 times) with the inclusion of flowing water (CFD–DEM simulations). The coupled CFD–DEM simulations for larger size ratios are run for a longer duration, as they were relatively faster than that of smaller size ratios. The additional time required for coupled CFD–DEM simulations is due to extra computational effort in resolving fluid flow and the complexity associated with it.

The initial gravel bed and final infiltration states for different size ratios at the end of the simulation can be seen in Figure 8. The Infiltration processes simulated with the coupled CFD–DEM approach appear to be quite similar to their pure DEM counterparts. For the size ratio of 0.154, fine sediment first settles at the bottom of

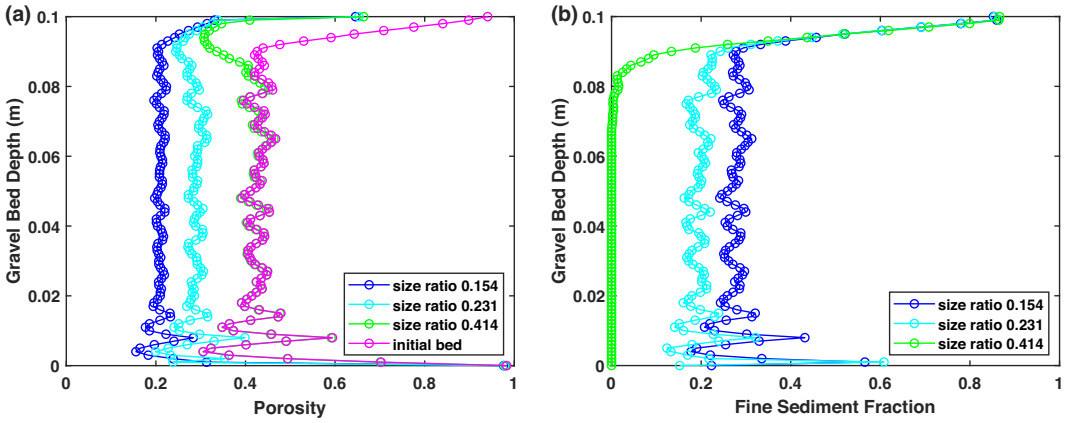

FIGURE 7 Variation of (a) porosity and (b) fine sediment fraction along the depth of gravel bed for different size ratios at the end of infiltration processes. [Color figure can be viewed at wileyonlinelibrary.com]

TABLE 2 Simulation run time and CPU time (or process time) for pure DEM and coupled CFD–DEM simulations.

	Pure DEM simulation		Coupled CFD–DEM simulation	
Size ratio	Simulation run time (in seconds)	CPU time (in hours)	Simulation run time (in seconds)	CPU time (in hours)
0.154	100	8.89	176	96
0.231	100	3.36	195	48
0.414	100	0.98	200	13.5

Abbreviations: CFD, computational fluid dynamics; DEM, discrete element method; CPU, central processing unit.

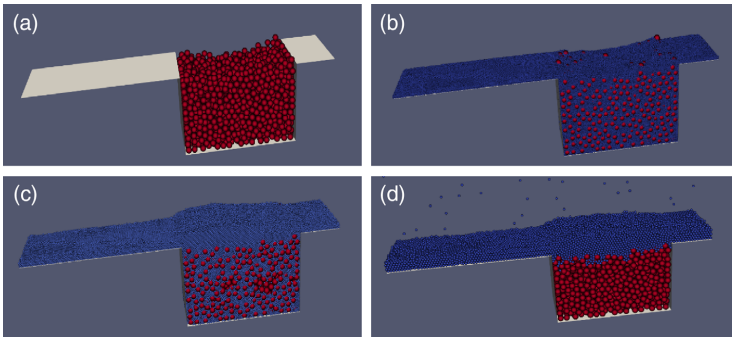

FIGURE 8 (a) Initial bed and coupled CFD–DEM simulated infiltration state at the end of simulation for size ratios (b) 0.154, (c) 0.231 and (d) 0.414. CFD, computational fluid dynamics; DEM, discrete element method. [Color figure can be viewed at wileyonlinelibrary.com]

TABLE 3 Initial and final porosity (after infiltration) for different size ratios.

Size ratio	Gravel diameter (mm)	Fine sediment diameter (mm)	Initial porosity	Final porosity	
				Pure DEM simulation	Coupled CFD–DEM simulation
0.154	8	1.232	0.454	0.2166	0.2238
0.231	8	1.848	0.454	0.2879	0.2866
0.414	8	3.312	0.454	0.4158	0.4155

Abbreviations: CFD, computational fluid dynamics; DEM, discrete element method.

the gravel bed and fills the voids from bottom to top onwards, representing the unimpeded static percolation. For the size ratio of 0.414, fine sediment gets clogged just below the surface layer of the gravel bed, representing the bridging infiltration process. For the size ratio of 0.231, a combination of both types of infiltration processes is observed. The coupled CFD–DEM and pure DEM simulations, for all size ratios, predict similar infiltration processes and final infiltration states as well. The initial and final (after infiltration) bulk porosity of the gravel bed for coupled CFD–DEM simulations and pure DEM simulations are shown in Table 3. The final porosities of the gravel bed for coupled CFD–DEM simulations are 0.2238, 0.2866, and 0.4155 for size ratios of 0.154, 0.231, and 0.414, respectively. For smaller size ratios (0.154 and 0.231), very dense packing is generated and a significant reduction in porosity is predicted. This reduction in porosity is almost uniform along the depth of the gravel bed. On the other hand, for a higher size ratio (0.414), fine sediment gets clogged in the top surface layer below the gravel bed and an overall decrease in porosity is marginal. The final porosity values simulated with coupled CFD–DEM approach, for each size ratio, are in a similar range as that of final porosities simulated with pure DEM approach (see Table 3). The difference in simulated final porosity values for coupled CFD–DEM and pure DEM simulations are marginal and only 3%, 0.4%, and 0.07% for size ratios 0.154, 0.231, and 0.414, respectively. This demonstrates that fine sediment infiltration into static gravel bed seems to be independent of the factor causing the infiltration process, that is, fine sediment infiltration process is gravity-dominated.

The predicted bridging depth for coupled CFD–DEM simulation (bridging case; size ratio 0.414) is also 2 cm (or 2.5 times the gravel diameter), exactly the same as predicted in pure DEM simulation. For the bridging case (size ratio 0.414), fine sediment could only infiltrate 2 cm in the gravel bed and this is true for both pure DEM and coupled CFD–DEM simulations. Predicting the same bridging depth, irrespective of the factor causing the infiltration process, again solidifies our observation that the infiltration process in fluvial deposits is gravity-dominated. Similar to pure DEM simulation, small fluctuations are also observed in the detailed porosity and fine sediment fraction profiles of our coupled CFD–DEM simulations. The probable reason for this fluctuating behaviour is already discussed in our previous pure DEM section.

The coupled CFD–DEM simulated porosity and fine sediment fraction profile plots for different size ratios, along with their pure DEM counterpart, can be seen in Figure 9. Figure 9a,c,e compare the coupled CFD–DEM simulated and pure DEM simulated porosity profiles for the size ratios of 0.154, 0.231, and 0.414, respectively. Figure 9b,d,f compare the coupled CFD–DEM simulated and pure DEM simulated fine sediment fraction profiles for the size ratios of 0.154, 0.231, and 0.414, respectively. It must be emphasized that the initial gravel beds used in pure DEM and coupled CFD–DEM simulations are not entirely the same and have a marginal variation in porosity and void connectivity, which can be seen in the initial porosity profile plots of the created gravel bed. This small difference in the initial gravel bed might be due to different wall treatments in pure DEM and coupled CFD–DEM simulations and consequently their effects on overall packing. To prepare the complex geometry in the coupled CFD–DEM simulation, STL files are considered as walls. Whereas, in pure DEM simulations simple rectangular box is considered by

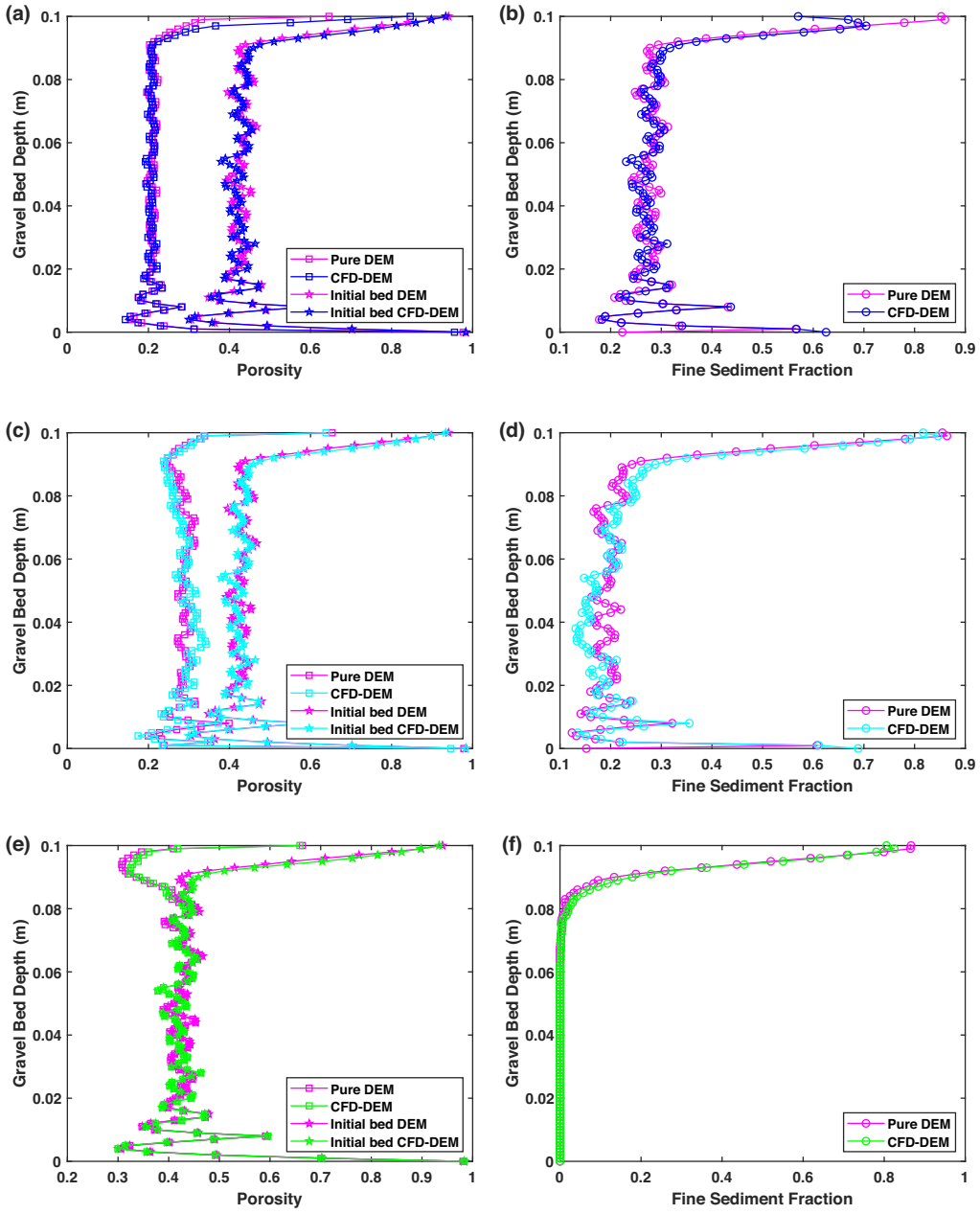

FIGURE 9 Comparison of coupled CFD–DEM simulated and pure DEM simulated infiltration processes in terms of porosity and fine sediment fraction for different size ratios. CFD, computational fluid dynamics; DEM, discrete element method. [Color figure can be viewed at wileyonlinelibrary.com]

treating planes as walls (no STL files). Additionally, the packing process is stochastic and might lead to small differences in created initial gravel beds, each time they are generated. Due to the marginal difference in the created initial gravel bed, a small difference in coupled CFD–DEM and pure DEM simulated final infiltration state is expected but the bulk behaviours of the infiltration process should

not change. For the size ratio of 0.154 unimpeded static percolation, for the size ratio of 0.414 bridging, and for the size ratio of 0.231 a combination of both infiltration processes is observed and these behaviours are consistent for pure DEM and coupled CFD–DEM simulations. For the unimpeded static percolation case (size ratio 0.154), fine sediment first settles at the bottom and filling occurs from bottom to top onwards. For the bridging case (size ratio 0.414), fine sediment gets clogged near the bed surface and the maximum depth, they could infiltrate, is 2 cm, which is equivalent to 2.5 times of gravel diameter. The bridging depth of 2.5 times the gravel diameter aligns with the previous observations (Beschta & Jackson, 1979; Diplas & Parker, 1992; Iseya & Ikeda, 1987). As discussed in our pure DEM section, the gravel bed depth must be thicker than the bridging depth (usually 2–5 times $d_{90,Gravel}$), so that the different infiltration processes can be distinguished. Although, our hypothesized definition of 'thick enough' gravel bed seems reasonable and logical, a more thorough investigation using numerical simulations and flume experiments might be necessary, where gravel bed depth, a wide range of gravel and fine sediment and non-sphericity of particles should also be addressed, before our hypothesized definition of 'thick enough' gravel bed is standardized.

3.3 | Effect of turbulence models on the infiltration process

We evaluate four different turbulence models, namely the kEpsilon, kOmega, RNGkEpsilon, and kOmegaSST model, in their ability to predict physical and realistic flow and infiltration process. For this purpose, we only consider the size ratio of 0.154 (unimpeded static percolation case). The streamwise mean (RANS resolved) and fluctuating velocity (modelled) profiles of water flow at the inlet, and porosity and fine sediment fraction profiles in the gravel bed region, for these turbulence models, are compared and summarized in Figure 10. It

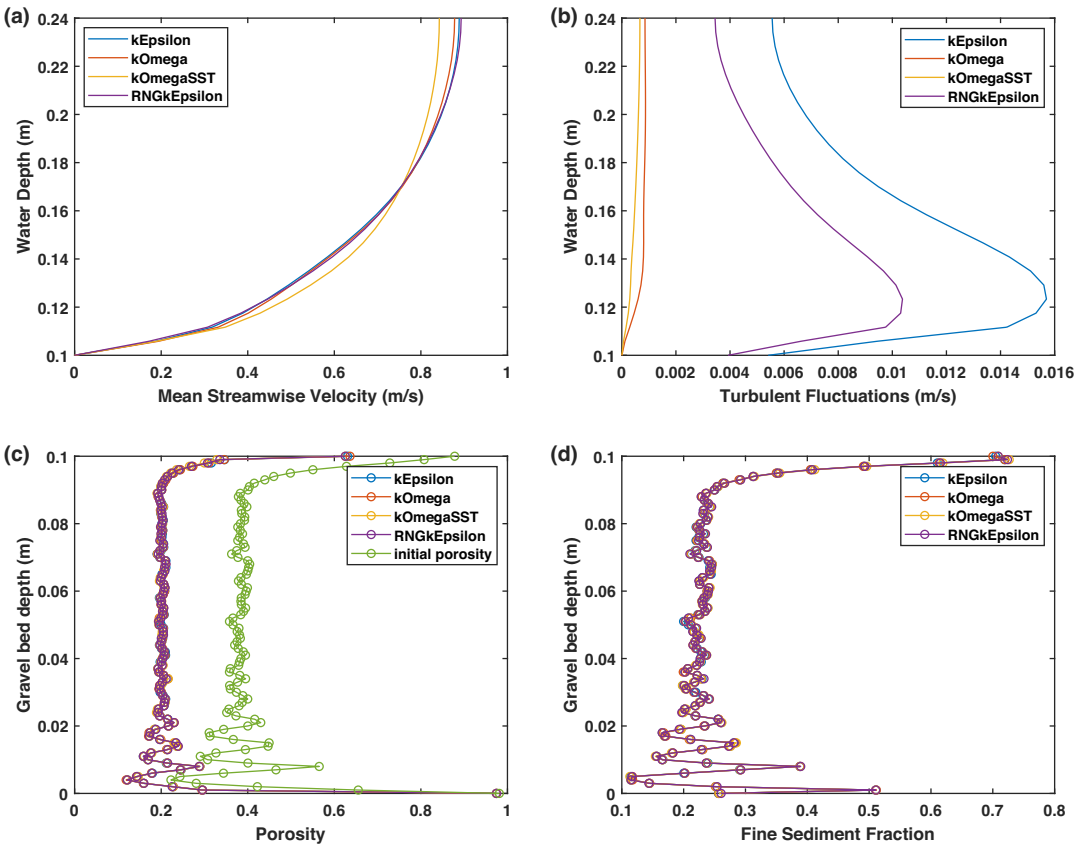

FIGURE 10 Comparison of RANS turbulence models in predicting (a) mean fluid velocity, (b) turbulent fluctuating velocity, (c) porosity and (d) fine sediment fraction profiles along the gravel bed depth. RANS, Reynolds Averaged Navier–Stokes. [Color figure can be viewed at wileyonlinelibrary.com]

must be emphasized that RANS resolves only up to mean flow statistics and the turbulent fluctuations are modelled using turbulence models by assuming the turbulence is isotropic in the whole domain. Turbulent fluctuations are simply calculated from modelled turbulent kinetic energy (k) as $u' = \sqrt{2k/3}$. Unfortunately, there were no detailed velocity profiles (both for mean flow and turbulent fluctuations) measured in the reference experiment. However, qualitative observation of the velocity profiles reveals that, all the RANS turbulence models, considered, are able to predict realistic mean fluid velocity profiles (Figure 10a). Omega-based models predict small and physically realistic turbulent fluctuations, whereas Epsilon-based models predict large turbulent fluctuations (Figure 10b). As seen in Figure 10c,d, there is hardly any difference in predicted final porosity and fine sediment fraction profiles, for the turbulence models considered. It can be seen that the final porosity and fine sediment fraction profiles, for all the turbulence models, are overlapping. This is due to the fact that only mean flow statistics are used to calculate fluid's effect on particle motion. As long as the mean flow fields are accurately captured by the turbulence model used, similar infiltration processes will be predicted irrespective of the turbulence model. However, this approach can only be applied for low-flow conditions, where the gravel bed remains static and fine sediment simply get transported over the gravel bed. The comparison of our pure DEM and coupled CFD–DEM simulations, for different size ratios considered, advocates that the process of fine sediment infiltration into static gravel bed is mainly gravity-dominated. Therefore, one may simply neglect the effect of turbulent fluctuations on the infiltration process. In high-flow conditions, to predict accurate and physically realistic sediment transport, a proper evaluation of turbulence fluctuations might be important and should be included by some additional models such as Stochastic dispersion models (Minier et al., 2014). Our results on different turbulence models demonstrate that for the low-flow conditions, where the process of fine sediment infiltration into the immobile gravel bed seems to be gravity-dominated, any of the turbulence models can be applied as long as it is able to capture mean flow statistics properly.

From Figure 10c,d, it can be seen that large predictions of turbulent fluctuations are not propagated to the infiltration process. Final porosity and fine sediment fraction profiles are overlapping for all the turbulence models considered. In the unresolved CFD–DEM method, the forces acting on particles, due to fluid flow, are calculated using empirical equations, mostly based on mean flow statistics. In a broader sense, the information on the fluid velocity at the particle's position (fluid velocity seen by particles) is used to calculate fluid–particle interaction forces (see Section 2.3). The more precisely flow fields are resolved, the more accurate estimation of the interaction forces is expected, thus more physical particle's trajectory is predicted. For example, direct numerical simulation (DNS) and large-eddy simulation (LES) in conjunction with DEM could be alternative approaches. As DNS and LES resolve flow beyond mean flow fields and eventually would result in a more accurate estimation of fluid–particle interaction terms. The DNS–DEM or LES–DEM is mostly not possible, especially for particles larger than typically resolved flow fields (Jaiswal et al., 2022). One has to compromise with the coarsely resolved flow fields, such as mean flow fields, resolved with the RANS approach, especially dealing with large particles such as gravel and sand. The RANS–DEM approach neglects the effects of turbulent fluctuations on the particle's trajectory and additional dispersion models would be required to recover the lost turbulent fluctuations due to RANS averaging (Bocksell & Loth, 2006; Jaiswal et al., 2022; Loth, 2000; Minier et al., 2014). However, the inclusion of the dispersion model should be decided based on the process under consideration and might not be necessary. It might be sufficient to include only mean flow statistics, yet able to capture realistic particle behaviour in a turbulent flow. In many physical processes, especially disperse-particle flow, it might be necessary to include the effect of turbulent fluctuations on particle motion. As our results demonstrated that the process of fine sediment infiltration into static gravel bed is mainly gravity dominant process, therefore the inclusion of additional dispersion models might not be necessary. We expect that the effects of turbulent fluctuations can only be neglected in low-flow conditions. As soon as the gravel particle starts to move, it cannot be simply assumed as a gravity-dominated process and under those scenarios, one should include the effect of turbulent fluctuations using dispersion models.

Among the two main factors (gravity and turbulence) describing the infiltration process, suggested by Huston (2014), an eddy-resolving approach could be applied to assess the turbulence effect on infiltration in greater detail. This can be achieved by employing a more detailed approach 'resolved CFD–DEM' to model the infiltration process. The eddy generation and dissipation process can be properly captured by DNS thus turbulence effects on the infiltration process can be in detail investigated. The resolved CFD–DEM method calculates interaction forces acting on particles (i.e., fluid–particle interaction force) by integrating fluid stresses on the surface of particles, rather than empirical models used in unresolved CFD–DEM. However, it requires enormous computational resources and is limited to the maximum order of 10^3 particles (Bérard et al., 2020; Kloss et al., 2012). Due to the small number of particles in resolved CFD–DEM method, the resolved CFD–DEM approach might not be appropriate to model and capture the bulk behaviour of large systems, such as fine sediment infiltration into gravel bed.

4 | DISCUSSION

From both pure DEM and coupled CFD–DEM simulations, it is evident that the claims made in several previous studies that only bridging type of infiltration process occurs in nature and fine sediment infiltrate only till limited depth and percolation is simply an artifact of the shallow gravel bed, is not true. As shown in our both pure DEM and coupled CFD–DEM simulations, both infiltration processes, sometimes a combination of both, could occur within the same gravel bed. The occurrence of bridging and percolation mainly depends on the relative size of fine sediment and gravel; in a broader sense it depends on relative grain size distributions of fine sediment and gravel. Gravel grain size distribution determines the size of voids formed and eventually the smallest size of fine sediment, which could pass through

it. Fine sediment distribution eventually decides if the packing (or infiltration) could occur by bridging or percolation mechanism. Based on our results, we advocate that it is the relative size ratio of fine sediment and gravel that ultimately determines, which type of infiltration would occur.

Furthermore, our results for pure DEM and coupled CFD–DEM simulations, for different size ratios, suggest that the infiltration process is gravity-dominated. Considering a realistic scenario of gravel beds in natural streams. Usually, there exists low permeable or impermeable strata below the gravel bed. This implies that there is an insignificant amount of downward flux (almost zero flow) along the direction of the bed depth due to the impermeable surface below the gravel bed in natural streams. Flume experiments are mostly aimed to model fluvial processes occurring in natural streams neglecting surface-ground water exchange. Our CFD–DEM setup is a representation of the infiltration process occurring in the flumes and natural streams, below which there exists an impermeable stratum. The hypothesis (Cui et al., 2008), suggesting that the process of fine sediment infiltration through intra-gravel flow is similar to the infiltration process driven by gravity, seems to be reasonable, even in scenarios, when there is a downward flux (flow along the gravel bed depth). We expect that the bridging and percolation should still be predominantly a function of pore space geometry and its connectivity. Even, when there is a downward flow (due to the permeable surface beneath the gravel bed, also called intra-gravel flow), it cannot push the fine particle further downward (if pore space is smaller than particle size), unless the gravel bed is mobilized. This argument strongly indicates that Cui's hypothesis might be valid even when there is downward flux. It must be emphasized that this hypothesis does not hold true for high-flow conditions, when the gravel bed becomes dynamic and mobile. As soon as the gravel particles in the bed start to move, which would typically be expected in high-flow conditions, the infiltration processes can no longer be simulated as a gravity-driven configuration and the water flow and turbulence effects must be included in the numerical simulations. However, as long as the gravel bed remains immobile, typically in low-flow conditions, one can simply simulate the infiltration process considering the system as pure granular media and yet able to predict realistic infiltration processes with much lesser computational resources and time, as shown by our pure DEM and coupled CFD–DEM simulations. However, this can be further investigated and verified by making the surface below the gravel bed permeable in coupled CFD–DEM simulations.

Our hypothesized definition of a 'thick enough' gravel bed (thicker than five times the coarsest gravel diameter) seems to be reasonable, as the maximum bridging depth is 2–5 times the $d_{90,\text{Gravel}}$. One would need a thicker gravel bed to distinguish between the bridging and percolation behaviours. In our case, the gravel bed thickness is 10 times the gravel bed diameter (sufficiently thick). We could simulate both types of infiltration processes within the same bed thickness. This demonstrates that bridging and percolation infiltration processes could occur in the same gravel bed and it mainly depends on the size ratios of considered fine sediment and gravel, rather than the gravel bed thickness.

One question that should be addressed here is: if both percolation and bridging could occur within the same depth of the gravel bed, which is thick enough, then why did Wooster et al. (2008) observe only bridging (or clogging) behaviour, despite using various combinations of gravel and fine sediment in their flume experiment? This hints towards the possibility that the materials, used in their experiment, might coincidently fall below the threshold for the bridging ($d_{15,\text{Gravel}}/d_{85,\text{Fine Sediment}} < 10.6$). To check for this possibility, we analyzed the data presented in their paper against the size ratio thresholds for bridging and percolation of Gibson et al. (2009). The $d_{15,\text{Gravel}}$ for different zones (different locations in flume) is directly extracted from the gradation curves provided in their paper. Unfortunately, for the fine sediment, only geometric mean (D_g) and standard deviation (σ_g) were reported in their paper, rather than a full gradation curve. Often, natural sediments follow a log-normal distribution and $d_{84.1}$ ($\sim d_{85}$) and $d_{15.9}$ ($\sim d_{15}$) can be approximated (Sundar & Sannasiraj, 2019) with geometric mean (D_g) and standard deviation (σ_g). Assuming fine sediment, used in Wooster et al.'s flume experiment, follow a log-normal distribution, a simple model is used to approximate the $d_{85,\text{Fine Sediment}}$, using the following relation:

$$Dg = (d_{84.1} d_{15.9})^{1/2}, \tag{20}$$

$$\sigma g = \log\left(\frac{d_{84.1}}{d_{15.9}}\right)^{1/2}. \tag{21}$$

We analyze the dataset presented in their paper and our approximated $d_{15,\text{Gravel}}/d_{85,\text{Fine Sediment}}$ for each zone can be seen in Figure 11. Almost all combinations of fine sediment and gravel used in their experiment lie below the size ratio threshold for bridging ($d_{15,\text{Gravel}}/d_{85,\text{Fine Sediment}} < 10.6$), except one section (Zone 4; refer to their paper for details). In Zone 4, the approximated $d_{15,\text{Gravel}}/d_{85,}$

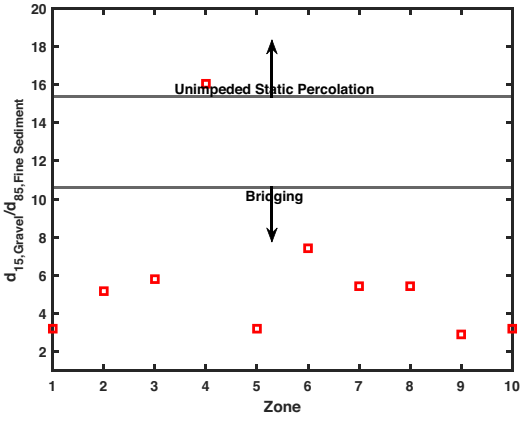

FIGURE 11 $d_{15,\text{Gravel}}/d_{85,\text{Fine Sediment}}$ for each zone in flume experiment of Wooster et al. (2008). [Color figure can be viewed at wileyonlinelibrary.com]

$_{Fine\ Sediment}$ is found to be 16 (near 15.4; percolation limit). Being at the border of bridging and percolation limits, the combination of bridging and percolation should have occurred in Zone 4. As the experiment was stopped by visual observation by looking through the glass walls of the flume, when the top surface layers of the whole flume (almost all zones) were clogged with fine sediments. Zone 4 might have remained unsaturated by the time the flume experiment was stopped. This section of the flume (Zone 4) could have shown the percolation behaviour (or combination of bridging and percolation) if the flume experiment would have run for a longer duration. As the size ratios, for most of the fine sediment and gravel combinations used in their experiment, corresponded to the bridging process, they observed only the bridging type of infiltration. Second, their observation of bridging behaviour in Zone 4 might be also due to different equilibrium fine sediment transport rates upstream and downstream of Zone 4. As different gravel sizes were used in each zone, they would be requiring different equilibrium fine sediment rates. This would affect the fine sediment transport process in other zones, depending on if the upstream or downstream section (zone) has more or less transport capacity than fine sediment entering that zone. One would have to run the experiment for a sufficiently long duration to make sure that the effects of different equilibrium fine sediment transport in different zones are vanished. The above discussion hints that Wooster's observation of only the bridging infiltration process, in their flume experiment, might be due to (a) the most of gravel and fine sediment material lying below the threshold for the bridging process, and (b) the short run-time of the flume experiment.

Another limitation, of not only the applied unresolved CFD–DEM method but also in general of the CFD–DEM method, is its inability to resolve fluid-air interphase. While, modelling systems involving multi-phases such as open channel flow with sediment transport (air, water, and particle), it might be important to capture the dynamics of the free surface. This would require the extension of the applied CFD–DEM method by coupling it with some interphase resolving methods, such as the level set method or volume of fluid method (VOF) (Harikrishnan & Mahapatra, 2021; Nan et al., 2023; Washino et al., 2023). However, the infiltration process occurs far from the free surface, as fine sediment infiltrates into the gravel bed as a result of bed load transport. Therefore, resolving the interphase between air and water (free surface) should not be causing any significant change in modelling infiltration processes and the final state of infiltration.

Furthermore, we have considered only spherical particles in our simulations but natural sediment particles have non-spherical shapes. Non-spherical particles behave much differently than spherical particles and particle shape could have significant effects on fluid–particle interactions and resultant particle movement (Washino et al., 2023). Additionally, natural sediment consists of various grain size distributions (non-uniform/polydisperse particles). We expect that a more realistic and accurate infiltration process could be obtained with numerical simulations by considering the non-sphericity and non-uniformity of particles into account.

5 | CONCLUSION

The process of fine sediment infiltration into static gravel bed is investigated by means of numerical simulation, where the mechanical behaviour of particles is considered using the DEM and fluid flow (water) is resolved using CFD. Due to various limitations of the applied unresolved CFD–DEM method, concerning the number and size of particles, and computational requirements, a smaller domain size, with monodisperse spherical particles for gravel and fine sediment, is considered. Two separate sets of simulations, namely pure DEM and coupled CFD–DEM simulations, are performed. Numerical simulations are based on the assumption that the process of fine sediment infiltration into a static gravel bed can be represented by a binary mixture of mono-sized spherical particles. Theoretical packing limits corresponding to the different geometrical configurations are considered for both sets of simulations. Taken together, the following conclusions can be drawn from the conducted study:

- The pure DEM (neglecting water flow) and coupled CFD–DEM (considering water flow) simulations of fine sediment infiltration into static gravel bed demonstrate that the process seems to be gravity-dominated. Our results and discussion advocates for Cui's hypothesis that fine sediment infiltration through intra-gravel flow is similar to fine sediment infiltration driven by gravity. This implies that the process could simply be simulated and studied using models developed for pure particle systems, such as stochastic models, analytical packing models, and also pure DEM simulations. However, this holds true for low-flow conditions, where the gravel bed remains immobile (static). As soon as gravel starts to move, the process cannot be modelled with pure particle models and flowing water and turbulence effects must be included.
- In contrast to the consensus in the field, we could able to simulate both bridging and percolation types of infiltration processes within the same gravel bed. For the size ratio of 0.154, 0.414, and 0.231, unimpeded static percolation, bridging, and a combination of bridging and percolation are observed, respectively. This shows that the occurrence of bridging and percolation processes are independent of gravel bed thickness, rather it only depends on the relative grain size distribution of fine sediment and gravel (size ratio).
- A sufficient thick gravel bed is necessary to distinguish between bridging and percolation behaviours. Based on our predictions and previous observations of bridging depths, we hypothesize that a gravel bed deeper than five times the coarsest gravel diameter can be considered as a thick bed. Although, our hypothesis seems reasonable, a more thorough investigation is required considering different gravel bed depths, detailed grain size distributions (polydisperse particles) and non-sphericity of particles, before our hypothesis is standardized.
- Previous claims that there is only a bridging type of infiltration occurs in nature and percolation behaviour is simply an artifact of the shallow gravel bed, supported also by recent studies of Cui et al. (2008) and Wooster et al. (2008), are not true. Our analysis indicates that almost all gravel-fine sediment combinations used in

their experiment lie below the bridging threshold. Additionally, their observations might also be due to the short run-time of the flume experiment.

- As long as the mean flow fields are correctly captured and the gravel bed remains immobile, the turbulence models seem not to affect the final state of infiltration. This also indicates that the fine sediment infiltration into static gravel bed is a predominantly gravity-driven process. However, our simulations are based on fluid–particle interaction forces, which do not consider the effect of turbulent fluctuations into account. It might be interesting to include the effects of the turbulent fluctuations either by simple dispersion models or by turbulence-resolving methods (resolved CFD–DEM) and simulate the infiltration process. This would solidify our observations that fine sediment infiltration is in-fact gravity dominant.

We have restricted ourselves to mono-disperse (uniform) gravel and fine sediment, due to computational and time restrictions. It might be interesting and helpful to include polydisperse (non-uniform) gravel and fine sediment with varying flow conditions, different gravel bed depths, and possibly the non-sphericity of particles. Turbulence-resolving approaches (resolved CFD–DEM) would provide more detailed insights into flow and infiltration processes occurring through the gravel bed. The resolved CFD–DEM approach would be helpful to assess the effects of turbulence on the infiltration process and clogging depth by directly resolving the phenomena of production and dissipation of turbulent eddies. As mentioned before, the resolved CFD–DEM approach is probably not a suitable approach to model the infiltration process, due to its limitation concerning a very limited number of particles and heavy computational requirements. Despite several simplifications and assumptions made to model the infiltration process, results obtained in the current study with unresolved CFD–DEM method, are indeed able to fill some research gaps in the overall understanding of the infiltration mechanism. A more detailed study, considering larger domain size and actual grain size distributions of fine sediment and gravel, would be helpful to solidify our conclusions. However, the applied unresolved CFD–DEM method (or CFD–DEM method in general) is computationally demanding and limited to a definite number of particles. With a large number of particles and varying PSD, the computational requirement will increase exponentially. This would be very difficult with currently available computer architecture, solution, and coupling algorithm and without proper and efficient parallelization (MPI load balancing). GPU-based codes for CFD–DEM coupling will also be helpful to simulate the process in realistic timeframes.

ACKNOWLEDGEMENTS

We would like to thank the Leibniz Supercomputing Centre (LRZ) for providing the computational resources required for our study. The study was conducted during the PhD research at TUM with KAS scholarship, we are greatly thankful to Konrad-Adenauer-Stiftung (KAS) for making this possible. Valuable suggestions and continuous encouragement from Prof. Nils Rüther (Technical University of Munich; TUM) is specially acknowledged. Open Access funding enabled and organized by Projekt DEAL.

CONFLICT OF INTEREST STATEMENT

On behalf of all authors, the corresponding author states that there is no conflict of interest.

DATA AVAILABILITY STATEMENT

The data that support the findings of this study are available from the corresponding author upon reasonable request.

ORCID

Atul Jaiswal https://orcid.org/0000-0003-0228-5778

REFERENCES

Armenio, V., & Fiorotto, V. (2001). The importance of the forces acting on particles in turbulent flows. *Physics of Fluids*, *13*(8), 2437–2440. https://doi.org/10.1063/1.1385390

Bednarek, A. T. (2001). Undamming rivers: A review of the ecological impacts of dam removal. *Environmental Management*, *27*(6), 803–814. https://doi.org/10.1007/s002670010189

Bérard, A., Patience, G. S., & Blais, B. (2020). Experimental methods in chemical engineering: Unresolved CFD-DEM. *The Canadian Journal of Chemical Engineering*, *98*(2), 424–440. https://doi.org/10.1002/cjce.23686

Beschta, R. L., & Jackson, W. L. (1979). The intrusion of fine sediments into a stable gravel bed. *Journal of the Fisheries Research Board of Canada*, *36*(2), 204–210. https://doi.org/10.1139/f79-030

Bocksell, T. L., & Loth, E. (2006). Stochastic modeling of particle diffusion in a turbulent boundary layer. *International Journal of Multiphase Flow*, *32*(10–11), 1234–1253. https://doi.org/10.1016/j.ijmultiphaseflow.2006.05.013

Born, S. M., Genskow, K. D., Filbert, T. L., Hernandez-Mora, N., Keefer, M. L., & White, K. A. (1998). Socioeconomic and institutional dimensions of dam removals: The Wisconsin experience. *Environmental Management*, *22*(3), 359–370. https://doi.org/10.1007/s002679900111

Bui, V. H., Bui, M. D., & Rutschmann, P. (2019a). Advanced numerical modeling of sediment transport in gravel-bed Rivers. *Water*, *11*(3), 550. https://doi.org/10.3390/w11030550

Bui, V. H., Bui, M. D., & Rutschmann, P. (2019b). Combination of discrete element method and artificial neural network for predicting porosity of gravel-bed river. *Water*, *11*(7), 1461. https://doi.org/10.3390/w11071461

Carling, P. A. (1984). Deposition of fine and coarse sand in an open-work gravel bed. *Canadian Journal of Fisheries and Aquatic Sciences*, *41*(2), 263–270. https://doi.org/10.1139/f84-030

Cui, Y., Parker, G., Braudrick, C., Dietrich, W. E., & Cluer, B. (2006). Dam removal express assessment models (DREAM). *Journal of Hydraulic Research*, *44*(3), 291–307. https://doi.org/10.1080/00221686.2006.9521683

Cui, Y., & Wilcox, A. C. (2005). Numerical modeling of sediment transport upon dam removal: Application to Marmot Dam in Sandy River, Oregon. In: Sedimentation engineering, ASCE Manual 54, No. Vol. 2.

Cui, Y., Wooster, J. K., Baker, P. F., Dusterhoff, S. R., Sklar, L. S., & Dietrich, W. E. (2008). Theory of fine sediment infiltration into immobile gravel bed. *Journal of Hydraulic Engineering*, *134*(10), 1421–1429. https://doi.org/10.1061/(ASCE)0733-9429(2008)134:10(1421)

Cundall, P. A., & Strack, O. D. L. (1979). A discrete numerical model for granular assemblies. *Géotechnique*, *29*(1), 47–65. https://doi.org/10.1680/geot.1979.29.1.47

Diplas, P., & Parker, G. (1992). Deposition and removal of fines in gravel-bed streams. In: P. Billi, R. D. Hey, C. R. Thorne, & P. Tacconi (Eds.), *Dynamics of Gravel-Bed Rivers* (pp. 313–329). John Wiley.

Doyle, M. W., Stanley, E. H., & Harbor, J. M. (2003). Channel adjustments following two dam removals in Wisconsin. *Water Resources Research*, *39*(1), 1011–1025. https://doi.org/10.1029/2002WR001714

Einstein, H. A. (1968). Deposition of suspended particles in a gravel bed. *Journal of the Hydraulics Division*, *94*(5), 1197–1206. https://doi.org/10.1061/JYCEAJ.0001868

Evans, E., & Wilcox, A. C. (2014). Fine sediment infiltration dynamics in a gravel-bed River following a sediment pulse. *River Research and Applications*, *30*(3), 372–384. https://doi.org/10.1002/rra.2647

Frostick, L. E., Lucas, P. M., & Reid, I. (1984). The infiltration of fine matrices into coarse-grained alluvial sediments and its implications for stratigraphical interpretation. *Journal of the Geological Society*, *141*(6), 955–965. https://doi.org/10.1144/gsjgs.141.6.0955

Gibson, S., Abraham, D., Heath, R., & Schoellhamer, D. (2009). Vertical gradational variability of fines deposited in a gravel framework. *Sedimentology*, *56*(3), 661–676. https://doi.org/10.1111/j.1365-3091.2008.00991.x

Gimenez, J. M., Idelsohn, S. R., Oñate, E., & Löhner, R. (2021). A multiscale approach for the numerical simulation of turbulent flows with droplets. *Archives of Computational Methods in Engineering: State of the Art Reviews*, *28*(6), 4185–4204. https://doi.org/10.1007/s11831-021-09614-6

Harikrishnan, S., & Mahapatra, P. S. (2021). Effect of liquid–air interface on particle cloud dynamics in viscous liquids. *Physics of Fluids*, *33*(6), 63306. https://doi.org/10.1063/5.0048895

Herrero, A., & Berni, C. (2016). Sand infiltration into a gravel bed: A mathematical model. *Water Resources Research*, *52*(11), 8956–8969. https://doi.org/10.1002/2016WR019394

Herrero, A., Berni, C., Camenen, B., & Thollet, F. (2015). Laboratory analysis on silt infiltration into a gravel bed: Modélisation physique de l'infiltration dans un lit de graviers. https://hal.science/hal-01362697

Honjo, Y., & Veneziano, D. (1989). Improved filter criterion for cohesionless soils. *Journal of Geotechnical Engineering*, *115*, 75–94.

Huston, D. (2014). Clogging of fine sediment within gravel substrates: Macro-analysis and momentum-impulse model (These and Dissertation-Civil Engineering), Lexington, Kentucky. https://uknowledge.uky.edu/ce_etds/24

Indraratna, B., & Locke, M. R. (1999). Design methods for granular filters—Critical review. *Proceedings of the Institution of Civil Engineers—Geotechnical Engineering*, *137*(3), 137–147. https://doi.org/10.1680/gt.1999.370303

Indraratna, B., & Vafai, F. (1997). Analytical model for particle migration within base soil-filter system. *Journal of Geotechnical and Geoenvironmental Engineering*, *123*(2), 100–109. https://doi.org/10.1061/(ASCE)1090-0241(1997)123:2(100)

Iseya, F., & Ikeda, H. (1987). Pulsations in bedload transport rates induced by a longitudinal sediment sorting: A flume study using sand and gravel mixtures. *Geografiska Annaler Series A-Physical Geography*, *69*, 15–27.

Jaiswal, A., Bui, M. D., & Rutschmann, P. (2022). Evaluation of RANS-DEM and LES-DEM methods in OpenFOAM for simulation of particle-laden turbulent flows. *Fluids*, *7*(10), 337. https://doi.org/10.3390/fluids7100337

Johnson, K. L. (1987). Contact mechanics (1st pbk. ed. (with corrections)). Cambridge University Press. https://doi.org/10.1017/CBO9781139171731

Kenney, T. C., Chahal, R., Chiu, E., Ofoegbu, G. I., Omange, G. N., & Ume, C. A. (1985). Controlling constriction sizes of granular filters. *Canadian Geotechnical Journal*, *22*(1), 32–43. https://doi.org/10.1139/t85-005

Kloss, C., Goniva, C., Hager, A., Amberger, S., & Pirker, S. (2012). Models, algorithms and validation for opensource DEM and CFD-DEM. *Progress in Computational Fluid Dynamics, An International Journal*, *12*(2/3), 140. https://doi.org/10.1504/PCFD.2012.047457

Koch, D. L., & Hill, R. J. (2001). Inertial effects in suspension and porous-media flows. *Annual Review of Fluid Mechanics*, *33*(1), 619–647. https://doi.org/10.1146/annurev.fluid.33.1.619

Kuerten, J. G. M. (2016). Point-particle DNS and LES of particle-laden turbulent flow—a state-of-the-art review. *Flow, Turbulence and Combustion*, *97*(3), 689–713. https://doi.org/10.1007/s10494-016-9765-y

Latham, J. P., Munjiza, A., & Lu, Y. (2002). On the prediction of void porosity and packing of rock particulates. *Powder Technology*, *125*(1), 10–27. https://doi.org/10.1016/S0032-5910(01)00493-4

Lauck, T. (1991). A simulation model for the infiltration of sediment into spawning gravel (Master's thesis). Humboldt State University.

Lisle, T. E. (1989). Sediment transport and resulting deposition in spawning gravels, north coastal California. *Water Resources Research*, *25*(6), 1303–1319. https://doi.org/10.1029/WR025i006p01303

Lone, M. A., Hussain, B., & Asawa, G. L. (2005). Filter design criteria for graded cohesionless bases. *Journal of Geotechnical and Geoenvironmental Engineering*, *131*(2), 251–259. https://doi.org/10.1061/(ASCE)1090-0241(2005)131:2(251)

Loth, E. (2000). Numerical approaches for motion of dispersed particles, droplets and bubbles. *Progress in Energy and Combustion Science*, *26*(3), 161–223. https://doi.org/10.1016/S0360-1285(99)00013-1

Lunt, I. A., & Bridge, J. S. (2007). Formation and preservation of open-framework gravel strata in unidirectional flows. *Sedimentology*, *54*(1), 71–87. https://doi.org/10.1111/j.1365-3091.2006.00829.x

Minier, J. P., Chibbaro, S., & Pope, S. B. (2014). Guidelines for the formulation of Lagrangian stochastic models for particle simulations of single-phase and dispersed two-phase turbulent flows. *Physics of Fluids*, *26*(11), 113303. https://doi.org/10.1063/1.4901315

Minshall, G. W., Royer, T. V., & Robinson, C. T. (2001). Response of the Cache Creek macroinvertebrates during the first 10 years following disturbance by the 1988 Yellowstone wildfires. *Canadian Journal of Fisheries and Aquatic Sciences*, *58*(6), 1077–1088. https://doi.org/10.1139/f01-056

Nan, X., Shen, Z., Hou, J., & Li, G. (2023). High-resolution model of complexly shaped bodies motion using an IBM-VOF-DEM coupling method. *Powder Technology*, *413*, 118005. https://doi.org/10.1016/j.powtec.2022.118005

NCASI. (1981). *Factors affecting changes in the percent of fine sediment in gravel bedded channels* (No. Technical Bulletin No. 0354). NCASI.

Parker, G., Cui, Y., Imran, J., & Dietrich, W. E. (1996). Flooding in the lower Ok Tedi, Papua New Guinea due to the disposal of mine tailings and its amelioration. In: International Seminar on Recent Trends of Floods and Their Preventative Measures, Hokkaido Disaster Prevention Research Center.

Pollard, A. I., & Reed, T. (2004). Benthic invertebrate assemblage change following dam removal in a Wisconsin stream. *Hydrobiologia*, *513*(1), 51–58. https://doi.org/10.1023/B:hydr.0000018164.17234.4f

Sakthivadivel, R., & Einstein, H. A. (1970). Clogging of porous column of spheres by sediment. *Journal of the Hydraulics Division*, *96*(2), 461–472. https://doi.org/10.1061/JYCEAJ.0002332

Schälchli, U. (1992). The clogging of coarse gravel river beds by fine sediment. *Hydrobiologia*, *235–236*(1), 189–197. https://doi.org/10.1007/BF00026211

Schuler, U., & Brauns, J. (1993). Behaviour of coarse and well-graded filters. In: J. Brauns, M. Heibaum, & U. Schuler (Eds.), *Filters in Geotechnical and Hydraulic Engineering* (pp. 3–18). Balkema.

Sherard, J. L., & Dunnigan, L. P. (1986). Filters and leakage control in embankment dams. *International Journal of Rock Mechanics and Mining Sciences & Geomechanics Abstracts*, *23*(5), 202. https://doi.org/10.1016/0148-9062(86)90266-4

Sherard, J. L., & Dunnigan, L. P. (1989). Critical filters for impervious soils. *Journal of Geotechnical Engineering*, *115*, 927–947.

Stanley, E. H., Luebke, M. A., Doyle, M. W., & Marshall, D. W. I. (2002). Short-term changes in channel form and macroinvertebrate communities following low-head dam removal. *Journal of the North American Benthological Society*, *21*, 172–187.

Sundar, V., & Sannasiraj, S. A. (Eds.). (2019). *Advanced series on ocean engineering: Volume 47. Coastal engineering: Theory and practice*. World Scientific Publishing Co. Pte. Ltd. https://doi.org/10.1142/ASOE

Swanson, F. J., & Dyrness, C. T. (1975). Impact of clear-cutting and road construction on soil erosion by landslides in the western Cascade Range, Oregon. *Geology*, *3*(7), 393. https://doi.org/10.1130/0091-7613(1975)3<393:IOCARC>2.0.CO;2

Vieira, N. K. M., Clements, W. H., Guevara, L. S., & Jacobs, B. F. (2004). Resistance and resilience of stream insect communities to repeated hydrologic disturbances after a wildfire. *Freshwater Biology*, *49*(10), 1243–1259. https://doi.org/10.1111/j.1365-2427.2004.01261.x

Washino, K., Chan, E. L., Tsujimoto, T., Tsuji, T., & Tanaka, T. (2023). Development of resolved CFD–DEM coupling model for three-phase flows with non-spherical particles. *Chemical Engineering Science*, *267*, 118335. https://doi.org/10.1016/j.ces.2022.118335

Wooster, J. K., Dusterhoff, S. R., Cui, Y., Sklar, L. S., Dietrich, W. E., & Malko, M. (2008). Sediment supply and relative size distribution effects on fine sediment infiltration into immobile gravels. *Water Resources Research*, *44*(3), W03424. https://doi.org/10.1029/2006WR005815

Yu, A. B., & Standish, N. (1991). Estimation of the porosity of particle mixtures by a linear-mixture packing model. *Industrial & Engineering Chemistry Research*, *30*(6), 1372–1385. https://doi.org/10.1021/ie00054a045

Yu, A. B., & Standish, N. (1993). Limitation of proposed mathematical models for the porosity estimation of nonspherical particle mixtures. *Industrial & Engineering Chemistry Research*, *32*(9), 2179–2182. https://doi.org/10.1021/ie00021a043

Yu, A. B., Zou, R. P., & Standish, N. (1996). Modifying the linear packing model for predicting the porosity of nonspherical particle mixtures. *Industrial & Engineering Chemistry Research*, *35*(10), 3730–3741. https://doi.org/10.1021/ie950616a

Zhou, Z. Y., Kuang, S. B., Chu, K. W., & Yu, A. B. (2010). Discrete particle simulation of particle–fluid flow: Model formulations and their applicability. *Journal of Fluid Mechanics*, *661*, 482–510. https://doi.org/10.1017/S002211201000306X

How to cite this article: Jaiswal, A., Bui, M. D., & Rutschmann, P. (2023). On the process of fine sediment infiltration into static gravel bed: A CFD–DEM modelling perspective. *River Research and Applications*, 1–20. https://doi.org/10.1002/rra.4215

Chapter 6

Influence of Rolling Resistance and Particle Size Distribution in the Simulation of Sand Infiltration into the Static Gravel Bed

This chapter is published as:
Jaiswal, A.; Bui, M.D.; Rüther, N.; Rutschmann, P. Influence of Rolling Resistance and Particle Size Distribution in the Simulation of Sand Infiltration into the Static Gravel Bed. *Water* 2024, 16, 1947.
https://doi.org/10.3390/w16141947

water

MDPI

Article

Influence of Rolling Resistance and Particle Size Distribution in the Simulation of Sand Infiltration into the Static Gravel Bed

Atul Jaiswal *, Minh Duc Bui, Nils Rüther and Peter Rutschmann

Chair of Hydraulic Engineering, Technical University of Munich (TUM), 80333 Munich, Germany
* Correspondence: atul.jaiswal@tum.de; Tel.: +49-(89)-289-23161

Abstract: Fine sediment infiltration and subsequent clogging in a gravel bed affect several fluvial, ecological, and biological processes, resulting in the degradation of the river ecosystem. Despite many experimental and a few numerical studies, the process is yet to be entirely understood. We employed a pure Lagrangian framework, called the Discrete Element Method (DEM), to numerically investigate the infiltration process. Special attention is given to tackling the issue of non-spherical and irregular particle shapes and particle size distributions (PSDs) in numerical simulations. Due to computational limitations, these aspects were either not considered or simplified in previous numerical studies. We implicitly included non-spherical and irregular shape effects through rolling resistance models, which do not cause excessive computational overhead. Our study shows that rolling resistance models greatly influence packing and fine sediment infiltration. However, they may also lead to unphysical particle behavior; thus, they should be carefully used in numerical simulations. Oversimplified PSDs do not mirror natural systems, and full PSDs pose computational challenges. Sufficient grain classes are needed to mimic the non-homogeneity and poly-dispersity found in natural fluvial sediments. The infiltrating characteristics of sand concerning PSD and shape effects are linked to size ratio $D_{15,Gravel}/D_{85,Sand}$, assuring physical and realistic modeling of the infiltration process.

Keywords: fine sediment infiltration; static gravel bed; particle shape; particle size distributions (PSDs); discrete element method (DEM); rolling resistance models

check for updates

Citation: Jaiswal, A.; Bui, M.D.; Rüther, N.; Rutschmann, P. Influence of Rolling Resistance and Particle Size Distribution in the Simulation of Sand Infiltration into the Static Gravel Bed. *Water* **2024**, *16*, 1947. https://doi.org/10.3390/w16141947

Academic Editors: Michele Mossa and Giuseppe Pezzinga

Received: 28 May 2024
Revised: 27 June 2024
Accepted: 6 July 2024
Published: 10 July 2024

1. Introduction

The gravel bed and the pore space within the bed structures are crucial in sustaining a healthy river ecosystem [1–3]. Fish and other microorganisms utilize the pore space in the gravel bed for reproduction and living purposes. Fine sediment clogging (e.g., sand, silt, and clay) in the gravel bed harms several ecological processes, such as fish spawning [4], macrophytes' root length [5], and habitat of subsurface invertebrates, and may cause subsurface contamination [6,7]. Additionally, it hinders surface–subsurface interaction, which is a function of pore space and permeability of the gravel bed [8,9]. Fine sediments are flushed during dam removal operations, which are a standard practice to recover the reservoir's capacity [10–16]. Fine sediment can also join the river systems through landslides, forest fires, changes in land use and land cover, mining activities, and dredging [17–21]. The fine sediment, joining the river system, fills the coarse sediment deposit downstream, decreasing the pore space in the gravel bed and eventually degrading the river ecology. An understanding of variation in pore space along the depth of the gravel bed, as a result of fine sediment infiltration, is required to have a better sediment management strategy to sustain the healthy river ecosystem.

The fluvial sediments consist of different particle sizes and non-spherical and irregular particles, which pose a major challenge in accurately predicting packing structures and pore space variation. The process of infiltration/packing can be mainly studied using three different approaches: (a) experimental investigations, (b) analytical and stochastic

models, and (c) numerical simulations. In this regard, a set of experimental works has been conducted to study the packing and infiltration process. Experimental investigations are most accurate but time- and resource-consuming. Furthermore, controlling all the interdependent parameters in the experimental investigations is difficult. The second approach is analytical and stochastic models, which are usually based on simple process equations. A limited number of analytical models have been developed to predict the packing behavior. In analytical and stochastic approaches, simple equations are developed and solved. The two most famous analytical models are linear and linear-mixture packing models [22–24], which were developed to model the random packing of particles. However, these analytical approaches are limited to a binary or ternary mixture. Moreover, incorporating the shape effects in the existing analytical models is very challenging since sediment particles have random shapes, which might differ significantly from one another. Some stochastic models, based on relative pore space geometry and particle size, have also been developed [25,26]. The analytical and stochastic models have many constraints in relation to particle shape, particle size distributions (PSDs), and water flow effects. Therefore, simple analytical and stochastic models cannot be directly used to replicate the infiltration process in the natural systems, where these aspects become significantly important. The third approach, so-called numerical simulations, can also be employed to study the sand infiltration process. In numerical simulations, equations based on physical laws describing the process are numerically solved. Compared to the experimental, analytical, and stochastic approaches, the numerical simulations allow us to have better control over parameters, which are mainly responsible for the physical process under consideration. Additionally, numerical simulations can provide more detailed information with relatively fewer resources such as money and time. Numerical simulations can be categorized into 1D, 2D, and 3D modeling approaches, which solve fluid flow to a certain extent of detailing, coupled with sediment transport equations. The relatively simple empirical equations for sediment transport are governed by mean flow, which is usually a function of resistance parameters. The flow resistance formulations that consider different effects can be found elsewhere [27]. However, simple sediment transport and flow resistance equations are not enough to obtain particle scale information. Therefore, one has to consider more advanced simulation approaches (e.g., Lagrangian particle tracking), which resolve each particle present in the system.

With recent advancements in computational architecture, efficient solution algorithms, and relatively easy accessibility to high-performance computing (HPC) facilities, numerical simulations can be performed in much greater detail, which was almost impossible a decade ago. One such advanced numerical method allows us to track each particle individually, along with its interaction with fluid and other contacting particles (Lagrangian particle tracking). Such a detailed numerical simulation can be further subcategorized into coupled or uncoupled approaches, which can be adopted depending on the process under consideration, the level of complexity, and the computational resources available to accommodate that level of complexity. In the coupled approach, computational fluid dynamics (CFD) is utilized to solve flow fields, and particles are tracked in the Lagrangian framework using Newton's second law of motion, also called the Discreet Element method (DEM). The coupled CFD–DEM approach allows for a comprehensive inclusion of fluid–particle interaction terms in the governing DEM equations; however, it adds computational overhead on top of expensive DEM computations. In the uncoupled approach, particles can be tracked simply with the DEM equations, neglecting the flow effects. In this paper, we employ the pure Lagrangian framework (DEM) to simulate and investigate the sand infiltration process by considering PSDs and implicitly accounting for the effects of non-sphericity and irregularities in particle shape.

The process of sand infiltration into the gravel bed has been experimentally studied for over 75 years, from the first study by Einstein [28] to many other experimental studies [19,29–37]. These experiments were performed on different experimental setups with different flow conditions and different gravel and sand compositions and by using various measurement techniques. The experimental investigations have resulted in the

development of empirical equations, usually limited to similar scenarios as experimental conditions. A straightforward comparison between different experimental works is not possible, yet researchers have been able to observe two distinct infiltration processes. One of them, where the filling of the gravel bed occurs from the bottom to the top, is called unimpeded static percolation, and the other is called bridging or clogging, where most of the sand becomes clogged in the upper surface layer. The occurrences of these two distinct infiltration processes are mainly a function of the relative sizes of sand and gravel, more precisely on $D_{15,Gravel}/D_{85,Sand}$ [38,39]. $D_{15,Gravel}$ and $D_{85,Sand}$ represent the gravel and sand sizes at which 15 and 85 percent of the material is finer. Some studies have observed only unimpeded static percolation [28–33]. In contrast, many researchers have claimed that the bridging type on infiltration is predominant, and percolation is simply an artifact of a shallow gravel bed [8,19,34–37]. This behavior is also supported by recent studies [8,40], which advocates that the bridging behavior is dominant in the natural fluvial systems. However, both bridging and percolation behavior in sufficiently thick gravel beds have been observed in the recent experimental [38] and numerical investigations [41–43].

The sand infiltration process has also been studied with advanced numerical simulations (e.g., particle tracking methods). Recently, Bui et al. [41,42] replicated Gibson's experiment numerically and were able to obtain quite good agreement with experimental data. However, they neglected the effects of flowing water (modeled in a pure DEM framework), simplified the PSD with a simple distribution with a mean and standard deviation, and did not consider the effects of non-sphericity and irregularities in particle shape as well. The work has been extended by Jaiswal et al. [43] by including the effects of flowing water on the infiltration process (modeled in the coupled CFD–DEM framework). However, they only considered the binary mixture to represent the gravel–sand system with free-rolling spherical particles. Despite several simplifications in the above-mentioned numerical studies, significant contributions to the understanding of the sand infiltration process have been made. Jaiswal et al. [43] numerically showed that bridging and percolation could occur within the same gravel deposit despite being subjected to the same flow conditions, as reported in the experimental study of Gibson et al. [38]. Jaiswal et al. [43] emphasized that the gravel bed should be sufficiently thick to distinguish between the above-mentioned two distinct infiltration processes, and accordingly, they suggested a suitable gravel bed thickness (minimum of five times the coarsest gravel diameter) for such a purpose. Furthermore, they also confirmed that the process of sand infiltration into static gravel beds is mainly gravity-dominated, which was first hypothesized by Cui et al. [40]. However, the above-mentioned numerical studies, based on the Lagrangian framework [41–43], have entirely neglected the effect of particle shape on the overall packing and sand infiltration process. Additionally, in previous numerical studies [41–43], particle size distributions (PSDs) of gravel and sand are simplified by a binary mixture or simple PSDs with a mean and standard deviation.

Particle size distributions (PSDs), particle shape, and texture are essential in how gravel bed packing is formulated and how fine sediment infiltrates into the gravel deposit. As mentioned above, previous numerical studies have neglected these aspects. Many studies on various fluid–particle systems have indicated that particle shape can have a significant role in the particle–particle and fluid–particle interaction terms [44–47]; thus, it cannot be neglected. The particle shape effects can be either included by resolving the actual particle shape or by including the shape effects implicitly by adding some rolling resistance to the particles [45]. Resolving different shapes is computationally expensive and adds an extra burden on top of the complexity and limitations in the Lagrangian framework, especially when dealing with a large number of particles. Some simplified non-spherical objects (e.g., ellipsoid, cube, multi-sphere, and super-quadric) can be used to consider non-spherical particles [48–51]. However, they also do not represent natural sand and gravel shapes, which can be very different from one another. Another approach to consider particle shape effects implicitly is by restricting the rolling of the particles with simple models, which seem to be an efficient tool to investigate shape effects on the

sand infiltration process. Other physical and chemical factors may also become relevant depending on the particle size and system under consideration. Several studies on the fine sediment migration in porous media that considered the effects of these factors and focused on chemical engineering applications can be found in the recent literature [52–55]. The current study focuses on the sand–gravel system, where these effects seem insignificant. We employ three different rolling resistance models and compare their abilities to capture particle shape effects on the process of sand infiltration into the static gravel bed.

Moreover, the inclusion of exact/full PSDs of gravel and sand (poly-disperse nature of sediments) in the analytical and stochastic models is incredibly difficult and not well-established. Considering full PSDs is also a challenging issue in numerical simulations, where broader PSDs result in a larger number of particles. When full PSDs are included, instead of simpler PSDs with fewer grain classes, a larger number of particles are required for the same mass or volume of sediments. Most of the numerical studies on the infiltration process have simplified the PSDs by considering fewer grain classes than exact gravel and sand compositions. In this paper, we test both full PSDs and simplified versions of PSDs for the adapted experiment to shed more light on the effect of particle size distribution on the numerical simulation of the sand infiltration process.

To our knowledge, there are very few studies on the process of sand infiltration into the gravel bed using the Lagrangian framework, where each particle is resolved and tracked. However, with the recent advancements in computational architecture, solution algorithms, and accessibility to supercomputing facilities, advanced numerical methods (e.g., Lagrangian particle tracking) are becoming popular tools for investigating complex physical problems. Nevertheless, the previous pure DEM and coupled CFD–DEM studies have simplified the particle size distributions (PSDs) and entirely neglected particle shape effects on the sand infiltration process. Considering the fact that the process of sand infiltration into the static gravel bed is gravity-dominated, and due to computational constraints, we chose to perform pure DEM simulations and focus on particle shape and PSD aspects. Thus, we model the particle shape (non-sphericity and irregularity) effects by including it implicitly with rolling resistance models in the DEM equations. Several infiltration cases (corresponding to bridging and percolation) are considered, dealing with a wide range of gravel sand compositions. Special attention is given to the conditions, which might lead to situations where rolling resistance should be avoided to obtain the correct behavior of infiltrating sand particles. Moreover, we tested the effects of the particle size distributions (PSDs) on the sand infiltration into the static gravel bed by reducing the number of grain classes in sand and gravel PSDs. The paper is arranged into the following sections: first, the governing equations and rolling resistance models are described; this is followed by the numerical setup of the adopted experiments; after that, the results are presented and discussed, followed by the main conclusions of this study.

2. Governing Equations and Rolling Resistance Models

The advanced numerical approach in the pure Lagrangian framework is considered to track each particle (sand and gravel), along with their interaction with each other. Particles are described as discrete entities and tracked using Newton's second law of motion, and the so-called Discrete Element Method (DEM) is employed. The DEM simulates the interactions between individual grains. It is of special interest because it is able to investigate particulate systems at the particle scale, in which the packing structure of a particle assembly is observable and the process of particle rearrangement can be traced through the time domain. The DEM approach was first proposed by Cundell and Strack [51] to model the mechanical behavior of granular materials with the consideration of particle interaction with other particles and walls using the soft-sphere approach. The translational and rotational motion of particle i with mass m_i and moment of inertia I_i can be described with the following equations:

$$m_i \frac{dv_i}{dt} = \sum_{j=1}^{k_c} \left(F_{n,ij} + F_{t,ij}\right) + m_i g \quad (1)$$

$$I_i \frac{d\omega_i}{dt} = \sum_{j=1}^{k_c} \left(M_{t,ij} + M_{r,ij} \right) \quad (2)$$

where v_i and ω_i are translational and angular velocities of the particle i and k_c is the number of particles interacting with the particle i. The forces acting on particles are contact forces and gravity, i.e., the gravitational force $m_i g$ and inter-particle forces, which include the normal particle–particle contact force $F_{n,ij}$ and tangential particle–particle contact force $F_{t,ij}$. The torque acting on particle i by particle j includes two components, i.e., $M_{t,ij}$, generated by tangential force, and $M_{r,ij}$, commonly known as the rolling friction torque and caused mainly by the non-sphericity of particles. The normal and tangential forces between particles are calculated based on the linear spring dashpot model, usually known as the Hertz–Mindlin model. More details on the Hertz–Mindlin model can be found elsewhere [56] and are not discussed here as the model is well-established and widely accepted. Figure 1 illustrates schematics of the rolling friction torque model (due to non-spherical particles) in addition to sliding and damping force models.

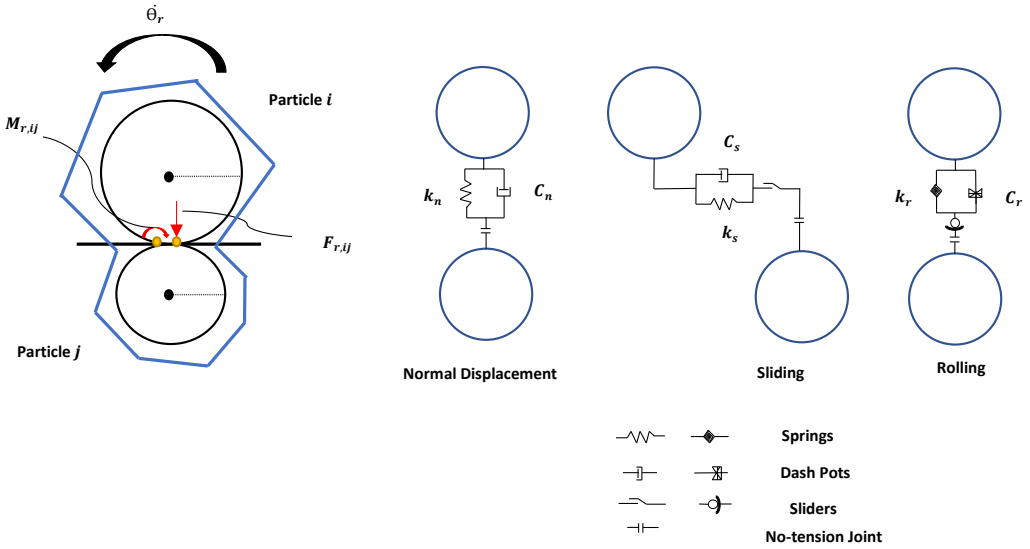

Figure 1. Rolling resistance torque acting on the rotating particle, along with the contact models for normal and tangential forces, and rolling resistance torque calculations [47,57].

In the conventional DEM approach [51], the particle–particle (and particle–wall) interactions consist of contact spring and damping forces in both normal and tangential directions with the "free rolling" of particles $(M_{r,ij} = 0)$. The normal and tangential components of sliding and damping forces are calculated by the famous Hertz–Mindlin contact model [56]. However, the significance of the rotational inertia and energy loss in the rotation of particles has been highlighted in both numerical studies [57–59] and physical experiments [60–62]; therefore, rolling friction (rolling torque $M_{r,ij}$) should not be neglected. The rolling resistance can also arise from other contact behaviors, including micro-slip, friction on the contact surface, plastic deformation around the contact, viscous hysteresis, surface adhesion, and particle shape [63]. However, in our numerical simulations, we assume that the particle shape is the main factor restricting the particle's rotation.

The rolling friction models can be mainly categorized into four subgroups, namely Constant Directional Torque (CDT) models, Viscous models, Elastic-Plastic Spring-Dashpot (EPSD) models, and contact-independent models. The contact-independent models have been shown to be highly deficient because the contact pair torques are not in equilibrium

and Viscous models do not provide any quasi-static torque; so, it is not effective in modeling pseudo-static systems [63]. Therefore, we considered and compared CDT and EPSD models. These rolling friction models are briefly touched upon in the following subsections. It must be mentioned that a thorough investigation of the fundamental mechanisms of rolling is beyond the scope of this paper. Rather, we focus on the effects of rolling resistance models in simulating a quasi-static system of sand infiltration into the static gravel bed.

2.1. Constant Directional Torque (CDT) Model

The CDT model and its derivatives apply a constant torque on a particle, which restricts the particle's rotation and implicitly takes into account particle shape [63]. The direction of the rolling friction torque is always in the opposite direction of the relative rotation between the particles in contact. The CDT model uses a simple equation (Equation (3)) to model the rolling friction between contacting particles, which is a function of relative angular velocity ($\omega_{rel} = \omega_i - \omega_j$) of contacting particles i and j.

$$M_{r,ij} = -\frac{\omega_{rel}}{|\omega_{rel}|}\mu_r R_r F_{n,ij} \tag{3}$$

where ω_i and ω_j are the angular velocities of particles i and j, respectively, μ_r is the coefficient of rolling resistance, and $R_r = r_i r_j/(r_i + r_j)$ is the rolling radius, with r_i and r_j representing the radii of particles i and j, respectively.

2.2. Elastic-Plastic Spring-Dashpot (EPSD) Model

The EPSD model and its derivatives (e.g., EPSD2 and EPSD3) divide the rolling friction torque $(M_{r,ij})$ into two components: a mechanical spring torque $\left(M^k_{r,ij}\right)$ and a viscous damping torque $\left(M^d_{r,ij}\right)$, shown in Equation (4) and Equation (5), respectively [63].

$$M_{r,ij} = M^k_{r,ij} + M^d_{r,ij} \tag{4a}$$

If the spring torque at time t is $M^k_{r,ij}(t)$ and the incremental torque in Δt is $\Delta M^k_{r,ij}$, the following relations can be established.

$$\begin{cases} M^k_{r,ij}(t+\Delta t) = M^k_{r,ij}(t) + \Delta M^k_{r,ij} \\ M^k_{r,ij}(t+\Delta t) \le M^m_{r,ij} \end{cases} \tag{4b}$$

$$M^m_{r,ij} = \mu_r R_r F_{n,ij} \tag{4c}$$

$$\Delta M^k_{r,ij} = -K_r \Delta\theta_r \tag{4d}$$

$$K_r = 2.25 K_n \mu_r^2 R_r^2 \tag{4e}$$

$M^m_{r,ij}$ is the limiting torque, which is achieved at a full mobilization rolling angle, μ_r is the coefficient of rolling friction, $\Delta\theta_r$ is the incremental relative rotation between two particles, and K_n and K_r are the normal contact and rolling friction stiffness, respectively.

The viscous damping torque $M^d_{r,ij}$ is assumed to be dependent on the relative angular velocity $\dot{\theta}_r$ between the two contacting particles and the damping constant C_r.

$$M^d_{r,ij} = \begin{cases} -C_r\dot{\theta}_r \; if \; \left|M^k_{r,ij}(t+\Delta t)\right| < M^m_{r,ij} \\ -fC_r\dot{\theta}_r \; if \; \left|M^k_{r,ij}(t+\Delta t)\right| = M^m_{r,ij} \end{cases} \tag{5a}$$

$$C_r = \eta_r C_r^{crit} \tag{5b}$$

$$C_r^{crit} = 2\sqrt{I_r k_r} \tag{5c}$$

$$I_r = 1/\left(\frac{1}{I_i + m_i r_i^2} + \frac{1}{I_j + m_j r_j^2}\right) \tag{5d}$$

where C_r is the rolling viscous damping coefficient, η_r is the rolling viscous damping ratio, C_r^{crit} is the critical viscous damping constant, f is the factor controlling full mobilization (damping is disabled at full mobilization $(f = 0)$), and I_r is the equivalent moment of inertia for the relative rotational vibration mode about the contact point between the two contacting particles.

Another version of the Elastic-Plastic Spring-Dashpot type of the rolling resistance model is called the EPSD2 model. The EPSD2 model neglects the contribution of the viscous damping torque $\left(M_{r,ij}^d = 0\right)$, and the original rolling stiffness is modified (Equation (6)) and assumed to be a function of the tangential stiffness (K_t) and rolling radius (R_r).

$$K_r = K_t R_r^2 \tag{6}$$

In this study, we test the CDT, EPSD, and EPSD2 rolling resistance models for a pseudo-static system of sand infiltration into the static gravel bed. The ability of these models to capture the correct infiltration behavior is tested, and accordingly, the most suitable rolling resistance model for the sand infiltration process is proposed.

3. Methodology and Numerical Setup

To investigate the effects of non-sphericity and irregularities in particle shape (implicitly with rolling resistance models) and particle size distributions (PSDs) on infiltrating characteristics of sand in the gravel bed, we adapted the infiltration experiment [38], also considered in previous pure DEM [41,42] and coupled CFD–DEM studies [43]. Previous numerical studies have simplified the particle size distributions of sand and gravel and have completely neglected the particle shape effects (without any consideration of rolling resistance). Several experiments, covering a wide range of gravel and sand combinations, are considered. We chose to perform DEM simulations for experiments 1, 2, and 3, which are run1, run2, and run3 of the reference flume experiment. Experiments 1 and 2 correspond to the bridging type of infiltration, and experiment 3 corresponds to the percolation type of infiltration.

The simulations are performed in LIGGGHTS−PFM (version-23.02), a CPU-based DEM code written in C++, developed by Johannes Kepler University, Linz, Austria. LIGGGHTS−PFM allows parallel computations by utilizing the MPI (Message Passing Interface), which decomposes the 3D domain into specified numbers of sub-domains in each direction and assigns one processor per sub-domain. It must be mentioned here that the DEM calculations are computationally demanding and limited to a definite number of particles [64]. The maximum number of particles that can be simulated with the DEM approach, even in large clusters/supercomputers, is in the order of 10^7 [65]. Unfortunately, LIGGGHTS−PFM has not yet been extended and modified to run on GPU systems. Due to these limitations and heavy computational requirements in the DEM method, a reduced domain size (0.15 m in length, 0.075 m in width, and 0.25 m in height) is considered, which is much smaller than the actual flume experiment but sufficient to capture the bulk behavior of particles. This strategic decision allowed us to perform the simulations in a reasonable timeframe with limited computational resources.

The simulations are performed in two stages. In the first stage, a gravel bed is prepared by pouring gravel particles into the domain under gravity. Once the gravel particles have reached equilibrium and achieved a steady-state condition after 1 s, where almost no gravel particle is moving and the system's kinetic energy is minimal, sand particles are inserted in the second stage, from 2 s onwards. Particle size distributions have a significant impact on the created gravel bed; for example, mono-sized (mono-disperse) and poly-sized (poly-disperse) particle assemblies have porosities of 0.454 and 0.407, respectively [66]. Considering this, we prepared a gravel bed with predefined bulk porosities of 0.454 and

0.407 for mono-disperse and poly-disperse cases, respectively, which resulted in a graved bed with a height of 0.1 m precisely, the same as in the original experiment. Sand particles are inserted from a region above the gravel bed with a specified mass flow rate for a specified duration. Several sets of DEM simulations are performed to investigate the effects of particle shape and size distribution on sand infiltration. We tested CDT, EPSD, and EPSD2 rolling resistance models while keeping the same PSD and other DEM settings. For the particle size distribution test, PSDs for gravel and sand are simplified, and different cases corresponding to full PSDs, simplified PSDs, and oversimplified PSDs are simulated. The simulations are performed until the bridging layer is formed in the upper gravel layer, precluding subsequent infiltration (bridging behavior). However, in some cases, especially for smaller sand sizes and cases resulting in undesired results, simulations were not further pursued until the final steady-state condition. The following sections will mention these cases explicitly, explaining the reason for not pursuing them further upon their arrival. The main reason is the limitation concerning the number of particles, which is explained in greater detail in the following paragraphs.

In total, 10 cases are simulated, taking references from three experiments (two corresponding to bridging and one corresponding to percolation, which are run1, run2, and run3 of the reference flume experiment, respectively). These 10 cases aim to cover this study's intended objectives: investigating particle shape and PSD effects on the sand infiltration process. Experiment 1 (run1), a bridging case, is simulated without any rolling resistance model (free-rolling) and with CDT, EPSD, and EPSD2 rolling resistance models. It must be noted that simplified PSDs (four gravel and five sand classes) are considered for rolling resistance tests (in our first set of simulations). This decision should not lead to any non-physical results as simulations aim to test the effects of rolling resistance, keeping the particle size distribution constant. This decision is taken strategically to perform several simulations within a limited timeframe and computational resources. From the first set of simulations, the best-performing rolling resistance model (EPSD model) is found and considered for the following sets of simulations. Two cases for each experiment (experiments 2 and 3) are simulated without and with the EPSD rolling resistance model. Moreover, experiment 1 is simulated, considering different PSDs for sand and gravel, resulting in three cases (full PSDs, simplified PSDs, and oversimplified PSDs). More details of each set of simulations covering rolling resistance and particle size distribution tests are summarized in Table 1.

Figure 2 shows the PSDs considered for sand and gravel for the rolling resistance test. The median sand diameter (D_{50}) in experiment 1 was 0.4 mm, while it was 0.22 mm and 0.21 mm in experiments 2 and 3, respectively. It must be noted that experiment 2 and experiment 3 had 2,527,852 and 2,872,822 particles, respectively, after 5 and 4 s of simulation, while experiment 1 had 2,267,073 particles even after 17 s of simulation (substantially fewer than experiments 2 and 3). The number of particles directly correlates with particle size because more particles are required to represent the same mass for smaller than larger particles. Therefore, experiments 2 and 3 were not further (until the steady-state condition) simulated due to computational limitations, especially concerning the number of particles (max. number of particles, which could be simulated in LIGGGHTS ~ O (10^7)).

In the third set of simulations, the effects of PSDs on the infiltrating characteristics of sand are tested. Here, the rolling resistance model is kept the same (based on the best-performing rolling resistance model from the first set of simulations), and PSDs for gravel and sand are varied by considering the full particle size distributions (full PSDs: 9 gravel and 10 sand classes), simplified particle size distributions (simplified PSDs: 4 gravel and 5 sand classes), and oversimplified particle size distributions (oversimplified PSDs: 1 gravel and 1 sand classes). The particle size classes are grouped with the weighted average method to simplify the full (exact) PSDs of sand and gravel. If two particle classes have diameters d_i and d_j with respective fractions f_i and f_j, then the new size class d_{new} and

its corresponding size fraction f_{new} are calculated using Equations (7a) and (7b). Figure 3 shows the considered PSDs for several cases examined for the particle size distribution test.

$$d_{new} = \frac{d_i f_i + d_j f_j}{f_i + f_j} \tag{7a}$$

$$f_{new} = f_i + f_j \tag{7b}$$

Table 1. Overview of different sets of simulations performed.

Rolling Resistance Test	**Experiment 1 (run1)**	**Experiment 2 (run2)** [a]	**Experiment 3 (run3)** [a]
Process observed in the experiment	Bridging	Bridging	Percolation
Rolling resistance models	Free-rolling, CDT, EPSD, and EPSD2	Free-Rolling and EPSD	Free-Rolling and EPSD
Particle size distribution (number of grain classes)	4 Gravel and 5 sand	4 Gravel and 5 sand	4 Gravel and 4 sand
Young's modulus (Y)	5×10^6	5×10^6	5×10^6
Poisson's ratio (ϑ)	0.45	0.45	0.45
Coefficient of restitution (e)	0.4	0.4	0.4
Coefficient of friction (μ)	0.4	0.4	0.4
Coefficient of rolling friction (μ_r)	0.5 [b]	0.5 [b]	0.5 [b]
Coefficient of rolling viscous damping (C_r)	0.5 [b]	0.5 [b]	0.5 [b]
DEM time step (s)	1×10^{-6}	1×10^{-6}	1×10^{-6}
Bulk porosity of initial gravel bed	0.407	0.407	0.407
Sand insertion rate (kg/s)	0.01	0.01	0.01
Simulation run time (s)	17	5	4
Total number of particles (sand + gravel)	2,267,073	2,527,852	2,872,822
Particle Size Distribution Test [c]	**Full PSD**	**Simplified PSD**	**Oversimplified PSD**
Experiment considered	Experiment 1 (run1)	Experiment 1 (run1)	Experiment 1 (run1)
Particle size distribution (number of grain classes)	9 Gravel and 10 sand	4 gravel and 5 sand	1 Gravel and 1 sand
Rolling resistance model	EPSD	EPSD	EPSD
DEM time step (s)	1×10^{-6}	1×10^{-6}	5×10^{-5}
Bulk porosity of initial gravel bed	0.407	0.407	0.454
Sand insertion rate (kg/s)	0.01	0.01	0.01
Simulation run time (s)	15.8	18.3	40
Total number of particles (sand + gravel)	2,207,512	2,400,200	1,613,433

Notes: [a] Experiment 2 and experiment 3 cases were not further pursued (until the steady-state infiltration state) due to computational and time constraints and an excessively large number of particles. [b] Coefficient of rolling friction and rolling viscous damping between gravel particles are considered to be zero to obtain a flat dense gravel bed of 0.1 m height without significant modulations. [c] The same materialistic properties for the rolling resistance test are considered for the particle size distribution test.

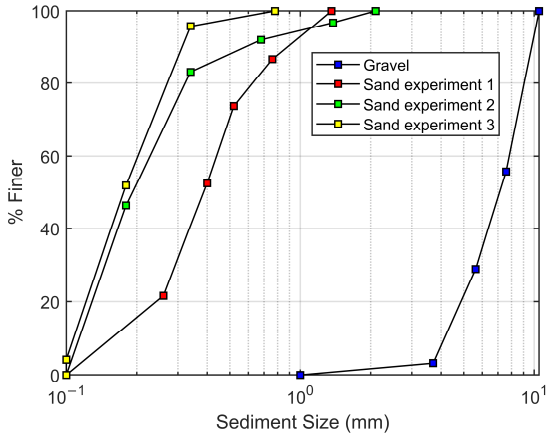

Figure 2. The considered PSDs for gravel and sand (in simplified form) for the rolling resistance test. Note: the gravel bed is the same across the different experiments.

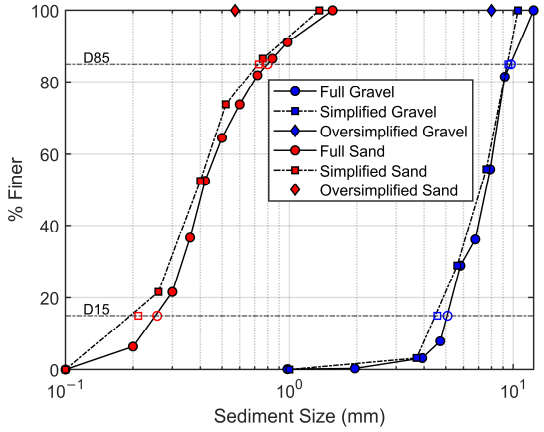

Figure 3. The considered PSDs for gravel and sand in experiment 1 in their full, simplified, and oversimplified versions. Note: empty squares and circles represent D_{15} and D_{85} of different PSDs.

In DEM simulations, the time step is determined by the Rayleigh and Hertz time criteria (Equations (8a) and (8b)), which should be between 10 and 20% of Rayleigh and Hertz times to avoid unphysical particle behavior. In all the numerical simulations, it is ensured that the DEM time step does not exceed 15% of the Rayleigh (dt_R) and Hertz (dt_H) times.

$$dt_R = \frac{\pi r \sqrt{\rho/G}}{0.1631\vartheta + 0.8766} \tag{8a}$$

$$dt_H = 2.87 \left(\frac{{m_{eff}}^2}{\left(R_{eff} \times Y_{eff}^2 \times v_{\max} \right)} \right)^{0.2} \tag{8b}$$

where ρ is the particle density, G is the shear modulus, ϑ is the Poisson's ratio, m_{eff}, R_{eff}, *and* Y_{eff} are the effective mass, effective radius, and effective Young's modulus, and $v_{\max}$ is the maximum relative velocity. It is evident from the equations above that the Rayleigh time is dependent on individual particle characteristics, but the Hertz time is dependent on the characteristics of contacting particles. The time step requirements are proportional to

particle size, which is one of the major challenges in dealing with many particles with a wide range of particle size distributions.

DEM simulations are computationally demanding, and this requirement increases exponentially with smaller particles and (or) a greater number of particles. We had a total number of particles (sand + gravel) in the order of 10^6, which is only one order smaller than the method's limitation concerning a maximum number of particles (O~10^7). All the simulations were performed on SuperMUC (High-Performance Computing; HPC) with 240 processors. The 240 processors were distributed over five nodes with 96 GB RAM. Each simulation was run for a minimum of 48 physical h, costing a minimum of 11,520 CPU h for a simulation. The decision to use 240 processors for the simulations was based on initial trials for finding the optimal number of processors for the considered domain size and particles.

As mentioned, some cases are not pursued until the final steady state/equilibrium infiltration state due to computational and time constraints. For those unfinished cases, the infiltration state is qualitatively analyzed only by comparing the snapshot of the gravel bed at the achieved simulation time. The cases that could be simulated until the final steady state/equilibrium infiltration state are both qualitatively and quantitatively analyzed. Other than looking at snapshots of the infiltration state, the final infiltration state in terms of porosity and sand fraction profiles along the depth of the gravel bed was compared to experimental data. Sand fraction content and porosity profiles were extracted from simulated results. A similar methodology was used to plot the sand content and porosity profiles along the depth of the gravel bed, as considered by Jaiswal et al. [43] in their study. The 3D bed is cut at several cross-sections, generating circles of different diameters, which represent sediments of different sizes. The porosity and sand content are calculated based on the area of sand and gravel particles at the cross-sections. A total of 100 such cross-sections are generated, cutting over 10 cm of the depth of the gravel bed, resulting in sand content and porosity values at 1 mm from the top to the bottom of the gravel bed. More details can be found in their paper, as demonstrated in Figure 4.

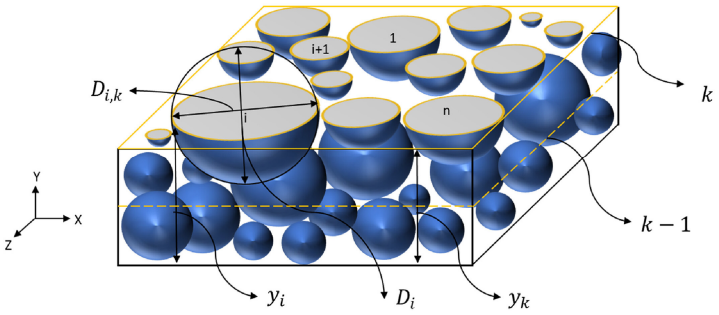

Figure 4. A plane cutting and generating circles across the cutting plane in 3D packing of the gravel bed [43].

Only the sand content profiles were available from the experimental data. Therefore, simulated sand and measured sand content were used to perform statistical analysis to evaluate the simulation's efficiency. We calculated four different statistical parameters to evaluate the performance of our simulation against the experimental data. Four statistical parameters were considered, as shown in the following equations: Mean Average Error (MAE), Mean Square Error (MSE), Root Mean Square Error (RMSE), and Correlation Coefficient (R), where n is the number of data points, y_i and $\hat{y}_i$ are the measured and simulated values, respectively, and $\overline{y}$ and $\overline{\hat{y}}$ are the means of measured and simulated data, respectively.

$$MAE = \frac{1}{n}\sum_{i=1}^{n}|y_i - \hat{y}_i| \quad (9)$$

$$MSE = \frac{1}{n}\sum_{i=1}^{n}(y_i - \hat{y}_i)^2 \quad (10)$$

$$RMSE = \left[\frac{1}{n}\sum_{i=1}^{n}(y_i - \hat{y}_i)^2\right]^{1/2} \quad (11)$$

$$R = \frac{\sum_{i=1}^{n}(y_i - \overline{y})(\hat{y}_i - \overline{\hat{y}})}{\sqrt{\sum_{i=1}^{n}(y_i - \overline{y})^2}\sqrt{\sum_{i=1}^{n}(\hat{y}_i - \overline{\hat{y}})^2}} \quad (12)$$

4. Results and Discussion

4.1. Effects of Non-Sphericity and Irregularities in Particle Shape

Natural sediment particles are non-spherical and irregular. To investigate particle shape effects on the infiltration characteristics of sand in the gravel bed, we implicitly included their effects by restricting the particle's rotational movement with simple models. Experiment 1 (run1) of the reference flume experiment is considered with simplified PSDs for gravel and sand (four gravel and five sand classes). Experiment 1 corresponds to the bridging type of infiltration process, which means that the numerical simulations should also capture most of the sand particles in the upper surface layer, precluding subsequent infiltration. Three rolling resistance models, i.e., CDT, EPSD, and EPSD2, were tested for their ability to capture shape effects. A separate case without any rolling resistance (free-rolling) is also simulated.

The simulations are performed until the bridging layer is formed (minimum of 17 s). The bulk porosity of the initial clean gravel bed (at 1 s) and of infiltration at different times (14, 17, and 18 s) are summarized in Table 2. One can see that a marginal change in porosity occurs after 17 s, indicating that a steady-state condition has been reached at 17 s of simulation. The case with the free-rolling (without any rolling resistance model) is an exception as it has not been pursued further after observing that it results in percolation instead of the desired bridging behavior. The bulk porosities of the gravel bed before and after the sand infiltration at different simulation times for different rolling resistance models considered in this study result in very similar values, indicating that all the rolling resistance models can capture shape effects. Depending on the model used, time and resources allotted to them, each case was run till different simulation times. All three cases were run for a minimum of 17 s and seemed to reach the steady state/equilibrium state; therefore, the results for different simulations are compared after 17 s.

Table 2. Bulk porosities of the initial clean gravel bed and infiltrated gravel bed at different simulation times with different rolling resistance models.

Simulation Time (s)	Bulk Porosity		
	CDT Model	EPSD Model	EPSD2 Model
1	0.409 (initial bulk porosity)		
14	0.3665	0.3672	0.3670
17	0.3578	0.3596	0.3592
18	0.3550	0.3574	-

Figures 5 and 6 show the snapshots of the infiltration state after 17 s of simulation for all four cases from frontal and top perspectives, respectively. It must be emphasized that the reference case (experiment 1; run1) is a bridging case, and numerical simulation should also result in a bridging type of infiltration behavior. It is evident that sand fills the coarse gravel deposit predominantly by percolation for the free-rolling case (no rolling resistance case; Figures 5a and 6a), which is the exact opposite of what had been observed in the reference flume experiment 1. Ideally, as observed in experiment 1, most of the sand particles should have been clogged in the upper surface layer. In the numerical simulation of the free-rolling case, this incorrect behavior of sand particles can be related to the simplification

made in DEM simulations, where gravel and sand particles are simplified as spheres. In the reference flume experiment, natural sediments were considered, which are indeed non-spherical in shape. To capture the shape effects in the infiltration process, it should be considered in numerical simulations. Here, we have included the shape effects with simple rolling resistance models. Contrary to the free-rolling case, the bridging behavior is captured in the three cases with rolling resistance models, as observed in the reference experiment, where most of the sand particles become clogged in the upper surface layer. This indicates that particle shape effects can be implicitly included with simple models but could capture the physically correct infiltration behavior. Figure 5b–d show the infiltration state after 17 s from the frontal perspective for CDT, EPSD, and EPSD2 models, respectively. Figure 6b–d show the infiltration state after 17 s from the top perspective for CDT, EPSD, and EPSD2 models, respectively. Qualitatively, all the rolling resistance models perform very similarly and could capture the anticipated bridging behavior of sand in the static gravel bed.

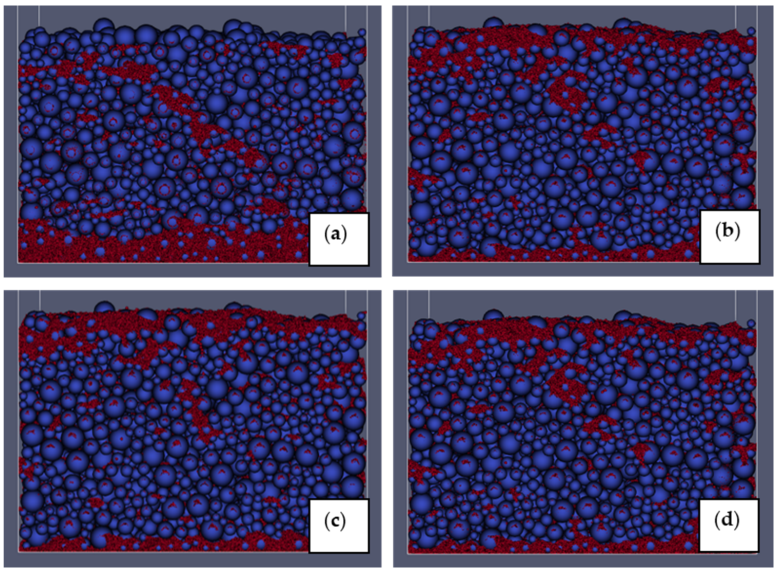

Figure 5. Front view of snapshots of sand infiltration state after 17 s of simulation for experiment 1 with (**a**) free-rolling (without any rolling resistance model), (**b**) CDT model, (**c**) EPSD model, and (**d**) EPSD2 model. Note: the particles are colored by their types (sand in red and gravel in blue).

To evaluate the performance of considered rolling friction models in greater detail, the sand content and porosity profiles are shown in Figure 7. Figure 7a compares the measured and simulated sand content profiles along the depth of the gravel bed for CDT, EPSD, and EPSD2 rolling resistance models, along with the free-rolling case. The profiles are plotted after a steady state/equilibrium has been reached (after 17 s of simulation). We can see that all the rolling resistance models could capture the bridging behavior, as observed in the reference experiment. Most sand particles become trapped in the upper surface layer, precluding subsequent infiltration, resulting in an exponential decay function for sand content. The maximum sand content is found at the top of the gravel bed, which keeps on decreasing along the depth of the gravel bed. The simulated sand content for CDT, EPSD, and EPSD2 rolling resistance models overlap, indicating that all the rolling resistance models considered could be used to include the particle shape effects and capture more particles in the upper surface layer. Compared to the cases with rolling resistance models, the free-rolling case results in very different sand content and porosity profiles

and is far from the observed data in experiment 1. It must be mentioned that the free-rolling case was not pursued further after realizing that it results in percolation instead of bridging behavior. It also means that the data used in the free-rolling case has not reached the steady-state/equilibrium condition. Another important point is that in the free-rolling case (without rolling resistance models), bridging behavior is not captured (see Figures 5a and 6a). An outlier in the experimental data that could have resulted from human, measurement, and/or process-based errors was not compared to the simulated data. Figure 7b shows the porosity profiles along the depth of the gravel bed before and after the infiltration process (steady-state/equilibrium) for different rolling resistance models considered for numerical simulations. Here, CDT, EPSD, and EPSD2 rolling resistance models again resulted in overlapping porosity profiles similar to simulated sand content profiles. The free-rolling case shows very low porosity at the bottom of the gravel bed, indicating that most of the sand particles are reaching the bottom and that the filling of the gravel bed occurs from the bottom to the top. For the cases with rolling resistance models, the bridging type of infiltration is evident from the porosity profile curve, where significant porosity is reduced in the upper surface layer (approx. first 3–4 cm of the gravel bed), and the reduction in porosity is minimal below this depth. This depth is termed bridging or clogging depth. In the experimental studies, the bridging depth is usually 2–5 times the $D_{90,Gravel}$ [31,34,67]. The $D_{90,Gravel}$ is 10 mm in the considered experiment, and accordingly, the bridging depth should be 2–5 cm. Our simulated bridging depth (3–4 cm) aligns well with previously observed bridging depth.

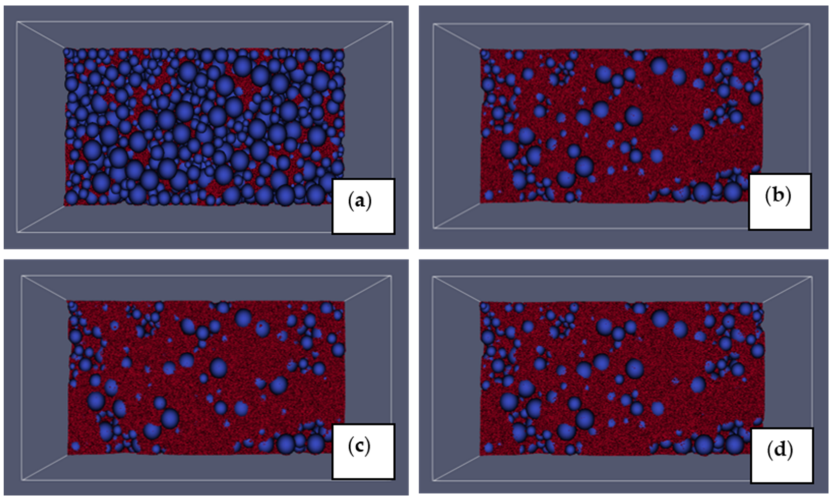

Figure 6. Top view of snapshots of sand infiltration state after 17 s of simulation for experiment 1 with (**a**) free-rolling (without any rolling resistance model), (**b**) CDT model, (**c**) EPSD model, and (**d**) EPSD2 model. Note: the particles are colored by their types (sand in red and gravel in blue).

Furthermore, we evaluated the efficiency of different cases performed for the rolling resistance test with some statistical parameters. The results of the statistical evaluation are summarized in Table 3. While the opposite trend of percolation instead of bridging is evident with a negative correlation coefficient for the free-rolling case, rolling resistance models perform very well with high efficiency and lower error. The CDT model is the least efficient in capturing the shape effects compared to EPSD and EPSD2 models. EPSD and EPSD2 models result in almost the same efficiency, but the EPSD model seems to be slightly better. The EPSD2 model neglects the contribution of the viscous damping torque $\left(M^d_{r,ij} = 0\right)$, but EPSD considers both mechanical spring torque $\left(M^k_{r,ij}\right)$ and a viscous

damping torque $\left(M^d_{r,ij}\right)$. Although the viscous damping torque is marginal compared to the mechanical spring torque, it can be said that both torques should be included to capture correct particle behaviors with high efficiency. We conclude that the EPSD model is most efficient in capturing the particle shape effects for pseudo-static systems such as the process of sand infiltration into the static gravel bed. Therefore, we considered EPSD models for further sets of simulations.

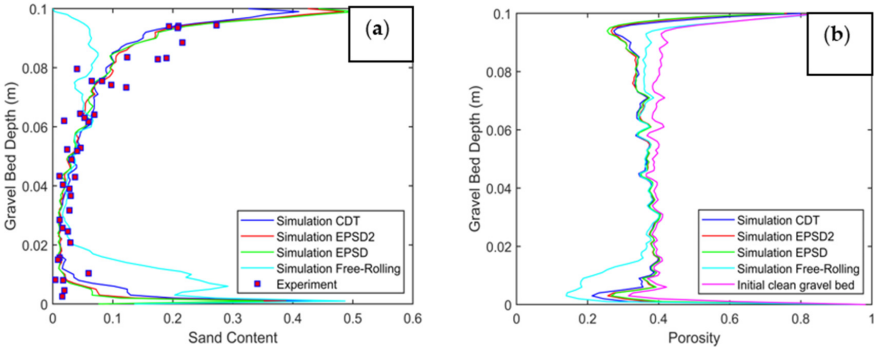

Figure 7. Sand content (**a**) and porosity (**b**) profiles along the depth of the gravel bed after 17 s of simulation for experiment 1.

Table 3. Statistical evaluation of different rolling resistance models against the experiment data.

Statistical Parameter	CDT Model	EPSD Model	EPSD2 Model	Free-Rolling
MAE	0.0278	0.0234	0.0232	0.0708
MSE	0.0018	0.0011	0.0011	0.0109
RMSE	0.0427	0.0334	0.0336	0.1046
R	0.8029	0.8890	0.8875	−0.1528

The second set of simulations, considering experiment 2 (run2) and experiment 3 (run3) of the reference flume experiment, is performed. Experiment 2 corresponds to bridging behavior, and experiment 3 corresponds to the percolation type of infiltration processes. We simulated four cases for the second set of simulations, where the efficiency of the EPSD model is further evaluated. In total, four cases referring to experiments 2 and 3 are simulated without (free-rolling) and with the EPSD rolling resistance model. Unfortunately, these cases are not pursued until the final steady state/equilibrium due to computational and time constraints. Reaching the final infiltration state for experiments 2 and 3 could have resulted in many more particles than the method's limitation concerning the number of particles (O~10^7). As mentioned before, the numbers of particles in numerical simulations were ~2.6×10^6 (in 5 s) and ~2.8×10^6 (in 4 s) for experiment 2 and experiment 3, respectively, approaching the maximum number of particles in the DEM method. Additionally, the simulation becomes extremely slow with an increase in the number of particles and a decrease in the particle size, which further requires extremely small DEM time steps. Furthermore, the time and computational resources available for this study could not have allowed us to simulate experiments 2 and 3 further within a reasonable timeframe. Considering the above-mentioned constraints, we could not simulate these cases for a longer duration. Although these cases were not simulated until the steady state/equilibrium, the results could still be used to investigate shape effects and, thus, the rolling friction model.

Figure 8 shows the snapshot of the infiltration state after 5 s of simulation for experiment 2. Figure 8a shows the infiltration state for the free-rolling case (without any rolling

resistance), and Figure 8b shows the infiltration state for the EPSD rolling friction model. It is evident that more sand particles are clogged when the EPSD rolling friction model is considered, while with the free-rolling case, sand particles directly infiltrate into the bottom of the gravel bed. Since experiment 2 is also a bridging case, most sand particles should be clogged in the upper surface layer. Figure 8c shows the sand content profiles for free-rolling and EPSD model cases in the first 5 cm of gravel bed depth. One can see that sand content is almost zero for the free-rolling case. Contrary to the free-rolling case, the bridging layer appears in the upper layer, where the sand content is higher. More bridges would have been formed, precluding further infiltration of sand, if the case had been persuaded further. The fact that more particles are becoming clogged when the rolling resistance model (ESPD) is also considered for experiment 2. The above discussion indicates that particle shape (thus rolling resistance) is important in capturing the physically correct particle behavior and justifies our approach of including particle shape effects implicitly.

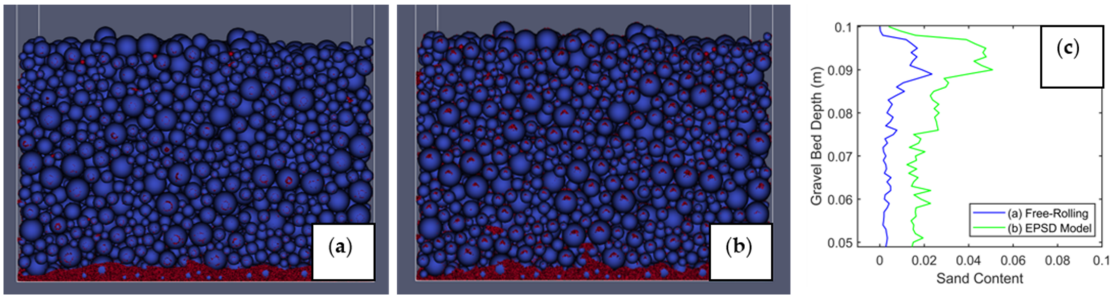

Figure 8. Front view of snapshots of sand infiltration state after 5 s of simulation for experiment 2 with (**a**) free-rolling (without any rolling resistance model), (**b**) EPSD model, and (**c**) the sand content in the first 5 cm of the gravel bed for free-rolling and EPSD model cases. Note: the particles are colored by their types (sand in red and gravel in blue).

Figure 9 shows the snapshot of the infiltration state after 4 s of simulation for experiment 3. Figure 9a shows the infiltration state for the free-rolling case (without any rolling resistance), and Figure 9b shows the infiltration state with the EPSD rolling friction model. Experiment 3 corresponds to the percolation type of infiltration, where sand particles fill the coarse gravel deposit from the bottom to the top without being clogged in the upper layers of the gravel bed. Figure 9c shows the sand content profiles for free-rolling and EPSD model cases in the first 5 cm of gravel bed depth. Here, the sand content is almost zero in the upper layer for the free-rolling case, indicating that all sand particles first reach the bottom of the gravel bed, and filling occurs from the bottom to the top. Sand particles become clogged throughout the gravel bed when the rolling resistance model (EPSD) is considered. We observe that numerical simulations result in a percolation type of behavior when the particles are free to roll (without any rolling resistance model). On the other hand, when the rolling resistance (EPSD) model is considered, the particles start to become clogged in the upper surface layer of the gravel bed. Compared to previous cases (bridging cases), where the rolling resistance model helped us obtain the correct infiltration behavior, it leads towards an incorrect trend for the percolation case. Among all the cases considered for the rolling resistance test (particle shape), it can be stated that the inclusion of rolling resistance could help capture more particles in the upper layer and indirectly consider shape effects in the infiltration process. In percolation cases, the inclusion of rolling resistance seems to be unnecessary, and the percolation trend was evident with free-rolling particles (see Figure 9a).

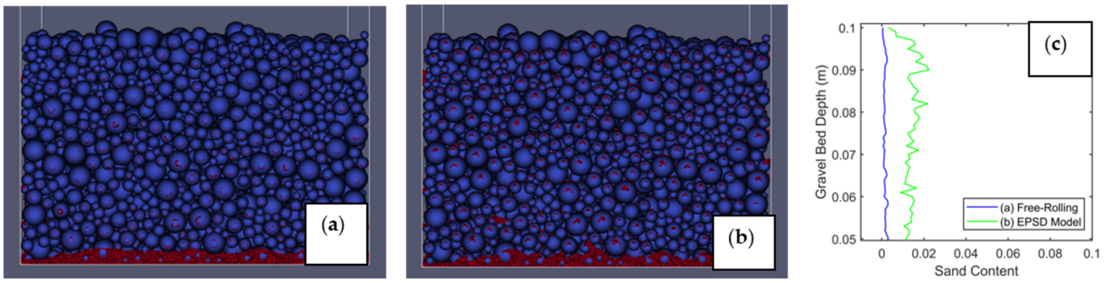

Figure 9. Front view of snapshots of sand infiltration state after 4 s of simulation for experiment 3 with (**a**) free-rolling (without any rolling resistance model), (**b**) EPSD model, and (**c**) the sand content in the first 5 cm of the gravel bed for free-rolling and EPSD model cases. Note: the particles are colored by their types (sand in red and gravel in blue).

Our observation that rolling resistance models are not necessary for percolation cases could probably be explained by the concept of controlling constriction size (smallest pore size) and its relation to sand and gravel sizes. Percolation occurs when controlling constriction is larger than the coarsest sand particle. Hence, no sand particle should become clogged until it reaches the bottom of the gravel bed. On the other hand, if the controlling constriction size is smaller than the sand particles (at least some), sand particles start to become clogged at the pores that are more diminutive than their sizes, forming bridges. Once some pores are blocked, they subsequently preclude sand infiltration, forming more bridges. For bridging cases (experiments 1 and 2), $D_{15,Gravel}/D_{85,Sand} < 10.6$, and for percolation cases (experiment 3), $D_{15,Gravel}/D_{85,Sand} > 15.4$. Here, $D_{85,Sand}$ represents the larger portion of sand as 85% of sand is smaller than that size, and $D_{15,Gravel}$ not only indicates that 15% of gravel is smaller than that size but also indirectly represents the approx. size of the pores in the gravel bed [68–71]. It must be emphasized that $D_{15,Gravel}$ representing the pore sizes, is only a simplified representation, but the pore sizes vary from one another and follow size distributions like particles. However, $D_{15,Gravel}$ can represent the average pore size in a gravel bed to a reasonable approximation and is useful in practical engineering applications. For percolation to happen, pore size ($D_{15,Gravel}$) must be at least 15.4 times larger than $D_{85,Sand}$. In other words, percolation occurs when the sand size is extremely small compared to pore sizes in the gravel bed. Because of considerable differences in the largest sand particle and pore size, particle shape could not remain significant in governing infiltration. This also suggests that when there is a huge difference in the largest sand particle and pore space, the sand particles shape (in terms of shpericity and irregularities) does not play any role within the context of infiltration. Shape effects are important and can play a significant role when they are of similar sizes, at least of the same order. This indicates that rolling resistance models are not necessary for smaller sand sizes ($D_{15,Gravel}/D_{85,Sand} > 15.4$).

Another possible reason for our observation that rolling resistance is not required for percolation cases, more specifically when $D_{15,Gravel}/D_{85,Sand} > 15.4$, could be related to the history of sand particles (how and since when the sand particles are in the river system) and the fluvial process (how sand particles have been transported in the river system). There is a possibility that smaller sand particles tend to be rounder and more spherical than larger sand particles. The rounding of sand particles is possible, and a study has shown that any rounding of sand grains by aqueous traction transportation requires transportation over many thousands of miles [72]. Sand particles found in natural river systems go through several fluvial processes from their origin to several transport regimes in the river system, resulting in shape evolution by bed load transport [73]. Smaller sand particles in the river system could become smoother, rounder, and probably spherical as a result of erosive and abrasive actions, which happen during transportation. Additionally, flowing

water can favor the smoothing of sand grains, which could become more significant as particles become smaller and smaller. It is possible that smaller sand particles are rounder and spherical and, therefore, might not necessarily require any treatment (explicitly or implicitly) to include non-sphericity. If non-sphericity is included for spherical particles, it would result in an incorrect behavior, as seen in the numerical simulation of experiment 3. However, historical information is very difficult to acquire and generally not available. Further field investigations are necessary to gather more evidence for the hypothesis that sand particles become rounder, smoother, and spherical as they become smaller due to the fluvial transport process.

Another interesting observation could be made from performed DEM simulations: irrespective of the infiltration process (bridging or percolation), some sand particles could always reach the bottom of the gravel bed. This behavior is also persistent in cases where the rolling resistance models are considered or discarded. In other words, a small portion of sand particles could always reach the bottom of the gravel bed, at least at the beginning of the infiltration process, even in bridging cases. Gibson et al. [38] also observed this behavior and called it granular sorting, which is predominant in the infiltration process. Smaller particles preferentially pass through pore spaces, advancing deeper into the gravel framework. The infiltration process is primarily a function of the pore throat and sand gradation distributions. There is always a possibility that some sand particles are smaller than some pore throats and traverse through the pore connections until they approach pore throat (opening of pore connection) smaller than approaching sand particle, which restricts the subsequent sand to be trapped, resulting in the formation of bridges. Additionally, the large values of sand fraction and porosity reduction at the bottom could be related to wall effects and wall–particle interactions. A sudden increase in the sand content at the bottom of the gravel bed could be due to the wall effects as larger pore sizes between walls and gravel particles result in more pore space available for sand particles to accumulate.

4.2. Effects of Particle Size Distribution (PSD)

The third set of simulations was aimed at investigating the effects of different PSDs on the process of sand infiltration into a static gravel bed. Natural sediments contain a wide range of particle sizes. To simplify the system, the grain sizes are grouped with corresponding fractions, resulting in particle size distribution (PSD) curves. The more grain classes there are, the more accurately the PSD represents the natural system. On the other hand, considering wide particle sizes in numerical simulations, especially in the Lagrangian framework (DEM method), is very challenging due to the heavy computational requirements and limitations of the method concerning number of particles. As mentioned in several instances in this paper, the maximum number of particles that could be simulated with the DEM method in LIGGGHTS software (version 23.02) is in O~10^7; therefore, considering a decent domain size with a PSD resembling the complex natural sediments is difficult and may cross the limit concerning the maximum number of particles depending on the particle size range. Our simulations of experiments 2 and 3 approached the maximum number of particles despite the consideration of simplified PSDs (four gravel and five sand classes for experiment 2 and four gravel and four sand classes for experiment 3). Experiment 3, a percolation case, would be especially vulnerable to limitations concerning the maximum number of particles in the DEM method. A simplification of PSDs is necessary to simulate the infiltration processes. However, the question remains: What simplification is justified enough to capture the required process?

We aim to answer this question by considering three different combinations of PSDs for gravel and sand, varying from exact to very simplified PSDs. Three separate cases are simulated by considering full PSDs (9 gravel and 10 sand classes), simplified PSDs (4 gravel and 5 sand classes), and oversimplified PSDs (1 gravel and 1 sand classes), keeping the same rolling resistance model (EPSD) and other DEM settings. The simulation time each case takes to reach the steady state/equilibrium differs from one another, depending on the number of particles and particle sizes. Experiment 1 (run1) of the flume experiment [38]

is considered, which is a bridging case, for particle size distribution (PSD) effects on the sand infiltration process. Snapshots of the infiltration state are compared for different cases. Furthermore, porosity and sand content profiles are compared, and statistical analysis is performed against the experimental data regarding their ability to capture correct results.

Figure 10 shows the snapshots of the infiltration state for numerical simulations for experiment 1 with different PSD combinations. Figure 10a–c show the snapshots from the frontal perspective for full PSDs, simplified PSDs, and oversimplified PSDs, respectively. Figure 10d–f show the snapshots from the top perspective for full PSDs, simplified PSDs, and oversimplified PSDs, respectively. Cases for full, simplified, and oversimplified PSDs are run for 15.8, 18, and 40 s of simulation, respectively. One can see that bridging behavior is observed in the cases of full and simplified PSDs. However, in the oversimplified PSD case, the percolation type of infiltration is observed instead of the desired bridging process. It is evident from the full PSD case (Figure 10a,d) that it captures most of the sediments in the upper surface layer, and by the time the steady state/equilibrium is approaching (15.8 s), a bridging layer is distinctly visible. A small portion of sand could still reach the bottom of the gravel bed, but it is marginal, and the overall behavior is mainly the bridging type of infiltration. Similarly, the sand clogging pattern in the upper layer of the gravel bed is observed for the case of simplified PSDs (see Figure 10b,e). Compared to the full PSD case, more sand particles could reach the bottom of the gravel bed for the simplified PSD case, but the overall infiltration behavior is still a bridging type of infiltration. A portion of sand could always reach the bottom of the gravel bed due to gradational sorting until larger sand particles approach the pore and bridges are formed, precluding subsequent infiltration, described in greater detail in Section 4.1. Both the full and simplified PSD cases could capture the bridging behavior observed in experiment 1. The case with oversimplified PSDs resulted in the opposite behavior, where the filling of the gravel bed occurs from the bottom to the top (percolation behavior). One can see that pores in the lower layer of the gravel bed are fully packed with sand particles at 40 s of simulation, and the upper layer of the gravel bed still has some unclogged pores (see Figure 10c,f). The rest of the gravel bed (upper layer) would have been also filled with sand particles, resulting in a fully packed gravel bed, if the case was run further beyond 40 s of simulation. We intentionally did not pursue the oversimplified case after 40 s. The oversimplified PSD case resulted in an incorrect infiltration behavior (percolation instead of bridging). Therefore, it would have been a waste of computational resources if pursued further. The full PSD case requires much more computational time and resources to reach the steady-state condition, while the simplified PSD case is faster and is able to capture the correct bridging behavior, indicating that the grain classes can be simplified and that the correct particle behavior can be captured. However, the simplifications in PSDs should be performed carefully, and oversimplification might lead to incorrect particle behavior, as shown by our oversimplified case (one gravel and one sand class), which was indeed much faster than the other two cases but could not capture the correct particle behavior within the context of sand infiltration into the static gravel bed. The simplifications in PSDs are necessary to realize the numerical simulation of infiltration processes with reasonable computational resources and time, but it may lead to an incorrect behavior; therefore, it needs to be addressed properly. Oversimplification should be avoided.

Detailed sand content and porosity profiles are shown in Figure 11. Figure 11a shows the sand content profiles for different PSDs considered in numerical simulations against the experimental data. In the cases with full PSDs and simplified PSDs, the maximum sand content is found in the upper layer, which decreases exponentially with the depth of the gravel bed. It is possible that the full PSD case did not reach the final steady-state infiltration state before 15.8 s of simulation due to computational and time constraints. However, it seems to be approaching the steady-state condition as it could capture the correct infiltration behavior with quite good agreement with the experimental data. On the other hand, the oversimplified PSD case results in the maximum sand content at the bottom of the gravel bed, which remains relatively high along the height of the gravel bed (from the

bottom to the top). Please note that the sand content for the oversimplified case is plotted at 40 s. Moreover, by that time, the gravel bed had not reached equilibrium. Although the sand content profile for the oversimplified case does not represent the final infiltration state, it still shows a distinct pattern of percolation behavior, where filling occurs from the bottom to the top. In the original experiment, the adopted case corresponds to bridging behavior. Figure 11b,c show the initial and final porosity profiles for different PSDs considered, respectively. The initially created gravel bed has higher porosity for oversimplified PSDs than simplified and full PSD cases, which eventually resulted in different packing/infiltration processes and quite different final porosities than expected for bridging cases. It has also shown that mono- and poly-disperse particle assemblies have different initial porosities and that PSD plays a crucial role in how the packing is formulated [66]. Due to the simplification of PSDs, not only are the gravel bed characteristics modified but the characteristics of the infiltrating sand are also mutated, which has consequences for the sand infiltration process. Interestingly, the simplified PSD case results in more or less similar initial and final porosity profiles as the full PSD case, indicating that the packing characteristics are not modified significantly and resolved enough to capture the correct infiltration behavior. We observe that oversimplification can lead to wrong infiltration behavior. At the same time, a simplification can still be helpful and give correct results, provided the simplification of PSDs does not result in significant changes in the characteristics of the gravel bed and infiltrating sand (pore size, pore connectivity, and sizes of sediments itself).

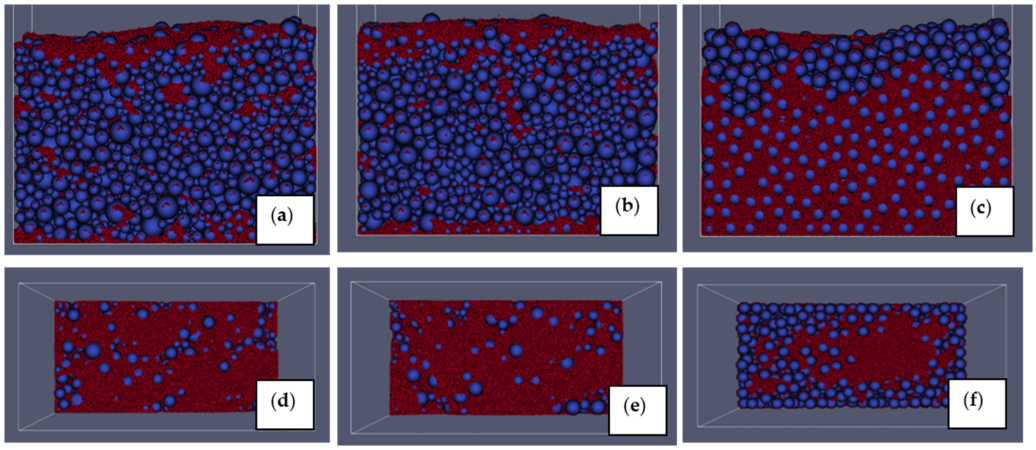

Figure 10. Frontal (**a**–**c**) and top (**d**–**f**) perspectives of snapshots of sand infiltration state simulation for experiment 1 considering full PSDs after 15.8 s (**a**,**d**), simplified PSDs after 18 s (**b**,**e**), and oversimplified PSDs after 40 s (**c**,**f**). Note: the particles are colored by their types (sand in red and gravel in blue).

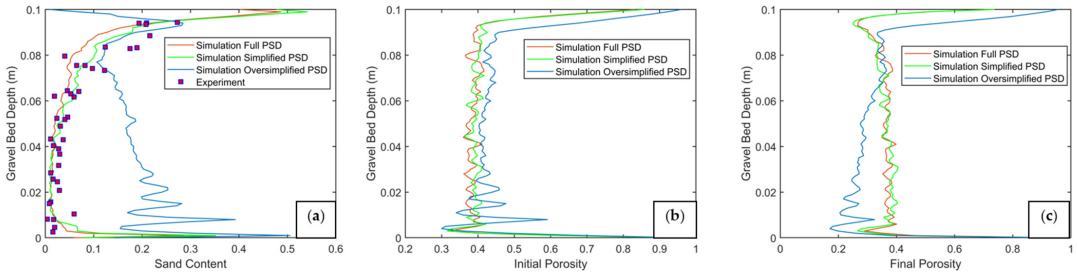

Figure 11. Sand content (**a**), initial porosity (**b**), and final porosity (**c**) profiles along the depth of the gravel bed considering different particle size distributions (PSDs) for sand and gravel.

Statistical analysis was also performed for the particle size distribution test, similar to the rolling resistance test, with some statistical parameters (MAE, MSE, RMSE, and R), and is summarized in Table 4. Again, only sand content data were available in the experiment. Therefore, the statistical analysis is based on sand content only. The oversimplified PSD case resulted in an incorrect infiltration behavior, demonstrated by high error values and a negative correlation coefficient. A negative correlation coefficient for the oversimplified PSD case also means that the predicted trend is opposite to the one observed in the experiment. Interestingly, the simplified PSD case has a slightly higher correlation coefficient, and MAE, MSE, and RMSE are marginally higher for the full PSD case. Compared to the simplified PSD case reaching a steady state in 18 s, the full PSD case might not have reached the final steady state of infiltration in 15.8 s; therefore, statistically, it seems to be less accurate than the simplified case. Another reason for the full PSD case being statistically less accurate than the simplified PSD case could be the larger DEM time steps and considered materialistic properties in the full PSD case. The full PSD case would show better performance in the statistical analysis if simulated beyond 15.8 s and with further calibration with even smaller DEM time steps and more suitable materialistic properties. Overall, the simplified and full PSD cases resulted in reasonably good agreement with the experimental data, indicating that the simplification of PSDs of sand and gravel could still capture a correct infiltration behavior, but it needs to be carefully handled as oversimplification could entirely modify the gravel bed and infiltrating characteristics, which do not represent the actual system considered for numerical simulations.

Table 4. Statistical evaluation of different PSDs considered for numerical simulations against the experiment data.

Statistical Parameter	Full PSDs *	Simplified PSDs	Oversimplified PSDs #
MAE	0.0264	0.0234	0.1329
MSE	0.0015	0.0011	0.0251
RMSE	0.0387	0.0334	0.1584
R	0.8765	0.8890	−0.0139

Notes: * The full PSD case was simulated for 15.8 s only, and it might not have achieved the final steady-state infiltration state at 15.8 s of simulation. # The oversimplified PSD case was not pursued further after 40 s. Reason being that it resulted in percolation instead of anticipated bridging behavior.

Table 5 summarizes the computational performances for cases considered for the particle size distribution test, with the respective numbers of particles. Please note that sand particles are inserted continuously as the simulation progresses. After every 1 s, 146,799, 133,127, and 40,279 sand particles are poured over the gravel bed for the full, simplified, and oversimplified PSDs, respectively, equivalent to a 0.01 kg/s sand insertion rate. One can see that more sand particles are required to represent the same mass rate when more grain classes (wider PSDs) are considered. The increase in the number of particles also results in extra computational overhead, which slows down the simulations due to the continuous increase in the number of particles. The full PSD case is more vulnerable to the computational speed issue; therefore, the full PSD case was only pursued for 15.8 s of simulation.

Table 5. Computational performance of the full, simplified, and oversimplified PSD cases in terms of CPU hours and number of particles.

Computational Performance	Full PSDs *	Simplified PSDs	Oversimplified PSDs
Number of grain classes	9 Gravel and 10 sand	4 Gravel and 5 sand	1 Gravel and 1 sand
Simulation time (s)	15.8	18	40

Table 5. *Cont.*

Computational Performance	Full PSDs *	Simplified PSDs	Oversimplified PSDs
Number of particles (sand + gravel)	2,207,512	2,400,200	1,573,155
CPU hours	23,040	23,040	5760
Simulation time reached after 1 day (s)	12	14	40

Notes: * The full PSD case was simulated for 15.8 s only, and it might not have achieved the final steady-state infiltration state at 15.8 s of simulation.

Figure 12 shows the isometric view of the infiltration state of full and simplified PSD cases after 15.8 s and 18 s of simulation duration, respectively. It is evident that both cases result in very similar results concerning the sand infiltration process over the static gravel bed. Despite simplifying the PSDs for sand and gravel with reduced grain classes, the simplified PSD case could capture the correct infiltration behavior with excellent statistical performance, indicating that the basic characteristics of the gravel bed and infiltrating sand remain similar to the full PSD case. As mentioned in the previous section, $D_{15,Gravel}$ and $D_{85,Sand}$ are crucial parameters that govern the infiltration process. The $D_{15,Gravel}$ represents the average pore size of the gravel bed, and $D_{85,Sand}$ represents the larger portion of the infiltrating sand [68–71]. In order to capture the correct infiltration behavior, these two parameters should not be modified significantly. For the simplified PSD case, the $D_{15,Gravel}$ and $D_{85,Sand}$ is very similar to the full PSD case (see Figure 3), while $D_{15,Gravel}$ and $D_{85,Sand}$ for the full PSD case are 5.09 mm and 0.79 mm, respectively, resulting in the packing ratio $D_{15,Gravel}/D_{85,Sand}$ = 6.44. For simplified PSD cases, $D_{15,Gravel}$ and $D_{85,Sand}$ are 4.58 mm and 0.73 mm, respectively, resulting in the packing ratio $D_{15,Gravel}/D_{85,Sand}$ = 6.14. One can see that the $D_{15,Gravel}/D_{85,Sand}$ ratio is around 6 for both simplified and full PSD cases, which corresponds to the bridging infiltration process as per the threshold ($D_{15,Gravel}/D_{85,Sand}$ < 10.6) suggested by Gibson et al. [38]. On the other hand, the oversimplified PSD case represented the gravel and sand by a binary system and had mono-disperse sand and gravel, with particle sizes of 8 mm and 0.572 mm, respectively. As the case was mono-disperse, having only one size for both sand and gravel, $D_{15,Gravel}$ and $D_{85,Sand}$ could be calculated. Still, the size ratio could be related to the thresholds suggested by Gibson et al. [38]. Due to the oversimplification, the gravel bed and sand characteristics are entirely modified and no longer represent the experimental conditions, demonstrated by the size ratio of D_{Gravel}/D_{Sand} = 14, which is much higher than the threshold for bridging ($D_{15,Gravel}/D_{85,Sand}$ < 10.6). Therefore, the oversimplified PSD case resulted in a percolation type of infiltration instead of bridging behavior. If the oversimplification of PSDs for gravel and sand is unavoidable due to computational limitations, one could extract the $D_{15,Gravel}$ and $D_{85,Sand}$ from the particle size distribution curve and consider them to represent the binary mixture of the gravel–sand combination. Thus, the size ratio is the same and within the thresholds for different infiltration processes. However, representing the gravel and sand with $D_{15,Gravel}$ and $D_{85,Sand}$ is not appropriate because $D_{85,Sand}$ still represents the larger portion of sand (85% of sand smaller than that size) but $D_{15,Gravel}$ only represents the smaller portion of gravel (15% of gravel smaller than that size). We suggest that simplification is justified as long as the basic characteristics of the gravel bed and infiltrating sand remain similar to PSDs used in the reference experiment (full or exact PSDs). This would not only result in the anticipated infiltration process but also could save significant computational resources.

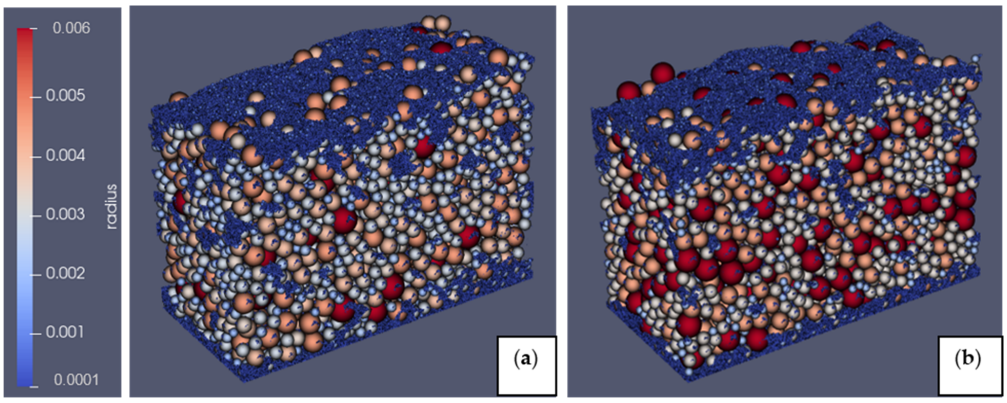

Figure 12. Isometric view of snapshots of sand infiltration state simulation for experiment 1 considering full PSDs after 15.8 s (**a**) and simplified PSDs after 18 s (**b**). Note: the particles are colored by their sizes.

5. Conclusions

This work investigates particle shape effects, which arise due to non-sphericity and irregularities in particle shape. This study also focuses on the effects of particle size distributions (PSDs) on the infiltrating characteristics of sand in a static gravel bed. Particle shape is included implicitly by adding rolling resistance to particles, which indirectly incorporates particle shape effects. The applied Lagrangian particle tracking method (DEM method) is computationally expensive and still limited to a definite number of particles (O~10^7). Therefore, with the available computational resources, resolving particle shapes for both gravel and sand present in the system is impossible, and including shape effects implicitly seems to be the most efficient way. We tested three different rolling resistance models, namely CDT, EPSD, and EPSD2 models. Separate cases without rolling resistance models (free-rolling) have also been simulated to represent the infiltration process for free-rolling spherical particles. Furthermore, particle size distributions (PSDs) of sand and gravel were simplified to investigate the PSD's effects on the numerical simulation of sand infiltration process. To do so, the ability of full PSD and simplified versions of PSDs to capture the observed infiltration process were tested in the adapted flume experiment.

We showed that the threshold for bridging and percolation ($D_{15,Gravel}/D_{85,Sand}$) could help decide the number of grain classes for sand and gravel in the DEM simulations, which not only results in the anticipated infiltration process but also saves significant computational resources. Additionally, the $D_{15,Gravel}/D_{85,Sand}$ ratio can be used to decide whether the rolling friction should be considered for numerical simulations, providing information on scenarios when the shape effect plays a crucial role. Due to computational and time constraints, we could not pursue some cases, especially cases with very small sand sizes (percolations and full PSD cases), until final steady-state infiltration, which can be attempted in future studies. Despite not reaching the steady state/equilibrium for those cases, we could capture the bridging or percolation trend as observed in the original experiment. We intentionally avoided the flowing water effects in this study and focused more on the particle shape and PSD effects, which were either simplified or neglected in previous studies. The process of sand infiltration into the static gravel bed is predominantly gravity-dominated as sand infiltration driven by intra-gravel flow is similar to sand infiltration driven by gravity, as hypnotized by Cui et al. [40] and confirmed by Jaiswal et al. [43]. The findings from this study should also be valid for cases with flowing water, provided the gravel bed remains immobile. In this study, we considered a relatively smaller domain size than the actual flume experiment to simulate a decent number of cases with a reasonable timeframe and with limited computational resources. A more

detailed study covering larger domain sizes and an even wider range of gravel and sand compositions would help to confirm our observations. Future studies focusing on these aspects could shed more light on the process of sand infiltration into the static gravel bed. Taken together, the following conclusions can be drawn from the conducted study:

- Rolling resistance models efficiently incorporate effects of non-sphericity and irregularities in particle shape when modeling quasi-static systems such as sand infiltration into a static gravel bed. For the bridging cases ($D_{15,Gravel}/D_{85,Sand} < 10.6$), rolling resistance models are vital for correct or anticipated infiltration behavior.
- Contrary to the bridging cases, for the percolation cases ($D_{15,Gravel}/D_{85,sand} > 15.4$), excluding the rolling friction model (free-rolling case) could capture the physically correct percolation type of infiltration, indicating that when pore size becomes significantly larger than infiltrating sand particles, particle shape effects tend to vanish. Shape effects are more important for coarser than finer sand particles. Therefore, the rolling resistance models in modeling percolation should be avoided.
- A comparison of different rolling resistance models shows that all the considered models (CDT, EPSD, and EPSD2) are able to capture particle shape effects wherever the shape effects seem to be vital. The EPSD model performs marginally better than the other two models. Applying these models, we can implicitly consider the effects of particle shape by adding artificial resistance to particle rotation. These models can help obtain the correct infiltration behavior for bridging cases, but the inclusion of rolling resistance can also lead to non-physical and undesirable results for percolation cases. Therefore, it should be used carefully depending on the relative sand–gravel size.
- The DEM method is computationally expensive and limited to a definite number of particles with the currently available computational resources, architecture, and solution algorithms. This usually requires the particle size distributions (PSDs) for sand and gravel to be simplified to represent the required volume or mass of sediments by a lower number of particles. Simplification is necessary to realize the numerical simulations, but oversimplification could entirely modify the characteristics of gravel beds and infiltrating sand, resulting in completely different infiltration behaviors than anticipated.
- A sufficient number of gravel and sand classes (4–5 grain classes) could be a good compromise between the accuracy and realizability of numerical simulations with a decent domain size, which can capture the bulk behavior of sand and gravel beds. Simplified cases (with four grain classes for gravel and five for sand) could capture the correct bridging behavior and perform very well in statistical evaluation against the experimental data. For this purpose, $D_{15,Gravel}/D_{85,Sand}$ could be considered as a measure of the gravel bed and infiltrating sand characteristics. If the $D_{15,Gravel}/D_{85,Sand}$ remain similar to the exact/full PSDs for sand and gravel, then the simplification is justified and should not lead to any non-physical behavior concerning the infiltration process being investigated.

Author Contributions: A.J. (Conceptualization, Investigation, Data Curation, and Writing—Original Draft), M.D.B. (Supervision, Writing Review and Editing), N.R. (Resources and Writing—Review and Editing), and P.R. (Supervision). All authors have read and agreed to the published version of the manuscript.

Funding: This research received no external funding.

Data Availability Statement: The data that support the findings of this study are available from the corresponding author upon reasonable request.

Acknowledgments: We would like to thank the Leibniz Supercomputing Centre (LRZ) for providing the computational resources required for our study. This study was conducted as part of a PhD research project at TUM with the KAS scholarship. We are very thankful to Konrad-Adenauer-Stiftung (KAS) for making this possible. We would also like to thank Roser Casas Mulet and Subhojit Kadia, both from TUM, for their valuable suggestions. We acknowledge the support of Martin Ohlerich

from LRZ for guiding the corresponding author in understanding the workflow and architecture of the supercomputing facility.

Conflicts of Interest: The authors declare no conflict of interest.

References

1. Ock, G.; Gaeuman, D.; McSloy, J.; Kondolf, G.M. Ecological functions of restored gravel bars, the Trinity River, California. *Ecol. Eng.* **2015**, *83*, 49–60. [CrossRef]
2. Hauer, F.R.; Locke, H.; Dreitz, V.J.; Hebblewhite, M.; Lowe, W.H.; Muhlfeld, C.C.; Nelson, C.R.; Proctor, M.F.; Rood, S.B. Gravel-bed river floodplains are the ecological nexus of glaciated mountain landscapes. *Sci. Adv.* **2016**, *2*, e1600026. [CrossRef]
3. Casas-Mulet, R.; Pander, J.; Prietzel, M.; Geist, J. The HydroEcoSedimentary tool: An integrated approach to characterise interstitial hydro-sedimentary and associated ecological processes. *River Res. Appl.* **2021**, *37*, 988–1002. [CrossRef]
4. Greig, S.M.; Sear, D.A.; Carling, P.A. A review of factors influencing the availability of dissolved oxygen to incubating salmonid embryos. *Hydrol. Process.* **2007**, *21*, 323–334. [CrossRef]
5. Wood, P.J.; Armitage, P.D. Biological Effects of Fine Sediment in the Lotic Environment. *Environ. Manag.* **1997**, *21*, 203–217. [CrossRef]
6. Walling, D.; Owens, P.; Carter, J.; Leeks, G.; Lewis, S.; Meharg, A.; Wright, J. Storage of sediment-associated nutrients and contaminants in river channel and floodplain systems. *Appl. Geochem.* **2003**, *18*, 195–220. [CrossRef]
7. Jones, J.I.; Collins, A.L.; Naden, P.S.; Sear, D.A. The relationship between fine sediment and macrophytes in rivers. *River Res. Appl.* **2012**, *28*, 1006–1018. [CrossRef]
8. Wooster, J.K.; Dusterhoff, S.R.; Cui, Y.; Sklar, L.S.; Dietrich, W.E.; Malko, M. Sediment supply and relative size distribution effects on fine sediment infiltration into immobile gravels. *Water Resour. Res.* **2008**, *44*. [CrossRef]
9. East, A.E.; Pess, G.R.; Bountry, J.A.; Magirl, C.S.; Ritchie, A.C.; Logan, J.B.; Randle, T.J.; Mastin, M.C.; Minear, J.T.; Duda, J.J.; et al. Large-scale dam removal on the Elwha River, Washington, USA: River channel and floodplain geomorphic change. *Geomorphology* **2015**, *228*, 765–786. [CrossRef]
10. Bednarek, A.T. Undamming rivers: A review of the ecological impacts of dam removal. *Environ. Manag.* **2001**, *27*, 803–814. [CrossRef]
11. Born, S.M.; Genskow, K.D.; Filbert, T.L.; Hernandez-Mora, N.; Keefer, M.L.; White, K.A. Socioeconomic and Institutional Dimensions of Dam Removals: The Wisconsin Experience. *Environ. Manag.* **1998**, *22*, 359–370. [CrossRef]
12. Cui, Y.; Parker, G.; Braudrick, C.; Dietrich, W.E.; Cluer, B. Dam Removal Express Assessment Models (DREAM). *J. Hydraul. Res.* **2006**, *44*, 291–307. [CrossRef]
13. Cui, Y.; Wilcox, A.C. Numerical modeling of sediment transport upon dam removal: Application to Marmot Dam in Sandy River, Oregon. In *Sedimentation Engineering, ASCE Manual*; Oregon: Reston, VA, USA, 2005; Volume 54.
14. Doyle, M.W.; Stanley, E.H.; Harbor, J.M. Channel adjustments following two dam removals in Wisconsin. *Water Resour. Res.* **2003**, *39*, 1011. [CrossRef]
15. Pollard, A.I.; Reed, T. Benthic invertebrate assemblage change following dam removal in a Wisconsin stream. *Hydrobiologia* **2004**, *513*, 51–58. [CrossRef]
16. Stanley, E.H.; Luebke, M.A.; Doyle, M.W.; Marshall, D.W.I. Short-Term Changes in Channel Form and Macroinvertebrate Communities Following Low-Head Dam Removal. *J. N. Am. Benthol. Soc.* **2002**, *21*, 172–187. [CrossRef]
17. Minshall, G.W.; Royer, T.V.; Robinson, C.T. Response of the Cache Creek macroinvertebrates during the first 10 years following disturbance by the 1988 Yellowstone wildfires. *Can. J. Fish. Aquat. Sci.* **2001**, *58*, 1077–1088. [CrossRef]
18. Vieira, N.K.M.; Clements, W.H.; Guevara, L.S.; Jacobs, B.F. Resistance and resilience of stream insect communities to repeated hydrologic disturbances after a wildfire. *Freshw. Biol.* **2004**, *49*, 1243–1259. [CrossRef]
19. Lisle, T.E. Sediment transport and resulting deposition in spawning gravels, north coastal California. *Water Resour. Res.* **1989**, *25*, 1303–1319. [CrossRef]
20. Swanson, F.J.; Dyrness, C.T. Impact of clear-cutting and road construction on soil erosion by landslides in the western Cascade Range, Oregon. *Geology* **1975**, *3*, 393. [CrossRef]
21. Parker, G.; Cui, Y.; Imran, J.; Dietrich, W.E. Flooding in the lower Ok Tedi, Papua New Guinea due to the disposal of mine tailings and its amelioration. In Proceedings of the Recent Trends of Floods and Their Preventive Measures, Hokkaido River Disaster Prevention Res. Res. Cent., Sapporo, Japan, 20–21 June 1996.
22. Yu, A.B.; Standish, N. Estimation of the porosity of particle mixtures by a linear-mixture packing model. *Ind. Eng. Chem. Res.* **1991**, *30*, 1372–1385. [CrossRef]
23. Yu, A.B.; Standish, N. Limitation of proposed mathematical models for the porosity estimation of nonspherical particle mixtures. *Ind. Eng. Chem. Res.* **1993**, *32*, 2179–2182. [CrossRef]
24. Yu, A.B.; Zou, R.P.; Standish, N. Modifying the Linear Packing Model for Predicting the Porosity of Nonspherical Particle Mixtures. *Ind. Eng. Chem. Res.* **1996**, *35*, 3730–3741. [CrossRef]
25. Lauck, T. A Simulation Model for the Infiltration of Sediment into Spawning Gravel. Master's Thesis, Humboldt State University, Arcata, CA, USA, 1991.
26. Herrero, A.; Berni, C. Sand infiltration into a gravel bed: A mathematical model. *Water Resour. Res.* **2016**, *52*, 8956–8969. [CrossRef]

27. Shen, E.; Liu, G.; Jia, Y.; Dan, C.; Abd Elbasit, M.A.; Liu, C.; Gu, J.; Shi, H. Effects of raindrop impact on the resistance characteristics of sheet flow. *J. Hydrol.* **2021**, *592*, 125767. [CrossRef]
28. Einstein, H.A. Deposition of Suspended Particles in a Gravel Bed. *J. Hydr. Div.* **1968**, *94*, 1197–1206. [CrossRef]
29. Herrero, A.; Berni, C.; Camenen, B.; Thollet, F. Laboratory Analysis on silt Infiltration into a Gravel bed. Modélisation Physique de L'infiltration Dans un lit de Graviers. 2015. Available online: https://hal.science/hal-01362697 (accessed on 27 May 2024).
30. NCASI. *Factors Affecting Changes in the Percent of Fine Sediment in Gravel Bedded Channels*; Technical Bulletin No. 0354; NCASI: Research Triangle Park, NC, USA, 1981.
31. Diplas, P.; Parker, G. Deposition and removal of fines in gravel-bed streams. *Dyn. Gravel-Bed Rivers* **1992**, 313–329.
32. Evans, E.; Wilcox, A.C. Fine sediment infiltration dynamics in a gravel-bed river following a sediment pulse. *River Res. Applic.* **2014**, *30*, 372–384. [CrossRef]
33. Lunt, I.A.; Bridge, J.S. Formation and preservation of open-framework gravel strata in unidirectional flows. *Sedimentology* **2007**, *54*, 71–87. [CrossRef]
34. Beschta, R.L.; Jackson, W.L. The Intrusion of Fine Sediments into a Stable Gravel Bed. *J. Fish. Res. Bd. Can.* **1979**, *36*, 204–210. [CrossRef]
35. Carling, P.A. Deposition of Fine and Coarse Sand in an Open-Work Gravel Bed. *Can. J. Fish. Aquat. Sci.* **1984**, *41*, 263–270. [CrossRef]
36. Frostick, L.E.; Lucas, P.M.; Reid, I. The infiltration of fine matrices into coarse-grained alluvial sediments and its implications for stratigraphical interpretation. *J. Geol. Soc.* **1984**, *141*, 955–965. [CrossRef]
37. Schälchli, U. The clogging of coarse gravel river beds by fine sediment. *Hydrobiologia* **1992**, *235–236*, 189–197. [CrossRef]
38. Gibson, S.; Abraham, D.; Heath, R.; Schoellhamer, D. Vertical gradational variability of fines deposited in a gravel framework. *Sedimentology* **2009**, *56*, 661–676. [CrossRef]
39. Gibson, S.; Abraham, D.; Heath, R.; Schoellhamer, D. Bridging Process Threshold for Sediment Infiltrating into a Coarse Substrate. *J. Geotech. Geoenviron. Eng.* **2010**, *136*, 402–406. [CrossRef]
40. Cui, Y.; Wooster, J.K.; Baker, P.F.; Dusterhoff, S.R.; Sklar, L.S.; Dietrich, W.E. Theory of Fine Sediment Infiltration into Immobile Gravel Bed. *J. Hydraul. Eng.* **2008**, *134*, 1421–1429. [CrossRef]
41. Bui, V.H.; Bui, M.D.; Rutschmann, P. Combination of Discrete Element Method and Artificial Neural Network for Predicting Porosity of Gravel-Bed River. *Water* **2019**, *11*, 1461. [CrossRef]
42. Bui, V.H.; Bui, M.D.; Rutschmann, P. Advanced Numerical Modeling of Sediment Transport in Gravel-Bed Rivers. *Water* **2019**, *11*, 550. [CrossRef]
43. Jaiswal, A.; Bui, M.D.; Rutschmann, P. On the process of fine sediment infiltration into static gravel bed: A CFD–DEM modelling perspective. *River Res. Appl.* **2024**, *40*, 29–48. [CrossRef]
44. Elmsahli, H.S.; Sinka, I.C. A discrete element study of the effect of particle shape on packing density of fine and cohesive powders. *Comput. Part. Mech.* **2021**, *8*, 183–200. [CrossRef]
45. Soltanbeigi, B.; Papanicolopulos, S.A.; Ooi, J.Y. An insight into the micro-mechanism of the directional constant torque model in quasi-static flow. In Proceedings of the CFDEM® Project User Group Meeting and Workshop, Linz, Austria, 14–15 March 2016.
46. Guo, Y.; Yang, Y.; Yu, X. Influence of particle shape on the erodibility of non-cohesive soil: Insights from coupled CFD–DEM simulations. *Particuology* **2018**, *39*, 12–24. [CrossRef]
47. Fukumoto, Y.; Sakaguchi, H.; Murakami, A. The role of rolling friction in granular packing. *Granul. Matter* **2013**, *15*, 175–182. [CrossRef]
48. Favier, J.F.; Abbaspour-Fard, M.H.; Kremmer, M.; Raji, A.O. Shape representation of axi-symmetrical, non-spherical particles in discrete element simulation using multi-element model particles. *Eng. Comput.* **1999**, *16*, 467–480. [CrossRef]
49. Favier, J.F.; Abbaspour-Fard, M.H.; Kremmer, M. Modeling Nonspherical Particles Using Multisphere Discrete Elements. *J. Eng. Mech.* **2001**, *127*, 971–977. [CrossRef]
50. Potyondy, D.O.; Cundall, P.A. A bonded-particle model for rock. *Int. J. Rock Mech. Min. Sci.* **2004**, *41*, 1329–1364. [CrossRef]
51. Cundall, P.A.; Strack, O.D.L. A discrete numerical model for granular assemblies. *Géotechnique* **1979**, *29*, 47–65. [CrossRef]
52. Yang, Y.; Yuan, W.; Hou, J.; You, Z. Review on physical and chemical factors affecting fines migration in porous media. *Water Res.* **2022**, *214*, 118172. [CrossRef]
53. You, Z.; Osipov, Y.; Bedrikovetsky, P.; Kuzmina, L. Asymptotic model for deep bed filtration. *Chem. Eng. J.* **2014**, *258*, 374–385. [CrossRef]
54. Badalyan, A.; You, Z.; Aji, K.; Bedrikovetsky, P.; Carageorgos, T.; Zeinijahromi, A. Size exclusion deep bed filtration: Experimental and modelling uncertainties. *Rev. Sci. Instrum.* **2014**, *85*, 15111. [CrossRef]
55. Yuan, H.; You, Z.; Shapiro, A.; Bedrikovetsky, P. Improved population balance model for straining-dominant deep bed filtration using network calculations. *Chem. Eng. J.* **2013**, *226*, 227–237. [CrossRef]
56. Johnson, K.L. *Contact Mechanics*, 1st ed.; with Corrections; Cambridge University Press: Cambridge, UK, 1987.
57. Iwashita, K.; Oda, M. Rolling Resistance at Contacts in Simulation of Shear Band Development by DEM. *J. Eng. Mech.* **1998**, *124*, 285–292. [CrossRef]
58. Bardet, J.P.; Huang, Q. Numerical modeling of micropolar effects in idealized granular materials. *Am. Soc. Mech. Eng. Mater. Div. (Publ.)* **1992**, *37*, 85–92.

59. Bardet, J.P. Observations on the effects of particle rotations on the failure of idealized granular materials. *Mech. Mater.* **1994**, *18*, 159–182. [CrossRef]
60. Oda, M.; Konishi, J.; Nemat-Nasser, S. Experimental micromechanical evaluation of strength of granular materials: Effects of particle rolling. *Mech. Mater.* **1982**, *1*, 269–283. [CrossRef]
61. Calvetti, F.; Combe, G.; Lanier, J. Experimental micromechanical analysis of a 2D granular material: Relation between structure evolution and loading path. *Mech. Cohes.-Frict. Mater.* **1997**, *2*, 121–163. [CrossRef]
62. Misra, A.; Jiang, H. Measured kinematic fields in the biaxial shear of granular materials. *Comput. Geotech.* **1997**, *20*, 267–285. [CrossRef]
63. Ai, J.; Chen, J.-F.; Rotter, J.M.; Ooi, J.Y. Assessment of rolling resistance models in discrete element simulations. *Powder Technol.* **2011**, *206*, 269–282. [CrossRef]
64. Bérard, A.; Patience, G.S.; Blais, B. Experimental methods in chemical engineering: Unresolved CFD-DEM. *Can. J. Chem. Eng.* **2020**, *98*, 424–440. [CrossRef]
65. Kloss, C.; Goniva, C.; Hager, A.; Amberger, S.; Pirker, S. Models, algorithms and validation for opensource DEM and CFD-DEM. *Prog. Comput. Fluid Dyn. Int. J.* **2012**, *12*, 140. [CrossRef]
66. Latham, J.P.; Munjiza, A.; Lu, Y. On the prediction of void porosity and packing of rock particulates. *Powder Technol.* **2002**, *125*, 10–27. [CrossRef]
67. Iseya, F.; Ikeda, H. Pulsations in Bedload Transport Rates Induced by a Longitudinal Sediment Sorting: A Flume Study using Sand and Gravel Mixtures. *Geogr. Ann. Ser. A-Phys. Geogr.* **1987**, *69*, 15–27. [CrossRef]
68. Honjo, Y.; Veneziano, D. Improved filter criterion for cohesionless soils. *J. Geotech. Eng.* **1989**, *115*, 75–94. [CrossRef]
69. Indraratna, B.; Vafai, F. Analytical Model for Particle Migration within Base Soil-Filter System. *J. Geotech. Geoenviron. Eng.* **1997**, *123*, 100–109. [CrossRef]
70. Sherard, J.L.; Dunnigan, L.P. Filters and leakage control in embankment dams. *Int. J. Rock Mech. Min. Sci. Geomech. Abstr.* **1986**, *23*, 202.
71. Indraratna, B.; Locke, M.R. Design methods for granular filters—Critical review. *Proc. Inst. Civ. Eng.-Geotech. Eng.* **1999**, *137*, 137–147. [CrossRef]
72. Twenhofel, W.H. The Rounding of Sand Grains. *J. Sediment. Res.* **1945**, *15*, 59–71. [CrossRef]
73. Novák-Szabó, T.; Sipos, A.Á.; Shaw, S.; Bertoni, D.; Pozzebon, A.; Grottoli, E.; Sarti, G.; Ciavola, P.; Domokos, G.; Jerolmack, D.J. Universal characteristics of particle shape evolution by bed-load chipping. *Sci. Adv.* **2018**, *4*, eaao4946. [CrossRef]

Chapter 7

Conclusion and Outlook

This dissertation reports the efforts to utilize high-fidelity CFD coupled with particle tracking method (DEM) to improve our existing knowledge on a specific fluid-particle system characterized by a sub-process of sediment transport, namely the fine sediment infiltration into static gravel bed. The numerical simulation performed in this study aims to deepen our understanding of the fine sediment infiltration process in relation to the effects of flowing water, turbulence, particle shape and particle size distribution (PSD) characteristics. In completing the dissertation, I would like to conclude the main findings, along with some recommendations for fine sediment management and mention some future research avenues.

7.1 Conclusion

The main findings of the research conducted within the doctoral project and some recommendations based on the results presented can be summarized as follows:

- High-fidelity CFD coupled with the DEM method, the so-called CFD-DEM approach, opens new doors of possibilities for investigating fluid-particle systems. However, the limitations concerning the number and size of particles, with heavy computations involving fluid-particle and particle-particle interactions, restrict its application for simpler cases with a defined CFD resolution and a limited number of particles.
- Particle size must be smaller than CFD cells under the unresolved CFD-DEM framework. This also means that it is not always possible to resolve finer CFD meshes, especially near the walls required by the turbulence-resolving methods (e.g., $y^+ \sim 1$ for LES-DEM). Under such scenarios, dynamic LES turbulence models (e.g. DynamickEqn) could capture accurate fluid flow statistics in terms of turbulent mean and fluctuating velocities.
- Under the RANS-DEM approach, the simple dispersion models based on the Discrete Random Walk (DRW) are inefficient in recovering the effects of turbulence fluctuations on the particle's trajectory. More sophisticated turbulent dispersion models such as the Continuous Random Walk (CRW) or direct forcing in NS equation could be better options for such purposes.
- Compared to the standard OpenFOAM solver "DPMFoam", the self-compiled solver "pimpleLPTFoam" could save significant computational resources yet could provide as accurate

particle behaviour in turbulent flow as "DPMFoam." However, one can only neglect the effect of particle fraction in each computational cell, demonstrated by pimpleLPTFoam, only when particle concentration $\epsilon_p \leq 10^{-5}$ (dispersed fluid-particle systems within one- and two-way coupling regime). Particle fraction in each computational cell must be taken into account for denser particle systems.

- The unresolved CFD-DEM framework is further exploited to investigate a denser fluid-particle system, characterized by fine sediment infiltration into static gravel bed. Here, the coupled framework of OpenFOAM, LIGGGHTS and CFDEM-Coupling, instead of standalone particle tracking solvers in OpenFOAM, is successfully employed to study fine sediment infiltration into static gravel bed.

- Investigation of flowing water effects on the fine sediment infiltration suggests that the process is predominantly gravity-dominated. The observation supports Cui's hypothesis (Cui et al., 2008) that the fine sediment infiltration driven by intra-gravel flow is similar to fine sediment infiltration driven by gravity. This implies that the fine sediment infiltration process can be studied efficiently, considering the system as a pure granular system, as long as the gravel bed remains immobile.

- Both bridging and percolation types of infiltration processes can occur within the same gravel substrate, even under the same flow conditions. The occurrence of bridging or percolation is independent of gravel bed thickness and is purely a function of relative sand-to-gravel size. Nevertheless, the gravel bed should be sufficiently thick enough to distinguish between these infiltration behaviours. In this direction, we hypothesized that a gravel bed thicker than five times the largest gravel diameter can be considered as thick enough gravel bed.

- Among the different turbulence models under RANS-DEM, any of the RANS turbulence models can be used to model the fine sediment infiltration into static gravel bed, provided it can capture the mean flow fields accurately. This observation also has its roots in the fact that the flowing water has almost no effects on the final state of infiltration as the process of fine sediment infiltration into static gravel bed is gravity-dominated.

- Considering our observation that fine sediment infiltration is predominantly a gravity-dominated process, the system is described as a pure-granular system and simulated in a pure DEM framework. Here, other aspects of granular media, such as particle shape and particle size distribution (PSD), are investigated. These aspects are important in deciding the realizability of the simulation in terms of domain size, total number of particles and materialistic properties. The infiltration characteristics of fine sediment into static gravel bed concerning irregularity and non-sphericity in particle and PSD are related to thresholds for bridging and percolation behaviours $D_{15,\mathrm{Gravel}}/D_{85,\mathrm{Sand}}$.

- The size ratio $D_{15,\mathrm{Gravel}}/D_{85,\mathrm{Sand}}$ is important parameter, which governs the fine sediment infiltration process. For $D_{15,\mathrm{Gravel}}/D_{85,\mathrm{Sand}} < 10.6$ bridging, and for $D_{15,\mathrm{Gravel}}/D_{85,\mathrm{Sand}} > 15.4$ percolation behavior should occur.

- Particle shape effects are included implicitly by restricting the particle's rotation with rolling resistance models. The rolling resistance models seem to be the most efficient way to include

shape effects without resolving the actual shape of particles, because each sediment particle in the natural river system can be very different from one another. Rolling resistance models (thus particle shape) must be included for cases when $D_{15,Gravel}/D_{85,Sand} < 10.6$ (bridging behaviour) and are not necessary for cases when $D_{15,Gravel}/D_{85,Sand} > 15.4$ (percolation behaviour).

- Number of grain-size classes in PSD is a crucial factor in DEM simulations in terms of simulation time and computational resources. More grain-size classes would result in a larger number of particles and eventually smaller DEM time steps to capture proper contact among the smallest particles accurately. The reduction in the number of grain-size classes is only justified if it does not modify $D_{15,Gravel}$ and $D_{85,Sand}$ significantly, and the size ratio $D_{15,Gravel}/D_{85,Sand}$ is within the thresholds for bridging or percolation behaviours. Based on the study, it is recommended to consider 4-5 grain-size classes to capture the realistic behaviour of sand and gravel particles.

- For fine sediment management strategies, it can be taken as a rule of thumb that infiltration through percolation behaviour should be avoided while flushing the fine sediment from dams. This can be made sure by simply comparing the $D_{15,Gravel}$ of the gravel substrate downstream of the dam with the $D_{85,Sand}$ of deposited fine sediment in the upstream of the dam.

- If the size ratio $D_{15,Gravel}/D_{85,Sand} < 10.6$, the flushing of fine sediment is recommended. The deposited and infiltrated fine sediment, as a result of the carried flushing event, can be remobilized in an attempt to clean the gravel deposit with an artificial flood event.

- If the size ratio $D_{15,Gravel}/D_{85,Sand} > 15.4$, the expected fine sediment infiltration would occur predominantly through percolation, which can lead the fine sediment to infiltrate very deep into the gravel substrate, which is almost impossible to remove. Under such conditions, flushing is not recommended; rather, dredging could be a possible fine sediment management strategy. Alternatively, if flushing is unavoidable, several nature based approaches could be employed to minimize the fine sediment infiltration or to protect specific ecological regions of interest. This could be done by formations of gravel structure (Haun et al., 2023; Kunz et al., 2021) or wood placements (Noack et al., 2020; Schalko et al., 2024; Schwindt et al., 2023), downstream of the dam, to pass the fine sediment through specific zones in the river course or generate artificial turbulence using these gravel structures to prevent extensive fine sediment infiltration. In this direction, some initial studies, field investigations and restoration measures are taking place in the right direction with field scale monitoring tools (e.g. MultiPAC).

7.2 Outlook

The CFD-DEM approach is relatively new in the field of hydraulic engineering and holds enormous potential for studying fluvial systems in greater detail, focusing on particle-scale interactions on the DEM side and highly resolved fluid flow fields on the CFD side. However, the method has specific limitations depending on whether the resolved or unresolved CFD-DEM approach is used to study the fluid-particle system under consideration. Despite being in the early developmental stage, the method is becoming more accessible to researchers due to recent advancements in computational science, both in software and hardware aspects. I would like to highlight some of the future research

avenues, which are:

Larger Domain and Wider PSD Studies: Future research could explore larger domain sizes and a wider variety of sand and gravel mixtures to validate and extend the current findings. Experimental Studies from Wooster et al. (2008) could serve as reference cases, where not only the PSD for fine sediment but also PSD for gravel are varied within several flume experiments.

Flushing Efficiency: Investigating various scenarios of fine sediment remobilization and removal during high flood events would be beneficial for sediment management. Simulations could provide insights into effective flushing mechanisms to maintain clean gravel beds.

Dynamic Meshing: Developing dynamic meshing approaches within unresolved CFD-DEM could help achieve high-resolution flow fields with moving particles, ensuring that particles remain smaller than the CFD cell size throughout the simulation domain. Alternatively, the resolved CFD-DEM approach could be used, but due to its limitation to only a few thousand particles, it would be difficult to simulate a decently sized domain with broader PSDs for gravel and sand.

GPU Optimization: Optimizing particle tracking solvers for GPU systems could significantly enhance computational efficiency, making it feasible to perform large-scale simulations with broader PSDs for gravel and fine sediment.

Advanced Particle Interaction Models: Further research into sophisticated models for inter-particle calculations for non-spherical particles is encouraged. This could improve the accuracy of DEM simulations in replicating natural fluvial systems.

Machine Learning Integration: Integrating machine learning methodologies, such as Artificial Neural Networks (ANNs) and Physics Informed Neural Networks (PINNs), with CFD-DEM data could provide efficient tools for predicting sediment and porosity profiles during infiltration and remobilization stages. Training models on extensive datasets could offer quick and reliable predictions for site-specific conditions.

Exploring Other Sediment Transport Regimes: Future studies could employ the CFD-DEM method to investigate other sediment transport regimes, including dunes, ripples, and suspension modes, which were beyond the scope of this dissertation. Detailed particle-scale information could reveal new insights into these processes.

Taken together, these findings and future research avenues underscore the potential of the CFD-DEM approach to advance our understanding of fluid-particle systems significantly. Continued advancements in computational methods and technologies will likely make these studies even more impactful, providing deeper insights into sediment transport processes and their practical applications.

Annexure

Structure of self-compiled solver "pimpleLPTFoam"

The solver "pimpleLPTFoam" was developed by modifying the single-phase incompressible transient solver "pimpleFoam" by adding a lagrangian library **intermediate**, which takes care of the particle tracking part. The new fields were created. The **basicKinematicCollidingCloud** is initialized in **createFields.H** and called in **PimpleLPTFoam.C** to include particle-particle and particle-wall interactions. **UEqns.H** was modified to include fluid-particle interaction momentum (two-way coupling). Additional necessary executables and libraries are included in **Make/options**. The location newly created particle-tracking solver "pimpleLPTFoam" was specified in **Make/files**.

Note: The solver was compiled on the basis of the tutorial shown by Dr. Robert Kasper during the German OpenFOAM User Meeting 2018 (GOFUN 2018). We complied the solver "pimpleLPTFoam" in OpenFOAM-v-1912, which required marginal changes.

A.1: correctPhi.H

correctPhi.H

```
CorrectPhi
(
    U,
    phi,
    p,
    dimensionedScalar("rAUf", dimTime, 1),
    geometricZeroField(),
    pimple
);
#include "continuityErrs.H"
```

A.2: createFields.H

```
#include "readGravitationalAcceleration.H"
Info<< "Reading field p\n" << endl;
volScalarField p
(
    IOobject
    (
        "p",
        runTime.timeName(),
        mesh,
        IOobject::MUST_READ,
        IOobject::AUTO_WRITE
    ),
    mesh
);
Info<< "Reading field U\n" << endl;
volVectorField U
(
    IOobject
    (
        "U",
        runTime.timeName(),
        mesh,
        IOobject::MUST_READ,
        IOobject::AUTO_WRITE
    ),
    mesh
);
#include "createPhi.H"
label pRefCell = 0;
scalar pRefValue = 0.0;
setRefCell(p, pimple.dict(), pRefCell, pRefValue);
mesh.setFluxRequired(p.name());
singlePhaseTransportModel laminarTransport(U, phi);
autoPtr<incompressible::turbulenceModel> turbulence
(
    incompressible::turbulenceModel::New(U, phi, laminarTransport)
);
#include "createMRF.H"
Info<< "Reading transportProperties\n" << endl;
IOdictionary transportProperties
(
```

```
IOobject
(
"transportProperties",
runTime.constant(),
mesh,
IOobject::MUST_READ_IF_MODIFIED,
IOobject::NO_WRITE
)
);
dimensionedScalar rhoInfValue
(
transportProperties.lookup("rhoInf")
);
dimensionedScalar invrhoInf("invrhoInf",(1.0/rhoInfValue));
volScalarField rhoInf
(
IOobject
(
"rho",
runTime.constant(),
mesh,
IOobject::NO_READ,
IOobject::AUTO_WRITE
),
mesh,
rhoInfValue
);
volScalarField mu
(
IOobject
(
"mu",
runTime.constant(),
mesh,
IOobject::NO_READ,
IOobject::AUTO_WRITE
),
laminarTransport.nu()
*rhoInfValue
);
const word kinematicCloudName
(
args.get<word>("cloudName", "kinematicCloud")
);
```

```
Info<< "Constructing kinematicCloud " << kinematicCloudName << endl;
basicKinematicCollidingCloud kinematicCloud
(
kinematicCloudName,
rhoInf,
U,
mu,
g
);

#include "createFvOptions.H"
```

A.3: pEqn.H

```
volScalarField rAU(1.0/UEqn.A());
volVectorField HbyA(constrainHbyA(rAU*UEqn.H(), U, p));
surfaceScalarField phiHbyA
(
    "phiHbyA",
    fvc::flux(HbyA)
  + MRF.zeroFilter(fvc::interpolate(rAU)*fvc::ddtCorr(U, phi, Uf))
);
MRF.makeRelative(phiHbyA);
if (p.needReference())
{
    fvc::makeRelative(phiHbyA, U);
    adjustPhi(phiHbyA, U, p);
    fvc::makeAbsolute(phiHbyA, U);
}
tmp<volScalarField> rAtU(rAU);
if (pimple.consistent())
{
    rAtU = 1.0/max(1.0/rAU - UEqn.H1(), 0.1/rAU);
    phiHbyA +=
        fvc::interpolate(rAtU() - rAU)*fvc::snGrad(p)*mesh.magSf();
    HbyA -= (rAU - rAtU())*fvc::grad(p);
}
if (pimple.nCorrPISO() <= 1)
{
    tUEqn.clear();
}
// Update the pressure BCs to ensure flux consistency
constrainPressure(p, U, phiHbyA, rAtU(), MRF);

// Non-orthogonal pressure corrector loop
while (pimple.correctNonOrthogonal())
{
    fvScalarMatrix pEqn
    (
        fvm::laplacian(rAtU(), p) == fvc::div(phiHbyA)
    );
    pEqn.setReference(pRefCell, pRefValue);
    pEqn.solve(mesh.solver(p.select(pimple.finalInnerIter())));
    if (pimple.finalNonOrthogonalIter())
    {
```

```
        phi = phiHbyA - pEqn.flux();
    }
}
#include "continuityErrs.H"

// Explicitly relax pressure for momentum corrector
p.relax();
U = HbyA - rAtU*fvc::grad(p);
U.correctBoundaryConditions();
fvOptions.correct(U);

// Correct Uf if the mesh is moving
fvc::correctUf(Uf, U, phi);

// Make the fluxes relative to the mesh motion
fvc::makeRelative(phi, U);
```

A.4: pimpleLPTFoam.C

```
#include "fvCFD.H"
#include "dynamicFvMesh.H"
#include "singlePhaseTransportModel.H"
#include "turbulentTransportModel.H"
#include "pimpleControl.H"
#include "CorrectPhi.H"
#include "fvOptions.H"
#include "basicKinematicCollidingCloud.H"

int main(int argc, char *argv[])
{
    #include "postProcess.H"
    #include "addCheckCaseOptions.H"
    #include "setRootCaseLists.H"
    #include "createTime.H"
    #include "createDynamicFvMesh.H"
    #include "initContinuityErrs.H"
    #include "createDyMControls.H"
    #include "createFields.H"
    #include "createUfIfPresent.H"
    #include "CourantNo.H"
    #include "setInitialDeltaT.H"

    turbulence->validate();
    Info<< "\nStarting time loop\n" << endl;
    while (runTime.run())
    {
        #include "readDyMControls.H"
        #include "CourantNo.H"
        #include "setDeltaT.H"
        ++runTime;
        Info<< "Time = " << runTime.timeName() << nl << endl;
        // --- Pressure-velocity PIMPLE corrector loop
        while (pimple.loop())
        {
            if (pimple.firstIter() || moveMeshOuterCorrectors)
            {
                // Do any mesh changes
                mesh.controlledUpdate();
                if (mesh.changing())
                {
```

```
                    MRF.update();
                    if (correctPhi)
                    {
                        // Calculate absolute flux
                        // from the mapped surface velocity
                        phi = mesh.Sf() & Uf();
                        #include "correctPhi.H"
                        // Make the flux relative to the mesh motion
                        fvc::makeRelative(phi, U);
                    }
                    if (checkMeshCourantNo)
                    {
                        #include "meshCourantNo.H"
                    }
                }
            }
            #include "UEqn.H"
            // --- Pressure corrector loop
            while (pimple.correct())
            {
                #include "pEqn.H"
            }
            if (pimple.turbCorr())
            {
                laminarTransport.correct();
                turbulence->correct();
            }
        }
        Info<< "\nEvolving " << kinematicCloud.name() << endl;
        kinematicCloud.evolve();
        runTime.write();
        runTime.printExecutionTime(Info);
    }
    Info<< "End\n" << endl;
    return 0;
}
```

A.5: UEqn.H

```
// Solve the Momentum equation
MRF.correctBoundaryVelocity(U);
tmp<fvVectorMatrix> tUEqn
(
    fvm::ddt(U) + fvm::div(phi, U)
  + MRF.DDt(U)
  + turbulence->divDevReff(U)
 ==
    fvOptions(U)
    + invrhoInf*kinematicCloud.SU(U)
);
fvVectorMatrix& UEqn = tUEqn.ref();
UEqn.relax();
fvOptions.constrain(UEqn);
if (pimple.momentumPredictor())
{
    solve(UEqn == -fvc::grad(p));
    fvOptions.correct(U);
}
```

A.6: Make/options

```
EXE_INC = \
    -Iintermediate/lnInclude \
    -I$(LIB_SRC)/finiteVolume/lnInclude \
    -I$(LIB_SRC)/meshTools/lnInclude \
    -I$(LIB_SRC)/sampling/lnInclude \
    -I$(LIB_SRC)/TurbulenceModels/turbulenceModels/lnInclude \
    -I$(LIB_SRC)/TurbulenceModels/incompressible/lnInclude \
    -I$(LIB_SRC)/transportModels \
    -I$(LIB_SRC)/transportModels/incompressible/singlePhaseTransportModel \
    -I$(LIB_SRC)/dynamicMesh/lnInclude \
    -I$(LIB_SRC)/dynamicFvMesh/lnInclude \
    -I$(LIB_SRC)/lagrangian/basic/lnInclude \
    -I$(LIB_SRC)/regionModels/surfaceFilmModels/lnInclude \
    -I$(LIB_SRC)/regionModels/regionModel/lnInclude

EXE_LIBS = \
    -L$(FOAM_USER_LIBBIN) \
    -lPimpleLPTLagrangianIntermediate \
    -llagrangian\
    -lfiniteVolume \
    -lfvOptions \
    -lmeshTools \
    -lsampling \
    -lturbulenceModels \
    -lincompressibleTurbulenceModels \
    -lincompressibleTransportModels \
    -ldynamicMesh \
    -ldynamicFvMesh \
    -ltopoChangerFvMesh \
    -latmosphericModels
```

A.7: Make/files

```
pimpleLPTFoam.C

EXE = $(FOAM_USER_APPBIN)/pimpleLPTFoam
```

Bibliography

Ahadi, M., Bergstrom, D.J., Mazurek, K.A., 2019. Application of the two-fluid model to prediction of sediment transport in turbulent open channel flow. Physics and Chemistry of the Earth, Parts A/B/C 113, 73–82. doi:10.1016/j.pce.2019.06.001.

Anderson, T.B., Jackson, R., 1967. Fluid mechanical description of fluidized beds. equations of motion. Industrial & Engineering Chemistry Fundamentals 6, 527–539. doi:10.1021/i160024a007.

Armenio, V., Fiorotto, V., 2001. The importance of the forces acting on particles in turbulent flows. Physics of Fluids 13, 2437–2440. doi:10.1063/1.1385390.

Asegehegn, T.W., Schreiber, M., Krautz, H.J., 2011. Numerical simulation and experimental validation of bubble behavior in 2d gas–solid fluidized beds with immersed horizontal tubes. Chemical Engineering Science 66, 5410–5427. doi:10.1016/j.ces.2011.07.056.

Bagchi, P., Balachandar, S., 2003. Effect of turbulence on the drag and lift of a particle. Physics of Fluids 15, 3496–3513. doi:10.1063/1.1616031.

Bakhtyar, R., Yeganeh-Bakhtiary, A., Barry, D.A., Ghaheri, A., 2009. Euler—euler coupled two-phase flow modeling of sheet flow sediment motion in the nearshore. Journal of Coastal Research , 467–471URL: http://www.jstor.org/stable/25737620.

Bednarek, A.T., 2001. Undamming rivers: a review of the ecological impacts of dam removal. Environmental management 27, 803–814. doi:10.1007/s002670010189.

Benra, F.K., Dohmen, H.J., Pei, J., Schuster, S., Wan, B., 2011. A comparison of one-way and two-way coupling methods for numerical analysis of fluid-structure interactions. Journal of applied mathematics 2011, 853560. doi:https://doi.org/10.1155/2011/853560.

Bérard, A., Patience, G.S., Blais, B., 2020. Experimental methods in chemical engineering: Unresolved cfd–dem. The Canadian Journal of Chemical Engineering 98, 424–440. doi:10.1002/cjce.23686.

Born, Genskow, Filbert, Hernandez-Mora, Keefer, White, 1998. Socioeconomic and institutional dimensions of dam removals: The wisconsin experience. Environmental management 22, 359–370. doi:10.1007/s002679900111.

Bui, V.H., 2019. Modelling of sediment exchange processes and morphodynamics of gravel-bed Rivers of gravel-bed Rivers. Dissertation. Technical University of Munich. Munich, Germany. URL: https://mediatum.ub.tum.de/1521800.

Burns, A.D., Frank, T., Hamill, I., Shi, J.M., et al., 2004. The favre averaged drag model for turbulent dispersion in eulerian multi-phase flows, in: 5th international conference on multiphase flow, ICMF, ICMF. pp. 1–17.

Burton, T.M., Eaton, J.K., 2005. Fully resolved simulations of particle-turbulence interaction. Journal of Fluid Mechanics 545, 67–111. doi:10.1017/S0022112005006889.

Chauchat, J., Cheng, Z., Nagel, T., Bonamy, C., Hsu, T.J., 2017. Sedfoam-2.0: a 3-d two-phase flow numerical model for sediment transport. Geoscientific Model Development 10, 4367–4392. doi:10.5194/gmd-10-4367-2017.

Chen, S.F., Lei, H., Wang, M., Yang, B., Dai, L.J., Zhao, Y., 2019. Two-way coupling calculation for multiphase flow and decarburization during rh refining. Vacuum 167, 255–262. doi:https://doi.org/10.1016/j.vacuum.2019.06.018.

Cheng, Z., Hsu, T.J., Calantoni, J., 2017. Sedfoam: A multi-dimensional eulerian two-phase model for sediment transport and its application to momentary bed failure. Coastal Engineering 119, 32–50. doi:10.1016/j.coastaleng.2016.08.007.

Chiodi, F., Claudin, P., Andreotti, B., 2014. A two-phase flow model of sediment transport: transition from bedload to suspended load. Journal of Fluid Mechanics 755, 561–581. doi:10.1017/jfm.2014.422.

Cloete, S., Johansen, S.T., Amini, S., 2012. An assessment of the ability of computational fluid dynamic models to predict reactive gas–solid flows in a fluidized bed. Powder Technology 215-216, 15–25. doi:10.1016/j.powtec.2011.08.033.

Crowe, C.T., 2012. Multiphase flows with droplets and particles. 2nd ed. ed., CRC Press, Boca Raton, FL. doi:10.1201/b11103.

Cui, Y., Parker, G., Braudrick, C., Dietrich, W.E., Cluer, B., 2006. Dam removal express assessment models (dream). Journal of Hydraulic Research 44, 291–307. doi:10.1080/00221686.2006.9521683.

Cui, Y., Wilcox, A., 2005. Numerical modeling of sediment transport upon dam removal: Application to marmot dam in sandy river, oregon. Sedimentation engineering, ASCE Manual 54.

Cui, Y., Wooster, J.K., Baker, P.F., Dusterhoff, S.R., Sklar, L.S., Dietrich, W.E., 2008. Theory of fine sediment infiltration into immobile gravel bed. Journal of Hydraulic Engineering 134, 1421–1429. doi:10.1061/(ASCE)0733-9429(2008)134:10(1421).

Cundall, P.A., Strack, O.D.L., 1979. A discrete numerical model for granular assemblies. Géotechnique 29, 47–65. doi:10.1680/geot.1979.29.1.47.

Dehbi, A., 2008. Stochastic models for turbulent particle dispersion in general inhomogeneous flows. Paul Scherrer Institut: Villigen PSI, Switzerland .

Dey, S., 2014. Fluvial Hydrodynamics: Hydrodynamic and Sediment Transport Phenomena. GeoPlanet. 1st ed. 2014 ed., Springer Berlin Heidelberg and Imprint: Springer, Berlin Heidelberg.

Di Felice, R., 1994. The voidage function for fluid-particle interaction systems. International Journal of Multiphase Flow 20, 153–159. doi:10.1016/0301-9322(94)90011-6.

Dietrich, W.E., Kirchner, J.W., Ikeda, H., Iseya, F., 1989. Sediment supply and the development of the coarse surface layer in gravel-bedded rivers. Nature 340, 215–217. doi:10.1038/340215a0.

Downs, P.W., Cui, Y., Wooster, J.K., Dusterhoff, S.R., Booth, D.B., Dietrich, W.E., Sklar, L.S., 2009. Managing reservoir sediment release in dam removal projects: An approach informed by physical and numerical modelling of non-cohesive sediment. International Journal of River Basin Management 7, 433–452. doi:10.1080/15715124.2009.9635401.

Elghobashi, S., 1994. On predicting particle-laden turbulent flows. Applied Scientific Research 52, 309–329. doi:10.1007/BF00936835.

Elmsahli, H.S., Sinka, I.C., 2021. A discrete element study of the effect of particle shape on packing density of fine and cohesive powders. Computational Particle Mechanics 8, 183–200. doi:10.1007/s40571-020-00322-9.

Feng, Y.Q., Yu, A.B., 2004. Assessment of model formulations in the discrete particle simulation of gas-solid flow. Industrial and Engineering Chemistry Research 43, 8378–8390. doi:10.1021/ie049387v.

Fessler, J.R., Eaton, J.K., 1999. Turbulence modification by particles in a backward-facing step flow. Journal of Fluid Mechanics 394, 97–117. doi:10.1017/S0022112099005741.

Gibson, S., Abraham, D., Heath, R., Schoellhamer, D., 2009. Vertical gradational variability of fines deposited in a gravel framework. Sedimentology 56, 661–676. doi:10.1111/j.1365-3091.2008.00991.x.

Gibson, S., Abraham, D., Heath, R., Schoellhamer, D., 2010. Bridging process threshold for sediment infiltrating into a coarse substrate. Journal of Geotechnical and Geoenvironmental Engineering 136, 402–406. doi:10.1061/(ASCE)GT.1943-5606.0000219.

Gidaspow, D., 1994. Multiphase flow and fluidization: Continuum and kinetic theory descriptions. Academic Press, Boston. URL: http://www.sciencedirect.com/science/book/9780080512266.

Grams, P.E., Wilcock, P.R., 2014. Transport of fine sediment over a coarse, immobile riverbed. Journal of Geophysical Research: Earth Surface 119, 188–211. doi:10.1002/2013JF002925.

Guo, Y., Yang, Y., Yu, X., 2018. Influence of particle shape on the erodibility of non-cohesive soil: Insights from coupled cfd–dem simulations. Particuology 39, 12–24. doi:10.1016/j.partic.2017.11.007.

Haun, S., Dietrich, S., 2021. Advanced methods to investigate hydro–morphological processes in open–water environments. Earth Surface Processes and Landforms 46, 1655–1665. doi:10.1002/esp.5131.

Haun, S., Negreiros, B., Schwindt, S., Aybar Galdos, A., Noack, M., Wieprecht, S., 2023. MultiPAC as a tool to monitor the sustainability of riverbed restoration measures. doi:10.5194/egusphere-egu23-7152.

He, L., Liu, Z., Zhao, Y., 2024. Study on a semi-resolved cfd-dem method for rod-like particles in a gas-solid fluidized bed. Particuology 87, 20–36. doi:10.1016/j.partic.2023.07.014.

Ishii, M., Hibiki, T., 2010. Thermo-Fluid Dynamics of Two-Phase Flow. Springer Science & Business Media.

Jackson, R. (Ed.), 1963. The mechanics of fluidized beds. PartI. The stability of the state of uniform fluidization. volume 13-21, Tans. Inst. Chem. Engng.

Jaiswal, A., Bui, M.D., Rutschmann, P., 2022. Evaluation of rans-dem and les-dem methods in openfoam for simulation of particle-laden turbulent flows. Fluids 7, 337. doi:10.3390/fluids7100337.

Jaiswal, A., Bui, M.D., Rutschmann, P., 2024. On the process of fine sediment infiltration into static gravel bed: A cfd–dem modelling perspective. River Research and Applications 40, 29–48. doi:10.1002/rra.4215.

Kitagawa, A., Murai, Y., Yamamoto, F., 2001. Two-way coupling of eulerian–lagrangian model for dispersed multiphase flows using filtering functions. International journal of multiphase flow 27, 2129–2153. doi:https://doi.org/10.1016/S0301-9322(01)00040-4.

Kloss, C., Goniva, C., Hager, A., Amberger, S., Pirker, S., 2012. Models, algorithms and validation for opensource dem and cfd-dem. Progress in Computational Fluid Dynamics, An International Journal 12, 140. doi:10.1504/PCFD.2012.047457.

Koch, D.L., , Hill, R.J., 2001. Inertial effects in suspension and porous-media flows. Annual Review of Fluid Mechanics 33, 619–647. doi:10.1146/annurev.fluid.33.1.619.

Kuczaj, A.K., Geurts, B.J., 2006. Mixing in manipulated turbulence. Journal of Turbulence 7, N67. doi:10.1080/14685240600827534.

Kuerten, J.G.M., Vreman, A.W., 2005. Can turbophoresis be predicted by large-eddy simulation? Physics of Fluids 17, 011701–011701–4. doi:10.1063/1.1824151.

Kunz, M., Negreiros, B., Schwindt, S., Haun, S., Noack, M., Wieprecht, S., 2021. Inn-ovative morphological restoration efforts, in: Wyss, C., De Cesare, G., Lane, S., Marti, C., Nitsche, M., Pauli, M., Schweizer, S., Weitbrecht, V. (Eds.), Proceedings of the International Sympoisium on Bedload Management 2021, pp. 52–55. doi:10.3929/ethz-b-000513098.

Laviéville, J., Mérigoux, N., Guingo, M., Baudry, C., Mimouni, S., 2017. A generalized turbulent dispersion model for bubbly flow numerical simulation in neptune_cfd. Nuclear Engineering and Design 312, 284–293. doi:https://doi.org/10.1016/j.nucengdes.2016.11.003.

Lisle, T.E., 1989. Sediment transport and resulting deposition in spawning gravels, north coastal california. Water Resources Research 25, 1303–1319. doi:10.1029/WR025i006p01303.

Liu, Y., 2014. Two-fluid modeling of gas-solid and gas-liquid flows: solver development and application. Ph.D. thesis. Technische Universität München. URL: https://mediatum.ub.tum.de/1226724.

M Kuerten, J.G., 2016. Point-particle dns and les of particle-laden turbulent flow - a state-of-the-art review. Flow, turbulence and combustion 97, 689–713. doi:10.1007/s10494-016-9765-y.

Mayar, M.A., Haun, S., Schmid, G., Wieprecht, S., Noack, M., 2022. Measuring vertical distribution and dynamic development of sediment infiltration under laboratory conditions. Journal of Hydraulic Engineering 148. doi:10.1061/(ASCE)HY.1943-7900.0001980.

Minier, J.P., Chibbaro, S., Pope, S.B., 2014. Guidelines for the formulation of lagrangian stochastic models for particle simulations of single-phase and dispersed two-phase turbulent flows. Physics of Fluids 26, 113303. doi:10.1063/1.4901315.

Minshall, G.W., Royer, T.V., Robinson, C.T., 2001. Response of the cache creek macroinvertebrates during the first 10 years following disturbance by the 1988 yellowstone wildfires. Canadian Journal of Fisheries and Aquatic Sciences 58, 1077–1088. doi:10.1139/f01-056.

Negreiros, B., Galdos, A.A., Seitz, L., Noack, M., Schwindt, S., Wieprecht, S., Haun, S., 2023. A multi–parameter approach to quantify riverbed clogging and vertical hyporheic connectivity. River Research and Applications 39, 1659–1666. doi:10.1002/rra.4145.

Noack, M., Seitz, L., Mayar, M.A., Haun, S., Wieprecht, S., 2020. How to address colmation best? – field and laboratory investigations at different scales, in: Uijttewaal, W.S.J. (Ed.), River flow 2020. CRC Press/Balkema, Leiden, The Netherlands, pp. 1451–1458. doi:10.1201/b22619-201.

Papanicolaou, A.N., Elhakeem, M., Krallis, G., Prakash, S., Edinger, J., 2008. Sediment transport modeling review—current and future developments. Journal of Hydraulic Engineering 134, 1–14. doi:10.1061/(ASCE)0733-9429(2008)134:1(1).

Parker, G., Cui, Y., Imran, J., Dietrich, W., 1996. Flooding in the lower ok tedi, papua new guinea due to the disposal of mine tailings and its amelioration, in: Proceedings, pp. 21–48.

Patankar, N.A., Singh, P., Joseph, D.D., Glowinski, R., Pan, T.W., 2000. A new formulation of the distributed lagrange multiplier/fictitious domain method for particulate flows. International Journal of Multiphase Flow 26, 1509–1524. doi:https://doi.org/10.1016/S0301-9322(99)00100-7.

Petticrew, E.L., Krein, A., Walling, D.E., 2007. Evaluating fine sediment mobilization and storage in a gravel-bed river using controlled reservoir releases. Hydrological Processes 21, 198–210. doi:https://doi.org/10.1002/hyp.6183.

Picano, F., Breugem, W.P., Brandt, L., 2015. Turbulent channel flow of dense suspensions of neutrally buoyant spheres. Journal of Fluid Mechanics 764, 463–487. doi:10.1017/jfm.2014.704.

Pollard, A.I., Reed, T., 2004. Benthic invertebrate assemblage change following dam removal in a wisconsin stream. Hydrobiologia 513, 51–58. doi:10.1023/B:hydr.0000018164.17234.4f.

Ruetsch, G., Meiburg, E., 1994. Two-way coupling in shear layers with dilute bubble concentrations. Physics of Fluids 6, 2656–2670. doi:https://doi.org/10.1063/1.868155.

Salih, S.Q., Aldlemy, M.S., Rasani, M.R., Ariffin, A.K., Ya, T.M.Y.S.T., Al-Ansari, N., Yaseen, Z.M., Chau, K.W., 2019. Thin and sharp edges bodies-fluid interaction simulation using cut-cell immersed boundary method. Engineering Applications of Computational Fluid Mechanics 13, 860–877. doi:10.1080/19942060.2019.1652209.

Schälchli, U., 1992. The clogging of coarse gravel river beds by fine sediment. Hydrobiologia 235-236, 189–197. doi:10.1007/BF00026211.

Schalko, I., Ponce, M., Lassar, S., Schwindt, S., Haun, S., Nepf, H., 2024. Flow and turbulence due to wood contribute to declogging of gravel bed. Geophysical Research Letters 51. doi:10.1029/2023GL107507.

Schiller, L., 1933. ber die grundlegenden berechnungen bei der schwerkraftaufbereitung. Z. Vereines Deutscher Inge. 77, 318. URL: https://cir.nii.ac.jp/crid/1570291224729687808.

Schwindt, S., Negreiros, B., Ponce, M., Schalko, I., Lassar, S., Barros, R., Haun, S., 2023. Fuzzy-logic indicators for riverbed de-clogging suggest ecological benefits of large wood. Ecological Indicators 155, 111045. doi:10.1016/j.ecolind.2023.111045.

Shi, H., Yu, X., 2015. An effective euler–lagrange model for suspended sediment transport by open channel flows. International Journal of Sediment Research 30, 361–370. doi:10.1016/j.ijsrc.2015.03.012.

Shirgaonkar, A.A., MacIver, M.A., Patankar, N.A., 2009. A new mathematical formulation and fast algorithm for fully resolved simulation of self-propulsion. Journal of Computational Physics 228, 2366–2390. doi:https://doi.org/10.1016/j.jcp.2008.12.006.

Shuai, W., Zhenhua, H., Huilin, L., Goudong, L., Jiaxing, W., Pengfei, X., 2012. A bubbling fluidization model using kinetic theory of rough spheres. AIChE Journal 58, 440–455. doi:10.1002/aic.12590.

Simonin, O., Deutsch, E., Minier, J.P., 1993. Eulerian prediction of the fluid/particle correlated motion in turbulent two-phase flows. Applied Scientific Research 51, 275–283. doi:10.1007/BF01082549.

Song, S., Park, S., 2020. Unresolved cfd and dem coupled solver for particle-laden flow and its application to single particle settlement. Journal of Marine Science and Engineering 8, 983. doi:10.3390/jmse8120983.

Stanley, E.H., Luebke, M.A., Doyle, M.W., Marshall, D.W.I., 2002. Short-term changes in channel form and macroinvertebrate communities following low-head dam removal. Journal of the North American Benthological Society 21, 172–187. doi:https://doi.org/10.2307/1468307.

Stokes, G.G., 1880. Mathematical and physical papers, by George Gabriel Stokes. Reprinted from the original journals and transactions, with additional notes by the author. URL: https://name.umdl.umich.edu/AAT0146.0003.001.

Sun, R., Xiao, H., 2016a. Cfd–dem simulations of current-induced dune formation and morphological evolution. Advances in Water Resources 92, 228–239. doi:10.1016/j.advwatres.2016.03.018.

Sun, R., Xiao, H., 2016b. Sedifoam: A general-purpose, open-source cfd–dem solver for particle-laden flow with emphasis on sediment transport. Computers & Geosciences 89, 207–219. doi:10.1016/j.cageo.2016.01.011.

Swanson, F.J., Dyrness, C., 1975. Impact of clear-cutting and road construction on soil erosion by landslides in the western cascade range, oregon. Geology 3, 393–396. doi:https://doi.org/10.1130/0091-7613(1975)3<393:IOCARC>2.0.CO;2.

Syamlal, M., O'Brien, T.J., et al., 1989. Computer simulation of bubbles in a fluidized bed, in: AIChE Symp. Ser, Publ by AIChE. pp. 22–31.

Tayfur, G., 2021. Empirical, numerical, and soft modelling approaches for non-cohesive sediment transport. Environmental Processes 8, 37–58. doi:10.1007/s40710-020-00480-1.

Ten Cate, A., Derksen, J.J., Portela, L.M., Van Den Akker, H.E., 2004. Fully resolved simulations of colliding monodisperse spheres in forced isotropic turbulence. Journal of Fluid Mechanics 519, 233–271. doi:https://doi.org/10.1017/S0022112004001326.

Tryggvason, G., Dabiri, S., Aboulhasanzadeh, B., Lu, J., 2013. Multiscale considerations in direct numerical simulations of multiphase flows. Physics of Fluids 25. doi:10.1063/1.4793543.

Uhlmann, M., 2008. Interface-resolved direct numerical simulation of vertical particulate channel flow in the turbulent regime. Physics of Fluids 20. doi:10.1063/1.2912459.

Uijttewaal, W., Oliemans, R., 1996. Particle dispersion and deposition in direct numerical and large eddy simulations of vertical pipe flows. Physics of Fluids 8, 2590–2604. doi:https://doi.org/10.1063/1.869046.

Vega, F.G., Carlevaro, C.M., Sánchez, M., Pugnaloni, L.A., 2021. Stability and conductivity of proppant packs during flowback in unconventional reservoirs: A cfd–dem simulation study. Journal of Petroleum Science and Engineering 201, 108381. doi:10.1016/j.petrol.2021.108381.

Vieira, N.K.M., Clements, W.H., Guevara, L.S., Jacobs, B.F., 2004. Resistance and resilience of stream insect communities to repeated hydrologic disturbances after a wildfire. Freshwater Biology 49, 1243–1259. doi:10.1111/j.1365-2427.2004.01261.x.

Vreman, A.W., 2016. Particle-resolved direct numerical simulation of homogeneous isotropic turbulence modified by small fixed spheres. Journal of Fluid Mechanics 796, 40–85. doi:10.1017/jfm.2016.228.

Wang, Z., Teng, Y., Liu, M., 2019. A semi-resolved cfd–dem approach for particulate flows with kernel based approximation and hilbert curve based searching strategy. Journal of Computational Physics 384, 151–169. doi:10.1016/j.jcp.2019.01.017.

Wen, C.Y., Yu, Y.H., 1966. A generalized method for predicting the minimum fluidization velocity. AIChE Journal 12, 610–612. doi:10.1002/aic.690120343.

Wen, Z., Zhang, L., Tang, H., Zeng, J., He, X., Yang, Z., Zhao, Y., 2022. A review on numerical simulation of proppant transport: Eulerian–lagrangian views. Journal of Petroleum Science and Engineering 217, 110902. doi:10.1016/j.petrol.2022.110902.

Wharton, G., Mohajeri, S.H., Righetti, M., 2017. The pernicious problem of streambed colmation: a multi–disciplinary reflection on the mechanisms, causes, impacts, and management challenges. WIREs Water 4. doi:10.1002/wat2.1231.

Wilcock, P.R., DeTemple, B.T., 2005. Persistence of armor layers in gravel–bed streams. Geophysical Research Letters 32. doi:10.1029/2004GL021772.

Wildt, D., Hauer, C., Habersack, H., Tritthart, M., 2022. Les two-phase modelling of suspended sediment transport using a two-way coupled euler–lagrange approach. Advances in Water Resources 160, 104095. doi:10.1016/j.advwatres.2021.104095.

Wooster, J.K., Dusterhoff, S.R., Cui, Y., Sklar, L.S., Dietrich, W.E., Malko, M., 2008. Sediment supply and relative size distribution effects on fine sediment infiltration into immobile gravels. Water Resources Research 44. doi:10.1029/2006WR005815.

Wu, F.C., Huang, H.T., 2000. Hydraulic resistance induced by deposition of sediment in porous medium. Journal of Hydraulic Engineering 126, 547–551. doi:10.1061/(ASCE)0733-9429(2000)126:7(547).

Yeh, F., Lei, U., 1991. On the motion of small particles in a homogeneous isotropic turbulent flow. Physics of Fluids A: Fluid Dynamics 3, 2571–2586. doi:https://doi.org/10.1063/1.858198.

Yusuf, R., Halvorsen, B., Melaaen, M.C., 2011. Eulerian–eulerian simulation of heat transfer between a gas–solid fluidized bed and an immersed tube-bank with horizontal tubes. Chemical Engineering Science 66, 1550–1564. doi:10.1016/j.ces.2010.12.015.

Zhang, J., Li, T., Ström, H., Wang, B., Løvås, T., 2023. A novel coupling method for unresolved cfd-dem modeling. International Journal of Heat and Mass Transfer 203, 123817. doi:10.1016/j.ijheatmasstransfer.2022.123817.

Zhong, D., Wang, G., Sun, Q., 2011. Transport equation for suspended sediment based on two-fluid model of solid/liquid two-phase flows. Journal of Hydraulic Engineering 137, 530–542. doi:10.1061/(ASCE)HY.1943-7900.0000331.

Zhou, H., Wang, G., Jia, C., Li, C., 2019. A novel, coupled cfd-dem model for the flow characteristics of particles inside a pipe. Water 11, 2381. doi:10.3390/w11112381.

Zhou, L., Li, T., Ma, H., Liu, Z., Dong, Y., Zhao, Y., 2024. Development and verification of an unresolved cfd-dem method applicable to different-sized grids. Powder Technology 432, 119127. doi:10.1016/j.powtec.2023.119127.

Zhou, Z.Y., Kuang, S.B., Chu, K.W., Yu, A.B., 2010. Discrete particle simulation of particle–fluid flow: model formulations and their applicability. Journal of Fluid Mechanics 661, 482–510. doi:10.1017/S002211201000306X.

Zhu, H.P., Zhou, Z.Y., Yang, R.Y., Yu, A.B., 2007. Discrete particle simulation of particulate systems: Theoretical developments. Chemical Engineering Science 62, 3378–3396. doi:10.1016/j.ces.2006.12.089.